Absorption and dispersion in atomic vapours: Applications to interferometery

Graham Thomas Purves

Absorption And Dispersion In Atomic Vapours: Applications To Interferometery

Graham Thomas Purves

A thesis submitted in partial fulfilment
of the requirements for the degree of
Doctor of Philosophy

Department of Physics
University of Durham
31st August 2006

Absorption And Dispersion In Atomic Vapours: Applications To Interferometry

Graham Thomas Purves

Abstract

Continuous wave extended cavity diode lasers are used to measure the absorptive and dispersive properties of the $5\ ^2S_{1/2} \rightarrow 5\ ^2P_{3/2}$ resonance, at 780 nm, in Rubidium (Rb) vapour. The Doppler-broadened hyperfine transitions are studied both with and without a pump beam. The investigation concentrates on three-level Λ-systems, realized in the presence of a pump beam, exhibiting Electromagnetically Induced Transparency (EIT). Electromagnetically Induced Absorption (EIA) is also seen.

The EIT and EIA resonances can be several orders of magnitude narrower than the natural line width of the atomic transitions in the absence of the pump beam. Further, the EIT resonances are sensitive to applied magnetic fields.

The narrowest resonances measured in this work have a full-width at half-maximum of $\sim$ 80 kHz. This is limited by the transit time of the atoms through the probe and pump beams.

Predictions of theoretical calculations and models are compared to experimental results. The theory of beam splitters and interferometers is developed to enable the implementation of a Sagnac interferometer in a novel "biased" alignment. This allows the dispersion of atomic resonances to be measured directly.

The direct measurement of the dispersion of the narrow EIT features in a "biased" Sagnac interferometer is presented. Such a signal is ideally suited to precision measurement applications such as inertial sensing and magnetometry.

Dedicated to

Thomas Burns Purves and "the appliance of science".

Declaration

I confirm that no part of the material offered has previously been submitted by myself for a degree in this or any other University. Where material has been generated through joint work, the work of others has been indicated.

Graham Thomas Purves
Durham, 31st August 2006

Acknowledgements

It goes without saying that I acknowledge the assistance of my joint supervisors, Dr. Ifan Hughes and Prof. Charles Adams, without whom this work would not have been possible.

I am indebted to those who have proof read various sections of my thesis, providing valuable feedback and alternate spelling suggestions, especially Ifan, Charles, Matt Pritchard and Mark Bason.

Dr. David Smith, who essentially shared my lab during the afternoons of my PhD, cannot be allowed to go without comment. Nor can all of those who made the back corner of the coffee room an extension of the Atmol empire.

Thanks also go to Ian Manfren, Wayne Dobby and the other teaching lab technicians for the extended loan of much of the equipment which allowed me to complete my PhD. I must also thank Simon Cornish for the longest ever "week" long loan of a camera, that proved invaluable.

John Scott and Tom Jackson and the other members of the electronics workshop provided a great deal of help with the manufacture of devices and advice on various aspects of electronics. I am also grateful to the mechanical workshop for the machining of various vital pieces of equipment.

I would like to thank the legendary Prof. Derek Stacey for first introducing me to the world of atomic and optical physics.

Finally, I would like to express my thanks to my family and friends for support, food and appropriate drinks, to help me through the last 32 528 $\pm$ 7 hours.

Contents

List of Figures

List of Tables

Chapter 1

Introduction

This thesis undertakes an investigation into the absorption and dispersion of rubidium (Rb) vapour at room temperature. More specifically, the absorption and dispersion of Electromagnetically Induced Transparency (EIT) resonances on the D_2 transition of Rb are investigated using a Sagnac interferometer.

1.1 Motivation

Narrow resonances lend themselves to being used as the basis for making very sensitive measurements. Electromagnetically Induced Transparency resonances can be extremely narrow, hence they are of great interest in the field of metrology.

1.1.1 Applications of EIT

EIT is the phenomena of reducing the absorption of a probe beam passing through a medium, by applying a second pump beam to that medium. The spectral width of the reduced absorption, or transparency, can be extremely narrow, and is largely limited by the experimental parameters, not fundamental atomic line widths, § 3.3 .

Slow light

Associated with the modification to the absorption of a medium by EIT there is a concomitant modification of the dispersion. This modification of the dispersion of the medium can lead to significant changes in the group velocity of the medium. In the case of EIT this generally leads to a significant reduction in the group velocity of a probe pulse. However making use of Electromagnetically Induced Absorption (EIA), § 3.6, superluminal and even negative group velocities can be achieved. The excellent review article by Milonni, [1], addresses the whole field of modification of the group velocity of light.

Early measurements of "slow light" by Kasapi *et al.*, [2], and Schmidt *et al.*, [3], achieved group velocities of c/165 in lead vapour, and c/3000 in caesium vapour respectively.

Hau *et al.*, [4], first observed extremely slow group velocities, 17 ms^{-1}, in a sodium Bose-Einstein condensate at a temperature of 50 nK. This work was closely followed by that of Kash *et al.*, [5], and Budker *et al.*, [6]. Kash measured a group velocity of the order of 90 ms^{-1} in an optically dense ^{87}Rb vapour at 360 K, on the D_1 transition, whilst Budker, [6], achieved group velocities as low as 8 ms^{-1} in room temperature ^{85}Rb on the D_1 transition.

Lukin and Imamoğlu, [7], propose a scheme which utilises the reduced group velocity due to EIT to enable one single-photon pulse to "coherently control or manipulate the quantum state" of another pulse. This enables the entanglement of photon pulses and as such has applications in the field of quantum information processing.

A direct consequence of a reduced group velocity is a reduction in the spatial extent of a pulse of light. Light pulses are compressed by the ratio of c/v_g where c is the velocity of light in a vacuum and v_g is the group velocity of light. This in turn means that in the experiments of Hau, Kash and Budker, the length of the pulses of light were compressed by a factor of the order of 10^6–10^8, hence pulses that are normally several km in length are compressed to the extent that they could be wholly contained within a typical vapour cell.

A recent advance has shown that slow light allows a pulse of light to be deflected by a magnetic field. Karpa and Weitz, [8], demonstrate that dark-state

polaritons (light pulses stored as atomic excitations), [9], have a non-zero magnetic moment, in contrast to photons. A magnetic field is applied along the axis of a Rb vapour cell and pump and probe beams. The magnetic field has a gradient across the cell perpendicular to the pump and probe beams. The probe beam is deflected by an angle proportional to the magnetic field gradient and the magnetic moment of the polariton. The estimated magnetic moment of the polariton is found to be 5.1×10^{-24} J T^{-1} or 0.55 μ_B .

Stored light

The next logical step was to store such optical pulses within the "slow-light" medium. This would allow propagating light pulses to be stored as atomic excitations within a medium which, in principle, could be retrieved at a later time. These atomic excitations are known as "dark-state polaritons", [9], and they offer the potential to be used as a quantum memory for photons, [10]. The review article by Lukin, [11], thoroughly covers the field of trapping and manipulating the states of photons, with particular interest in the application to quantum information.

The storage of light pulses was achieved simultaneously by Liu *et al.*, [12], and by Phillips *et al.*, [13].

Liu *et al.* observed the storage of a pulse of light for 1 ms in a cloud of sodium, on the D_1 transition, at a temperature of 0.9 μK. EIT is used to slow a pulse of light. When that probe pulse is contained fully within the medium, the pump field is turned off. The probe pulse is stored in the medium. At some time later (1 ms) the pump field is turned on and the probe pulse is regenerated and leaves the medium.

Phillips *et al.* performed their measurements of stored light pulses in Rb vapour, on the D_1 transition, at a temperature of 343–363 K. The medium was prepared with a cw pump field. A weak orthogonally polarized pulse is sent into the medium. A fraction of the pulse is allowed to propagate through the medium before the pump field is turned off over a time of ~ 3 μs. After a time of order 100 μs the pump field is turned back on. The stored portion of the probe pulse is then seen to leave the medium.

More intricate schemes have since been proposed and implemented. One such

scheme utilises pump beams propagating both in forward and backward direction, setting up a standing wave in the medium, [14, 15]. This can allow for both storage and regeneration of a probe pulse as well as reflection of the probe beam. The difference between this scheme for storing optical pulses and those mentioned above is in the way that the pulses are stored in the medium. In this case as opposed to the pulse being stored as a dark-state polariton the authors argue that it is stored as an optical pulse. The standing wave of the pump beams leads to a modulation in the medium's absorption of the probe pulse. Bragg reflections off the sharp absorption peaks result in a vanishing group velocity for the probe pulse.

The first implementation of stored light in a solid was carried out by Longdell *et al.*, [16]. Using EIT in praseodymium doped Y_2SiO_5 storage times of greater than 1 s have been achieved.

Inertial sensing

Zimmer and Fleischhauer, [17], have proposed a scheme that takes advantage of the slow-light aspect of EIT to increase the sensitivity of Sagnac interferometers. Sagnac interferometers are widely used to detect the rotation of a system and will be addressed in greater detail in chapter 5. Sagnac interferometers consist of two arms counter-propagating around the same path. Shifts in the interference pattern at the output are seen when there is a phase shift for one arm relative to the other. Hence Sagnac interferometers are frequently used to detect rotations — the rotation having the effect of shortening the path length of one arm relative to the other.

Magnetometry

In the case that the levels within the system exhibiting EIT are magnetically sensitive, then a change in magnetic field shifts the frequency of the centre of the resonance. The steep change in dispersion associated with EIT at the centre of the resonance offers the potential to make sensitive measurements of magnetic field. In the narrow range about the centre of the resonance the dispersion varies linearly with frequency. For this reason measuring the dispersion offers a higher sensitivity as well as information on the direction of the shift, that would

not be afforded by measuring the absorption.

Such a scheme was first proposed by Scully and Fleischhauer, [18], and later extended by Lee *et al.*, [19]. This scheme would allow for a potential maximum sensitivity of 1 fT in 1 s, [20]. This potential sensitivity is superior to the best magnetometers today, both SQUID (superconducting quantum interference device) and optical pumping magnetometers, [20]. Measuring the transmission of a weak probe through a vapour cell will not directly give information on the dispersion of the medium. Scully proposes using a Mach-Zehnder interferometer to measure the dispersion of the medium.

Advances in this field have now led to the development of miniaturized magnetometers, 12 mm^3 in size, with a sensitivity of 50 pT $Hz^{-\frac{1}{2}}$, [21].

High efficiency photon detection

Independently Imamoğlu, [22], and James and Kwiat, [23], proposed similar methods for high efficiency optical detectors with photon number resolution.

Imamoğlu proposed a scheme involving four levels. Levels $|b\rangle$ and $|a\rangle$ are connected via a probe field. Levels $|c\rangle$ and $|a\rangle$ are connected via the pump field and together the three levels form a Λ system. Initially both the probe and pump field are turned on. The pump field is turned off adiabatically. The probe field is left stored as an atomic excitation in state $|c\rangle$. A detection beam is turned on that is resonant with $|c\rangle$ and a fourth state $|d\rangle$. Spontaneous emission from $|d\rangle$ to $|c\rangle$ is recorded, revealing the number of atoms in state $|c\rangle$, and hence the number of photons stored from the probe.

The scheme proposed by James and Kwiat also involves four different states. A pump field is resonant with $|c\rangle$ and $|a\rangle$. Spontaneous emission occurs from state $|a\rangle$ to state $|b\rangle$. Once the population has been pumped into $|b\rangle$, the photon field (to be measured) is directed into the medium along with a strong pulse. The photon field is detuned from the transition $|b\rangle$ to $|a\rangle$ and the strong pulse is detuned from the $|c\rangle$ to $|a\rangle$ transition in order that a two-photon Raman resonance is met between $|b\rangle$ and $|c\rangle$. Lastly a fourth beam is turned on that is resonant with the transition from $|c\rangle$ to $|d\rangle$. $|d\rangle$ is such that it can only decay spontaneously back to $|c\rangle$, and it does this on a very short time scale. The scattered light from the spontaneous emission is detected, this corresponds to

the number of atoms in pumped into state $|c\rangle$ via the Raman transition, and hence the number of photons in the original incident photon field.

Isotope discrimination

Isotope discrimination is another application of EIT. Kasapi, [24], has shown that by rendering one isotope opaque while rendering the other transparent it is possible to detect an isotope three-thousand times less abundant than the prevalent isotope. A system of two isotopes with non-identical spectra is considered. Pump and probe beams are applied that are on resonance for one isotope, while for the other isotope these beams are slightly off resonance. Hence one isotope is rendered maximally transparent to the probe whilst the other is not. By careful selection of the strength of the coupling beam it is possible to ensure that the second isotope is not only opaque, but is maximally opaque.

This thesis

Specific motivation arises from the fact that a Sagnac interferometer can be used to measure directly the dispersion of a medium, with an inherent stability against vibration greater than a Mach-Zehnder interferometer. Further motivation arises from the proposal that Electromagnetically Induced Transparency could enhance the rotational sensitivity of a Sagnac interferometer, [25, 26], to produce a hybrid optical-matter-wave Sagnac interferometer, [17].

At the outset of this work it is understood that no other research group have made measurements of Electromagnetically Induced Transparency using a Sagnac interferometer.

1.2 Thesis Layout

1.2.1 Chapters

Chapter 2

Chapter 2 addresses the absorption and dispersion of a weak probe beam in a two-level atom. Starting with the Liouville equations, the optical-Bloch equations are derived for the two-level atom. The solutions to the optical-Bloch equations are related to the complex susceptibility of the medium, which in turn is related to the complex refractive index. From the complex refractive index the absorption and dispersion of the medium can be derived.

As the atomic systems under consideration are at room temperature, Doppler broadening of the transition between the two levels is introduced. This in turn allows realistic calculations of the absorption profile of the D_2 line of Rb to be made.

The experimental apparatus necessary to make such weak probe measurements is addressed. Details are given on the construction and use of the Extended Cavity Diode Lasers and the photodiode circuits required to produce and measure the transmission of the weak probe respectively.

Measurements of the absorption are presented and compared to the theoretical predictions.

Finally natural line width spectroscopy is addressed. A second beam is introduced that allows for a significant increase in the resolution of the spectra. The experimental set-up required is introduced and the resulting spectra are presented.

Chapter 3

Chapter 3 expands to consider three-level systems interacting with two fields. The theory leading to Coherent Population Trapping (CPT) and Electromagnetically Induced Transparency (EIT) is presented.

The optical-Bloch equations are again used, this time to predict the absorption and dispersion of a three-level system interacting with a strong pump and a

weak probe beam. Mechanisms which lead to the modification, and specifically broadening, of the EIT resonances are introduced and their contributions are considered.

Electromagnetically Induced Absorption (EIA) is briefly addressed. This is a phenomenon that appears similar to EIT, but relies on the presence of more than three levels in the system under investigation.

Finally group velocity modification due to EIT resonances is addressed.

Chapter 4

In chapter 4 the experimental measurements of EIT and EIA transmission spectra are presented. The experimental procedures necessary to make such measurements are addressed initially. EIT and EIA spectra obtained using a double-scan technique are presented.

Finally more conventional single-scan EIT traces are presented. By carrying out fits of theoretical line shapes to the recorded spectra, the variation in width of the resonances is investigated for varying pump and probe powers, and for sensitivity to magnetic field.

Chapter 5

Chapter 5 presents the theory and background of the Sagnac interferometer.

The chapter begins with a brief review of the development of the Sagnac interferometer along with its main uses and the different types of Sagnac interferometer.

The behaviour of beam splitters is then addressed. This is used to calculate the output from a Sagnac interferometer in the case that the counter-propagating beams experience different susceptibilities of the medium. The case of "biased" alignment is considered, and the effect that this will have on the output signals is calculated.

Chapter 6

In chapter 6 the experimental Sagnac interferometer is studied. The experimental techniques required to align the interferometer and the photodiode circuit

used to measure the output are all addressed.

The output spectra from the Sagnac interferometer for both double-scan and single-scan measurements are presented. The process required to obtain the transmission and dispersion spectra from the Sagnac output is outlined.

The line shape of the EIT resonances is compared to three different theoretical models, and the width of the EIT resonances is studied as functions of pump and probe power.

Chapter 7

The conclusions drawn from the work presented in the preceding chapters is presented. Potential routes for future development of this project are also highlighted.

1.2.2 Appendices

The eight appendices at the end of this thesis provide supplementary information to the main contents of the main body of the thesis.

Appendix A contains Rb data and constants used in this work.

Appendix B outlines the error analysis used in the work presented in this thesis.

Appendix C outlines the full derivation of the optical-Bloch equations for both the two-level and three-level atom presented in chapters 2 and 3.

Appendix D contains the derivation of the linear approximation of the Doppler effect.

Appendix E contains the *Mathematica* code used to calculate weak probe absorption on the Rb D_2 line.

Appendix F shows the circuit diagram for the saw-tooth signal generating circuit, used to make the double-scan measurements.

Appendix G explains the principles behind lock-in detection.

Appendix H shows the relationship between the power in a Gaussian beam and the peak and mean intensity.

1.3 Published Work

During this PhD three papers have been written.

- *Non-Linear Sagnac Interferometry for Pump-Probe Dispersion Spectroscopy*,
  G. Jundt, G. T. Purves, C. S. Adams and I. G. Hughes,
  European Physical Journal D **27**, 273–276 (2003).
- *Refractive Index Measurement By Probe-Beam Deflection*,
  G. T. Purves, G. Jundt, C. S. Adams and I. G. Hughes,
  European Physical Journal D **29**, 433–436 (2004).
- *Sagnac Interferometry in a Slow-Light Medium*,
  G. T. Purves, C. S. Adams and I. G. Hughes,
  Physical Review A **74**, 023805 (2006).

Work published in these papers also appears in this thesis, especially, *Sagnac Interferometry in a Slow-Light Medium*, which is largely based on chapter 6, of this thesis.

Chapter 2

Weak Probe Beam Absorption and Dispersion

It is preferable to record the absorption and dispersion of a medium without modifying either of these properties in taking the measurement. To this end a weak probe beam is employed. A probe beam can be described as being weak if its intensity is sufficiently low that it does not modify the absorption properties of the medium under investigation.

An atom absorbing a photon on a closed transition will subsequently undergo spontaneous emission back to the original ground state, from which it can absorb another probe-beam photon. However if there is a mechanism whereby the atom can spontaneously decay, from the excited state, to a lower state which is off-resonance with the probe beam, then should this occur that atom will no longer absorb probe-beam photons.

If the probe is sufficiently intense that a significant proportion of the atoms is in the excited state, or has decayed to an off-resonant state, then the probe absorption will be modified and the beam cannot be considered to be weak.

An investigation into how the intensity of the probe beam affects the absorption of that probe beam is presented in the work of Smith and Hughes, [27]. The authors find that it is not sufficient to define the beam as weak if the intensity is small (for example $I \ll I_{\mathrm{SAT}}$, § 2.2.1). Instead consideration must be taken of the transit time of the atoms through the probe beam and how that compares to the hyperfine pumping time. If the hyperfine pumping time is comparable to

the transit time, the probe beam will pump the medium. Atoms in Rb vapour at room temperature will have a transit time, through a beam of diameter ~ 2 mm, of ~ 10 μs. For beam intensities of $I \ll I_{\mathrm{SAT}}$, the pumping time will be $\sim \tau \times I_{\mathrm{SAT}}/I$, where τ is the lifetime of the excited state.

2.1 Weak Probe Theory

Throughout this chapter, all calculations and theory are based upon a simple two-level picture of an atom with a near-resonant laser field, as shown in Fig. 2.1. The two levels are $|\mathrm{a}\rangle$, the excited state, and $|\mathrm{b}\rangle$, the ground state. The levels are separated by an energy $\hbar\omega_{\mathrm{ab}}$. The laser field has frequency ω_{pr} with a detuning from resonance δ_{pr}. The strength of the atom-field interaction is given by the Rabi frequency Ω_{pr} (see appendix C, equation C.6 on page 161). The line width of the excited and ground states are given by Γ_{a} and Γ_{b}, respectively.

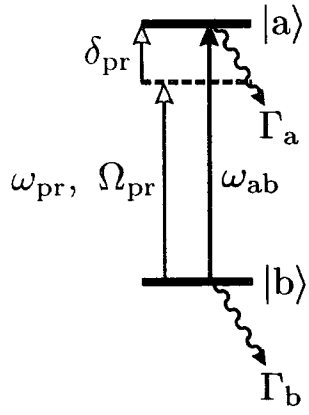

Figure 2.1: A two-level system. The two levels are linked by one laser field. The field has angular frequency ω_{pr} and Rabi frequency Ω_{pr}. The field has a detuning from resonance of δ_{pr}. The excited and ground state have line widths, Γ_{a} and Γ_{b}, respectively.

2.1.1 Density Matrix

Consider an ensemble of particles, all of which may be in a pure state. The state of the ensemble of particles will generally be a mixture of those states and

therefore not necessarily a pure state itself. In this case the ensemble cannot be represented by a wavefunction. Such a system can be described by a density operator, ρ. For a pure state, ρ is defined as:

$$\rho = |\psi\rangle\langle\psi| , \tag{2.1}$$

where $|\psi\rangle$ is the state under consideration. For an idealised two-level atomic system in the state,

$$|\psi\rangle = c_a|a\rangle + c_b|b\rangle , \tag{2.2}$$

the density matrix is:

$$\begin{pmatrix} \rho_{aa} & \rho_{ab} \\ \rho_{ba} & \rho_{bb} \end{pmatrix} = \begin{pmatrix} c_a c_a^* & c_a c_b^* \\ c_b c_a^* & c_b c_b^* \end{pmatrix} . \tag{2.3}$$

Each element in the density matrix is a product of probability amplitudes. The terms on the diagonal, ρ_{aa} and ρ_{bb}, give the population of the states, whereas the off-diagonal terms give the coherences between states.

For a non-pure, mixed state, the density matrix is defined as:

$$\rho = \sum_i P_i|\psi_i\rangle\langle\psi_i| , \tag{2.4}$$

where P_i is the probability of being in state $|\psi_i\rangle$.

Liouville Equation

When dealing with individual pure states the Schrödinger equation describes how the states evolve. In principle this can be extended to apply to many particle systems too. As the number of particles increases, the number of calculations necessary to describe how the whole system evolves soon becomes prohibitive. An alternative approach should be taken. Consider a state, $|\psi(t_0)\rangle$, that at some time, t, will have evolved to $|\psi(t)\rangle$, such that:

$$|\psi(t)\rangle = U(t, t_0)|\psi(t_0)\rangle , \tag{2.5}$$

obviously,

$$U(t = t_0, t_0) = 1 . \tag{2.6}$$

Substituting equation 2.5 into the Schrödinger equation,

$$|\dot{\psi}\rangle = -\frac{\mathrm{i}}{\hbar}\mathscr{H}|\psi\rangle \ , \tag{2.7}$$

we obtain,

$$\mathrm{i}\hbar\left[\frac{\partial U(t,t_0)}{\partial t}|\psi(t_0)\rangle + U(t,t_0)\frac{\partial|\psi(t_0)\rangle}{\partial t}\right] = |\psi(t_0)\rangle\mathscr{H}U(t,t_0) + U(t,t_0)\mathscr{H}|\psi(t_0)\rangle \ , \tag{2.8}$$

$$\therefore \ \mathrm{i}\hbar\frac{\partial U(t,t_0)}{\partial t} = \mathscr{H}U(t,t_0) \ . \tag{2.9}$$

From equations 2.6 and 2.9,

$$U(t,t_0) = e^{-\frac{\mathrm{i}}{\hbar}\mathscr{H}(t-t_0)} \ . \tag{2.10}$$

If we now consider a variable $\mathscr{D}$ which evolves when the state $|\psi(t)\rangle$ evolves as per equation 2.5 then,

$$\langle\psi(t)|\mathscr{D}|\psi(t)\rangle = \langle\psi(t_0)|U^\dagger\mathscr{D}U|\psi(t_0)\rangle \ , \tag{2.11}$$

$$= \langle\psi(t_0)|\mathscr{D}_0|\psi(t_0)\rangle \ , \tag{2.12}$$

$$\Rightarrow U^\dagger\mathscr{D}U = \mathscr{D}_0 \ , \tag{2.13}$$

and as

$$U^\dagger U = 1 \ , \tag{2.14}$$

then,

$$\mathscr{D} = U\mathscr{D}_0U^\dagger \ . \tag{2.15}$$

Differentiating with respect to t,

$$\frac{\mathrm{d}\mathscr{D}}{\mathrm{d}t} = U\mathscr{D}_0\frac{\partial U^\dagger}{\partial t} + U\frac{\partial\mathscr{D}_0}{\partial t}U^\dagger + \frac{\partial U}{\partial t}\mathscr{D}_0U^\dagger \ , \tag{2.16}$$

$$= \frac{1}{\mathrm{i}\hbar}(\mathscr{H}\mathscr{D} - \mathscr{D}\mathscr{H}) + U\frac{\partial\mathscr{D}_0}{\partial t}U^\dagger \ , \tag{2.17}$$

$$\Rightarrow \frac{\mathrm{d}\mathscr{D}}{\mathrm{d}t} = \frac{1}{\mathrm{i}\hbar}[\mathscr{H},\mathscr{D}] + \frac{\partial\mathscr{D}}{\partial t} \ . \tag{2.18}$$

If $\mathscr{D}$ is in fact the density matrix ρ, it follows that,

$$\dot{\rho} = \frac{\mathrm{i}}{\hbar}[\rho,\mathscr{H}] + \frac{\partial\rho}{\partial t} \ , \tag{2.19}$$

where,

$$\frac{\partial \rho}{\partial t} = -\gamma\rho \ , \tag{2.20}$$

$$\Longrightarrow \quad \dot{\rho} = \frac{\mathrm{i}}{\hbar}[\rho, \mathscr{H}] - \gamma\rho \ . \tag{2.21}$$

This is known as the Liouville equation, and it is the density operator equivalent of the Schrödinger equation.

2.2 Optical-Bloch Equations

The optical-Bloch equations are a useful tool for understanding the interaction of an atomic system with near-resonant monochromatic radiation. The evolution of both the coherences and the populations can be derived from the Liouville equation, equation 2.21.

For a two-level atom interacting with near-monochromatic radiation the Hamiltonian for the system is given by,

$$\mathscr{H} \ = \ \mathscr{H}_{\mathrm{A}} + V_{\mathrm{pr}} \ . \tag{2.22}$$

The interaction of the atoms with the radiation field is given by,

$$V_{\mathrm{pr}} \ = \ -\mathbf{d} \cdot \mathbf{E}_{\mathrm{pr}} \cos\left(\omega_{\mathrm{pr}} t\right) \ , \tag{2.23}$$

where $\mathbf{E}_{\mathrm{pr}} \cos\left(\omega_{\mathrm{pr}} t\right)$ is the laser field, and $\mathbf{d}$ is the atomic dipole. For the two-level atom, the dipole is given by,

$$\mathbf{d} \ = \ \mathbf{d}_{\mathrm{ba}} \left(|\mathrm{a}\rangle\langle \mathrm{b}| + |\mathrm{b}\rangle\langle \mathrm{a}|\right) \ . \tag{2.24}$$

The full derivation of the optical-Bloch equations is given in appendix C. In the case of a two-level atom with a near-resonant monochromatic field the equations of motion for the populations and coherences are given by, equations C.36, C.37, and C.38,

$$\dot{\widetilde{\rho}}_{\mathrm{ab}} \ = \ -\left(\gamma_{\mathrm{ab}} - \mathrm{i}\delta_{\mathrm{pr}}\right)\widetilde{\rho}_{\mathrm{ab}} + \frac{\mathrm{i}\Omega_{\mathrm{pr}}}{2}\left(\rho_{\mathrm{aa}} - \rho_{\mathrm{bb}}\right) \ ,$$

$$\dot{\rho}_{\mathrm{aa}} \ = \ \frac{\mathrm{i}\Omega_{\mathrm{pr}}}{2}\left(\widetilde{\rho}_{\mathrm{ab}} - \widetilde{\rho}_{\mathrm{ba}}\right) - \Gamma_{\mathrm{a}}\rho_{\mathrm{aa}} \ ,$$

$$\dot{\rho}_{\mathrm{bb}} \ = \ \frac{\mathrm{i}\Omega_{\mathrm{pr}}}{2}\left(\widetilde{\rho}_{\mathrm{ba}} - \widetilde{\rho}_{\mathrm{ab}}\right) - \Gamma_{\mathrm{b}}\rho_{\mathrm{bb}} + \Gamma_{\mathrm{a}}\rho_{\mathrm{aa}} \ ,$$

where $\widetilde{\rho}_{ab}$ and $\widetilde{\rho}_{ab}$ are the slow variables, see appendix C .

The Rabi frequency, Ω_{pr} , of the dipole interaction is given by equation C.6 ,

$$\Omega_{pr} = -\frac{\mathbf{d}_{ba} \cdot \mathbf{E}_{pr}}{\hbar} .$$

In the steady state,

$$\begin{aligned} \dot{\widetilde{\rho}}_{ab} &= \dot{\widetilde{\rho}}_{aa} , \\ &= \dot{\widetilde{\rho}}_{bb} , \\ &= 0 , \end{aligned} \tag{2.25}$$

and in the case that the two-level system is closed,

$$\Gamma_b = 0 , \tag{2.26}$$

$$\text{and} \quad \rho_{aa} + \rho_{bb} = 1 . \tag{2.27}$$

In this regime the optical-Bloch equations reduce to,

$$\Gamma_a \rho_{aa} = \frac{i\Omega_{pr}}{2} \cdot (\widetilde{\rho}_{ab} - \widetilde{\rho}_{ba}) , \tag{2.28}$$

$$(\gamma_{ab} - i\delta_{pr})\ \widetilde{\rho}_{ab} = \frac{i\Omega_{pr}}{2} \cdot (\rho_{aa} - \rho_{bb}) . \tag{2.29}$$

Substituting from equation 2.27 into equation 2.29 leads to,

$$\widetilde{\rho}_{ab} = \frac{i\Omega_{pr}}{2(\gamma_{ab} - i\delta_{pr})} \cdot (2\rho_{aa} - 1) . \tag{2.30}$$

Now substituting equation 2.30 and its complex conjugate into equation 2.28, allows the solution for ρ_{aa} to be obtained,

$$\Gamma_a \rho_{aa} = -\frac{\Omega_{pr}^2}{2(\gamma_{ab}^2 + \delta_{pr^2})} \cdot \gamma_{ab} (2\rho_{aa} - 1) , \tag{2.31}$$

$$\therefore \quad \rho_{aa} = \frac{1}{2} \cdot \frac{\Omega_{pr}^2 \gamma_{ab}}{\gamma_{ab}\Omega_{pr}^2 + \Gamma_a (\gamma_{ab}^2 + \delta_{pr}^2)} , \tag{2.32}$$

As the two-level system under consideration is closed which leads to $\Gamma_b = 0$, then from equation C.15 on page 162 ,

$$\gamma_{ab} = \frac{\Gamma_a}{2} . \tag{2.33}$$

Thus it follows that equation 2.32 reduces to,

$$\rho_{aa} = \frac{1}{2} \cdot \frac{\Omega_{pr}^2/2}{\Omega_{pr}^2/2 + (\Gamma_a/2)^2 + \delta_{pr}^2} , \tag{2.34}$$

To find the steady-state solution for the coherence between the two levels, substitute equation 2.34 into equation 2.30 ,

$$\widetilde{\rho}_{ab} = \frac{i\Omega_{pr}}{2\left(\Gamma_a/2 - i\delta_{pr}\right)} \cdot \left(2\left(\frac{1}{2} \cdot \frac{\Omega_{pr}^2/2}{\Omega_{pr}^2/2 + \left(\Gamma_a/2\right)^2 + \delta_{pr}^2} \right) - 1 \right) ,$$

$$\therefore \quad \widetilde{\rho}_{ab} = \frac{\Omega_{pr}}{2} \cdot \left(\frac{\delta_{pr} - i\left(\Gamma_a/2\right)}{\Omega_{pr}^2/2 + \left(\Gamma_a/2\right)^2 + \delta_{pr}^2} \right) . \tag{2.35}$$

Bloch Vector Components

An alternative representation of the solutions to the optical-Bloch equations is in the form of the components of the Bloch vector. The three components of the Bloch vector are,

$$u = \frac{\widetilde{\rho}_{ab} + \widetilde{\rho}_{ba}}{2} , \tag{2.36}$$

$$v = \frac{\widetilde{\rho}_{ba} - \widetilde{\rho}_{ab}}{2i} , \tag{2.37}$$

$$\text{and} \quad w = \frac{\rho_{aa} - \rho_{bb}}{2} . \tag{2.38}$$

Expressed in this way the solutions have a much more apparent physical significance. w is half the difference between the populations of $|a\rangle$ and $|b\rangle$, so,

$$w + \frac{1}{2} = \rho_{aa} . \tag{2.39}$$

To interpret the physical significance of u and v it is instructive to look at the expectation value of $\mathbf{d}$.

$$\langle \mathbf{d} \rangle = \mathrm{Tr}(\rho \mathbf{d}) , \tag{2.40}$$

$$= \mathbf{d}_{ba}(\rho_{ba} + \rho_{ab}) , \tag{2.41}$$

From equation C.22 ,

$$\langle \mathbf{d} \rangle = \mathbf{d}_{ba}(\widetilde{\rho}_{ba} e^{i\omega_{pr}t} + \widetilde{\rho}_{ab} e^{-i\omega_{pr}t}) , \tag{2.42}$$

$$= 2\mathbf{d}_{ba}\big(u\cos(\omega_{pr}t) - v\sin(\omega_{pr}t)\big) . \tag{2.43}$$

Hence u is proportional to the amplitude of the component of $\langle \mathbf{d} \rangle$ in phase with the incident laser field, and v is proportional to the amplitude of the component

of $\langle \mathbf{d} \rangle$ in quadrature with the incident laser field. Writing $\langle \mathbf{d} \rangle$ in terms of its real and imaginary components,

$$\langle \mathbf{d} \rangle = \mathbf{d}_{\mathrm{R}} + i\mathbf{d}_{\mathrm{I}} , \tag{2.44}$$

$$\Longrightarrow \quad \mathbf{d}_{\mathrm{R}} = 2\mathbf{d}_{\mathrm{ba}} u , \tag{2.45}$$

$$\Longrightarrow \quad \mathbf{d}_{\mathrm{I}} = 2\mathbf{d}_{\mathrm{ba}} v . \tag{2.46}$$

The steady state solutions of the Bloch vector equations can be derived by substituting equations 2.36, 2.37 and 2.38 into equations 2.35 and 2.34 ,

$$u_{\mathrm{st}} = \frac{\Omega_{\mathrm{pr}}}{2} \cdot \frac{\delta_{\mathrm{pr}}}{\delta_{\mathrm{pr}}^2 + (\Gamma_{\mathrm{a}}/2)^2 + \Omega_{\mathrm{pr}}^2/2} , \tag{2.47}$$

$$v_{\mathrm{st}} = \frac{\Omega_{\mathrm{pr}}}{2} \cdot \frac{\Gamma_{\mathrm{a}}/2}{\delta_{\mathrm{pr}}^2 + (\Gamma_{\mathrm{a}}/2)^2 + \Omega_{\mathrm{pr}}^2/2} , \tag{2.48}$$

$$w_{\mathrm{st}} + \frac{1}{2} = \frac{1}{2} \cdot \frac{\Omega_{\mathrm{pr}}^2/2}{\delta_{\mathrm{pr}}^2 + (\Gamma_{\mathrm{a}}/2)^2 + \Omega_{\mathrm{pr}}^2/2} . \tag{2.49}$$

2.2.1 Saturation of the Transition

The saturation parameter, S, describes the degree to which a given transition is saturated by a field of strength Ω_{pr}, and detuning δ_{pr},

$$S = \frac{{\Omega_{\mathrm{pr}}}^2/2}{\delta_{\mathrm{pr}}^2 + (\Gamma_{\mathrm{a}}/2)^2} . \tag{2.50}$$

Substituting the saturation parameter, equation 2.50 into the steady-state optical-Bloch equations 2.47, 2.48 and 2.49, leads to,

$$u_{\mathrm{st}} = \frac{\delta_{\mathrm{pr}}}{\Omega_{\mathrm{pr}}} \cdot \frac{S}{1+S} , \tag{2.51}$$

$$v_{\mathrm{st}} = \frac{\Gamma_{\mathrm{a}}}{2\Omega_{\mathrm{pr}}} \cdot \frac{S}{1+S} , \tag{2.52}$$

$$w_{\mathrm{st}} = -\frac{1}{2} \cdot \frac{1}{1+S} . \tag{2.53}$$

The saturation parameter is such that $S \to \infty$, $w_{\mathrm{st}} \to 0$, the transition is saturated and the populations of $|\mathrm{b}\rangle$ and $|\mathrm{a}\rangle$ are equal. The on-resonance saturation parameter, S_0 is given by,

$$S_0 = \frac{2\Omega_{\mathrm{pr}}^2}{\Gamma_{\mathrm{a}}^2} , \tag{2.54}$$

$$\equiv \frac{I}{I_{\mathrm{SAT}}} . \tag{2.55}$$

I_{SAT} is the saturation intensity for a transition. It can be thought of as the photon energy ($\hbar c/\lambda$) per unit time (Γ_a) per unit area (absorption cross-section $\sim \lambda^2$),

$$I_{SAT} = \frac{2\pi^2 \hbar \Gamma_a c}{3\lambda^3} \ . \tag{2.56}$$

In the case of the Rb D_2-line then from the spectroscopic data in appendix A,

$$I_{SAT} = 1.67 \text{ mW cm}^{-2} \ . \tag{2.57}$$

The on resonance Rabi frequency can be determined for a closed transition from,

$$\frac{I_{pr}}{I_{SAT}} = 2\left(\frac{\Omega_{pr}}{\Gamma_a}\right)^2 , \tag{2.58}$$

$$\Longrightarrow \quad \Omega_{pr} = \frac{\Gamma_a}{\sqrt{2}} \cdot \sqrt{\frac{I_{pr}}{I_{SAT}}} \ . \tag{2.59}$$

To expand the expression for the Rabi frequency to include open transitions, the transition probability for the open transition relative to the closed transition has to be introduced.

2.3 Line Width of Absorbing Transitions

2.3.1 Complex Susceptibility

The macroscopic polarization, **P**, for a medium with N oscillators per unit volume with a dipole moment **d**, is given by:

$$\mathbf{P} = N\langle \mathbf{d} \rangle \ . \tag{2.60}$$

From the assumption that **P** is proportional to the applied electric field **E**, **P** can be written as,

$$\mathbf{P} = \frac{1}{2}\epsilon_0 \mathbf{E}(\chi e^{-i\omega t} + \chi^* e^{i\omega t}) \ , \tag{2.61}$$

where χ is the complex susceptibility of the medium, [28].

From equations 2.42, 2.60 and equation 2.61,

$$N\mathbf{d}_{ba}\left(\tilde{\rho}_{ba}e^{i\omega t} + \tilde{\rho}_{ab}e^{-i\omega t}\right) = \frac{1}{2}\epsilon_0 \mathbf{E}\left(\chi e^{-i\omega t} + \chi^* e^{i\omega t}\right) \ . \tag{2.62}$$

Taking the dot product of equation 2.62 with $\mathbf{d}_{ba}$ and substituting from equation C.6 on page 161 leads to,

$$N d_{ba}^2 \left(\widetilde{\rho}_{ba} e^{i\omega t} + \widetilde{\rho}_{ab} e^{-i\omega t}\right) = -\frac{1}{2}\epsilon_0 \hbar \Omega_{pr} \left(\chi e^{-i\omega t} + \chi^* e^{i\omega t}\right) . \quad (2.63)$$

Equating coefficients of $e^{-i\omega t}$ leads to,

$$\chi = -2 \frac{N d_{ba}^2}{\epsilon_0 \hbar \Omega_{pr}} \widetilde{\rho}_{ab} . \quad (2.64)$$

From equations 2.36 and 2.37, it follows that,

$$\widetilde{\rho}_{ab} = u - iv . \quad (2.65)$$

Substituting equation 2.65 into equation 2.64, and taking the steady state solutions for u and v from equations 2.47 and 2.48,

$$\chi = -\frac{N d_{ba}^2}{\epsilon_0 \hbar} \left(\frac{\delta_{pr}}{\delta_{pr}^2 + (\Gamma_a/2)^2 + \Omega_{pr}^2/2} - i \frac{\Gamma_a/2}{\delta_{pr}^2 + (\Gamma_a/2)^2 + \Omega_{pr}^2/2} \right) , \quad (2.66)$$

$$\Longrightarrow \chi_R = -\frac{N d_{ba}^2}{\epsilon_0 \hbar} \left(\frac{\delta_{pr}}{\delta_{pr}^2 + (\Gamma_a/2)^2 + \Omega_{pr}^2/2} \right) , \quad (2.67)$$

$$\text{and } \chi_I = \frac{N d_{ba}^2}{\epsilon_0 \hbar} \left(\frac{\Gamma_a/2}{\delta_{pr}^2 + (\Gamma_a/2)^2 + \Omega_{pr}^2/2} \right) , \quad (2.68)$$

where χ_R and χ_I are the real and imaginary parts of the complex susceptibility, respectively.

2.3.2 Complex Refractive Index

From Maxwell's equations,

$$\nabla \cdot \mathbf{E} = \frac{\rho}{\epsilon_0} , \quad (2.69)$$

where ρ is the total charge density. This can be broken down into two components: the free charge density, ρ_{free}; and the polarization charge density, ρ_{pol}. Hence,

$$\nabla \cdot \mathbf{E} = \frac{\rho_{free} + \rho_{pol}}{\epsilon_0} , \quad (2.70)$$

$$= \frac{\rho_{free} - \nabla \cdot \mathbf{P}}{\epsilon_0} , \quad (2.71)$$

$$\nabla \cdot (\epsilon_0 \mathbf{E} + \mathbf{P}) = \rho_{free} . \quad (2.72)$$

This can be rewritten in terms of the relative permittivity, ϵ,

$$\nabla \cdot (\epsilon\epsilon_0 \mathbf{E}) = \rho_{\text{free}} , \tag{2.73}$$

$$\Longrightarrow \quad \epsilon = 1 + \chi . \tag{2.74}$$

The refractive index, n, can be related to the relative permittivity ϵ through the phase velocity, v,

$$\mathrm{v} = \frac{1}{\sqrt{\epsilon\epsilon_0\mu\mu_0}} , \tag{2.75}$$

$$= \frac{\mathrm{c}}{n} , \tag{2.76}$$

and as,

$$\mathrm{c} = \frac{1}{\sqrt{\epsilon_0\mu_0}} , \tag{2.77}$$

$$\Longrightarrow \quad n = \sqrt{\epsilon\mu} . \tag{2.78}$$

With the exception of ferromagnetic materials, at optical frequencies $\mu \simeq 1$, then,

$$n = \sqrt{\epsilon} , \tag{2.79}$$

$$\therefore \quad n = \sqrt{1+\chi} . \tag{2.80}$$

In gaseous media at sufficiently low pressure the index of refraction is close to unity, and as,

$$n^2 - 1 = (n+1)(n-1) , \tag{2.81}$$

then it follows that,

$$n^2 - 1 \simeq 2(n-1) . \tag{2.82}$$

Thus, from equation 2.80 and 2.82 ,

$$n = 1 + \frac{\chi}{2} . \tag{2.83}$$

The refractive index can be rewritten in terms of the real and imaginary parts, n_{R} and n_{I}, respectively,

$$n = n_{\mathrm{R}} + i n_{\mathrm{I}} , \tag{2.84}$$

where the real and imaginary parts of the refractive index are,

$$n_{\mathrm{R}} = 1 + \frac{\chi_{\mathrm{R}}}{2} , \tag{2.85}$$

$$n_{\mathrm{I}} = \frac{\chi_{\mathrm{I}}}{2} . \tag{2.86}$$

Kramers-Kronig Relations

Substituting from equations 2.67 and 2.68 into equations 2.85 and 2.86,

$$\Longrightarrow \quad n_{\mathrm{R}}(\delta_{\mathrm{pr}}) = 1 - \frac{N\mathrm{d}_{\mathrm{ba}}^2}{2\epsilon_0\hbar}\left(\frac{\delta_{\mathrm{pr}}}{\delta_{\mathrm{pr}}^2 + (\Gamma_{\mathrm{a}}/2)^2 + \Omega_{\mathrm{pr}}^2/2}\right), \tag{2.87}$$

$$\text{and} \quad n_{\mathrm{I}}(\delta_{\mathrm{pr}}) = \frac{N\mathrm{d}_{\mathrm{ba}}^2}{2\epsilon_0\hbar}\left(\frac{\Gamma_{\mathrm{a}}/2}{\delta_{\mathrm{pr}}^2 + (\Gamma_{\mathrm{a}}/2)^2 + \Omega_{\mathrm{pr}}^2/2}\right). \tag{2.88}$$

Plots of the normalized absorption coefficient $(n_{\mathrm{I}}(\delta_{\mathrm{pr}})/n_{\mathrm{I}}(\delta_{\mathrm{pr}} = 0))$ and dispersion coefficient $((n_{\mathrm{R}}(\delta_{\mathrm{pr}}) - 1)/n_{\mathrm{I}}(\delta_{\mathrm{pr}} = 0))$ are shown in Fig. 2.2(i) and (ii) respectively.

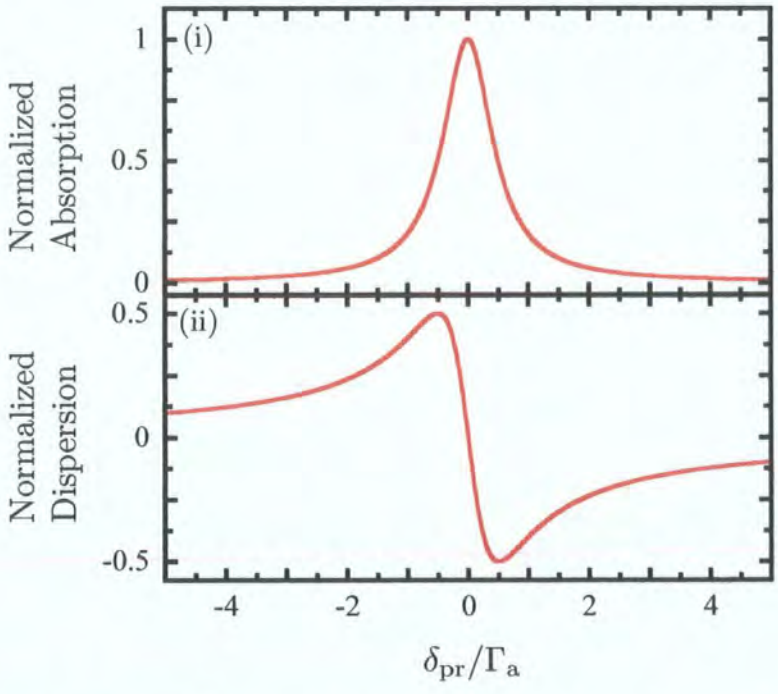

Figure 2.2: The normalized Lorentzian absorption coefficient $(n_{\mathrm{I}}(\delta_{\mathrm{pr}})/n_{\mathrm{I}}(\delta_{\mathrm{pr}} = 0))$ and dispersion coefficient $((n_{\mathrm{R}}(\delta_{\mathrm{pr}}) - 1)/n_{\mathrm{I}}(\delta_{\mathrm{pr}} = 0))$ for a two level atom, in the case that $\Gamma_{\mathrm{a}} \gg \Omega_{\mathrm{pr}}$, are plotted as a function of the detuning from line centre, δ_{pr}. The detuning is in units of the decay rate of the excited state, Γ_{a}. In these units the FWHM of the Lorentzian is 1 .

Equations 2.87 and 2.88 are specific examples of the Kramers-Kronig relations. They relate the absorption and dispersion of a medium through the complex

refractive indices. In the case of a two-level atom, the imaginary part of the refractive index, and hence the absorption of the medium, is of a Lorentzian form.

The specific case of the Kramers-Kronig relations for a Lorentzian line shape can be extended to the more general case, [29],

$$n_{\mathrm{R}}(\omega) = 1 + \frac{1}{\pi}\int_0^\infty \frac{\omega' n_{\mathrm{I}}(\omega')}{\omega'^2 - \omega^2}\mathrm{d}\omega' , \tag{2.89}$$

$$n_{\mathrm{I}}(\omega) = -\frac{\omega}{\pi}\int_0^\infty \frac{\omega' n_{\mathrm{R}}(\omega') - 1}{\omega'^2 - \omega^2}\mathrm{d}\omega' . \tag{2.90}$$

2.3.3 Transmission Intensity

Considering an electromagnetic-wave, $\mathbf{E} = \mathbf{E}_0 \exp\left[\mathrm{i}(k_{\mathrm{pr}} z - \omega_{\mathrm{pr}} t)\right]$, passing along z through a medium of refractive index n, the frequency remains unchanged but the wavevector k_{pr} becomes $k_{\mathrm{n}} = n k_{\mathrm{pr}}$. Separating the real and imaginary components of the refractive index leads to a field and an intensity given by,

$$\mathbf{E} = \mathbf{E}_0 \mathrm{e}^{-k_{\mathrm{pr}} n_{\mathrm{I}} z}\, \mathrm{e}^{\mathrm{i}(k_{\mathrm{pr}} n_{\mathrm{R}} z - \omega_{\mathrm{pr}} t)} , \tag{2.91}$$

$$\Longrightarrow \quad I = I_0 \mathrm{e}^{-2 n_{\mathrm{I}} k_{\mathrm{pr}} z} . \tag{2.92}$$

Consider a beam propagating a distance z through a medium with absorption coefficient α, then the intensity will be given by,

$$I(z) = I_0 \mathrm{e}^{-\alpha z} . \tag{2.93}$$

Comparing equation 2.92 to equation 2.93, it can be seen that the absorption coefficient is given by,

$$\alpha(\delta_{\mathrm{pr}}) = 2 n_{\mathrm{I}}(\delta_{\mathrm{pr}}) k_{\mathrm{pr}} . \tag{2.94}$$

$\alpha(\delta_{\mathrm{pr}})$ gives the absorption line shape which has a Lorentzian form. $n_{\mathrm{R}}(\delta_{\mathrm{pr}}) - n_0$ gives the dispersion profile, and as $n_0 \simeq 1$ in atomic vapours, then $n_{\mathrm{R}}(\delta_{\mathrm{pr}}) - 1$ gives the dispersion.

2.3.4 Doppler Broadening

Before the advent of the laser, spectroscopy of absorption and emission lines in gaseous media was limited to the Doppler width. The mechanism responsible

for this, Doppler broadening, is a consequence of the fact that the atoms in the medium have a non-zero velocity distribution. Atomic transitions which are not resonant with a monochromatic radiation field can still interact with that field, if their velocity is such that they are Doppler-shifted into resonance with it. Therefore a number of closely spaced atomic transitions can become indistinguishable from each other, if their separation is less than the Doppler broadening.

An atom with a resonance in its rest frame at ω_{ab} will absorb a photon with frequency ω_{pr}, in the laboratory frame. From appendix D,

$$\omega_{pr} = \omega_{ab}\left(1 + \frac{v}{c}\right) . \tag{2.95}$$

For atoms in a vapour in thermal equilibrium at temperature T, the number of atoms per unit volume, in the E_i level, with a velocity in the interval v_z to $v_z + \delta v_z$, is given by the Maxwellian velocity distribution. This velocity distribution takes the form:

$$N_i(v)\,dv = \frac{N_i}{v_p\sqrt{\pi}} \exp\left[-\left(\frac{v}{v_p}\right)^2\right] dv , \tag{2.96}$$

$v_p = \sqrt{\frac{2k_BT}{m}}$ is the most probable velocity, m is the mass of the atom and k_B is the Boltzmann constant. From equation 2.95:

$$dv = \frac{c}{\omega_{ab}} d\omega_{pr} . \tag{2.97}$$

Subsituting equation 2.97 into equation 2.96 gives the number of atoms with absorption frequency ω_{ab} shifted into the interval ω_{pr} to $\omega_{pr} + d\omega_{pr}$:

$$N_i(\omega_{pr})\,d\omega_{pr} = \frac{cN_i}{\omega_{ab}v_p\sqrt{\pi}} \exp\left[-\left(\frac{c(\omega_{pr} - \omega_{ab})}{\omega_{ab}v_p}\right)^2\right] d\omega_{pr} . \tag{2.98}$$

The emitted or absorbed radiant power $P(\omega)d\omega_{pr}$, is directly proportional to the density of atoms emitting or absorbing, $N_i(\omega_{pr})d\omega_{pr}$. Hence the intensity profile becomes:

$$I(\omega_{pr}) = I_0 \exp\left[-\left(\frac{c(\omega_{pr} - \omega_{ab})}{\omega_{ab}v_p}\right)^2\right] . \tag{2.99}$$

Voigt Profile

If an atom absorbs at a single frequency, Doppler broadening leads to a Gaussian absorption profile, equation 2.99. Atoms do not absorb at a single frequency, but instead absorb over a spread of frequencies due to the natural line width of the transition, given by a Lorentzian function. Thus the Doppler broadening of the transitions takes the form of a Gaussian function convolved with a Lorentzian function.

The convolution of a Lorentzian and a Gaussian function is known as a Voigt profile. It accurately describes the line shape of Doppler-broadened transitions. In the limits that the Lorentzian full-width at half-maximum (FWHM) is much greater than the Gaussian FWHM, then the Voigt profile can be well approximated by a Lorentzian function. In the limit that the Gaussian FWHM is much greater than the Lorentzian FWHM, the Voigt profile can be well approximated by a Gaussian function[1].

2.4 Rb D_2 Line

2.4.1 Vapour Pressure and Number Density

The vapour pressure, p, for solid Rb is given by the following equation, [34],

$$\begin{aligned} \log_{10} p &= -94.04826 - \frac{1961.258}{T} \\ &\quad - 0.03771687 \times T + 42.57526 \times \log_{10} T \ , \end{aligned} \tag{2.100}$$

T is the absolute temperature, p is the vapour pressure in Torr. From the vapour pressure it is trivial to calculate the number density, N.

$$N = \frac{133.3 \times p}{k_B T} \ , \tag{2.101}$$

the factor of 133.3 converts the vapour pressure from Torr to Pa and k_B is once again the Boltzmann constant. As there are two isotopes of Rb the number density of the separate isotopes should be calculated. The ratio of the abundance

[1] Lorentzian functions decay at a slower rate than Gaussian functions as the detuning from line centre increases. It should be noted that for large detunings from line centre the Gaussian fit to the Voigt profile will not be as valid as in the region around line centre.

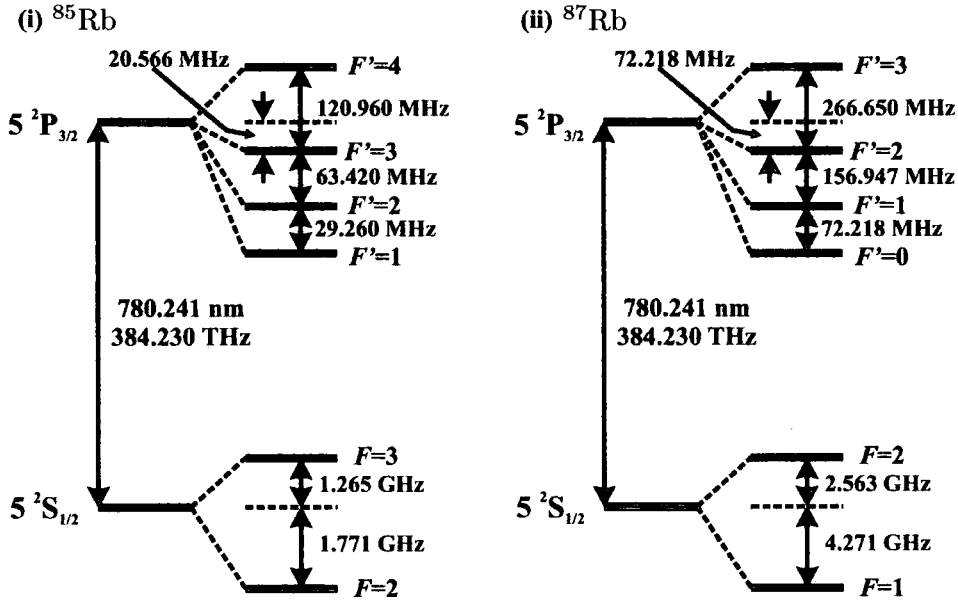

Figure 2.3: (i) The hyperfine levels involved in the ^{85}Rb D_2 transition, [30, 31]. (ii) The hyperfine levels involved in the ^{87}Rb D_2 transition, [32]. The wavelength of the transition is taken from the work of Morton, [33]. The (linear) frequency hyperfine-intervals are given as well as the wavelength (in vacuum) and frequency of the D_2 transition in the absence of hyperfine structure. The hyperfine levels of the upper term are labelled F' while the ground term hyperfine levels are labelled F.

of the two isotopes ^{85}Rb to ^{87}Rb is 0.72 : 0.28, [32]. So the number densities for the two isotopes, N_{85} and N_{87}, are given by,

$$N_{85} = 0.72 \times \frac{133.3 \times p}{k_B T}, \tag{2.102}$$

$$N_{87} = 0.28 \times \frac{133.3 \times p}{k_B T}. \tag{2.103}$$

2.4.2 Weak Beam Absorption Predictions

To make predictions of the absorption and dispersion based on equations 2.87 and 2.88, it is necessary to determine d_{ba}. As Rb is not a two-level atom, and exhibits fine, hyperfine and Zeeman structure, then the transition matrix elements for each of the Zeeman sub-levels involved in one transition must be calculated.

Initially consider the individual hyperfine transition matrix elements of the form,

$$\langle F_e, m_{F_e}|er|F_g, m_{F_g}\rangle \ , \tag{2.104}$$

previously referred to as d_{ba}. Using the Wigner-Eckart theorem, [35], it is possible to uncouple the angular momenta and to rewrite the transition in terms of $3-J$ symbols, $6-J$ symbols and the reduced matrix element, equation 2.105.

$$\begin{aligned}\langle F_e, m_{F_e}|er|F_g, m_{F_g}\rangle &= (-1)^{1+L_e+S+J_e+J_g+I-m_{F_e}}\langle L_e\|er\|L_g\rangle \\ &\times\sqrt{(2F_e+1)(2F_g+1)(2J_e+1)(2J_g+1)} \\ &\times\begin{Bmatrix} L_e & J_e & S \\ J_g & L_g & 1 \end{Bmatrix}\begin{Bmatrix} J_e & F_e & I \\ F_g & J_g & 1 \end{Bmatrix} \\ &\times\begin{pmatrix} F_g & 1 & F_e \\ m_{F_g} & q & -m_{F_e} \end{pmatrix} .\end{aligned} \tag{2.105}$$

The reduced matrix element is $\langle L_e\|er\|L_g\rangle$, it is the same for every transition within the angular momentum manifold. The $6-J$ symbols are those terms in $\{\}$ and the $3-J$ symbols those in $()$. I, J, L, S, F and m are the angular momentum quantum numbers, and q represents the change in m from the ground state to the excited state. The reduced dipole matrix element is dependent upon the wavelength of the transition and the lifetime of the excited state.

The susceptibility for each Zeeman level is calculated and multiplied by $1/g$, where g is the number of Zeeman levels in the ground term ($g = 12$ for ^{85}Rb and $g = 8$ for ^{87}Rb). This is to take account of the fact that we are assuming the population is evenly divided among the ground term Zeeman sub-levels.

The susceptibility of each hyperfine transition is the sum of the susceptibilities for all of the Zeeman transitions within each of the hyperfine manifolds. Integrating over the velocity component along the direction of the beam accounts for the Doppler broadening. The absorption coefficient is calculated for each hyperfine transition using *Mathematica*[2]. The absorption coefficient for each of the hyperfine transitions, on the Rb D_2 line, is plotted in Fig. 2.4 , at 293 K.

[2]The code for this calculation is included in appendix E .

The transmission of a weak probe beam is given by,

$$I = I_0 e^{-(\Sigma\alpha(T))z}, \tag{2.106}$$

where z is the length of the cell, and $\Sigma\alpha(T)$ is the sum of the absorption coefficients, each of which is a function of temperature. Using *Mathematica* this calculation has been carried out.

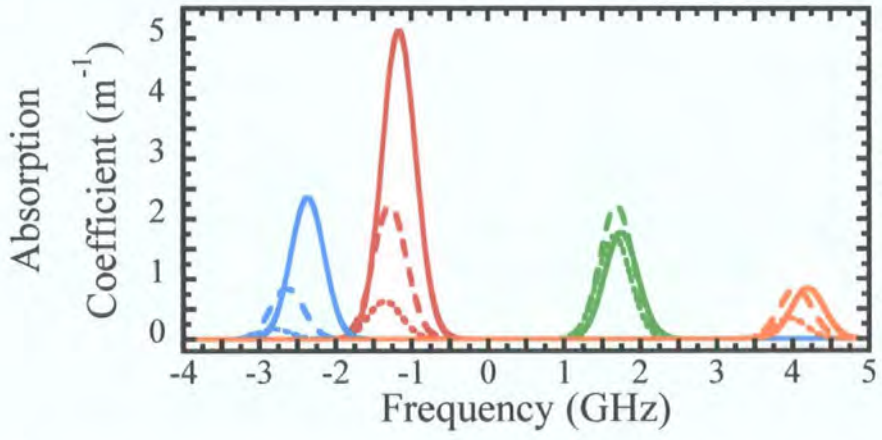

Figure 2.4: Plots of the absorption coefficients, at 293 K, for the hyperfine transition that make up the D_2 line of both ^{85}Rb and ^{87}Rb. The blue traces show the coefficients for the transitions ^{87}Rb 5 $^2S_{1/2}$ ($F = 2$) $\rightarrow$ 5 $^2P_{3/2}$ ($F' = 1,2,3$), the red traces ^{85}Rb 5 $^2S_{1/2}$ ($F = 3$) $\rightarrow$ 5 $^2P_{3/2}$ ($F' = 2,3,4$), green traces ^{85}Rb 5 $^2S_{1/2}$ ($F = 2$) $\rightarrow$ 5 $^2P_{3/2}$ ($F' = 1,2,3$) and the orange traces ^{87}Rb 5 $^2S_{1/2}$ ($F = 1$) $\rightarrow$ 5 $^2P_{3/2}$ ($F' = 0,1,2$). The solid lines show the coefficients for transitions between hyperfine states $F \rightarrow F' = F + 1$, dashed lines $F \rightarrow F' = F$, and dotted lines $F \rightarrow F' = F - 1$. The zero frequency corresponds to the weighted centre of the D_2 line.

Fig. 2.5 shows the transmission of a weak probe beam, scanned across the full Rb D_2 line at 293 K for two different length vapour cells. The hyperfine splitting of the excited term is less than the Doppler broadening of each of these transitions at 293 K. It is not possible to resolve the excited-term hyperfine structure. The ground-term hyperfine splitting is much larger than that of the excited term and larger than the Doppler broadening, hence this can be resolved.

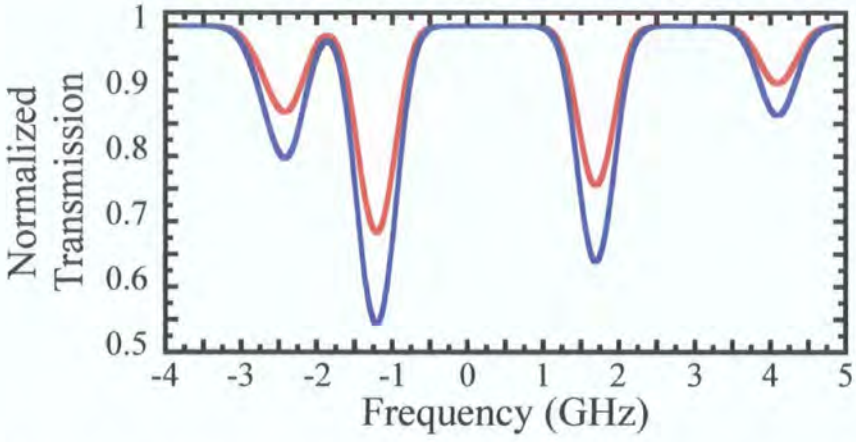

Figure 2.5: Calculated transmission profile of the Rb D_2 line at 293 K. Plots for a weak probe propagating through a 5 cm vapour cell (red) and an 8 cm long vapour cell (blue) are shown. These are the lengths of vapour cells used in this work. The zero frequency corresponds to the weighted centre of the D_2 line.

2.5 Weak Probe Experiment

2.5.1 Extended Cavity Diode Lasers

In this section the set-up and alignment of the laser used in this experimental work is addressed. Extended cavity diode lasers (ECDLs), [36, 37, 38, 39] are widely used for atomic spectroscopy. ECDLs provide a (relatively) cheap and reliable method of generating up to tens of mW of single-mode tuneable laser power.

The lasers used throughout this work were in-house designed ECDLs. The cavity is in the Littrow configuration, [39]. The diodes used in this work are Sanyo DL7140–201. The diode is housed in a brass block which stands on a thermo-electric cooler (TEC), Marlow Industries DT3–2.5. The brass block also houses a 100 kΩ thermistor to provide feedback to the TEC control. This allows the temperature of the brass block, and hence the diode, to be controlled. The temperature controller used is a Wavelength Electronics MPT–2500, with a quoted stability of 0.008 °C/24hrs.

The mounting of the laser diode and the external cavity is shown in Fig. 2.6.

The output of the diode is collimated using a lens ($f = 4.5$ mm) mounted in the same brass block as the diode. The lens is mounted, such that it is co-axial to the diode casing, on a screw thread allowing the lens-diode separation to be varied. The collimated beam reflects off a reflection grating with 1800 lines/mm. The zero order reflection is coupled out of the ECDL and into the experimental apparatus, whilst the minus first order is reflected back into the diode. The frequency of the light determines the angle of the non-zero orders of the reflection. Fine control of the frequency of light amplified in the cavity is gained from control of the cavity length. The light reflected into the diode seeds the gain medium, such that the diode will amplify and output light at the frequency of that light injected into it. It follows that scanning the length of the cavity will, in turn, scan the frequency output of the diode and hence of the ECDL.

The grating is mounted on a Thorlabs mirror mount, KC1. The mount has been modified with the addition of a piezo-electric transducer, Thorlabs AE0203D08 PZT, positioned such that it enables the angle and length of the cavity to be scanned. The piezo expands by 6.1 ± 1.5 μm/100 V. Applying a varying voltage to the piezo scans the frequency output of the ECDL.

The ECDL does not consist of a single cavity, as both surfaces of the diode are also reflecting. This in turn means that the laser does not always operate in a single mode at a single frequency, and furthermore the frequency of the ECDL cannot be scanned more than ~ 2.5 GHz, without discontinuous changes in its output — referred to as mode-hops.

When the laser is set up, care has to be taken to ensure that the laser will scan without mode hops across the region of each of the individual Doppler-broadened resonances.

The laser power-to-current characteristics are recorded. They provide a useful diagnostic tool for how the laser diode is operating and, specifically, whether the diode is showing signs of ageing. A typical plot of diode output power against current is shown in Fig. 2.7. Ageing of the diode will be shown by an increase in the threshold current. The threshold current is defined here as the intercept of a straight line fit to the data (see Fig. 2.7) with the frequency axis.

The diode current is increased until the output beam is visible on a viewing card, Newport F–IRC4. The diode is rotated such that the long axis of the

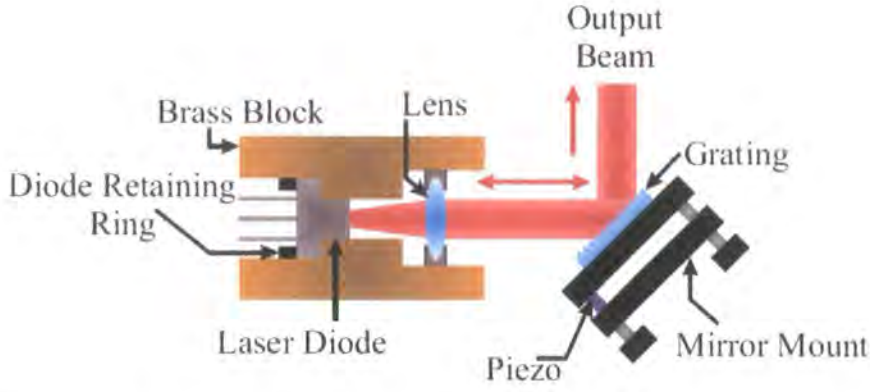

Figure 2.6: Diagram showing the cavity set up of the ECDL. The cavity is formed by the rear facet of the diode and the reflection grating. The cavity is in the Littrow configuration. The piezo is positioned in the mirror mount as shown in the diagram. Changes in length of the piezo change the length of the extended cavity. This in turn controls the frequency of the output of the ECDL (see the text for further details).

output beam profile is parallel to the optical bench. The output of the diode must next be collimated. The beam is allowed to propagate over as long a distance as possible, typically > 4 m. The separation of the lens and diode is then adjusted such that the divergence of the beam over the full distance is minimal, without there being any beam waists along the beam path.

With the grating in place, the output of the ECDL is monitored. Generally two spots can be seen. The alignment of the grating is adjusted until the spots overlap to as high a degree as possible. The current to the diode is reduced to just below its lasing threshold value. Using a power meter to monitor the output of the ECDL, the vertical alignment of the grating is adjusted until the ECDL starts to lase again. This process is repeated until further adjustment of the grating cannot start the laser lasing again. The vertical alignment is now optimized.

The laser diode current is set to a value to give the desired power output, and the temperature of the diode set at $\simeq 19°$C. A Rb cell is placed in the output beam path, and monitored for fluorescence. The horizontal angle of the grating mount is adjusted — hence adjusting the length of the cavity — until fluorescence can be seen. If fluorescence cannot be found the temperature of the

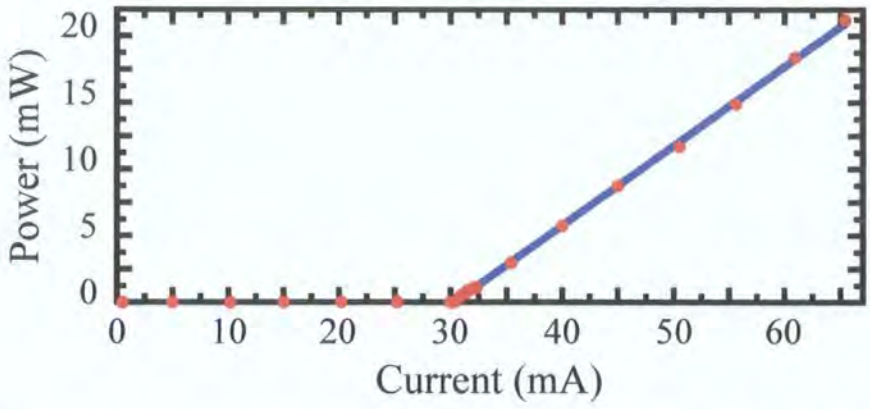

Figure 2.7: Laser diode output power is plotted against the current through the diode, shown by red dots. Note that the power increases at a low rate until the threshold current is reached, at 30.3 mA, this is the point at which the diode starts to lase. The blue line shows the straight-line least-squares fit to the data once the diode has started to lase. The threshold current is defined as the point at which the straight-line fit crosses the frequency axis.

diode is adjusted by a small amount ($\ll 1$ °C) and the horizontal adjustment of the grating varied once more. This process is repeated until fluorescence is seen.

Once fluorescence is seen, the piezo is scanned at a rate of $\simeq 10$ Hz over a range of ~ 10 V. Further adjustment is made to the laser current and the temperature of the diode until a full scan of the Doppler-broadened absorption can be made.

A saturated absorption spectroscopy set-up, § 2.6.1, is used to identify the transition. If the absorption in the absence of the pump beam does not agree with the predicted absorption § 2.4.2, then either the probe power is too high or the laser is not operating in a single mode. Reduction of probe power will show if the power is causing the diminished absorption, as with the reduction in power the absorption will increase. If this does not happen then the laser will not be operating on a single mode. If the laser is not operating in a single mode then the process of varying the current and temperature will have to be repeated.

Varying the amplitude of the voltage scan, and also using a smooth scan (sine-wave as opposed to sawtooth), can have the effect of increasing the scan range.

The output-beam profile of the ECDL can be well approximated by an elliptical Gaussian function. The long axis, with 1/e radius a, is in the horizontal plane and the short axis, with 1/e radius b, is in the vertical plane. In this case the the peak intensity of the beam, I_0, is related to the total power in the beam, P, by equation H.8 on page 186 ,

$$I_0 = \frac{P}{\pi\, a\, b}\,.$$

Optical Isolation

Diode lasers are exceptionally sensitive to feedback, [36], and as such care has to be taken to ensure eradication of unwanted feedback into the ECDL. Unfortunately the use of components such as optical fibres almost guarantees that there will be sufficient feedback to modify the output of the laser significantly. This means that an optical isolator must be used. The isolator used in this work was a Gsänger FI-780. This allows linearly polarized light to pass through in one direction but extinguishes light in the other direction to $>$ 30 dB irrespective of its polarization.

2.5.2 Photodiode circuits

Fig. 2.8 shows a basic reverse-biased photodiode circuit used to measure the power of probe beams transmitted through Rb vapour cells.

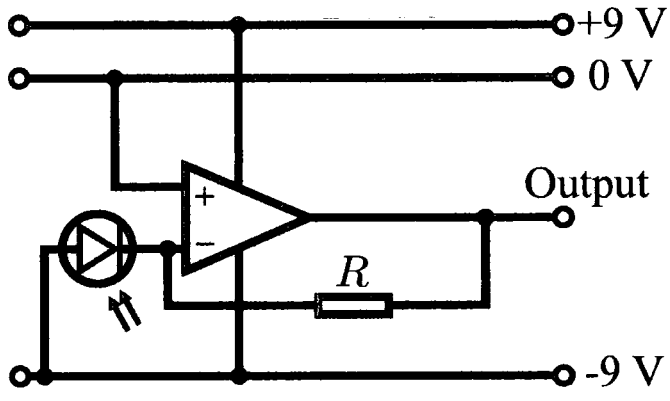

Figure 2.8: Reverse biased photodiode circuit used for measuring saturation spectroscopy.

The gain of such an operational amplifier (Op-Amp) circuit is given by the ratio of the output voltage V_{out} to the input voltage V_{in}, [40, 41].

$$\frac{V_{\text{out}}}{V_{\text{in}}} = -\left|\frac{Z_{\text{out}}}{Z_{\text{in}}}\right| , \tag{2.107}$$

$$\Longrightarrow \quad V_{\text{out}} = -\left|Z_{\text{out}}\right| \cdot \frac{V_{\text{in}}}{|Z_{\text{in}}|} \tag{2.108}$$

$$= -\left|Z_{\text{out}}\right| \cdot I_{\text{in}} , \tag{2.109}$$

where Z_{out} and Z_{in} are the output and input impedances, and I_{in} is the input current, generated by the light incident on the photodiode. In the case that the $Z_{\text{out}} = R$ it follows that,

$$V_{\text{out}} = I_{\text{in}} R . \tag{2.110}$$

It follows that the amplifier will not introduce any filtering of different frequency components, although the photodiode itself will have a limit on its response time. In the case of a BPX–65, the response time is $\simeq$ 12 ns, though the exact value depends on several parameters, [42].

Two 9 V cells are used to define the +9 V, 0 V, and −9 V. Cells are preferred to a DC supply powered from the mains, as they will not suffer from the potential noise fluctuations that could be expected on the mains derived power supply.

2.5.3 Experimental Weak Probe Measurements

The ECDL was set up to scan across each of the four Doppler-broadened features of the Rb D_2 line. A probe beam was passed through the 8 cm long Rb vapour cell. The beam was then focussed onto a photodiode (BPX-65), mounted in the circuit shown in Fig. 2.8. The frequency of the output of the ECDL was scanned by applying a sinusoidal control voltage to the piezo. The signal from the photodiode was recorded both with and without the ECDL beam blocked (S_{back} and S respectively). To obtain a normalized transmission signal (S_{norm}) the recorded signal ($S - S_{\text{back}}$) was divided by the off-resonance signal ($S_{\text{off}} - S_{\text{back}}$).

$$S_{\text{norm}} = \frac{S - S_{\text{back}}}{S_{\text{off}} - S_{\text{back}}} . \tag{2.111}$$

To determine the frequency scale the piezo-control voltage is recorded. A least squares fit of a sinusoidal function is made to the recorded control voltage. A

saturation spectroscopy signal is recorded simultaneously, § 2.6.1. The saturation spectroscopy trace is used to calibrate the voltage. The piezo voltage at which the natural line width features occur is recorded. A linear-least-squares fit is made of the voltage to the known separations (Fig. 2.3) of the the features. This linear fit is then used as the frequency scale for the plots, Fig. 2.9 and Fig. 2.11.

The four Doppler-broadened resonances are plotted against the ECDL frequency, shown in Fig. 2.9.

As can be seen from the comparison of Fig. 2.9 (i) and (ii), the ECDL scan is not linear over the range of the ^{87}Rb 5 $^2S_{1/2}$ $(F = 2)$ $\rightarrow$ 5 $^2P_{3/2}$ $(F' = 1, 2, 3)$ and ^{85}Rb 5 $^2S_{1/2}$ $(F = 3)$ $\rightarrow$ 5 $^2P_{3/2}$ $(F' = 2, 3, 4)$ transitions. A linear calibration of the frequency scale using the ^{87}Rb 5 $^2S_{1/2}$ $(F = 2)$ $\rightarrow$ 5 $^2P_{3/2}$ $(F' = 1, 2, 3)$ transitions instead of the ^{85}Rb 5 $^2S_{1/2}$ $(F = 3)$ $\rightarrow$ 5 $^2P_{3/2}$ $(F' = 2, 3, 4)$ transitions shows a discrepancy of 6%.

It is apparent that the measured depths of the absorptions do not perfectly match the predicted depths. Fitting single Gaussian functions to both the experimental and theoretical transmission allows a simple characterization of the absorptions through their amplitude and FWHM, Tables 2.1 and 2.2. Comparison of the amplitude and FWHM of the Gaussian fits shows that the predicted absorption is greater than the experimentally measured absorption for ^{85}Rb 5 $^2S_{1/2}$ $(F = 2)$ $\rightarrow$ 5 $^2P_{3/2}$ $(F' = 1, 2, 3)$ and ^{87}Rb 5 $^2S_{1/2}$ $(F = 1)$ $\rightarrow$ 5 $^2P_{3/2}$ $(F' = 0, 1, 2)$. This is not the case for the ^{87}Rb 5 $^2S_{1/2}$ $(F = 2)$ $\rightarrow$ 5 $^2P_{3/2}$ $(F' = 1, 2, 3)$ and ^{85}Rb 5 $^2S_{1/2}$ $(F = 3)$ $\rightarrow$ 5 $^2P_{3/2}$ $(F' = 2, 3, 4)$ transitions, where the measured absorption is greater than the predicted in Table 2.1 .

The absorption of the weak probe is highly sensitive to the temperature of the Rb vapour. At 293 K a change of 1 K in the temperature of the vapour will lead to a change of $\sim$ 10% in the absorption[3]. However this does not explain why two of the transitions show more absorption than expected and two show less. If the temperature of the vapour was higher than it was believed to be, all four Doppler-broadened absorptions would show an increase in absorption whereas a lower temperature would lead to reduced absorption on all four absorptions.

[3]Hence a normalized absorption of 0.20 at 293 K would be $\simeq$ 0.22 at 294 K.

Transition	Experimental Amplitudes	Predicted Amplitudes
^{87}Rb 5 $^2S_{1/2}$ ($F = 2$)	0.22	0.20
^{85}Rb 5 $^2S_{1/2}$ ($F = 3$)	0.49	0.46
^{85}Rb 5 $^2S_{1/2}$ ($F = 2$)	0.34	0.37
^{87}Rb 5 $^2S_{1/2}$ ($F = 1$)	0.11	0.14

Table 2.1: Normalized amplitude of experimentally measured and theoretically calculated Doppler-broadened hyperfine spectrum. The Doppler-broadened transitions are denoted by their common ground-term hyperfine states.

A potential explanation for the discrepancies in the expected and measured absorption are that they are due to optical pumping. Optical pumping is the redistribution of the population among the different states of the atom due to the presence of an optical field. In this case, population accumulates in the upper hyperfine levels of the ground term (^{87}Rb 5 $^2S_{1/2}$ ($F = 2$) and ^{85}Rb 5 $^2S_{1/2}$ ($F = 3$)), due to the presence of closed transitions[4] from these hyperfine states to the excited hyperfine states (^{87}Rb 5 $^2S_{1/2}$ ($F = 2, m_F = \pm 2$) $\rightarrow$ 5 $^2P_{3/2}$ ($F' = 3, m_{F'} = \pm 3$) and ^{85}Rb 5 $^2S_{1/2}$ ($F = 3, m_F = \pm 3$) $\rightarrow$ 5 $^2P_{3/2}$ ($F' = 4, m_{F'} = \pm 4$)). This in turn leads to more absorption when the probe is resonant with transitions from the upper hyperfine states of the ground term, and less when it is resonant with transitions from the lower hyperfine states of the ground term than would be expected in the absence of optical pumping.

The FWHM of the Gaussian fits are shown in Table 2.2 . The largest deviation between the experimental and predicted width is in the case of the ^{87}Rb 5 $^2S_{1/2}$ ($F = 2$) transition. This deviation is largely due to the non-linearity of the ECDL scan. If the frequency scale had been calibrated using the transition from the hyperfine state ^{87}Rb 5 $^2S_{1/2}$ ($F = 2$) instead of the transition from the hyperfine state ^{85}Rb 5 $^2S_{1/2}$ ($F = 3$), the FWHM would be 580 MHz.

[4]When population in a ground state can only be excited to one excited state, and population in that excited state can only decay back to the same ground state, that transition is said to be closed.

Transition	Experimental FWHM (MHz)	Predicted FWHM (MHz)
^{87}Rb 5 $^2S_{1/2}$ ($F = 2$)	550	620
^{85}Rb 5 $^2S_{1/2}$ ($F = 3$)	560	580
^{85}Rb 5 $^2S_{1/2}$ ($F = 2$)	530	550
^{87}Rb 5 $^2S_{1/2}$ ($F = 1$)	570	570

Table 2.2: FWHM of experimentally measured and theoretically calculated Doppler-broadened hyperfine spectrum. The Doppler-broadened transitions are denoted by their common ground-term hyperfine states.

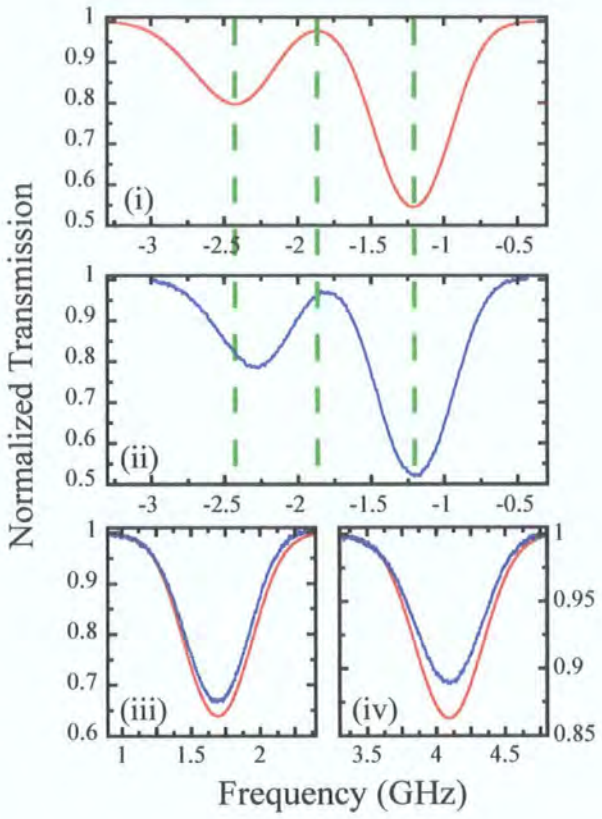

Figure 2.9: Plots of the transmission of a weak probe beam through an 8 cm long Rb vapour cell, at room temperature (293 K), on the four different Doppler-broadened resonances of the D_2 line.
(i) Theoretical transmission on the ^{87}Rb $5s_{1/2}$ $(F = 2) \rightarrow 5p_{3/2}$ $(F' = 1, 2, 3)$ and ^{85}Rb $5s_{1/2}$ $(F = 3) \rightarrow 5p_{3/2}$ $(F' = 2, 3, 4)$ transitions.
(ii) Experimental transmission on the ^{87}Rb $5s_{1/2}$ $(F = 2) \rightarrow 5p_{3/2}$ $(F' = 1, 2, 3)$ and ^{85}Rb $5s_{1/2}$ $(F = 3) \rightarrow 5p_{3/2}$ $(F' = 2, 3, 4)$ transitions The frequency scan is defined on the ^{87}Rb $5s_{1/2}$ $(F = 2) \rightarrow 5p_{3/2}$ $(F' = 1, 2, 3)$ transition. Comparison of (i) and (ii) shows a non-linearity in the ECDL scan across the two Doppler-broadened resonances. This is highlighted by the vertical green lines marking the centre of the two Doppler-broadened resonances and the maximum in transmission between the two absorptions.
(iii) Theoretical and experimental traces on the ^{85}Rb $5s_{1/2}$ $(F = 2) \rightarrow 5p_{3/2}$ $(F' = 1, 2, 3)$ transitions.
(iv) Theoretical and experimental traces on the ^{87}Rb $5s_{1/2}$ $(F = 1) \rightarrow 5p_{3/2}$ $(F' = 0, 1, 2)$ transitions.

2.6 Experimental Natural Line Width Spectroscopy

In order to increase the resolution beyond the limit of the Doppler broadening, it is necessary to be able to observe a signal made up only of those atoms which interact with the radiation close to the resonant frequency of the transition. There are a number of schemes that allow this to be done. One of the simplest methods is to measure the transmission of a weak probe beam perpendicular to a collimated atomic beam. The extent to which the atomic beam is collimated will limit the spread in velocity of the atoms in the direction of the laser beam. If this spread corresponds to a Doppler width which is less than the natural line width then we can essentially eliminate the Doppler broadening in the spectroscopy signals.

Other methods of Doppler-free spectroscopy involve the use of a strong pump beam, such as polarization spectroscopy, [43], and hyperfine pumping and saturation spectroscopy, [27, 37, 44]. Hyperfine pumping and saturation spectroscopy will be looked at in more depth later in this section. These techniques allow for resolution up to the natural line width. The natural line width of a transition is the limit on the resolution that can be achieved on a transition between two levels through a single photon, § 2.3.

2.6.1 Hyperfine Pumping and Saturated Absorption Spectroscopy

Hyperfine pumping and saturation spectroscopy utilises a relatively strong pump beam to modify the atomic medium that is probed by the weak beam.

Hyperfine pumping and saturation spectroscopy, [27, 37, 44], allows the natural line width of individual hyperfine transitions to be resolved. A basic experimental set-up for this type of spectroscopy is shown in Fig. 2.10.

The atoms which, due to their velocity, fall into resonance with both the strong pump and the weak probe beams at the same laser frequencies, show less absorption of the weak probe beam than they would in the absence of the strong pump beam. This occurs for different finite velocity classes of atoms: zero ve-

locity atoms with pump and probe on resonance with the same transition; and for non-zero velocity atoms with pump and probe on resonance with different hyperfine transitions. The latter are known as cross-over resonances. Cross-over resonances occur at a laser frequency bisecting the frequency of the two transitions that the pump and probe are individually resonant with. Hence in the case of the Rb D_2 line, where each Doppler-broadened feature comprises of three Doppler-broadened transitions, six different sub-Doppler features can be seen. Three of these features correspond to the transitions and three to the cross-over resonances.

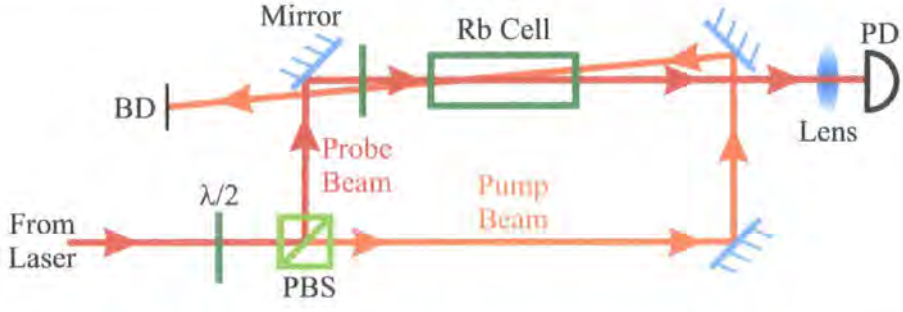

Figure 2.10: The two beams from the laser, separated at the polarizing beam splitting cube (PBS), are aligned as close to counter-propagating as possible. The frequency of both beams is scanned from the laser. The relative strengths of the beams can be set, by adjusting the angle of the half-wave plate ($\lambda/2$) upstream of the polarizing beam splitting cube, to optimize the signal. Note that as the beams are not perfectly counter-propagating, then there will be a small amount of Doppler broadening of the features, dependent upon the angle between the beams. The pump beam is terminated on a beam dump (BD) and the probe on a photodiode (PD).

The saturation spectrum depends upon the relative polarizations of the pump and probe beam. Fig. 2.11 shows traces recorded for perpendicular-linear polarizations.

On the Rb D_2 line at room temperature the Doppler broadening is such that for a single weak-probe beam, transitions from the different hyperfine states of the ground term are distinguishable, but transitions from the same hyperfine state of the ground term to different hyperfine states of the excited term significantly overlap and hence cannot be resolved. Fig. 2.11(i) to (iii) show the full Doppler-

broadened transitions showing the sub-Doppler features.

It should be noted that the sub-Doppler features vary in strength (it is not possible to resolve all six features in all of the traces). An explanation of this is beyond the scope of this thesis. The sub-Doppler features that can be seen in Fig. 2.11 are not natural line width limited. The pump and probe peak intensities used to record the spectra are ~ 4 mW cm^{-2} and ~ 0.2 mW cm^{-2} respectively, with beam diameters of ~ 1 mm. The probe intensity is an order of magnitude less than the saturation intensity, while the pump intensity is approximately a factor of 2 greater than the saturation intensity, equation 2.57.

It can be seen in Fig. 2.11 that the Doppler-broadened transmission of the weak probe beam remains largely unmodified by the pump beam. The exception being in the vicinity of the individual hyperfine and cross-over resonances. Further explanation of these spectra is beyond the scope of this work, a detailed explanation of the modification of the weak probe transmission is presented in the work of Smith and Hughes, [27].

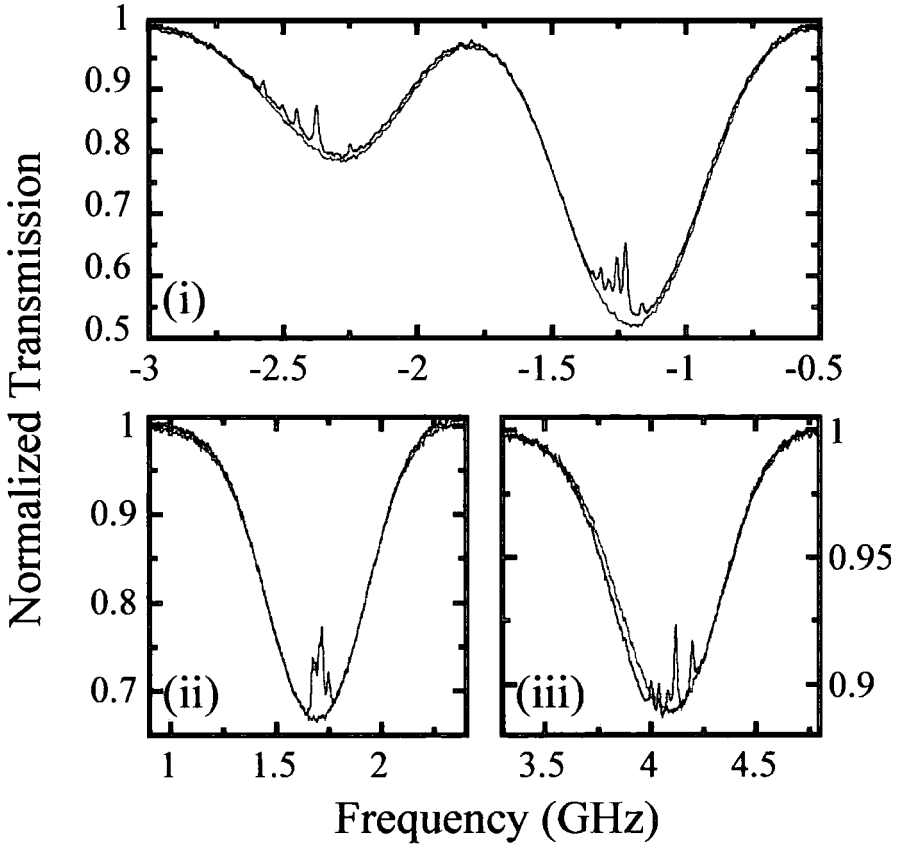

Figure 2.11: Plots of the transmission of a weak probe beam, through an 8 cm long Rb vapour cell at room temperature (293 K), on the four different Doppler-broadened absorptions of the D_2 line. The transmission is shown both with (blue trace) and without (green trace) a counter-propagating pump beam at the same frequency as the probe. The zero of the frequency scale is defined as the frequency of the transition in the absence of hyperfine splitting. The peak intensities of the pump and probe beam are ~ 4 mW cm^{-2} and ~ 0.2 mW cm^{-2} respectively.

(i) A continuous scan across the ^{87}Rb 5 $^2S_{1/2}$ $(F = 2) \rightarrow$ 5 $^2P_{3/2}$ $(F' = 1, 2, 3)$ and ^{85}Rb 5 $^2S_{1/2}$ $(F = 3) \rightarrow$ 5 $^2P_{3/2}$ $(F' = 2, 3, 4)$. The frequency scale is calibrated using the saturation spectroscopy features of the ^{85}Rb 5 $^2S_{1/2}$ $(F = 3) \rightarrow$ 5 $^2P_{3/2}$ $(F' = 2, 3, 4)$ Doppler-broadened transition.

(ii) ^{85}Rb 5 $^2S_{1/2}$ $(F = 2) \rightarrow$ 5 $^2P_{3/2}$ $(F' = 1, 2, 3)$.

(iii) ^{87}Rb 5 $^2S_{1/2}$ $(F = 1) \rightarrow$ 5 $^2P_{3/2}$ $(F' = 0, 1, 2)$.

Chapter 3

Theory of EIT in an Ideal Three-Level System

3.1 Three-Level Systems

So far the interaction of a two-level system (or series of two-level systems) with a near resonant, monochromatic field has been considered. This leads to the Doppler-broadened spectra and saturation spectra as shown in chapter 2 . The three-level system interacting with two monochromatic fields offers a vast array of new physics to be investigated. It is the development of monochromatic tuneable laser sources that has allowed such investigations to be undertaken.

There are essentially three different types of three-level system: Λ; cascade and V. These are shown in Fig. 3.1.

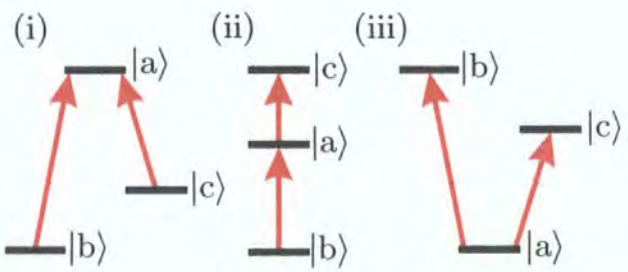

Figure 3.1: The three different three-level systems, with the optical transitions shown by the red arrows. (i) A Λ system, (ii) a cascade system and (iii) a V system.

3.2 Coherent Population Trapping

The application of two continuous-wave (cw) fields to a three-level atomic system puts the atom into a coherent superposition of states. This superposition of states is stable against absorption from the radiation field. Hence this phenomena is referred to as coherent population trapping (CPT).

The Hamiltonian for a three-level system, as shown in Fig. 3.1, is given by,

$$\mathscr{H} = \mathscr{H}_0 + V_1 + V_2 \, . \tag{3.1}$$

$\mathscr{H}_0$ is the bare atom Hamiltonian; V_1 is the potential due to the field with Rabi frequency Ω_1 and angular frequency ω_1; and V_2 is the potential due to the field with Rabi frequency Ω_2 and angular frequency ω_2. The Rabi frequencies are assumed to be real. Here,

$$\mathscr{H}_0 = \hbar\omega_a|a\rangle\langle a| + \hbar\omega_b|b\rangle\langle b| + \hbar\omega_c|c\rangle\langle c| \, , \tag{3.2}$$

$$V_1 = \frac{\hbar}{2}\Omega_1 e^{-i\omega_1 t}|b\rangle\langle a| + \frac{\hbar}{2}\Omega_1 e^{+i\omega_1 t}|a\rangle\langle b| \, , \tag{3.3}$$

$$\text{and } V_2 = \frac{\hbar}{2}\Omega_2 e^{-i\omega_2 t}|c\rangle\langle a| + \frac{\hbar}{2}\Omega_2 e^{+i\omega_2 t}|a\rangle\langle c| \, . \tag{3.4}$$

Considering the interaction of this Hamiltonian with the three-level system provides a simple one-atom model of CPT.

It is apparent that the eigenstates of $\mathscr{H}_0$ ($|a\rangle$, $|b\rangle$ and $|c\rangle$) are not eigenstates of $\mathscr{H}$. Instead the eigenstates of $\mathscr{H}$ are linear combinations of $|a\rangle$, $|b\rangle$ and $|c\rangle$. In the case that the two fields are on resonance, ($\omega_1 = \omega_a - \omega_b$ and $\omega_2 = \omega_a - \omega_c$), the three eigenstates of $\mathscr{H}$ are,

$$|C_1\rangle = \frac{1}{\sqrt{2}}\left(-|a\rangle + \frac{\Omega_1}{\sqrt{\Omega_1^2+\Omega_2^2}}|b\rangle + \frac{\Omega_2}{\sqrt{\Omega_1^2+\Omega_2^2}}|c\rangle\right) \, , \tag{3.5}$$

$$|C_2\rangle = \frac{1}{\sqrt{2}}\left(|a\rangle + \frac{\Omega_1}{\sqrt{\Omega_1^2+\Omega_2^2}}|b\rangle + \frac{\Omega_2}{\sqrt{\Omega_1^2+\Omega_2^2}}|c\rangle\right) \, , \tag{3.6}$$

$$|NC\rangle = \frac{\Omega_2}{\sqrt{\Omega_1^2+\Omega_2^2}}|b\rangle - \frac{\Omega_1}{\sqrt{\Omega_1^2+\Omega_2^2}}|c\rangle \, . \tag{3.7}$$

$|NC\rangle$ contains no component of $|a\rangle$ and hence there is no coupling between these two states. Thus any population in $|NC\rangle$ is trapped in that state. Both $|C_1\rangle$ and $|C_2\rangle$ contain components of $|a\rangle$ and hence couple to it.

Over a period of time, dependent upon the rate of spontaneous emission from the excited state, all of the population of the system will build up in $|NC\rangle$. Hence all of the population becomes coherently trapped in a dark state.

The first experimental realization of CPT was made by Alzetta *et al.*, [45]. In this work the fluorescence of Na atoms was observed. An inhomogeneous magnetic field was applied along the axis of the Na cell. At certain points along the length of the cell the fluorescence disappeared. These "black lines" were due to CPT taking place, in Λ systems, at positions where the magnetic field was such that the CPT resonance was met. A theoretical analysis of the coherence phenomena that lead to these effects was presented by Arimondo and Orriols, [46]. At the same time and independently Whitley and Stroud Jr., [47], produced a theoretical treatment of CPT in a three-level cascade system.

3.2.1 Applications of CPT

CPT has many potential areas of application. Ground states are generally much longer lived than excited states. Measuring the line width of a ground state would potentially increase the resolution of any device, which relied on the width of a spectral feature, by several orders of magnitude. Considering the interactions of two fields with three atomic levels, it is possible to measure a transition with line width orders of magnitude less than the excited state line width. The increase in interest in CPT was largely fuelled by applications in metrology, [48]. More recently there has been significant interest in the field of atomic clocks, [49, 50, 51], where the use of CPT has allowed all optical miniaturised atomic clocks to be produced.

Velocity selective coherent population trapping (VSCPT) is another application of CPT. The technique developed by Aspect *et al.*, [52], requires the formation of a Λ system comprising two degenerate Zeeman ground states with counter-propagating perpendicularly polarized beams. This results in only zero velocity atoms being resonant with the two beams, and thus only zero velocity atoms become trapped in the dark state. Atoms that are not in the correct velocity range for coherent population trapping to take place rely on momentum redistribution, due to optical pumping followed by spontaneous emission, to fall into the correct velocity range for the dark state. This cooling mechanism provides

for laser cooling to below both the Doppler limit and the single-photon recoil energy.

A number of review articles have been written on the subject, including the comprehensive review by Arimondo, [53], and the more recent article by Wynands and Nagel, [20].

3.3 Electromagnetically Induced Transparency

Electromagnetically induced transparency (EIT), [54, 55], is the cancellation of the absorption of a weak probe field. The cancellation is due to the application of a pump field, resonant with one of the levels of the original transition and a third level.

The immediate similarity to CPT is apparent. The difference between EIT and CPT being that CPT tends to refer to two fields of approximately equal Rabi frequency. EIT refers to the regime where one of the fields (pump) is much stronger than the other (probe). In the case of EIT the interest is in how the pump modifies the medium experienced by the probe.

As the only difference between EIT and CPT is the strength of the beams, then the brief theoretical treatment of a three-level system presented above can be extended to the case where, $\Omega_1 \ll \Omega_2$.

It follows from equations 3.5 , 3.6 and 3.7 that the coupling and non-coupling states become,

$$|\mathrm{C}\rangle = \frac{1}{\sqrt{2}}|\mathrm{C}_1\rangle + \frac{1}{\sqrt{2}}|\mathrm{C}_2\rangle \ , \tag{3.8}$$

$$= \frac{\Omega_2}{\sqrt{\Omega_1^2+\Omega_2^2}}|\mathrm{c}\rangle \ , \tag{3.9}$$

$$\simeq |\mathrm{c}\rangle \ , \tag{3.10}$$

$$|\mathrm{NC}\rangle = \frac{\Omega_2}{\sqrt{\Omega_1^2+\Omega_2^2}}|\mathrm{b}\rangle \ , \tag{3.11}$$

$$\simeq |\mathrm{b}\rangle \ . \tag{3.12}$$

Throughout this work the three-level systems under investigation are exclusively Λ-systems. The Λ-system with pump and probe fields is shown in Fig. 3.2.

The induced transparency is caused by the interference of coherences in the

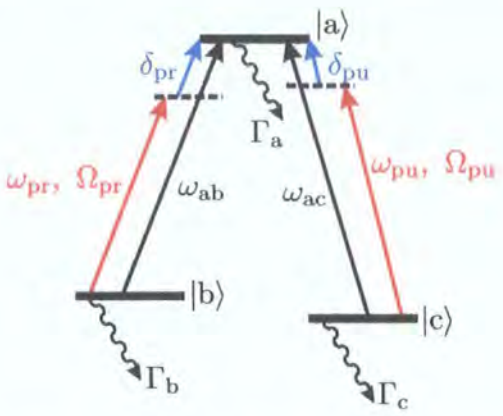

Figure 3.2: A three-level Λ-system. The three levels are linked by two fields, probe and pump. The two fields have angular frequency ω_{pr} and ω_{pu} and Rabi-frequency Ω_{pr} and Ω_{pu}, respectively. The probe field has a detuning from resonance of δ_{pr}, and the pump field a detuning δ_{pu}. Each of the levels $|i\rangle$ has a line width (FWHM) Γ_i.

atomic system. Alongside the modification of the absorption is the concomitant modification of the dispersion, [1, 56], encapsulated in the Kramers-Kronig relations, § 2.3.2. This is what makes EIT of such interest, the steep dispersion is coincident with a transparent window in the medium; normally such steep dispersion would be coincident with significant absorption.

Harris *et al.*, [54], demonstrated theoretically the possibility of rendering a medium transparent on a given allowed transition from a ground state to an excited state. This required the application of a pump beam resonant with a third state and the excited state. The first experimental realization of EIT was by Boller *et al.*, [55]. EIT was observed on a Λ system in strontium vapour. The transmission of a probe was increased from e^{-20} to e^{-1}.

Xiao *et al.*, [57], measured the dispersion due to EIT directly. This was accomplished using a Mach-Zehnder interferometer. The measurements were carried out, on a cascade system, in Rb vapour with the probe resonant with the D_2 transition and the pump resonant with $5P_{3/2} \rightarrow 5D_{5/2}$ transition.

The narrowest recorded EIT resonances in atomic vapours are of $\sim$ 30 Hz in a medium where the excited state line width is 6 MHz, [58]. This means that the transparent window is a factor of 2×10^5 narrower than the Doppler-free

transition in the absence of the pump beam.

In recent years there has been a vast amount of work done in the field of EIT. Some of the more important advances and potential applications are presented in § 1.1.1 . There are a number of good review articles covering this rapidly growing field, [11, 59, 60].

3.4 EIT via Optical-Bloch Equations

Consider an idealized three-level Λ-system as in Fig. 3.2 on the preceding page. There are obvious similarities to the idealized two-level system of Fig. 2.1 on page 12. In the same way that the complex susceptibility, and hence absorption and dispersion, of the two-level medium was calculated in chapter 2, it is possible to calculate the complex susceptibility of the three-level Λ-system. The Hamiltonian for this system is given by equation C.1,

$$\mathscr{H} = \mathscr{H}_{\mathrm{A}} + V_{\mathrm{pr}} + V_{\mathrm{pu}} \; ;$$

The interactions of the atoms with the probe and pump laser fields are given by equations C.8 and C.9 ,

$$\begin{aligned} V_{\mathrm{pr}} &= \frac{\hbar\Omega_{\mathrm{pr}}}{2}\left(|\mathrm{a}\rangle\langle\mathrm{b}|\mathrm{e}^{\mathrm{i}\omega_{\mathrm{pr}}t} + |\mathrm{b}\rangle\langle\mathrm{a}|\mathrm{e}^{-\mathrm{i}\omega_{\mathrm{pr}}t}\right) \; , \\ V_{\mathrm{pu}} &= \frac{\hbar\Omega_{\mathrm{pu}}}{2}\left(|\mathrm{a}\rangle\langle\mathrm{c}|\mathrm{e}^{\mathrm{i}\omega_{\mathrm{pu}}t} + |\mathrm{c}\rangle\langle\mathrm{a}|\mathrm{e}^{-\mathrm{i}\omega_{\mathrm{pu}}t}\right) \; , \end{aligned}$$

where the rotating wave approximation has been made.

The Hamiltonian can be rewritten in matrix form, equation C.10 ,

$$\mathscr{H} = \begin{pmatrix} \hbar\omega_{\mathrm{a}} & (\hbar\Omega_{\mathrm{pr}}/2)\,\mathrm{e}^{-\mathrm{i}\omega_{\mathrm{pr}}t} & (\hbar\Omega_{\mathrm{pu}}/2)\,\mathrm{e}^{-\mathrm{i}\omega_{\mathrm{pu}}t} \\ (\hbar\Omega_{\mathrm{pr}}/2)\,\mathrm{e}^{\mathrm{i}\omega_{\mathrm{pr}}t} & \hbar\omega_{\mathrm{b}} & 0 \\ (\hbar\Omega_{\mathrm{pu}}/2)\,\mathrm{e}^{\mathrm{i}\omega_{\mathrm{pu}}t} & 0 & \hbar\omega_{\mathrm{c}} \end{pmatrix} .$$

The density matrix for the three-level system is given by equation C.11 ,

$$\rho = \begin{pmatrix} \rho_{\mathrm{aa}} & \rho_{\mathrm{ab}} & \rho_{\mathrm{ac}} \\ \rho_{\mathrm{ba}} & \rho_{\mathrm{bb}} & \rho_{\mathrm{bc}} \\ \rho_{\mathrm{ca}} & \rho_{\mathrm{cb}} & \rho_{\mathrm{cc}} \end{pmatrix} .$$

Using the Liouville equation (equation 2.21),

$$\dot{\rho} = \frac{\mathrm{i}}{\hbar}[\rho, \mathscr{H}] - \gamma\rho \ ,$$

the equations of motion for the populations and coherences are derived in appendix C. The equations for the populations are given by equations C.28, C.29, and C.30 on page 163 ,

$$\begin{aligned}
\dot{\rho}_{aa} &= \frac{\mathrm{i}\Omega_{pr}}{2}\left(\widetilde{\rho}_{ab} - \widetilde{\rho}_{ba}\right) + \frac{\mathrm{i}\Omega_{pu}}{2}\left(\widetilde{\rho}_{ac} - \widetilde{\rho}_{ca}\right) - \Gamma_a\rho_{aa} \ , \\
\dot{\rho}_{bb} &= \frac{\mathrm{i}\Omega_{pr}}{2}\left(\widetilde{\rho}_{ba} - \widetilde{\rho}_{ab}\right) - \Gamma_b\rho_{bb} + \frac{\Gamma_a}{2}\rho_{aa} \ , \\
\dot{\rho}_{cc} &= \frac{\mathrm{i}\Omega_{pu}}{2}\left(\widetilde{\rho}_{ca} - \widetilde{\rho}_{ac}\right) - \Gamma_c\rho_{cc} + \frac{\Gamma_a}{2}\rho_{aa} \ .
\end{aligned}$$

Similarly the equations of motion for the coherences are given by equations C.33, C.34, and C.35 on page 164 ,

$$\begin{aligned}
\dot{\widetilde{\rho}}_{ab} &= -\left(\gamma_{ab} - \mathrm{i}\delta_{pr}\right)\widetilde{\rho}_{ab} + \frac{\mathrm{i}\Omega_{pr}}{2}\left(\rho_{aa} - \rho_{bb}\right) \\
&\quad - \frac{\mathrm{i}\Omega_{pu}}{2}\widetilde{\rho}_{cb} \ , \\
\dot{\widetilde{\rho}}_{ac} &= -\left(\gamma_{ac} - \mathrm{i}\delta_{pu}\right)\widetilde{\rho}_{ac} + \frac{\mathrm{i}\Omega_{pu}}{2}\left(\rho_{aa} - \rho_{cc}\right) \\
&\quad - \frac{\mathrm{i}\Omega_{pr}}{2}\widetilde{\rho}_{bc} \ , \\
\dot{\widetilde{\rho}}_{cb} &= -\left(\gamma_{cb} - \mathrm{i}\left(\delta_{pr} - \delta_{pu}\right)\right)\widetilde{\rho}_{cb} + \frac{\mathrm{i}\Omega_{pr}}{2}\widetilde{\rho}_{ca} \\
&\quad - \frac{\mathrm{i}\Omega_{pu}}{2}\widetilde{\rho}_{ab} \ .
\end{aligned}$$

In the steady state the rate of change of the coherences are given by,

$$\begin{aligned}
\dot{\widetilde{\rho}}_{ab} &= \dot{\widetilde{\rho}}_{ac} \ , \\
&= \dot{\widetilde{\rho}}_{cb} \ , \\
&= 0 \ .
\end{aligned} \tag{3.13}$$

Likewise the rates of change of populations in this regime are given by,

$$\begin{aligned}
\dot{\rho}_{aa} &= \dot{\rho}_{bb} \ , \\
&= \dot{\rho}_{cc} \ , \\
&= 0 \ .
\end{aligned} \tag{3.14}$$

Furthermore, in the steady state population will be trapped in the non-coupling state. In the case of EIT, where $\Omega_{pu} \gg \Omega_{pr}$, the dark state, $|NC\rangle$ is equivalent to the ground state of the probe transition, $|b\rangle$. Hence,

$$\begin{aligned} \rho_{aa} &\simeq \rho_{cc} , \\ &\simeq 0 , \end{aligned} \tag{3.15}$$

$$\rho_{bb} \simeq 1 . \tag{3.16}$$

Substituting from equations 3.13, 3.15, and 3.16 into the equations of motion for the coherences (equations C.33, C.34, and C.35) leads to

$$\frac{i\Omega_{pu}}{2}\widetilde{\rho}_{cb} \simeq -(\gamma_{ab} - i\delta_{pr})\,\widetilde{\rho}_{ab} - \frac{i\Omega_{pr}}{2} , \tag{3.17}$$

$$\frac{i\Omega_{pr}}{2}\widetilde{\rho}_{bc} \simeq -(\gamma_{ac} - i\delta_{pu})\,\widetilde{\rho}_{ac} , \tag{3.18}$$

$$\frac{i\Omega_{pu}}{2}\widetilde{\rho}_{ab} \simeq -(\gamma_{cb} - i\,(\delta_{pr} - \delta_{pu}))\,\widetilde{\rho}_{cb} + \frac{i\Omega_{pr}}{2}\widetilde{\rho}_{ca} . \tag{3.19}$$

In the case that the populations of two levels is small, then the coherence between those two levels will be correspondingly small. This in conjunction with the fact that $\Omega_{pr} \ll \Omega_{pu}$, then the term $(i\Omega_{pr}/2)\,\widetilde{\rho}_{ca}$ in equation 3.19 can be neglected.

The absorption and dispersion experienced by a probe beam scanned across the transition $|b\rangle \rightarrow |a\rangle$ is proportional to the imaginary and real components of the coherence $\widetilde{\rho}_{ab}$, as shown in chapter 2. To determine $\widetilde{\rho}_{ab}$, substitute equation 3.17 into equation 3.19 multiplied by $i\Omega_{pu}/2$. This leads to,

$$-\left(\frac{\Omega_{pu}}{2}\right)^2 \widetilde{\rho}_{ab} = (\gamma_{cb} - i\,(\delta_{pr} - \delta_{pu}))\left(\frac{i\Omega_{pr}}{2} + (\gamma_{ab} - i\delta_{pr})\,\widetilde{\rho}_{ab}\right) , \tag{3.20}$$

$$\Longrightarrow \quad \widetilde{\rho}_{ab}\left(\frac{(\Omega_{pu}/2)^2}{\gamma_{cb} - i\,(\delta_{pr} - \delta_{pu})} + (\gamma_{ab} - i\delta_{pr})\right) = -\frac{i\Omega_{pr}}{2} , \tag{3.21}$$

$$\therefore \quad \widetilde{\rho}_{ab} = -\frac{i\Omega_{pr}}{2} \cdot 1 \Bigg/ \left((\gamma_{ab} - i\delta_{pr}) + \frac{(\Omega_{pu}/2)^2}{\gamma_{cb} - i\,(\delta_{pr} - \delta_{pu})}\right) . \tag{3.22}$$

From equation 2.64 on page 20 the complex refractive index of the medium is given by

$$\chi = -2 \frac{N d_{ba}^2}{\epsilon_0 \hbar \Omega_{pr}} \widetilde{\rho}_{ab} \,. \tag{3.23}$$

Utilising the Bloch vector notation (equation 2.65 on page 20 and equations 2.85, 2.86 on page 21 and equation 2.94 on page 23) the absorption coefficient, α, and dispersion, n_R, can be derived,

$$\alpha = -2 \frac{N d_{ba}^2}{\epsilon_0 \hbar} k_{pr} \frac{v}{\Omega_{pr}} \,, \tag{3.24}$$

$$n_R = 1 - \frac{N d_{ba}^2}{\epsilon_0 \hbar} \cdot \frac{u}{\Omega_{pr}} \,. \tag{3.25}$$

In this case,

$$\frac{u}{\Omega_{pr}} = \mathrm{Re}\left\{ -\frac{i}{2} \cdot 1 \Big/ \left((\gamma_{ab} - i\delta_{pr}) + \frac{(\Omega_{pu}/2)^2}{\gamma_{cb} - i(\delta_{pr} - \delta_{pu})} \right) \right\} \,, \tag{3.26}$$

$$\frac{v}{\Omega_{pr}} = \mathrm{Im}\left\{ -\frac{i}{2} \cdot 1 \Big/ \left((\gamma_{ab} - i\delta_{pr}) + \frac{(\Omega_{pu}/2)^2}{\gamma_{cb} - i(\delta_{pr} - \delta_{pu})} \right) \right\} \,. \tag{3.27}$$

Plots are made of the components of the Bloch vector as given in equations 3.26 and 3.27 . Fig. 3.3 shows $v/(\Omega_{pr}/\gamma_{ab})$ and $u/(\Omega_{pr}/\gamma_{ab})$ as a functions of Ω_{pu}/γ_{ab} and δ_{pr}/γ_{ab}, where $\gamma_{cb}/\gamma_{ab} = 10^{-6}$, and $\delta_{pu} = 0$.

Fig. 3.4 shows $v/(\Omega_{pr}/\gamma_{ab})$ and $v/(\Omega_{pr}/\gamma_{ab})$ as functions of Ω_{pu}/γ_{ab} and δ_{pr}/γ_{ab}, where $\gamma_{cb}/\gamma_{ab} = 10^{-6}$, and $\delta_{pu} = 0$.

As can be seen clearly from Fig. 3.3 (iii) and (iv), the initial increase in the Rabi frequency of the pump field from 0 causes the appearance of the induced transparency and with it the concomitant modification to the dispersion profile. Fig. 3.3 (i) and (ii) show that the continued escalation of the Rabi frequency of the pump beam lead the amplitude of the modification, to both u and v, to saturate. As the amplitude increases the width of the resonance does too. Once the amplitude has saturated, at $v = 0$ and $u = \pm 0.5$ respectively, continued inflation of the Rabi frequency of the pump simply broadens the EIT resonance.

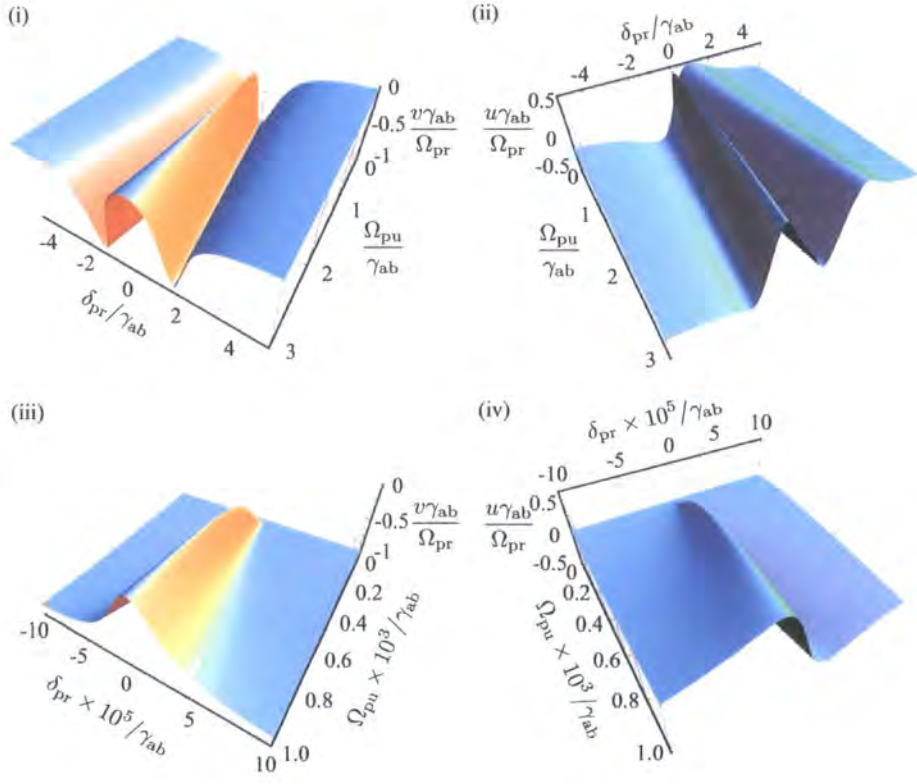

Figure 3.3: Three dimensional plots of the Bloch vector components (i) v and (ii) u, as a function of the Rabi frequency of the pump, Ω_{pu} and the detuning of the probe field from resonance, δ_{pr}. Both Ω_{pu} and δ_{pr} are plotted in units of the probe transition coherence decay rate, γ_{ab}. The ground state coherence decay rate, γ_{cb} is set to 10^{-6} γ_{ab}, and the pump beam detuning, $\delta_{pu} = 0$. (i) and (ii) show the progression of v and u respectively until the amplitude of the EIT features saturate at 0 and ± 0.5 respectively. Further increase in Ω_{pu} leads solely to broadening of the feature. (iii) and (iv) show the initial growth of the EIT feature in the narrow central region of the probe transition for small Rabi frequencies of the pump beam.

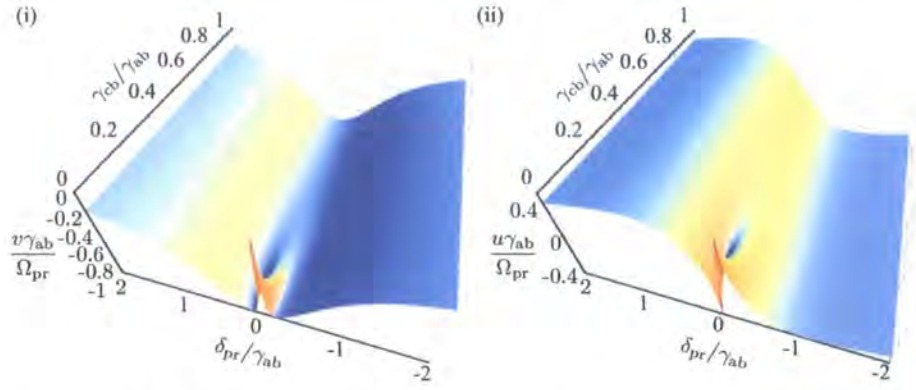

Figure 3.4: Three dimensional plots of the Bloch vector components (i) v and (ii) u, as a function of the ground state coherence decay rate, γ_{cb} and the detuning of the probe field from resonance, δ_{pr}. Both γ_{cb} and δ_{pr} are plotted in units of the probe transition coherence decay rate, γ_{ab}. The pump field has a Rabi frequency, $\Omega_{pu} = 0.3 \times \gamma_{ab}$, and is on resonance, $\delta_{pu} = 0$. As can be clearly seen in both plots an increase in the decay rate of the ground state coherence leads to significant reduction in the amplitude of the EIT resonance, such that when $\gamma_{ab} \simeq \Omega_{pu}$, the EIT signal is indistinguishable from the background.

Fig. 3.4 (i) and (ii) show $v/(\Omega_{pr}/\gamma_{ab})$ and $u/(\Omega_{pr}/\gamma_{ab})$ respectively as a function of γ_{cb}/γ_{ab} and δ_{pr}/γ_{ab}, where $\Omega_{pu}/\gamma_{ab} = 0.3$, and $\delta_{pu} = 0$. As is clearly shown in the two figures, the EIT feature is at its narrowest and largest amplitude when the coherence decay rate between the ground states is minimized. As the ground state coherence decay rate approaches the value of the Rabi frequency of the pump the EIT signal becomes indistinguishable from the background.

3.5 Line Broadening Mechanisms

It is apparent that in the case of a weak probe, the variables affecting the line width and amplitude of the EIT resonance are the Rabi frequency of the pump field, the lifetime of the coherences of the probe transition and the lifetime of the coherences between the ground states[1]. It is trivial to control the Rabi frequency of the pump simply by adjusting its intensity. The decay rates of the coherences have a minimum value derived from the natural line width of the ground and excited states, equation C.15. While it is not possible to increase the lifetimes of these states beyond the natural line width, it is possible to reduce their lifetimes through collisions with atoms and cell walls.

This section will concentrate on other mechanisms which either modify the width or shape of the EIT resonances. These include: the magnetic field; the relative directions of propagation of pump and probe beam; the line width of the lasers used to provide the pump and probe beam; the finite extent of the pump and probe beams and the intensity profile of the pump and probe beams.

In order to produce a theoretical model of EIT that would reproduce the experimentally observed spectra further measures have to be taken. EIT on the Rb D_2 line is not simply two fields interacting with three levels; there are in fact 60 different Zeeman sub-levels across both isotopes. A theoretical model taking account of all of the levels and the optical pumping between them is beyond the scope of this work. Doppler broadening of the hyperfine transitions is also relevant as it means that at any detuning of the pump beam within the Doppler-broadened hyperfine resonances will lead to the pump beam being resonant with different hyperfine transitions for different velocity classes of atoms.

[1] Collisional broadening can lead to broader resonances when it limits the relaxation rate of the atoms. This is not a factor in the work presented in this thesis. If the temperature or density of the Rb atoms was increased, or if a buffer gas was introduced, collisional broadening could become significant.

3.5.1 Magnetic Field Sensitivity

Three-level systems can be between three different hyperfine states or between Zeeman sublevels within two hyperfine states. As Zeeman levels are magnetically sensitive, it follows that resonances with Zeeman levels are subject to magnetic broadening in an inhomogeneous magnetic field.

Zeeman Effect

Every hyperfine state F has $2F + 1$ Zeeman sub-levels, denoted m_F, where $-F \leqslant m_F \leqslant F$. These Zeeman sub-levels are given by the projection of the total angular momentum F onto an external magnetic field $\mathbf{B}$.

The energy shift due to the Zeeman effect is ΔE_{Z}. Fig. 3.5 shows a Λ system with two ground states that are Zeeman sublevels of the same hyperfine state. It follows that the energy difference between the Zeeman sub-levels varies with $\mathbf{B}$, and in the region of interest, where $\Delta E_{\mathrm{Z}} \ll \Delta E_{\mathrm{HFS}}$ (where ΔE_{HFS} is the hyperfine splitting), it can be taken to vary linearly with the magnitude of the magnetic field, B. The Zeeman shift is

$$\Delta E_{\mathrm{Z}} = g_{\mathrm{F}} \mu_{\mathrm{B}} B m_F \,. \tag{3.28}$$

g_{F} is an effective Landé g-value, given by:

$$\begin{aligned} g_{\mathrm{F}} &= g_{\mathrm{J}} \frac{F(F+1) + J(J+1) - I(I+1)}{2F(F+1)} \\ &\quad - g_{\mathrm{I}}' \frac{F(F+1) - J(J+1) + I(I+1)}{2F(F+1)} \,, \end{aligned} \tag{3.29}$$

where,

$$\begin{aligned} g_{\mathrm{J}} &= \frac{J(J+1) + L(L+1) - S(S+1)}{2J(J+1)} \\ &\quad + g_{\mathrm{S}} \frac{J(J+1) - L(L+1) + S(S+1)}{2J(J+1)} \,, \end{aligned} \tag{3.30}$$

and,

$$g_{\mathrm{S}} \simeq 2 \,, \tag{3.31}$$

$$\Longrightarrow \quad g_{\mathrm{J}} = \frac{3J(J+1) - L(L+1) + S(S+1)}{2J(J+1)} \,. \tag{3.32}$$

As $g_I' \sim m/M$, where m is the electron mass and M is the proton mass, then $g_I' \ll g_J$. Hence,

$$g_F = \frac{3J(J+1) - L(L+1) + S(S+1)}{2J(J+1)} \times \frac{F(F+1) + J(J+1) - I(I+1)}{2F(F+1)} . \tag{3.33}$$

The notation used above is following that used in *Elementary Atomic Structure*, [61].

The values of g_F are calculated for all of the hyperfine states of the D-lines of ^{85}Rb and ^{87}Rb, and are shown in table 3.1 and 3.2, respectively. There is no g_F for $F = 0$.

Term	F			
	1	2	3	4
$^2S_{1/2}$		$-1/3$	$1/3$	
$^2P_{1/2}$		$-1/9$	$1/9$	
$^2P_{3/2}$	-1	$1/9$	$7/18$	$1/2$

Table 3.1: g_F for the hyperfine states of ^{85}Rb.

Term	F		
	1	2	3
$^2S_{1/2}$	$-1/2$	$1/2$	
$^2P_{1/2}$	$-1/6$	$1/6$	
$^2P_{3/2}$	$2/3$	$2/3$	$2/3$

Table 3.2: g_F for the hyperfine states of ^{87}Rb.

In the following chapters a Λ system made up of σ_+ and σ_- beams with the states $|b\rangle$ and $|c\rangle$ being $|F,\ m_F = -1\rangle$ and $|F,\ m_F = +1\rangle$ will be considered.

The linear frequency shift in the position of such a resonance is calculated and shown in tables 3.3 and 3.4 .

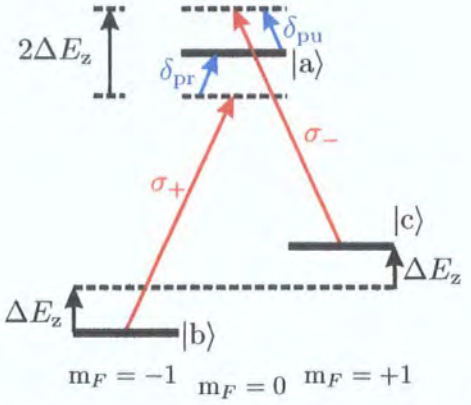

Figure 3.5: ΔE_z is the magnitude of the shift of the levels due to the Zeeman effect, in the absence of the B-field both σ_+ and σ_- would be on resonance with the states shown.

Term	F			
	1	2	3	4
$^2S_{1/2}$		−0.47	+0.47	
$^2P_{1/2}$		−0.16	+0.16	
$^2P_{3/2}$	− 1.4	+0.16	+0.54	+0.7

Table 3.3: Ratio of the Zeeman shift to m_F (MHz/G) for the hyperfine states of ^{85}Rb.

Term	F		
	1	2	3
$^2S_{1/2}$	−0.7	+0.7	
$^2P_{1/2}$	−0.23	+0.23	
$^2P_{3/2}$	+0.93	+0.93	+0.93

Table 3.4: Ratio of the Zeeman shift to m_F (MHz/G) for the hyperfine states of ^{87}Rb.

Magnetic Field Broadening

If the levels in an EIT system are magnetically sensitive, then it follows that a non-uniform magnetic field can cause position-dependent shifts in the frequency of the resonance.

Specifically, consider the case of a Λ system where both ground states are different Zeeman sub-levels of the same hyperfine level (see Fig. 3.5).

Any non-uniformity in magnetic field, $\Delta\mathbf{B}$ along the axis of the pump and probe beam, will lead to a broadening of any feature by an amount $\Delta\nu$. From equation 3.28,

$$\Delta\nu = \frac{g_F \mu_B \Delta B \Delta m_F}{h} , \tag{3.34}$$

where Δm_F is the difference in m_F values between the ground states.

3.5.2 Probe and Pump Beam Crossing Angle

When pump and probe fields were discussed previously it was in relation to saturation spectroscopy, § 2.6.1 on page 39, and counter-propagating beams were required. In order to determine the appropriate orientation for pump and probe beams for EIT in a Λ system the following analysis is required.

Consider a scheme in which a pump and a probe beam propagate at an angle θ to one another, Fig. 3.6. In addition consider an atom propagating at an angle α to the bisector of the pump and probe, with a velocity, $\mathbf{v}$. The atom's velocity can be resolved into two components, $\mathbf{v}_{\|}$, parallel to the bisector of the pump and probe and $\mathbf{v}_{\perp}$, perpendicular to the bisector. This causes a change in the detuning of both the probe and pump from the resonances, $|\mathrm{b}\rangle \rightarrow |\mathrm{a}\rangle$ and $|\mathrm{c}\rangle \rightarrow |\mathrm{a}\rangle$, respectively,

$$\delta_{\mathrm{pr}} \rightarrow \delta_{\mathrm{pr}} - \boldsymbol{k}_{\mathrm{pr}} \cdot \mathbf{v} , \tag{3.35}$$

$$\delta_{\mathrm{pu}} \rightarrow \delta_{\mathrm{pu}} - \boldsymbol{k}_{\mathrm{pu}} \cdot \mathbf{v} . \tag{3.36}$$

Thus the coherence, $\widetilde{\rho}_{\mathrm{ab}}$ (equation 3.22) that leads to the probe absorption and

dispersion, becomes,

$$\widetilde{\rho}_{ab} = \frac{-i\Omega_{pr}}{2} \times \left((\gamma_{ab} - i(\delta_{pr} - \boldsymbol{k}_{pr} \cdot \mathbf{v})) + \frac{(\Omega_{pu}/2)^2}{\gamma_{cb} - i(\delta_{pr} - \delta_{pu} + \boldsymbol{k}_{pu} \cdot \mathbf{v} - \boldsymbol{k}_{pr} \cdot \mathbf{v})} \right)^{-1} . \tag{3.37}$$

A shift in frequency of the two-photon resonance, $\delta_{\mathbf{v}}$, will result. For a Λ system this will take the form,

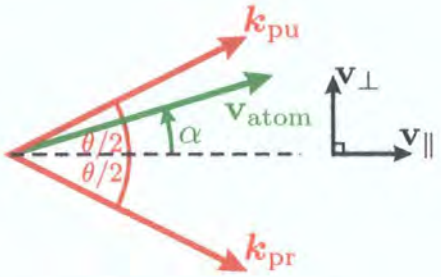

Figure 3.6: The diagram shows the crossing angle of the pump and probe beams, θ. The direction of propagation of the atoms in the medium is given by α. The reference coordinates are $\mathbf{v}_\parallel$, the bisector of the pump and probe beams, and $\mathbf{v}_\perp$ the perpendicular to the bisector of the pump and probe beams.

$$\begin{aligned} \delta_{\mathbf{v}} &= (\boldsymbol{k}_{pu} - \boldsymbol{k}_{pr}) \cdot \mathbf{v} , & (3.38) \\ &= k_{pu} v \cos\left(\frac{\theta}{2} - \alpha\right) - k_{pr} v \cos\left(\frac{\theta}{2} + \alpha\right) , \\ &= \left[k_{pu} \left(\cos\frac{\theta}{2} \cos\alpha + \sin\frac{\theta}{2} \sin\alpha \right) \right. \\ &\quad \left. - k_{pr} \left(\cos\frac{\theta}{2} \cos\alpha - \sin\frac{\theta}{2} \sin\alpha \right) \right] v . & (3.39) \end{aligned}$$

$$\begin{aligned} \text{Re-writing } k_{pu} &= k_{pr} + \delta k , & (3.40) \\ \text{then } \delta_{\mathbf{v}} &= \left[2k_{pr} \sin\frac{\theta}{2} \sin\alpha + \delta k \cos\left(\frac{\theta}{2} - \alpha\right) \right] v . & (3.41) \end{aligned}$$

For a Λ system where both ground states are Zeeman sub-levels of the same hyperfine state, δk_{pr} is given by the Zeeman splitting. In the case of the Rb D_2 line, $k_{pr} \simeq 8 \times 10^6$ m^{-1}. The Zeeman splitting between the two Λ groundstates

in the hyperfine state $F = 1$ of ^{87}Rb for a magnetic field of 1 G is 1.40 MHz (see table 3.4 on page 57) this gives $\delta k = 29.3 \times 10^{-3}$ m^{-1} , leading to:

$$\frac{\delta k}{k_{\rm pr}} \simeq 10^{-9} \; . \tag{3.42}$$

Resolving the velocity of the atom into its two components, $\mathrm{v}_{\|}$ and $\mathrm{v}_{\perp}$, where,

$$\mathrm{v}_{\|} = |\mathbf{v}| \cos\alpha \; , \tag{3.43}$$

$$\mathrm{v}_{\perp} = |\mathbf{v}| \sin\alpha \; . \tag{3.44}$$

In the case that $\delta k \ll k_{\rm pr}$, and by considering the velocity in terms the two perpendicular components equation 3.41 reduces to,

$$\delta_{\mathbf{v}} = 2k_{\rm pr} \sin(\theta/2)\mathrm{v}_{\perp} \; . \tag{3.45}$$

The single-photon detuning due to the Doppler shift of the probe is given by,

$$-\boldsymbol{k}_{\rm pr} \cdot \mathbf{v} = -k_{\rm pr}\mathrm{v}\cos\left(\frac{\theta}{2} + \alpha\right) \; , \tag{3.46}$$

$$= -k_{\rm pr}\mathrm{v}_{\rm pr} \; . \tag{3.47}$$

$\mathrm{v}_{\rm pr}$ is the component of the atom's velocity parallel to $\boldsymbol{k}_{\rm pr}$.

It follows that equation 3.37 can be written,

$$\widetilde{\rho}_{\rm ab} = -\frac{\mathrm{i}\Omega_{\rm pr}}{2} \times \left((\gamma_{\rm ab} - \mathrm{i}\,(\delta_{\rm pr} - k_{\rm pr}\mathrm{v}_{\rm pr})) + \frac{(\Omega_{\rm pu}/2)^2}{\gamma_{\rm cb} - \mathrm{i}\,(\delta_{\rm pr} - \delta_{\rm pu} + 2k_{\rm pr}\sin(\theta/2)\mathrm{v}_{\perp})} \right)^{-1} \; . \tag{3.48}$$

In a vapour cell the velocity distribution of the atoms is homogeneous and isotropic and is given by the Maxwellian distribution. From § 2.3.4 and equation 2.96 on page 24, the Maxwellian velocity distribution is given by,

$$N(\mathrm{v}_z)\,\mathrm{dv}_z = \frac{N}{\sqrt{\pi}} \cdot \sqrt{\frac{m}{2\mathrm{k_B}T}} \exp\left[-\left(\mathrm{v}_z \sqrt{\frac{m}{2\mathrm{k_B}T}} \right)^2 \right] \mathrm{dv}_z \; .$$

v_z is the velocity in one dimension. As the velocity is isotropic in the vapour cell, then the distribution of v_z is the same as the distribution of $\mathrm{v}_{\perp}$ and $\mathrm{v}_{\rm pr}$.

It follows that the absorption coefficient of the medium is given by,

$$\alpha \propto \int_{-\infty}^{\infty} \int_{-\infty}^{\infty} \mathrm{Im}\left\{\widetilde{\rho}_{\rm ab}\right\}(\mathrm{v}_{\rm pr}, \mathrm{v}_{\perp}) N(\mathrm{v}_{\rm pr})\, N(\mathrm{v}_{\perp})\, \mathrm{dv}_{\rm pr}\mathrm{dv}_{\perp} \; . \tag{3.49}$$

Using *Mathematica*, the absorption of such a medium has been calculated. The normalized absorption coefficient is given by,

$$\alpha_{\text{norm}} = \frac{\alpha}{\alpha\left(\delta_{\text{pr}} = 0,\ \Omega_{\text{pu}} = 0\right)} . \tag{3.50}$$

A plot of the line-centre normalized absorption coefficient is shown in Fig. 3.7 . As can be seen the EIT resonance dies away rapidly as the pump and probe move away from copropagating. As the temperature of the atomic ensemble increases, so does the rate at which the amplitude of the EIT resonance dies away with increasing angle between the pump and probe.

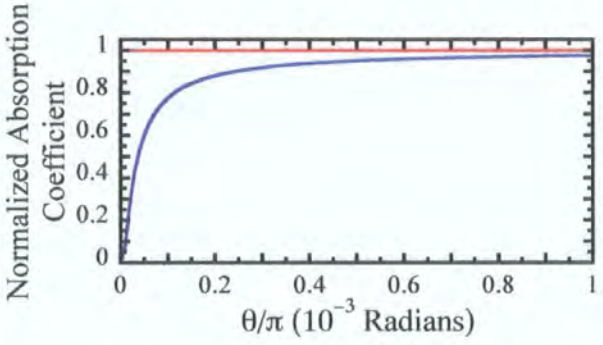

Figure 3.7: The normalized absorption coefficient for a Λ system is plotted as a function of angle between the pump and probe beam from $\theta = 0$ to $\theta = 10^{-3}\pi$. The red line shows the absorption for $\Omega_{\text{pu}} = 0$, whereas the blue line shows the absorption for $\Omega_{\text{pu}} = 0.4\gamma_{\text{ab}}$. The velocity distribution of the atomic ensemble is that of ^{87}Rb at room temperature, 293 K. For the purpose of this plot $\delta_{\text{pr}} = 0$, $\delta_{\text{pu}} = 0$, and $\gamma_{\text{cb}} = 10^{-6}\gamma_{\text{ab}}$.

An experimental verification of this has been provided by Carvalho *et al.*, [62].

Ideally in the three-level Λ and V type systems, the pump and probe should be perfectly co-propagating to cancel the Doppler broadening of the two-photon resonance (due to component of the atoms' velocity perpendicular to the bisector of the pump and probe beams) to as high a degree as possible.

3.5.3 Laser Line Width

Including the line widths of the lasers used in measuring EIT resonances (probe and pump) would lead to the increased rate of decay of atomic coherences, [63]. This would have the effect of broadening and reducing the amplitude of the EIT resonances as seen in Fig. 3.4.

This effect can be cancelled in a Λ system if there is a critical cross-correlation between the pump and probe, [64]. The critical cross-correlation causes any laser jitter to cancel in its effect on the Λ-system. This is often achieved by phase locking the pump and probe laser together, [20]. It is also possible to injection lock one laser to another by modulating the current to one laser, [65]. This induces sidebands on the output of the first laser. One of these sidebands is injected into the second laser. The output of the second laser is phase locked to the first and at a frequency separation given by the modulation frequency of the laser current.

An alternative method is to use one laser to provide both pump and probe beams. Any frequency offset between the pump and probe field can be provided by an optical element such as an acousto-optic modulator. Thus it is possible to measure resonances many orders of magnitude narrower than the line width of the laser.

3.5.4 Transit-Time Broadening

Atoms with a non-zero velocity perpendicular to the direction of propagation of the pump and probe beams will traverse the pump and probe beams in a finite time. In the atoms's frame of reference this takes the form of the pump and probe beams comprising of finite pulses as opposed to continuous wave laser beams. Any finite time pulse has a spread in frequency about the mean frequency of the continuous wave beam. The shorter the pulse the greater the spread in frequency. This leads to broadening of any spectral features, and is referred to as transit-time broadening.

The case in which the EIT resonance is transit time broadened is addressed by Thomas and Quivers Jr., [66]. They consider the scheme in which the pump and probe beams have a Gaussian intensity profile. When the groundstate

lifetime is much longer than the transit time of the atoms through the beams; the excited state lifetime is much less than the transit time of the atoms through the beam; and where the pump and probe powers are small enough that they do not contribute to the broadening, then the expected line shape is a cusp function, with a FWHM, Γ_{EIT}, given by,

$$\Gamma_{\mathrm{EIT}} = \frac{2\sqrt{2}\ \ln 2\ \mathrm{v}}{d} \ . \tag{3.51}$$

d is the 1/e beam diameter and v is the thermal speed of the atoms,

$$\mathrm{v} \ = \ \sqrt{\frac{2\mathrm{k_B}T}{m}} \ , \tag{3.52}$$

$\mathrm{k_B}$ is the Boltzmann constant, T is the temperature of the atoms and m is the atomic mass. A cusp function being a back-to-back exponential of the general form,

$$\exp\left(-\left|\frac{\omega-\omega_0}{\omega_\Delta}\right|\right) \ , \tag{3.53}$$

where ω_Δ is the 1/e half-width [2], ω is the frequency and ω_0 is the frequency of the centre of the resonance.

An experimental study of this has been made by Knappe *et al.*, [67]. Knappe *et al.* show that for narrow beam the cusp line shape gives a better fit than the standard Lorentzian model. However at line centre the cusp model does not fit the data, this is explained as being due to other broadening effects. As the width of the beam is increased, the cusp model becomes a less good fit, whilst the Lorenzian model accurately describes the resonance line shape.

3.5.5 Beam Profile Effect on Line Shape

In the previous subsection the case of transit-time broadening was addressed for beams with Gaussian intensity profiles. In the work that is presented in this thesis, the profiles of the probe and pump beams can not always be described by a Gaussian function. The pump and probe beams are expected to have a Gaussian profile when an optical fibre patchcord is used to ensure that they are overlapped. In all other cases the profile will not necessarily be uniform, nor

[2] For a cusp function the 1/e half width is equal to FWHM/(2 ln 2) .

Gaussian. This is due to the optical elements that the beams have traversed on their way to the vapour cell.

Taĭchenachev et al., [68], consider the effect of different beam profiles. The regime considered by Taĭchenachev *et al.* is that in which the relaxation rate of the atoms, Γ_L, is much greater than the diffusion rate of the atoms through the beams. For a buffer gas cell,

$$\Gamma_L \gg \frac{D}{r_0^2} , \tag{3.54}$$

and no for no buffer gas, where

$$\Gamma_L \gg \frac{v}{r_0} . \tag{3.55}$$

D is the diffusion constant, v is defined in equation 3.52 , and r_0 is the 1/e radius of the beam.

The two contrasting beam profiles are of the form,

$$I = I_0 f\left(\frac{r}{r_0}\right) , \tag{3.56}$$

where there is the standard Gaussian,

$$f\left(\frac{r}{r_0}\right) = e^{-(r/r_0)^2} , \tag{3.57}$$

and a step-like profile,

$$f\left(\frac{r}{r_0}\right) = 1, \quad r \leqslant r_0 ; \tag{3.58}$$

$$= 0, \quad r_0 \leqslant r . \tag{3.59}$$

The FWHM of the EIT features for Gaussian, Γ_G, and step-like, Γ_{STEP}, beams are given by,

$$\Gamma_G \simeq 0.86 Z_0 \gamma_{cb} , \tag{3.60}$$

$$\Gamma_{STEP} \simeq 2 Z_0 \gamma_{cb} , \tag{3.61}$$

respectively. γ_{cb} is the decay rate of coherence between the two lower states of the Λ system, and

$$Z_0 = 2 \cdot \frac{\Omega_{pr}^2 + \Omega_{pu}^2}{\Gamma_a^2} \cdot \frac{1}{\gamma_{cb}/\Gamma_a} , \tag{3.62}$$

$$= 2 \cdot \frac{\Omega_{pr}^2 + \Omega_{pu}^2}{\Gamma_a \gamma_{cb}} , \tag{3.63}$$

Substituting equation 3.63 into equations 3.60 and 3.61 leads to,

$$\Gamma_G \simeq 1.72 \cdot \frac{\Omega_{pr}^2 + \Omega_{pu}^2}{\Gamma_a} , \tag{3.64}$$

$$\Gamma_{STEP} \simeq 4 \cdot \frac{\Omega_{pr}^2 + \Omega_{pu}^2}{\Gamma_a} , \tag{3.65}$$

The step-like beam profile leads to the standard Lorentzian line shape. The Gaussian beam profile leads to a more complicated line shape, $\mathcal{R}_G$, which in the limit that,

$$Z_0 \gg 1 , \tag{3.66}$$

$$\text{is given by} \quad \mathcal{R}_G = 1 - \frac{\Delta}{Z_0} \cdot \arctan\left(\frac{Z_0}{\Delta}\right) , \tag{3.67}$$

where Δ is the two-photon detuning normalized to the ground state coherence decay rate, $(\delta_{pr} - \delta_{pu})/\gamma_{cb}$.

3.5.6 Doppler Broadening Effect on EIT Line Width

Javan et al., [69], have theoretically studied the effect of Doppler-broadening of a medium on the EIT line width. They find an explicit expression for the FWHM of an EIT resonance, Γ_{EIT}, in a Doppler-broadened medium.

$$\Gamma_{EIT}^2 = \frac{\gamma_{cb}\Omega_{pu}^2}{\Gamma_a} \cdot (1+x)\left(1 + \sqrt{1 + \frac{4x}{(1+x)^2}}\right) , \tag{3.68}$$

$$\text{where,} \quad x = \frac{\Gamma_a}{2\gamma_{cb}} \cdot \frac{\Omega_{pu}^2}{W_D^2} . \tag{3.69}$$

W_D is the FWHM of the Doppler-broadened resonance, Ω_{pu} is the Rabi frequency of the pump field, Γ_a is the excited state decay rate, and γ_{cb} is the decay rate of the groundstate coherence. Note that this is in the regime where the probe intensity is vanishingly small. Substituting equation 3.63 into equation 3.69, for comparison with the beam profile contribution to line shape, leads to

$$x = \frac{\Gamma_a^2}{4W_D^2} \cdot Z_0\,(\Omega_{pr} = 0) . \tag{3.70}$$

The two extreme limits of the model are for $x \ll 1$ and $x \gg 1$. From equation 3.70 it follows that the extremes correspond to,

$$\left(\frac{\Omega_{pu}}{W_D}\right)^2 \ll \frac{2\gamma_{cb}}{\Gamma_a}, \quad x \ll 1 ; \tag{3.71}$$

$$\left(\frac{\Omega_{pu}}{W_D}\right)^2 \gg \frac{2\gamma_{cb}}{\Gamma_a}, \quad x \gg 1 . \tag{3.72}$$

In the two extreme limits, this model gives two different functions for the width of the EIT resonance,

$$\Gamma_{EIT} = \sqrt{\frac{\gamma_{cb}}{\Gamma_a}} \cdot \Omega_{pu} , \quad x \ll 1 ; \tag{3.73}$$

$$= \frac{\Omega_{pu}^2}{W_D} , \quad x \gg 1 . \tag{3.74}$$

As the Rabi frequency is proportional to the square root of the beam intensity it follows that in the regime where $x \ll 1$, the width of the EIT feature increases in direct proportion to the square root of the intensity of the pump; in the regime where $x \gg 1$ the width of the EIT feature is proportional to the intensity of the pump.

3.6 Electromagnetically Induced Absorption

Electromagnetically Induced Absorption (EIA), [70, 71], is the increase in absorption of a probe beam by a medium due to the presence of a pump beam. There are four different systems in which EIA has been identified, [72, 73, 74, 75, 76]. Two mechanisms involve degenerate two-level systems. They rely on the transfer of coherence (TOC), [72, 73], and transfer of population (TOP), [72, 74], to generate the induced absorption.

EIA due to the transfer of coherence, EIA-TOC, requires that the pump and probe have different polarizations. EIA due to transfer of population, EIA-TOP, requires that the polarization of pump and probe should be the same.

The experimental work presented in the following chapters involves the use of orthogonally polarized pump and probe beams. Hence any EIA observed will be due to the transfer of coherence.

3.6.1 Transfer of Coherence

Taĭchenachev *et al.*, [77], first showed that EIA was due to TOC from the excited states to the ground states. No explanation was offered as to why there are systems where TOC takes place without resulting in EIA.

Goren *et al.*, [72, 73], clarified the conditions necessary for TOC to result in EIA. This can occur only when the pump and probe lasers have different polarizations and there is a significant pump-induced population in the excited state (for example one-sixth of the total population, [72]). The excited and ground hyperfine states must also meet the following criteria, $F_e = F_g + 1$ and $F_g > 0$.

EIA-TOC requires at least two degenerate ground levels and at least two degenerate excited states — the N-system, Fig. 3.8 . Coherence builds up between the degenerate excited states. Spontaneous emission causes a transfer of coherence from the degenerate excited states to the degenerate ground states, [77]. It is the transfer of coherence that leads to the induced absorption.

In order for the coherence to build up between the excited states it is necessary to have a significant fraction of the population in the excited states. To get a significant fraction of the population in the excited states normally requires

that one of the pump transitions should be closed. In ^{85}Rb the closed transition is $5\ ^2S_{1/2}\ F = 3,\ m_F = \pm 3 \rightarrow 5\ ^2P_{3/2}\ F = 4,\ m_F = \pm 4$ and in ^{87}Rb it is $5\ ^2S_{1/2}\ F = 2,\ m_F = \pm 2 \rightarrow 5\ ^2P_{3/2}\ F = 3,\ m_F = \pm 3$. These closed transitions correspond to the transition $|c\rangle \rightarrow |d\rangle$ in Fig. 3.8. Similarly the transition $|b\rangle \rightarrow |a\rangle$ in Fig. 3.8 corresponds to $5\ ^2S_{1/2}\ F = 3,\ m_F = \pm 3 \rightarrow 5\ ^2P_{3/2}\ F = 3,\ m_F = \pm 3$ in ^{85}Rb and $5\ ^2S_{1/2}\ F = 2,\ m_F = \pm 2 \rightarrow 5\ ^2P_{3/2}\ F = 2,\ m_F = \pm 2$ in ^{87}Rb.

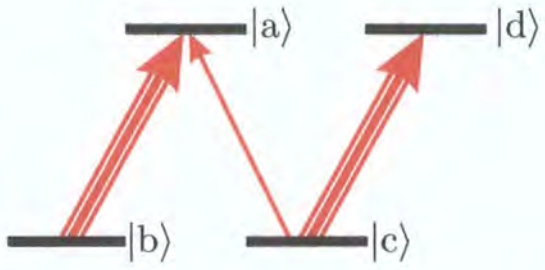

Figure 3.8: N system diagram. The two heavy red arrows show the pump transitions. The fine red arrow shows the probe transition. The difference in pump and probe polarization leads to the pump and probe being resonant with different transitions between the four states.

This normally would preclude open systems from exhibiting EIA, however open systems can exhibit EIA, [78]. An explanation of this is presented by Goren *et al.*, [72]. In this case EIA only occurs for relatively large pump Rabi frequencies. When the Rabi frequency of the pump is increased the excited state population increases and hence the excited state coherence is increased too. This leads to an increased TOC to the ground state, ultimately resulting in EIA.

Goren *et al.*, [73], carry out a full theoretical investigation of the N-system, varying the degree of TOC, and the strengths of the pump transitions[3]. It is noted that as the strength of either pump transition is reduced to zero, the spectra is consistent with what would be expected in an EIT Λ or V system. Reducing the TOC significantly reduces the predicted EIA, until for zero TOC EIT is predicted instead of EIA.

The behaviour of the N-system with TOC is also seen in the EIA spectra of the

[3]In the case that one pump beam is applied to two degenerate transitions, the strength of those transitions will not necessarily be the same. This is due to the different Clebsch-Gordan coefficients for the different transitions.

Hanle[4] configuration, as explained by Renzoni *et al.*, [80].

The recent work on optical-pumping-assisted EIT by Jiang *et al.*, [81], which shows increased transmission due to the application of a second pump field, bears many similarities to the N system involved in EIA-TOC. The most striking differences are the relative order of the pump and probe within the N system, and the significant deviation from degeneracy which prevents TOC.

3.7 Group Velocity

3.7.1 Group Velocity Derivation

In the case where an electromagnetic field does not have a single frequency, interference between the components with different frequencies will lead to a beat pattern. The rate at which the envelope of this pattern advances is known as the group velocity, v_g, and it is given by:

$$v_g = \frac{d\omega}{dk} . \tag{3.75}$$

As,

$$\omega = \frac{k\,c}{n_R} , \tag{3.76}$$

then substituting equation 3.76 into equation 3.75 leads to,

$$\begin{aligned} v_g &= \frac{c}{n_R} + k\,c\frac{d\,(1/n_R)}{dn_R} \cdot \frac{dn_R}{dk} , \\ &= \frac{c}{n_R} - \frac{k\,c}{n_R^2} \cdot \frac{dn_R}{d\omega} \cdot \frac{d\omega}{dk} , \end{aligned} \tag{3.77}$$

$$\implies v_g + v_g\frac{k\,c}{n_R^2} \cdot \frac{dn_R}{d\omega} = \frac{c}{n_R} . \tag{3.78}$$

Substituting equation 3.76 into equation 3.78, leads to:

$$v_g = \frac{c}{n_R + \omega\,(dn_R/d\omega)} . \tag{3.79}$$

3.7.2 Lorentzian Line Shape Group Velocity

The rate of change of the real part of the refractive index with respect to frequency, $dn_R/d\omega$, for a Lorentzian line shape can be derived from equation 2.87

[4]For an explanation of the Hanle effect see *Atomic and Laser Spectroscopy*, [79].

on page 22. In turn it is possible to determine the modification of group velocity at line centre. In the case that the probe is in the weak regime ($\Gamma_a \gg \Omega_{pr}$) then equation 2.87 becomes:

$$n_R - 1 = -\frac{N d_{ba}^2}{2\epsilon_0 \hbar} \cdot \frac{\delta_{pr}}{\delta_{pr}^2 + (\Gamma_a/2)^2} \cdot \tag{3.80}$$

Differentiating with respect to δ_{pr} leads to:

$$\frac{d(n_R - 1)}{d(\delta_{pr})} = \frac{N d_{ba}^2}{2\epsilon_0 \hbar} \left[\frac{2\delta_{pr}^2}{\left(\delta_{pr}^2 + (\Gamma_a/2)^2\right)^2} - \frac{1}{\delta_{pr}^2 + (\Gamma_a/2)^2} \right] , \tag{3.81}$$

and as,

$$\frac{d(n_R - 1)}{d(\delta_{pr})} = \frac{d(n_R - 1)}{dn_R} \cdot \frac{d\omega_{pr}}{d\delta_{pr}} \cdot \frac{dn_R}{d\omega_{pr}} , \tag{3.82}$$

$$= \frac{dn_R}{d\omega_{pr}} , \tag{3.83}$$

where,

$$\frac{d(n_R - 1)}{dn} = \frac{d\omega_{pr}}{d\delta_{pr}} \equiv 1 . \tag{3.84}$$

To find the frequency at which the group velocity is at its lowest, the second derivative of n_R with respect to ω_{pr} has to be found and set equal to 0.

$$\frac{d^2 n_R}{d\omega_{pr}^2} = \frac{N d_{ba}^2}{2\epsilon_0 \hbar} \left[\frac{4\,\delta_{pr}}{\left(\delta_{pr}^2 + (\Gamma_a/2)^2\right)^2} - \frac{8\,\delta_{pr}^3}{\left(\delta_{pr}^2 + (\Gamma_a/2)^2\right)^3} + \frac{2\,\delta_{pr}}{\left(\delta_{pr}^2 + (\Gamma_a/2)^2\right)^2} \right] , \tag{3.85}$$

$$= 0 , \tag{3.86}$$

$$\Longrightarrow \frac{3\,\delta_{pr}}{\left(\delta_{pr}^2 + (\Gamma_a/2)^2\right)^2} - \frac{4\,\delta_{pr}^3}{\left(\delta_{pr}^2 + (\Gamma_a/2)^2\right)^3} = 0 , \tag{3.87}$$

$$\Longrightarrow \delta_{pr} = 0 , \tag{3.88}$$

$$\text{or,} \quad 4\,\delta_{pr}^2 = 3\left(\delta_{pr}^2 + (\Gamma_a/2)^2\right) , \tag{3.89}$$

$$\Longrightarrow \delta_{pr} = \pm\frac{\sqrt{3}\Gamma_a}{2} . \tag{3.90}$$

On line centre, $\delta_{\rm pr} = 0$,

$$\frac{{\rm d}n_{\rm R}}{{\rm d}\omega_{\rm pr}} = -\frac{N{\rm d}_{\rm ba}^2}{2\epsilon_0\hbar} \cdot \frac{1}{(\Gamma_{\rm a}/2)^2} \ . \tag{3.91}$$

Whereas for $\delta_{\rm pr} = \pm\sqrt{3}\ (\Gamma_{\rm a}/2)$,

$$\frac{{\rm d}n_{\rm R}}{{\rm d}\omega_{\rm pr}} = \frac{N{\rm d}_{\rm ba}^2}{2\epsilon_0\hbar} \cdot \frac{1}{8\,(\Gamma_{\rm a}/2)^2} \ . \tag{3.92}$$

Hence $|{\rm d}n_{\rm R}/{\rm d}\omega|$ is at its greatest at line centre.

The line centre absorption can be derived from equations 2.88 and 2.94 on page 23.

$$\begin{aligned} \alpha(\delta_{\rm pr} = 0) &= 2n_{\rm I}(\delta_{\rm pr} = 0)k_{\rm ab} \ , \\ &= 2k_{\rm ab}\frac{N{\rm d}_{\rm ba}^2}{2\epsilon_0\hbar}\left(\frac{\Gamma_{\rm a}}{2}\right)^{-1} \ , \end{aligned}$$

$$\implies \quad \frac{\alpha(\delta_{\rm pr} = 0)}{k_{\rm ab}\Gamma_{\rm a}} = \frac{N{\rm d}_{\rm ba}^2}{2\epsilon_0\hbar} \cdot \frac{1}{(\Gamma_{\rm a}/2)^2} \ . \tag{3.93}$$

Substituting equation 3.93 into 3.92 leads to,

$$\left.\frac{{\rm d}n_{\rm R}}{{\rm d}\omega_{\rm pr}}\right|_{\delta_{\rm pr}=0} = -\alpha(\delta_{\rm pr} = 0)\frac{1}{k_{\rm ab}\Gamma_{\rm a}} \ . \tag{3.94}$$

Hence the line centre rate of change of the real part of the refractive index is directly proportional to the line centre absorption.

3.7.3 EIT Group Velocity

In the regime where the line shape of an EIT or EIA resonance is closely approximated by a Lorentzian function, then the results of the previous subsection can be used to determine the modification of the group velocity due to EIT or EIA. If the normalised transmission intensity of the EIT/EIA resonance, $I_{\rm EIT}$, is given by,

$$I_{\rm EIT} = I_{\rm BACK}\ {\rm e}^{-\alpha_{\rm EIT}z} \ , \tag{3.95}$$

where $I_{\rm BACK}$ is the intensity transmitted in the absence of the EIT/EIA resonance, it follows that,

$$\alpha_{\rm EIT} = \frac{1}{z}\ln\left|\frac{I_{\rm BACK}}{I_{\rm EIT}}\right| \ . \tag{3.96}$$

α_{EIT} is specifically the modification to the absorption coefficient due to the EIT/EIA resonance.

In order to determine the dispersion, and hence the group velocity, concomitant with an EIT/EIA resonance at the centre of the that resonance, equation 3.96 has to be substituted into equation 3.94 . This leads to,

$$\left.\frac{\mathrm{d}n_{\mathrm{R}}}{\mathrm{d}\omega_{\mathrm{pr}}}\right|_{\delta_{\mathrm{pr}}=0} = -\frac{1}{z}\ln\left|\frac{I_{\mathrm{BACK}}}{I_{\mathrm{EIT}}}\right| \cdot \frac{\mathrm{c}}{\omega_{\mathrm{ab}}} \cdot \frac{1}{\Gamma_{\mathrm{EIT}}}\,, \tag{3.97}$$

$$\Longrightarrow \quad \mathrm{v_g} = \frac{\mathrm{c}}{n_{\mathrm{R}} + (\mathrm{c}/z)\ln\left|\frac{I_{\mathrm{EIT}}}{I_{\mathrm{BACK}}}\right| (1/\Gamma_{\mathrm{EIT}})}\,, \tag{3.98}$$

where Γ_{EIT} is the FWHM of the EIT/EIA resonance.

In the work presented in this thesis the majority of measurements have been carried out on the $F = 1 \rightarrow F'$ hyperfine transitions of the ^{87}Rb D_2 line. In an 8 cm long Rb vapour cell at room temperature, as has been used throughout this work, this transition will give normalised transmission at the centre of the Doppler-broadened resonance of 0.9. Fig. 3.9 shows a plot of the predicted group velocity for a range of Lorentzian FWHM, $\Gamma_{\mathrm{EIT}}/2\pi$, of 40 kHz to 250 kHz and for normalised EIT amplitudes, $I_{\mathrm{EIT}} - I_{\mathrm{BACK}}$, of 0.01 to 0.045.

As can be seen in Fig. 3.9 the group velocity for a probe pulse is 0.006 c for an EIT resonance with FWHM 250 kHz and amplitude 0.01 . The group velocity falls to 2×10^{-4} c for a resonance of amplitude 0.045 with a FWHM 40 kHz.

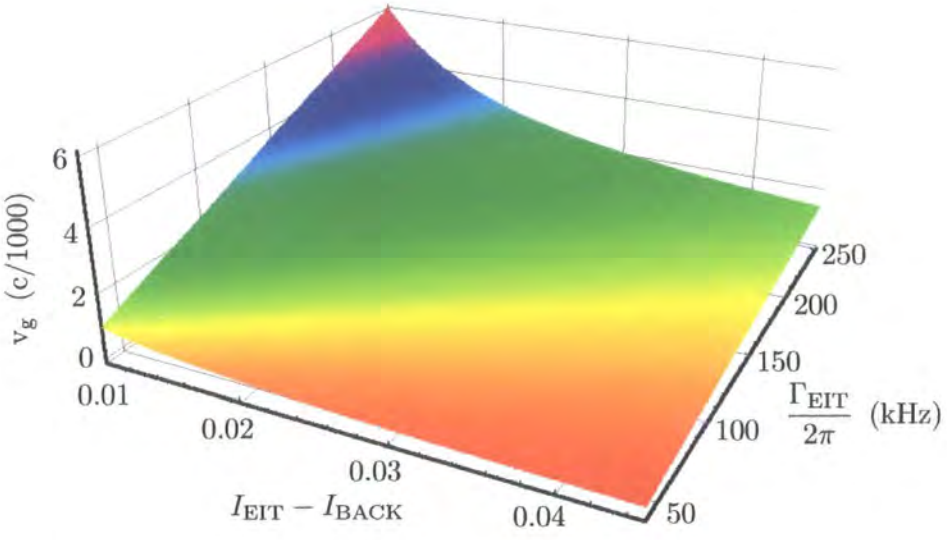

Figure 3.9: Theoretical plot of group velocity for ^{87}Rb vapour at room temperature in an 8 cm long vapour cell. The normalised transmission in the absence of the EIT feature is 0.9. The group velocity is shown for Lorentzian EIT features, with normalised amplitude ranging from 0.01 to 0.045 and FWHM form 40 kHz to 250 kHz.

Chapter 4

Transmission Measurements of EIT and EIA

This chapter is divided into three sections. § 4.1 addresses the experimental techniques used to make EIT and EIA transmission measurements; § 4.2 looks at the EIT and EIA spectra measured when both the single-photon and two-photon detuning are simultaneously scanned; and § 4.3 shows variation in width and the line shape, measured when the single-photon detuning is fixed and the two-photon detuning is scanned. Lock-in detection and control of the magnetic field are also presented in § 4.3.

4.1 Experimental Techniques

4.1.1 Two Lasers or One Laser?

As shown in chapter 3, EIT requires two fields: pump and probe. In order to measure the line shape and width of the EIT resonance it is necessary to have independent control over the frequencies of the pump and probe. The obvious method for producing two frequencies is to use two different lasers. Using two lasers gives completely independent control over the frequencies of the pump and probe beams — allowing any two different transitions to be chosen for the EIT system (provided of course that they share one level). In principle, using two lasers allows any three-level system to be chosen. It is not desireable to use

two free-running or independently locked lasers to produce the pump and probe beams, § 3.5.3 . It is almost inevitable that in this case the relative line width of the two lasers will provide the dominant contribution to the width of the EIT resonance. As a result the line width and shape will only give information on the coherence of the two lasers, rather than on the three-level system of interest.

Phase locking the two lasers significantly reduces the contribution of the coherence between the two lasers to the width of the resonance. The methods described by Snadden *et al.*, [65], and Schunemann *et al.*, [82], allow two lasers to be locked to one another with an offset in frequency between them provided by an independent oscillator. Oscillators can be chosen to provide offsets of up to 10 GHz. This was not an option in this work due to lack of the necessary equipment and funding. There are alternatives to using two separate lasers for the pump and probe fields. Using only one laser largely overcomes the problem of the relative coherence of the pump and probe. In order to derive two separate independently-controllable beams from one laser it is necessary to employ a non-linear device. The non-linear device, such as either an acousto-optic modulator (AOM) or an electro-optic modulator (EOM), modifies the frequency of the light from the laser. AOMs typically allow frequency offsets of $\sim$ 10 MHz to $\sim$ 100 MHz relative to the frequency of the input beam. EOMs allow frequency differences of $\lesssim$ 10 GHz to be achieved.

In the case of the Rubidium D-lines using EOMs or separate pump and probe lasers would allow three-level systems connecting the different ground-term hyperfine states to be investigated. The use of AOMs would restrict the investigation to three-level systems between different Zeeman sub-levels within the same ground-term hyperfine state, or three-level V-systems connecting excited term hyperfine states.

In the work presented in this thesis AOMs were used to investigate Λ-systems connecting different Zeeman sub-levels within the same hyperfine state of the ground term in both ^{85}Rb and ^{87}Rb isotopes.

4.1.2 Transmission Experimental Set-up

The experimental set-up used to make transmission measurements of EIT and EIA is shown in Fig. 4.1 .

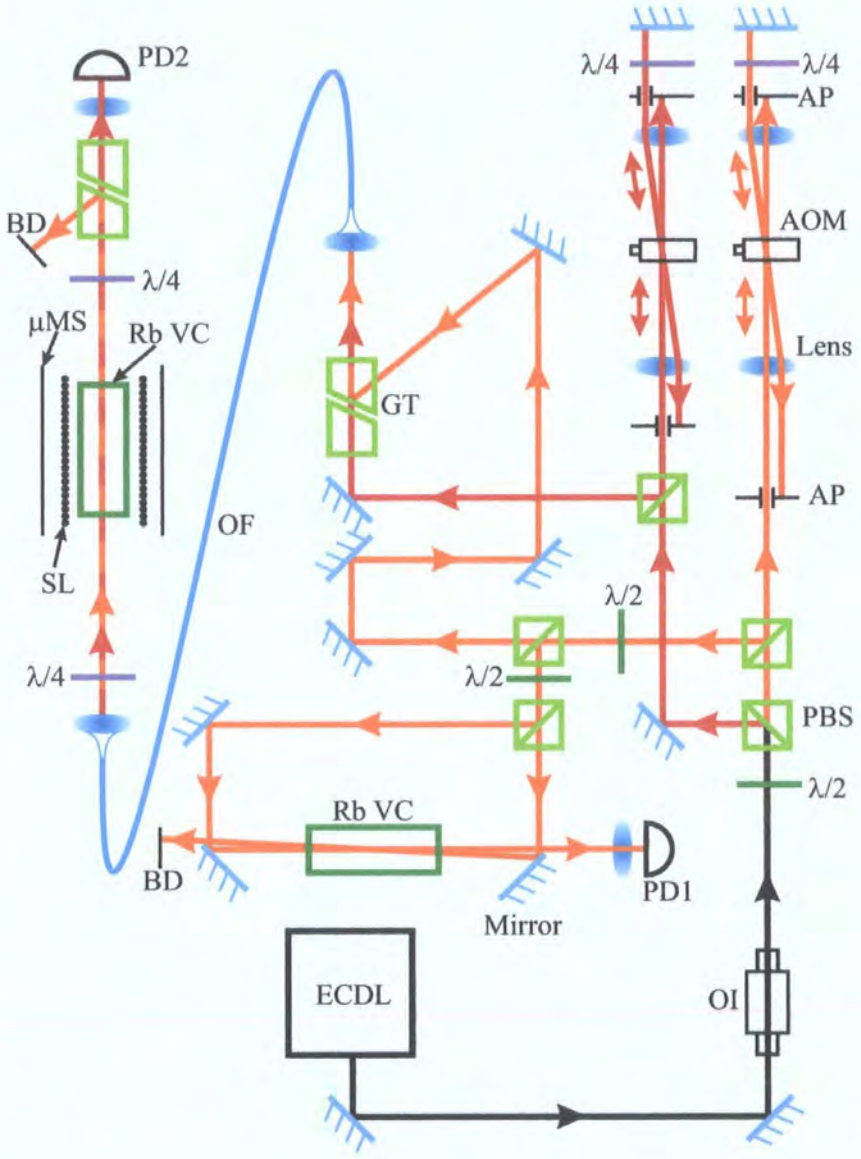

Figure 4.1: Experimental set-up for double-scanning EIT/EIA measurements. Black line — light out of ECDL; orange line — pump beam; and red line — probe beam. Abbreviations not defined in the text: OI — optical isolator; $\lambda/2$ half-wave plate; $\lambda/4$ — quarter-wave plate; PBS — polarization beam-splitting cube; AP — aperture; Rb VC — Rubidium vapour cell; PD — photodiode; GT — Glan-Taylor polarization beam splitter; OF — optical fibre; BD — beam dump; SL — solenoid; and μMS — μ-metal shield.

The remainder of § 4.1 describes how this set-up is used and how optical elements within it function.

4.1.3 Acousto-Optic Modulators

Acousto-optic modulators (AOMs) allow the frequency of light to be modified through a non-linear interaction. The incoming light Bragg-diffracts off acoustic waves in a non-linear crystal, Fig. 4.2.

Single-pass of an AOM

In the non-linear medium of the AOM crystal, the incoming optical beam has a wave vector of magnitude $k_{\mathrm{in}} = \omega_{\mathrm{in}}/c_n$, the diffracted wave has wave vector with magnitude $k_{\mathrm{d}} = \omega_{\mathrm{d}}/c_n$, and the acoustic wave has wave vector of magnitude $K = \omega_{\mathrm{AC}}/v$, Fig. 4.3. v is the speed of the acoustic wave in the crystal, c_n the speed of light (phase velocity) in the medium. From conservation of energy and momentum:

$$\omega_{\mathrm{d}} = \omega_{\mathrm{in}} \pm \omega_{\mathrm{AC}} , \tag{4.1}$$

$$\boldsymbol{k}_{\mathrm{d}} = \boldsymbol{k}_{\mathrm{in}} \pm \boldsymbol{K} , \tag{4.2}$$

respectively, where $\pm\omega_{\mathrm{AC}}$ and $\pm\boldsymbol{K}$ refer to the plus one and minus one order of diffration.

From equation 4.1 and the relations between the magnitude of the wave vectors and frequency.

$$\omega_{\mathrm{d}} = \omega_{\mathrm{in}}\left(1 \pm \frac{\omega_{\mathrm{AC}}}{\omega_{\mathrm{in}}}\right) , \tag{4.3}$$

$$k_{\mathrm{d}} = k_{\mathrm{in}}\left(1 \pm \frac{\omega_{\mathrm{AC}}}{\omega_{\mathrm{in}}}\right) . \tag{4.4}$$

As $\omega_{\mathrm{AC}}/\omega_{\mathrm{in}} \ll 1$ it follows that $k_{\mathrm{d}} \simeq k_{\mathrm{in}}$ and so the locus of the scattering interaction in momentum space is a circle of radius k_{in}. θ, known as the Bragg angle, is defined as,

$$\sin\theta = \frac{1}{2} \cdot \frac{K}{k_{\mathrm{in}}} . \tag{4.5}$$

Hence if the angle of the incident beam varies from θ, the intensity of the diffracted light goes to zero (for further details see the work of Gordon and the

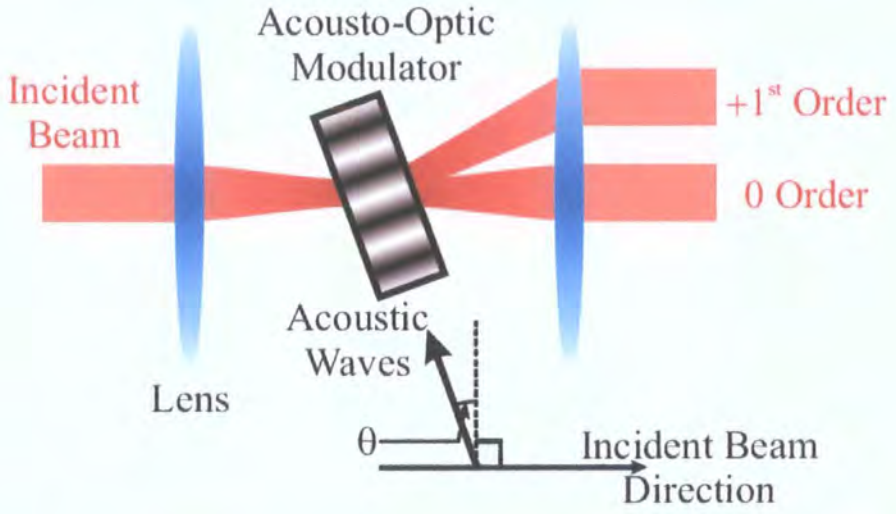

Figure 4.2: Acousto-optic modulator alignment, the acoustic waves propagate at an angle θ to the perpendicular to the direction of propagation of the incident optical beam.

work of Crystal Technology, [83, 84]). The above only describes what happens to the $\pm 1^{\text{st}}$ order outputs of the AOM. Similarly there are also higher order outputs but with lower efficiencies and they are not made use of in this work. Generally the frequency offset of the g^{th} order of diffraction is given by $g\omega_{\text{AC}}$, and the angle is given by,

$$\sin\theta_{\text{g}} = \frac{g}{2} \cdot \frac{K}{k_{\text{in}}} \,. \tag{4.6}$$

Double-pass of an AOM

Retroreflecting the output of the g^{th} order of the AOM (Fig. 4.4) for a second pass through the AOM leads to a frequency offset of $2g\omega_{\text{AC}}$ on the beam counter-propagating the input to the AOM (Fig. 4.5). The input of the second pass of the AOM is $-\boldsymbol{k}_{\text{d}}$.

$$-\boldsymbol{k}_{2\text{d}} = -\boldsymbol{k}_{\text{d}} + \boldsymbol{K} \,, \tag{4.7}$$

$$\omega_{2\text{d}} = \omega_{\text{d}} + \omega_{\text{AC}} \,. \tag{4.8}$$

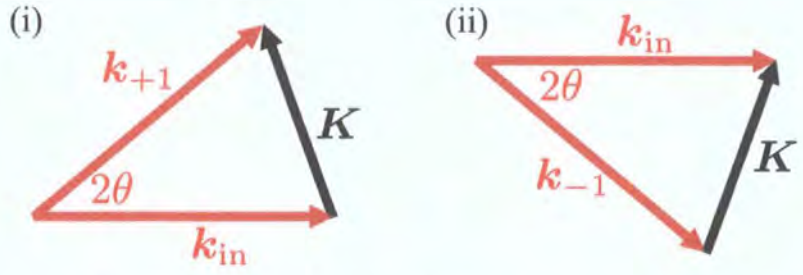

Figure 4.3: (i) The wavevector sum for the +1 output order of the AOM, $\boldsymbol{k}_{+1}$, is the diffracted output order of the AOM. (ii) Wavevector sum for the −1 output order of the AOM, $\boldsymbol{k}_{-1}$, is the diffracted output order of the AOM.

The angle that the first-order output of the second pass of the AOM makes to the first-order output of the first pass of the AOM is θ_2, where,

$$\sin\theta_2 = \frac{1}{2}\cdot\frac{K}{k_{\mathrm{d}}}\,. \tag{4.9}$$

The angle that the output of the $\pm 1^{\mathrm{st}}$ order of the second pass, of the $\pm 1^{\mathrm{st}}$ order of the first pass, makes with the input beam to the AOM, β, is given by,

$$\beta = 2\left(\arcsin\left(\frac{K}{2k_{\mathrm{in}}}\right) - \arcsin\left(\frac{K}{2k_{\mathrm{d}}}\right)\right)\,, \tag{4.10}$$

$$\text{and}\quad \frac{K}{2k_{\mathrm{d}}} = \frac{K}{2k_{\mathrm{in}}\left(1 \pm \omega_{\mathrm{AC}}/\omega_{\mathrm{in}}\right)}\,. \tag{4.11}$$

As $\omega_{\mathrm{AC}} \simeq 10^8$ and $\omega_{\mathrm{in}} \simeq 10^{14}$, then,

$$\frac{\omega_{\mathrm{AC}}}{\omega_{\mathrm{in}}} \simeq 10^{-6}\,, \tag{4.12}$$

hence

$$\beta \simeq 0\,. \tag{4.13}$$

Thereby changing ω_{AC} does not cause any steering of the first-order output of the second pass; the output of the second pass counter-propagates with the original input beam. Whilst this is desireable, as it allows the frequency to be changed without any steering of the output beam, it poses the problem of how to separate the path of the output beam from that of the input beam. The $\lambda/4$ waveplate, shown in Fig. 4.4, causes the second pass of the AOM to be orthogonally-linearly polarized with respect to the first pass. This allows the beam paths to be separated using a polarizing beam-splitting cube.

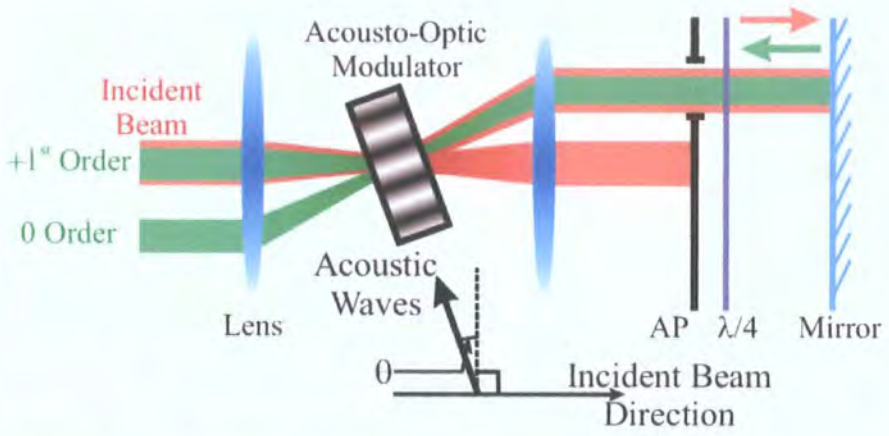

Figure 4.4: Acousto-optic modulator alignment, AP — aperture; $\lambda/4$ — quarter-wave plate. The red beams refer to the first pass through the AOM (Fig. 4.2), and the green beams refer to the second pass.

AOM Experimental Details

An AOM driver supplies the radio frequency (RF) signal to the AOM. This electrical signal is converted to an acoustic wave which propagates through the crystal at the frequency of the RF signal. It is this acoustic wave that the light Bragg-diffracts off. The AOMs used in this work are Crystal Technologies, AOMO 3080 – 122. The driver of the AOM is made up of three components: Minicircuits ZOS−100 Voltage Controlled Oscillator (VCO); Minicircuits ZX73 – 2500 Voltage Variable Attenuator (VVA); and a Minicircuits ZHL−3A Amplifier.

The VCO is connected to the VVA through a rigid SMA-to-SMA connector and the VVA to the amplifier through a SMA to BNC RG174 cable, the amplifier is connected to the AOM via a BNC to SMA RG174 cable, Fig. 4.6. The cable connecting the amplifier to the AOM is kept as short as possible to minimize the chance of any broadcasting, whilst ensuring that the amplifier is separated from the VCO to guard against heating from the amplifier affecting the VCO frequency.

The VCO provides a RF sine-wave output in the range of 50 to 100 MHz. The frequency of the RF output is determined by an applied control voltage (Fig. 4.7 on page 82), and varies approximately linearly with it. The VVA attenuates the

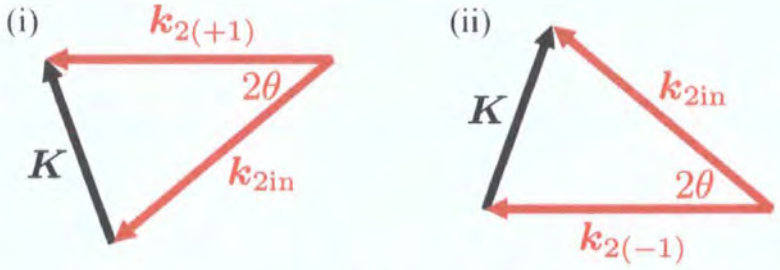

Figure 4.5: (i) The wavevector sum for the +1 output order of the second pass of the +1 order of the first pass through the AOM. (ii) Wavevector sum for the −1 output order of the second pass of the −1 output order from the first pass of the AOM.

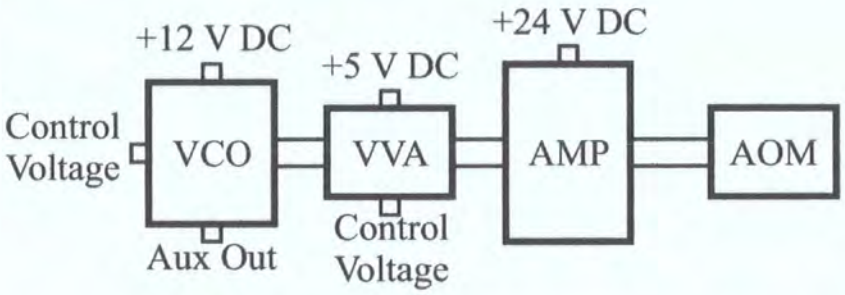

Figure 4.6: Schematic diagram showing how the VCO (Minicircuits ZOS−100), VVA (Minicircuits ZX73 − 2500) and amplifier (Minicircuits ZHL−3A) are connected to the AOM (Crystal Technologies, AOMO 3080 − 122).

amplitude of the output from the VCO by between 65 dB and 2 dB, the degree of attenuation is controlled by varying the applied control voltage to the VVA. The amplifier amplifies the output of the VVA by 24 dB, such that the RF output signal is sufficient to drive the AOM. The response of the AOM varies with the amplitude and frequency of the input RF signal.

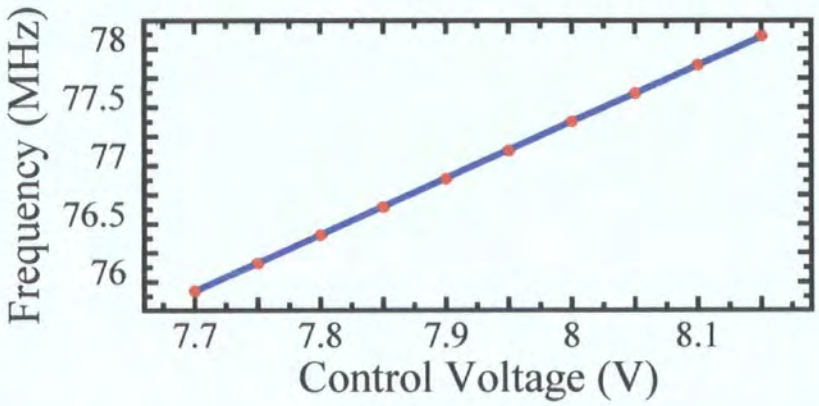

Figure 4.7: Frequency of the RF output of the probe-beam VCO. Circles show measured values and the line gives the straight line fit to the data. The straight line fit to the data gives a gradient of $4.847 \pm 0.003 \times 10^{-3}$ MHz V^{-1} and a zero voltage offset of $38.38 \pm 0.02 \times 10^{-2}$ MHz. The reduced χ^2 value for the fit is 5.1, which suggests that the variation of frequency with control voltage is not simply a linear relationship. The standard error on each data point is smaller than the extent of the red dots used to mark the data points on the graph.

4.1.4 Alignment of Pump and Probe Beams

As was shown in § 3.5.2 on page 58, it is vital to ensure that the pump and probe fields co-propagate to as high a degree as possible. While it is possible to align the beams using apertures, practically it is difficult to align the beams to better than $\sim$ 1 mrad; this will still lead to a broadening of $\sim$ 320 kHz [1] at room temperature. There are somewhat complex schemes which allow for extremely high degrees of alignment, [85], using split photodiodes.

The simplest way to ensure that the beams are co-propagating is to use an optical fibre. The pump and probe beams are focussed into the same single-mode polarization preserving fibre. This has the advantages of ensuring that the output beams have matching circularly-symmetric Gaussian profiles and that the alignment of the beams before the optical fibre is decoupled from the alignment of the beams after the optical fibre. Any misalignment in the beams before the fibre will only result in a drop in the power transmitted through the fibre. The main disadvantage associated with using optical fibres is loss of power, as the fibres will not transmit 100% of the incident beam due to imperfect mode matching of the input beams to the fibre.

It is preferable to record the probe beam signal without a DC offset due to the pump beam reaching the photodiode. In order to do this it is necessary to separate the pump and probe beams after they have passed through the Rb vapour cell. As the pump and probe beams are perfectly co-propagating, and are only separated by $\lesssim$ 100 MHz, the only practical way to separate the two fields is to make use of different polarizations. Hence the pump and probe beams are chosen to be linearly-perpendicularly polarized to one another. This requires that the optical fibre used should be polarization preserving, and that the polarization of the input beams should be aligned to the axes of the fibre. To separate the pump and probe beam, a polarization beam-splitting cube is used. The probe beam is transmitted through the PBS and the pump is reflected through 90°. The probe beam is then focussed onto a photodiode while the pump beam is terminated by a beam stop.

[1] From combining equation 3.45 on page 60 with the Maxwellian velocity distribution, equation 2.96 on page 24.

4.1.5 Beat Notes

Two co-propagating fields with the same polarization will interfere with one-another. The resulting interference pattern will vary with the difference in frequency between the two fields. Consider two electromagnetic fields, $\mathbf{E}_1$ and $\mathbf{E}_2$ where the frequency of one field is scanned relative to the frequency of the other. The resulting intensity due to the two fields is I, where,

$$\mathbf{E}_1 = \mathbf{E}_{1,0}\cos(\omega t + \delta\omega t) \ , \tag{4.14}$$

$$\mathbf{E}_2 = \mathbf{E}_{2,0}\cos(\omega t) \ , \tag{4.15}$$

$$I \propto |\mathbf{E}_1 + \mathbf{E}_2|^2 \ , \tag{4.16}$$

and $\delta\omega$ is a linear function of t. In the case that the two-fields have the same polarization,

$$\frac{\mathbf{E}_1}{E_1} = \frac{\mathbf{E}_2}{E_2} \ , \tag{4.17}$$

$$\Longrightarrow \quad I \propto (E_{1,0}\cos(\omega t + \delta\omega t) + E_{2,0}\cos(\omega t))^2 \ , \tag{4.18}$$

$$= I_{1,0}\cos^2(\omega t + \delta\omega t) + I_{2,0}\cos^2(\omega t) + \sqrt{I_{1,0}I_{2,0}}\cos(\omega t + \delta\omega t)\cos(\omega t) \ . \tag{4.19}$$

$$= \frac{I_{1,0}}{2}(1 + \cos((\omega + \delta\omega)t)) + \frac{I_{2,0}}{2}(1 + \cos(\omega t)) + \sqrt{I_{1,0}I_{2,0}}(\cos((2\omega + \delta\omega)t) + \cos(\delta\omega t)) \ . \tag{4.20}$$

In practice when signals are recorded a time averaging is introduced, for example due to the response time of a photodiode or the digitization of an oscilloscope. This time averaging has the effect of reducing the amplitude of the beat pattern as the frequency between the two beams is increased.

Fig. 4.8 shows a beat note as it would appear on a recorded trace, calculated using *Mathematica*. $t = 0$ corresponds to zero frequency difference between the two fields. $E_1 = \sin\left((\omega + \delta\omega)t\right)$ and $E_2 = 0.1\sin(\omega t)$. The time averaging is over a period of 0.02 ms. It is obvious that any spectral feature at a frequency close to $\delta = 0$ will be obscured by the beat signal. In order to minimize the effect of the beat signal on the EIT resonance, the pump and probe beams are

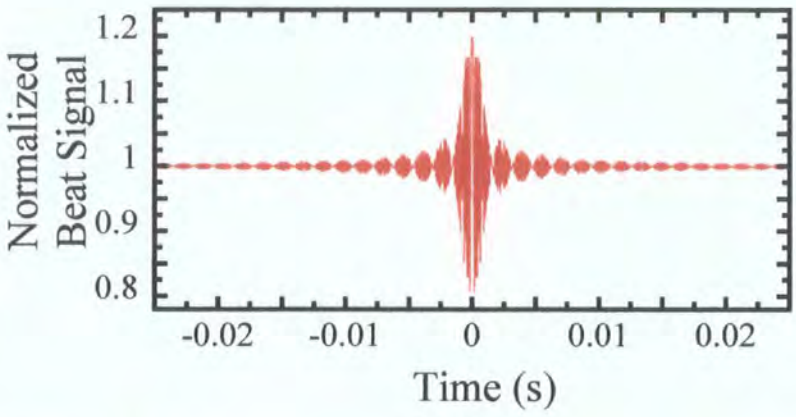

Figure 4.8: Plot of the calculated time-averaged beat signal for two beams. For the trace shown, one beam is scanned in frequency relative to the other, over a range of 5 MHz, as a linear function of time. At $t = 0$ the beams are at the same frequency. The scanned beam has an intensity 100 times greater than the fixed frequency beam. A time averaging of 2×10^{-5} s represents time averaging that is due to the photodiode circuit and digital oscilloscope.

perpendicularly polarized to as high a degree as possible to try to ensure that only the probe beam reaches the photodiode. Furthermore, applying a magnetic field to the Rb vapour cell lifts the degeneracy of the Zeeman sub-levels in the Λ system, and hence moves the two-photon EIT resonance away from the centre of the beat signal.

4.1.6 Photodiode Circuits

The photodiode circuit used to record EIT and EIA traces presented in this chapter is shown in Fig. 4.9. The modification from the basic photodiode circuit shown in Fig. 2.8 on page 33, is the introduction of the capacitor in parallel with the output resisitor. This capacitor has the effect of introducing a low-pass filter to the photodiode circuit. From equation 2.109 on page 34 the response of this circuit to different frequencies can be calculated. The output impedance

of the circuit is given by,

$$\frac{1}{Z_{\text{out}}} = \frac{1}{R} + \mathrm{i}\omega C \,, \tag{4.21}$$

$$\Longrightarrow \quad |Z_{\text{out}}| = \sqrt{\frac{1}{(1/R^2) + \omega^2 C^2}} \,, \tag{4.22}$$

$$= R\sqrt{\frac{1}{1 + (\omega CR)^2}} \,. \tag{4.23}$$

Hence the output voltage of the photodiode circuit is given by,

$$V_{\text{out}} = -\frac{I_{\text{in}} R}{\sqrt{1 + (\omega CR)^2}} \,, \tag{4.24}$$

where I_{in} is the current generated by the photodiode. The output voltage falls to $1/\sqrt{2}$ of its value for DC components at a frequency of $\omega = 1/(RC)$.

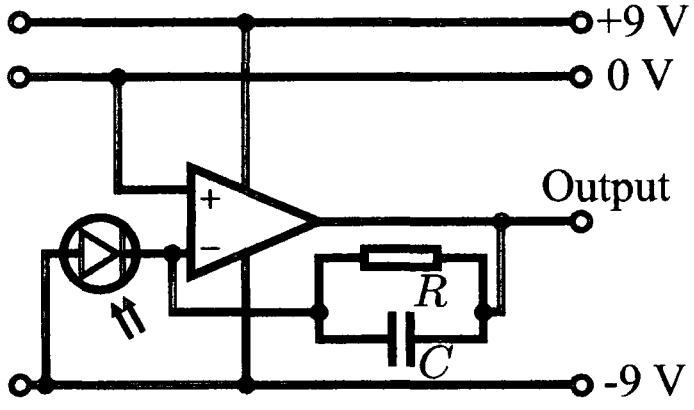

Figure 4.9: Circuit diagram for the photodiode circuit used to make transmission measurements for EIT and EIA. The photodioide is a BPX–65, the op-amp is either an AD548 or AD648. The values of R and C are either 100 kΩ and 47 pF or 1 MΩ and 4.7 pF, respectively.

The output impedance of the two photodiode circuits used in the data presented in this chapter is plotted in Fig. 4.10. $RC = 4.7$ μs, $R = 1$ MΩ with $C = 4.7$ pF or $R = 100$ kΩ and $C = 47$ pF.

Without the capacitor in place high frequency signals can lead to "ringing" in the photodiode circuit. This amplifies the high frequency beat signals disproportionately to the lower frequency spectral features which are of interest. Fig. 4.11(i) shows the response of the photodiode circuit, without the capacitor,

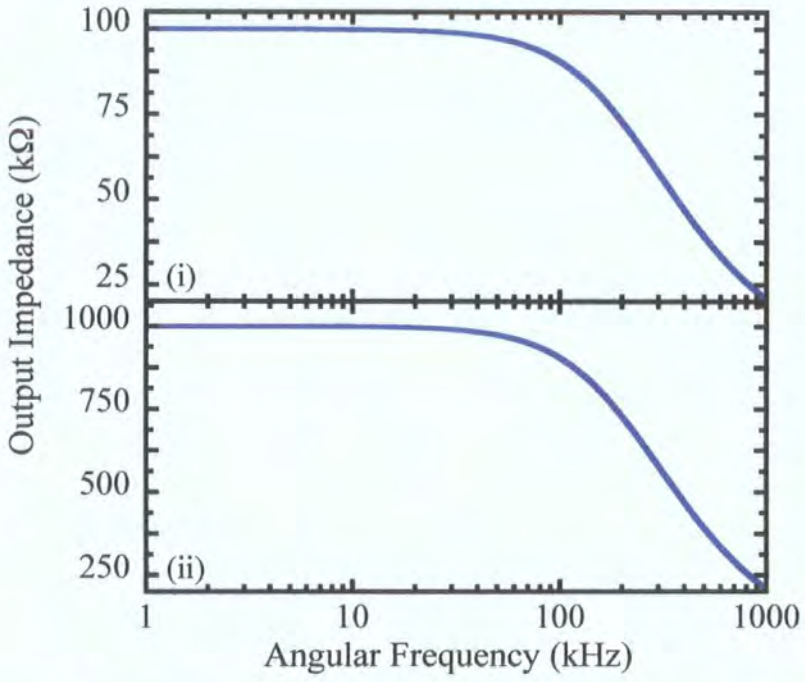

Figure 4.10: The impedance of the photodiode circuit shown in Fig. 4.9 is plotted as a function of frequency. For both circuits $RC = 4.7$ μs. (i) $R = 100$ kΩ and $C = 47$ pF. (ii) $R = 1$ MΩ and $C = 4.7$ pF. As can be seen the frequency response for the two sets of parameters are the same, while the impedance at a given frequency is proportional to the value of R.

to a series of "square" light pulses. Ringing can clearly be seen when the signal falls to zero. Fig. 4.11(ii) shows the output from the photodiode circuit with the capacitor included ($R = 100$ kΩ and $C = 47$ pF), as expected the ringing is removed. Fig. 4.10 shows the calculated output impedance $|Z_{\text{out}}|$ for the photodiode of circuit of Fig. 4.9, with $R = 100$ kΩ, $C = 47$ pF and $R = 1$ MΩ, $C = 4.7$ pF for (i) and (ii) respectively. As can be seen the impedance starts to fall for frequencies $\gg 100$ kHz, hence the photodiode circuit response time will be ~ 10 μs.

The frequency of the beat notes is significantly higher than the rate at which the pump and probe fields are scanned — it follows that the frequency components that make up the beat notes are higher than those that make up the EIT resonances. Therefore it is possible to filter out, electronically, the higher frequency components of the signal incident on the photodiode, thus reducing the

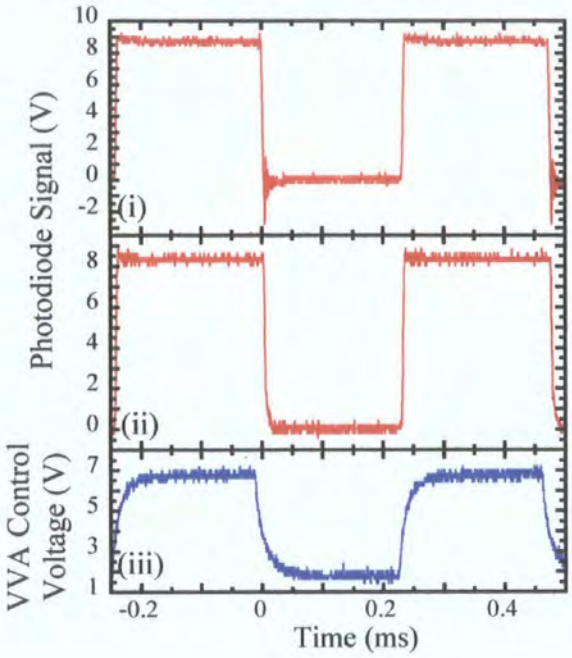

Figure 4.11: This figure shows the ringing introduced on signals due to the photodiode circuit (i), and how that ringing can be overcome with the introduction of a capacitor to the photodiode circuit (ii). (i) Square wave pulses measured on the photodiode circuit as shown in Fig. 4.9, with $R = 100$ kΩ and no capacitor. (ii) Square wave pulses as measured on the photodiode circuit with $R = 100$ kΩ and $C = 4.7$ pF. (iii) The "square"-wave control voltage supplied to the AOM VVA to provide the optical square-wave train to the photodiode circuit.

amplitude of the beat notes without significantly affecting the EIT resonances.

4.1.7 Pump and Probe Beam Relative Line Width

To determine the minimum line width that the experimental apparatus will be able to resolve, light that has double-passed through two AOMs is beat against light that has not been offset in frequency by either of the AOMs. There is a resulting constant frequency difference between the two beams of 67 kHz Using a BPX–65 photodiode in series with a 51 Ω resistor (which should give a response time $\simeq$ 12 ns, [42]) the beat pattern is measured and recorded on a Tektronix TDS 3014B oscilloscope. The measured pattern is shown in Fig. 4.12. The figure shows the central one-hundred data points recorded, to show the oscillation of the signal. The timebase on the oscilloscope is chosen to record as large a trace as possible, whilst ensuring that the interval between data points is small enough to define the individual oscillations (approximately 8 per oscillation in this case).

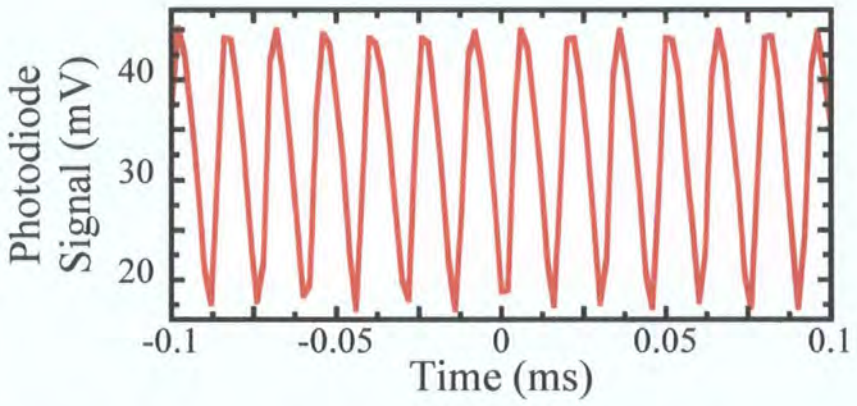

Figure 4.12: A plot of the central area of the beat signal recorded over 20 ms on a Tektronix TDS 3014B digital oscilloscope. The regular oscillatory nature of the beat signal can be clearly seen.

A Fast Fourier Transform (FFT) is then carried out in *Excel*, on just under half of the data (the maximum number of data points that *Excel* can handle for a FFT is 4096, compared to 10000 data points recorded). The amplitude of the FFT is then plotted against frequency, the full trace of the FFT is shown in Fig. 4.13 — (i) shows the full FFT, while (ii) shows a blow-up of the area of interest, along with a Lorentzian least-squares fit to line shape. The width of the Lorentzian fit is 1.9 kHz, suggesting that the ultimate limit on the resolution

that can be achieved with this system is ~ 1.9 kHz.

The finite extent of the data train (8.2 ms) would give a FWHM $\simeq 1.5$ kHz ($\simeq (4\pi/8.2$ ms)). It is likely that the limited number of data points recorded per period of oscillation also contributes to the width of the beat note.

So the maximum resolution of this system is expected to be $\lesssim 400$ Hz ($= 1.9-1.5$ kHz). This is expected to be largely due to the stability of the oscillators generating the RF for the AOMs.

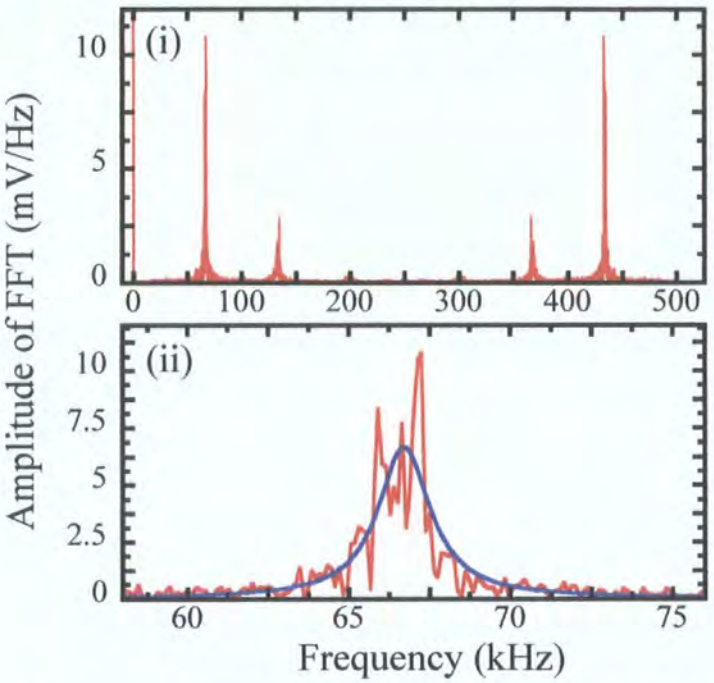

Figure 4.13: (i) Shows the full FFT trace of an 8.2 ms section of the beat signal shown in Fig. 4.12, produced in *Excel*. Six peaks can be seen, discounting the peak at 0 MHz. The three highest frequency peaks are due to aliasing of the three lower frequency peaks. The peak at 67 kHz is the main FFT peak, the peaks at ~ 130 kHz and ~ 200 kHz are the second and third harmonics of the main frequency peak. (ii) Shows a blow-up of the FFT around the main peak at 67 kHz, the red line shows the data and the blue line a Lorentzian least-squares fit. The Lorentzian fit has a full-width at half-maximum of 1.9 kHz.

4.2 Double-Scan EIT/EIA

Initially, to observe the EIT/EIA features[2], a double-scanning technique was used, [86, 87]. The single-photon detuning of the pump, δ_{pu}, is scanned over the full Doppler-broadened transition of one of the ground-term hyperfine states once; at the same time, the two-photon detuning $\delta_{\mathrm{pr}} - \delta_{\mathrm{pu}}$ is scanned m times over a range of several hundreds of kHz with the AOM (Fig. 4.14). This leads

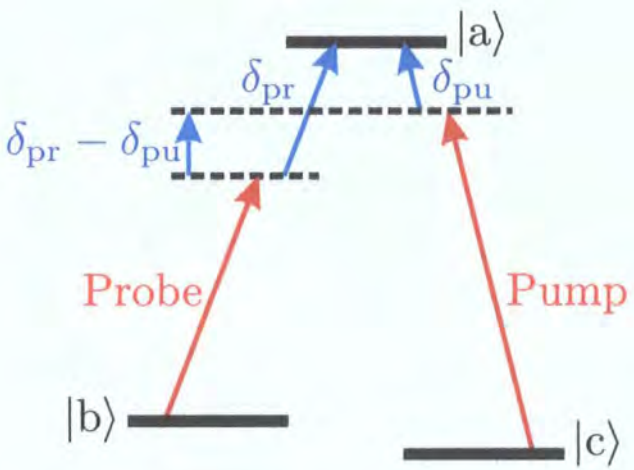

Figure 4.14: δ_{pu} is the single-photon detuning of the pump beam from resonance, while $\delta_{\mathrm{pr}} - \delta_{\mathrm{pu}}$ is the detuning of the probe beam from the two-photon resonance.

to m EIT/EIA features occurring within the range of the Doppler-broadened transition. The frequency scale of such a plot is not straight-forward — the centres of the different EIT features and the Doppler-broadened resonance are defined by a frequency given by the ECDL scan $\delta_{\mathrm{pu}}/2\pi$, whilst the width of the features is determined by the AOM scan $(\delta_{\mathrm{pr}} - \delta_{\mathrm{pu}})/2\pi$. In order that on successive scans of the ECDL frequency the EIT/EIA resonances occur at the same single-photon detunings within the Doppler-broadened scan, it was necessary to ensure that the VCO control scan and the piezo supply voltage scan were locked to one another. This was achieved using a custom built signal generator that produced two saw-tooth voltage scans, appendix F . This signal generator was built by the Durham University, Physics Department, Electronics Design

[2]To make transmission EIT/EIA resonances the experimental set-up shown in Fig. 4.1 on page 76 was used.

and Development Workshop. The two outputs of the signal generator, 1 and 2, were scanned at frequencies $\nu_{\rm p}$ and $20\nu_{\rm p}$ respectively, shown in Fig. 4.15(i). Output 1 was used to drive the piezo after being passed through a high voltage amplifier. Output 2 was used as the control voltage for the VCO in the probe arm of the experimental set-up. Fig. 4.15(ii) shows a plot of the two-photon detuning $((\delta_{\rm pr} - \delta_{pu})/2\pi)$ against the detuning of the pump beam $(\delta_{\rm pu}/2\pi)$.

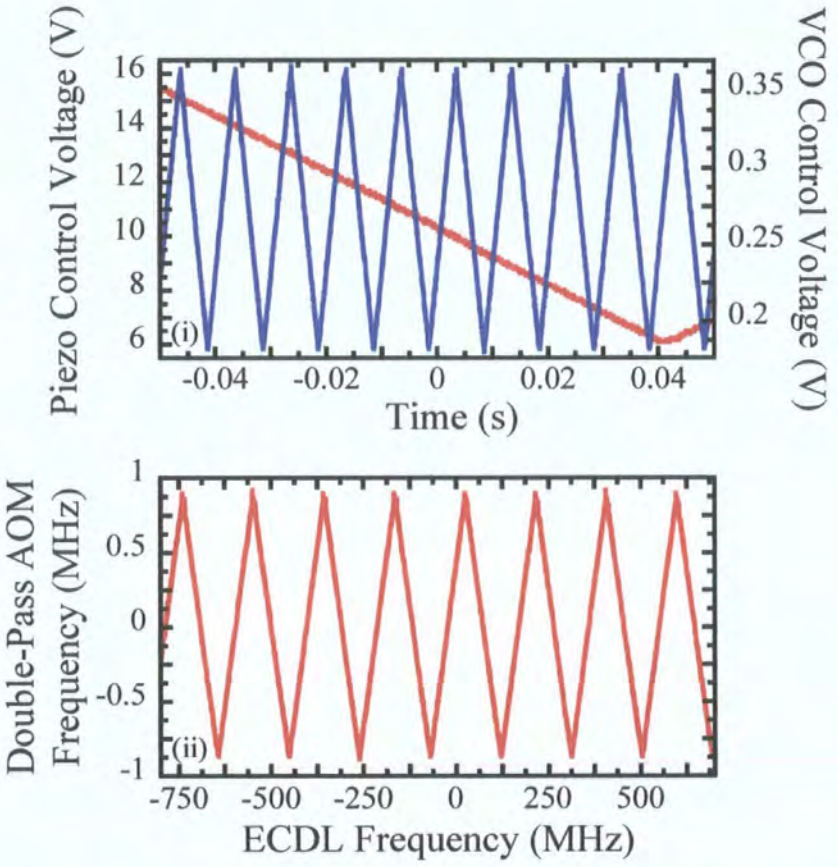

Figure 4.15: (i) Shows how the piezo control voltage (red) and VCO control voltage scan (blue) vary with time. The VCO control voltage, as shown has a DC offset of $\simeq$ 7 V. (ii) The calibrated AC component of the double-pass AOM frequency scan on the probe beam (two-photon detuning) against ECDL frequency (single-photon detuning).

4.2.1 Double-Scan Results

Fig. 4.16 on page 96 shows double-scan spectra for the Rb D_2 line. The four panels show the transitions from the four hyperfine ground term levels: (i) ^{85}Rb $F = 2 \rightarrow F'$; (ii) ^{85}Rb $F = 3 \rightarrow F'$; (iii) ^{87}Rb $F = 1 \rightarrow F'$; and (iv) ^{87}Rb $F = 2 \rightarrow F'$. In each case F' can take anyone of three different values. Hence, multiple Λ systems are probed simultaneously. The red traces show the recorded probe beam transmission in the presence of the pump beam. The blue traces show the recorded probe beam transmission in the absence of the pump beam. Both electromagnetically induced absorption (EIA) and electromagnetically induced transparency (EIT) along with optical pumping (the offset between the Doppler-broadened backgrounds) can be clearly seen in the four panels of the figure.

In all four panels of Fig. 4.16 there is no applied magnetic field and the probe and pump have orthogonal-linear polarizations.

Fig. 4.16(i) In the presence of the pump beam, where the two-photon resonance is met, there are sharp increases in the transmission of the probe beam through the medium. These are examples of EIT. Away from the two-photon resonance there is still $\sim$ 10% more transmission when the pump beam is present. The increase in transmission is due to optical pumping by the pump beam. The pump beam excites the transition at a rate such that the absorption of the probe beam is reduced across the full Doppler-broadened resonance.

Fig. 4.16(ii) In the case of ^{85}Rb $F = 3 \rightarrow F'$, when the two-photon resonance condition is met the transmission is significantly decreased. These are examples of EIA. The EIA troughs only show more absorption, than is seen in the absence of the pump beam, for ECDL frequency offsets of 0 to 300 MHz. This is due to optical pumping of the medium. The region 0 to 300 MHz is where the Doppler-broadened transmission is dominated by the contribution of the $F = 3 \rightarrow F' = 4$ hyperfine transition. It is the closed transition $F \rightarrow F' = F + 1$ that leads to EIA, (§ 3.6).

Fig. 4.16(iii) ^{87}Rb $F = 1 \rightarrow F'$ exhibits EIT. The sharp increase in transmission at the two-photon resonances are the EIT signals. The amplitude of the EIT features is greatest on the low frequency side of the Doppler-broadened resonance. This is the region dominated by the $F = 1 \rightarrow F' = 0, 1$ hyper-

fine transitions. The effect of optical pumping appears to be less significant in this Doppler-broadened transition than in the other three Doppler-broadened transitions of the Rb D_2 line.

Fig. 4.16(iv) ^{87}Rb $F = 2 \rightarrow F'$ exhibits strong EIA. Similar to ^{85}Rb $F = 3 \rightarrow F'$ optical pumping lessens the effect of the increase in absorption on the two-photon resonance. The EIA troughs are significantly deeper, increasing the absorption beyond that recorded in the absence of the pump beam by a much greater amount than in ^{85}Rb. The EIA features are again more significant in the region where the hyperfine transition $F \rightarrow F' = F + 1$ makes the dominant contribution to the Doppler-broadened transition.

4.3 Single Frequency Scan

In order to make quantitative measurements of the widths and line shapes of the two-photon resonances, the remainder of the experimental work in this thesis will concentrate on the Λ-systems of the ^{87}Rb $F = 1 \rightarrow F'$ transitions of the D_2 line, using orthogonally-circularly polarized pump and probe beams.

4.3.1 Lock-In Detection

Lock-in detection is a widely used method for retrieving signals of interest from noisy backgrounds, that obscure the signal of interest. In appendix G a short introduction to the working of lock-in amplifiers will be presented. It follows that presented in *The Art of Electronics*, [88].

In the results presented later in this chapter a technique equivalent to the large square-wave modulation (appendix G) is used. The probe beam is left unmodulated, while the amplitude of the pump beam is modulated (from a maximum value to zero) at ν_{mod} by modulating the control voltage to the pump beam VVA. The output of the lock-in is proportional to the probe-with-pump signal minus the probe-only signal.

One further complication to consider is the effect that modulating the pump beam will have on the EIT resonance. The rate at which the pump beam is modulated will lead to a spread in frequency of the pump beam. This spread in

frequency is of the order of the modulation frequency. While it is clear that the modulation of the pump beam will affect the width of the EIT resonances, it is not clear what the exact form of this broadening takes. It seems reasonable to assume that it will be of the order of the modulation frequency, as this gives the spread in frequency of the pump beam. Further modification to the EIT resonances would be expected due to the modification of transit time of the Rb atoms through the pump beam.

In order to make measurements of EIT resonances, at pump and probe powers where the EIT signal would normally be lost in the background noise of the detection system, an EG&G 7220 DSP lock-in amplifier was used. The lock-in detector was used to filter out signals occurring at all other frequencies. The use of the lock-in detector resulted in significant improvements in the signal to noise ratio, Fig. 4.17 on page 97.

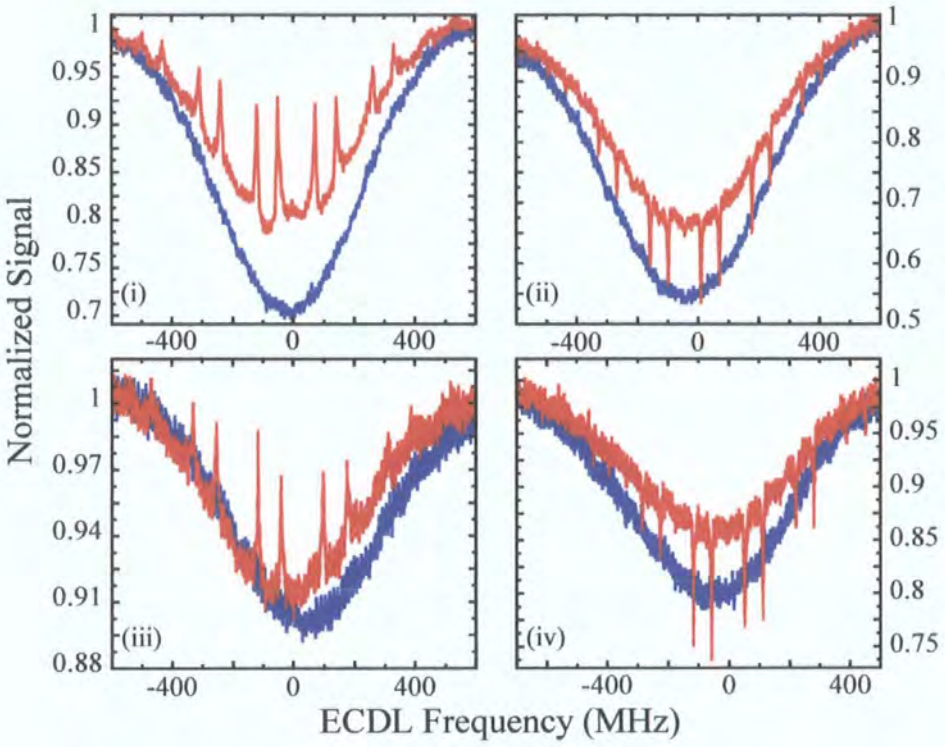

Figure 4.16: Plots of normalized transmission through a room temperature, 8 cm long Rb vapour cell, against ECDL frequency ($\delta_{\rm pu}/2\pi$). This gives the separation of the successive EIT/EIA features. The width of the EIT/EIA features is given by the scan range of the AOM ($(\delta_{\rm pr} - \delta_{\rm pu})/2\pi$); this is such that in each of the four plots the AOM scans 11 MHz between next nearest features. (i) ^{85}Rb $F = 2 \rightarrow F'$. (ii) ^{85}Rb $F = 3 \rightarrow F'$. (iii) ^{87}Rb $F = 1 \rightarrow F'$. (iv) ^{87}Rb $F = 2 \rightarrow F'$. The red traces show the data for both pump and probe beam (~ 100 μW and ~ 5 μW respectively, with diameters $\simeq 3$ mm, with the exception of (i) where the pump power is 180 μW), the blue traces for probe beam only. The actual scan of the ECDL is over a greater frequency than is shown in the figure, hence the two-photon resonance is met less often than might be expected in the Doppler-broadened absorption. Beat notes are present and coincident with the two-photon resonances. Greater cancellation of the pump beam, in the collection of this data, means that the beat notes are less significant than in work presented later in this thesis.

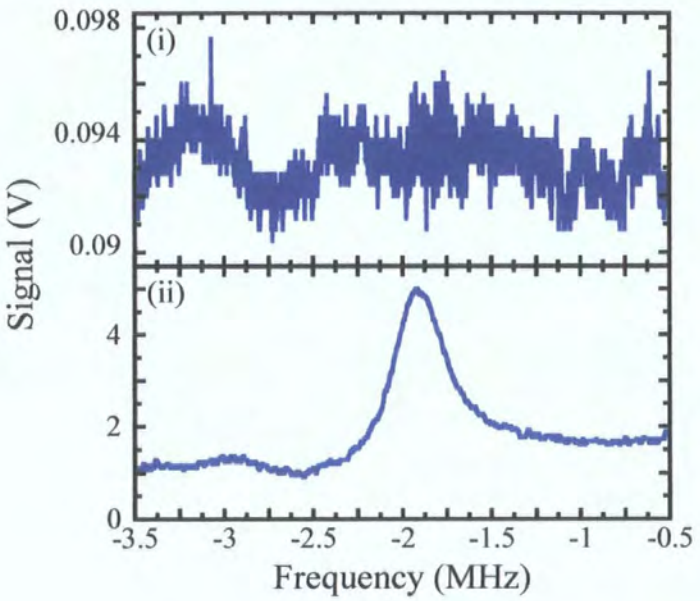

Figure 4.17: (i) Raw photodiode signal. (ii) Photodiode signal after lock-in amplifier. The pump power is 97 μW and the probe power is 3 μW, with beam diameters of $\approx$ 3 mm. The pump beam amplitude is modulated at $\approx$ 30 kHz, while the duration of the AOM scan is 6×10^{-3} s ($\simeq$ 170 Hz). The frequency scale is the difference between the frequency of the probe and pump beam, $((\delta_{\mathrm{pr}} - \delta_{\mathrm{pu}})/2\pi)$.

4.3.2 Magnetic Sensitivity

Using Zeeman sub-levels as the two groundstates in the EIT Λ system means that the position of the resonance in frequency space is sensitive to changes in magnetic field, as explained in § 3.5.1 on page 55. The Rb vapour cell is mounted in a solenoid, itself mounted within a μ-metal shield, as shown in Fig. 4.18.

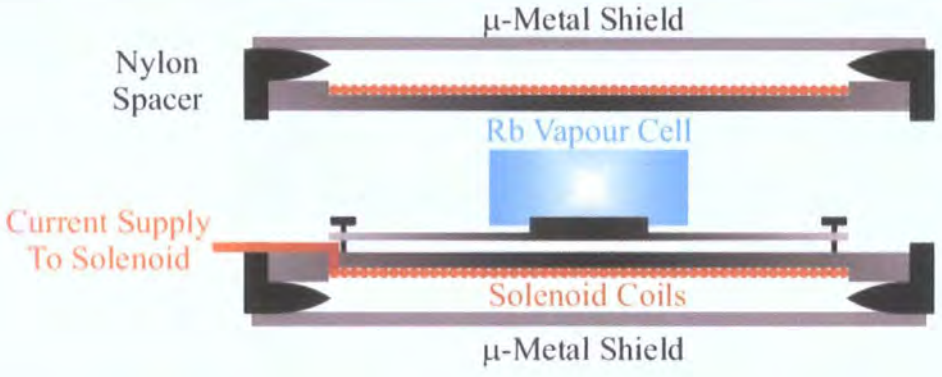

Figure 4.18: Diagram showing the mounting of the Rb cell and solenoid inside the cylindrical μ-metal shield.

Solenoid

The solenoid used in this work was built by Henry Ashworth[3]. The solenoid was specifically designed to mount up to an 8 cm long, 1" diameter, vapour cell at its centre and to produce an axial magnetic field constant over the length of the cell. The solenoid is 300 mm long, with a diameter of 54 mm, and is wound from 0.8 mm diameter enamelled copper wire, capable of carrying a current of 1 A. The fluctuation in the on-axis axial magnetic field, over the range of the length of the Rb vapour cell, is $\lesssim 0.1$ G [4], when the current through the solenoid is 1 A (hence the on-axis axial field at the centre of the solenoid is 14.5 G, from Fig. 4.19). From § 3.5.1 on page 58, this will lead to a limit on the width of the EIT feature of $\lesssim 9.7$ kHz G^{-1}. The on-axis axial field at the centre

[3]An undergraduate summer student supported by a Nuffield bursary in 2003 .

[4]Measured by H. Ashworth.

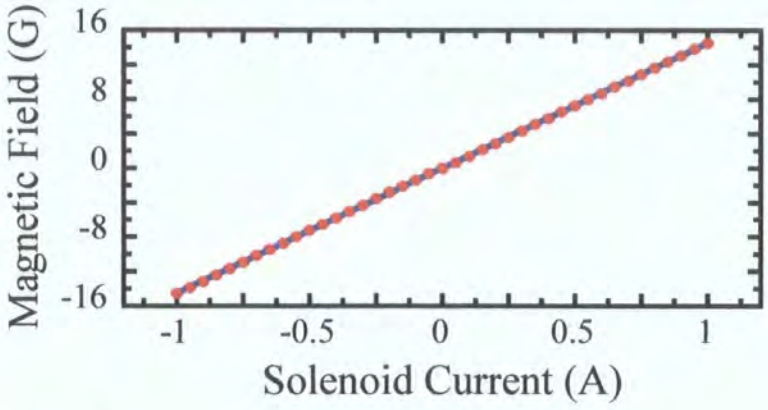

Figure 4.19: Circles show the measured values and the line gives the straight line fit to the data. The straight line fit to the data has a gradient of 14.54 ± 0.01 G A^{-1} with a zero current offset of $(5 \pm 8) \times 10^{-3}$ G. The reduced χ^2 value for the fit is 1.16, and the range of the error bars are smaller than the spread of the data point markers.

of the solenoid is determined from a straight-line χ^2 fit to the field, plotted as a function of solenoid current, Fig. 4.19.

μ-Metal Shield

The μ-metal shield was designed to house the solenoid, and to minimize the residual laboratory field at the centre of the solenoid.

The cylindrical μ-metal shield was manufactured by Magnetic Shields Ltd., from 1 mm thick μ-metal — an alloy of nickel, iron and smaller quantities of copper and molybdenum. It is 345 mm long and has an internal diameter of 70 mm.

The combination of the μ-metal shield and the solenoid allow the magnetic field in the Rb vapour cell to be controlled throughout the experimental work. Axial fields up to $\sim$ 14 G can be applied both in the direction of the propagation of the pump and probe beams, and in the opposite direction too. Any off-axis fields due to the laboratory's magnetic field can be cancelled by a factor of ~ 100.

Fig. 4.20 on the following page shows the effect of the μ-metal shield and solenoid. The μ-metal shield narrows the resonance as can be seen from Fig. 4.20 (i) and (ii). In (i) and (ii), where there is no field due to the solenoid, the EIT

feature is coincident with the beat note at 0 MHz. The application of the solenoid field shifts the EIT resonance to −2 MHz (Fig. 4.20 (iii)) moving it away from the beat signal — hence allowing systematic analysis of the width and shape of the EIT resonance. Here the levels that make up the magnetically

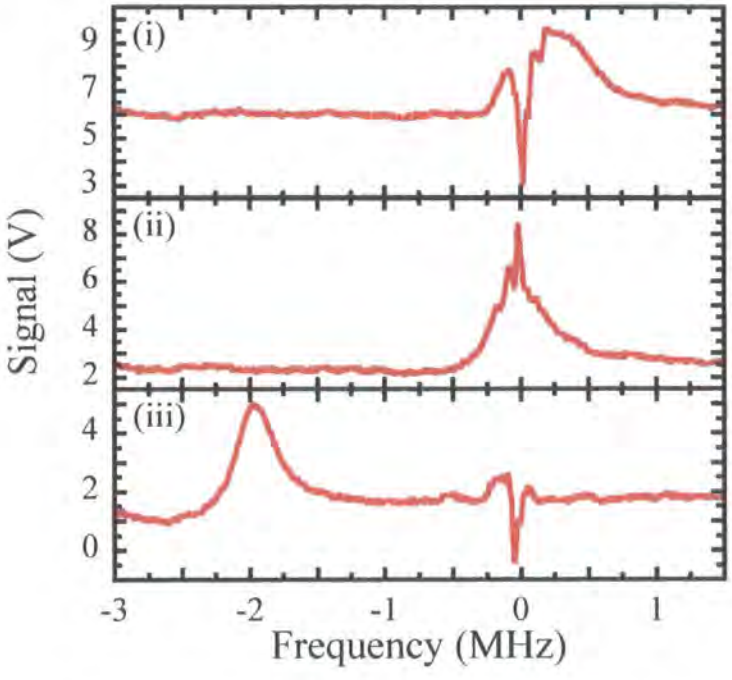

Figure 4.20: Plots showing the scan of the two-photon detuning, $((\omega_{\rm pr} - \omega_{\rm pu})/2\pi)$, over the EIT resonance: (i) no μ-metal shield or solenoid magnetic field; (ii) μ-metal shield in place, no solenoid magnetic field; and (iii) μ-metal shield and axial magnetic field of magnitude $\simeq$ 1.5 G. The probe power is 3 μW and the pump power is 97 μW, with beam diameters of $\approx$ 3 mm and a pump modulation frequency of 30 kHz.

sensitive Λ system, Fig. 3.5 on page 57 , are given by,

$$\begin{aligned} |\mathrm{a}\rangle &\equiv {}^{87}\mathrm{Rb}\ {}^{2}\mathrm{P}_{3/2}\ F = 0, 1, 2;\ m_F = 0\ ; \\ |\mathrm{b}\rangle &\equiv {}^{87}\mathrm{Rb}\ {}^{2}\mathrm{S}_{1/2}\ F = 1;\ m_F = -1\ ; \\ |\mathrm{c}\rangle &\equiv {}^{87}\mathrm{Rb}\ {}^{2}\mathrm{S}_{1/2}\ F = 1;\ m_F = +1\ . \end{aligned}$$

The probe being close to resonance with $|\mathrm{b}\rangle \rightarrow |\mathrm{a}\rangle$, and the pump with $|\mathrm{c}\rangle \rightarrow |\mathrm{a}\rangle$.

4.3.3 Line Shape

Using the lock-in detector enables signals to be recorded with a significant improvement in the signal-to-noise ratio. Such a high signal-to-noise ratio enables theoretical fits of line shapes to be made to the EIT signals. Fig. 4.21 shows

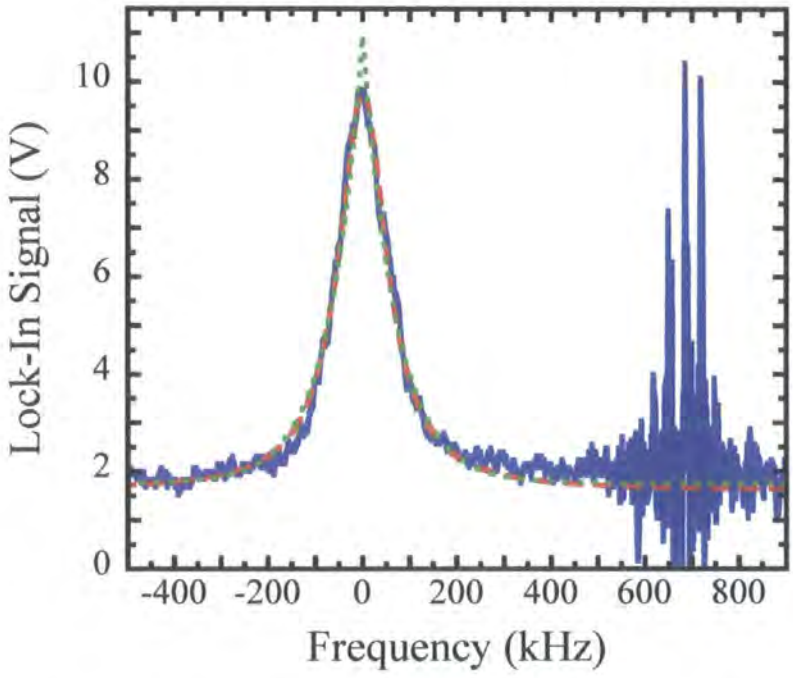

Figure 4.21: The blue solid line shows the data recorded using the lock-in amplifier, the red dashes show a Lorentzian least squares fit, and the green short dashes show a cusp least squares fit to the data. The signal in Volts is plotted against the two-photon detuning, $((\delta_{\rm pr}-\delta_{\rm pu})/2\pi)$. Note that the two-photon resonance has been shifted by 0.7 MHz from the beat note, using an axial magnetic field. The pump is modulated at $\approx$ 30 kHz, the probe power is 6 μW, the pump power is 40 μW, and the beam diameters are $\approx$ 1 cm.

both Lorentzian and cusp least square fits (cusp fits being appropriate to the case in which the dominant contribution to the line width is transit-time broadening) for a typical data set, in this case with a probe power of 6 μW, a pump power of 40 μW and an axial magnetic field of 0.5 G. As can be seen in this case the Lorentzian function provides the better fit to the data.

Measured Position Of Two-Photon EIT Resonance

To ensure that the calibrations of the frequency of the probe field (due to the AOM scan) and the magnetic field due to the solenoid were correct, spectra were recorded for different axial magnetic fields. Lorentzian fits were made to the EIT line shapes, and the centre of the line shape in each case was recorded. The centre of the line shape was then plotted against the magnetic field. Five different values of magnetic field were used and for each value five spectra were recorded. The resulting plot can be seen in Fig. 4.22. Accompanying the data is a least-squares best fit straight line. This has a gradient consistent with the theoretical value of 1.40 MHz G^{-1}, § 3.5.1.

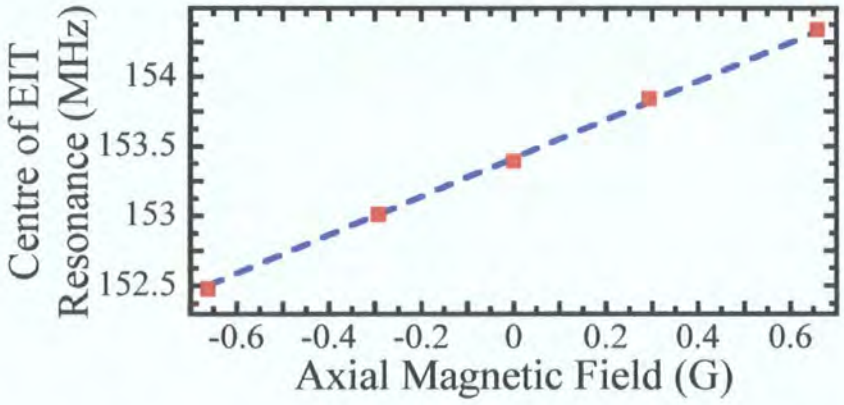

Figure 4.22: Red squares show the measured position centre of EIT resonance. The blue line shows a χ^2 straight line fit to the data. The gradient of the fit is 1.39 ± 0.01 MHz G^{-1}. The probe power is 2 μW and the pump power is 90 μW. The reduced χ^2 value for the fit is 2.4 and the error bars are smaller than the red squares used as data markers. The vertical scale is the frequency offset due to the probe beam AOM.

This confirms that the independent calibrations of the probe beam frequency and the axial magnetic field are consistent with one-another.

4.3.4 Magnetic Field Broadening

If the axial magnetic field inside the solenoid is not uniform over the length of the Rb cell, then variation in the magnetic field along the length of the

Rb vapour cell will lead to the centre frequency of the two-photon resonance varying with position along the cell. This will lead to broadening of the feature measured in the 8 cm long Rb vapour cells, § 3.5.1.

Data were recorded for different solenoid currents varying from 0.05 A to 0.80 A. From the calibration of the solenoid field, Fig. 4.19 on page 99, these currents correspond to magnetic fields varying from 0.73 G to 11.6 G. The pump power was recorded as 5.7 μW and the probe power as 2.2 μW. Lorentzian fits are made to the traces, and the full-width at half-maximum (FWHM) of these fits are plotted against the axial magnetic field. As can be seen in Fig. 4.23, the

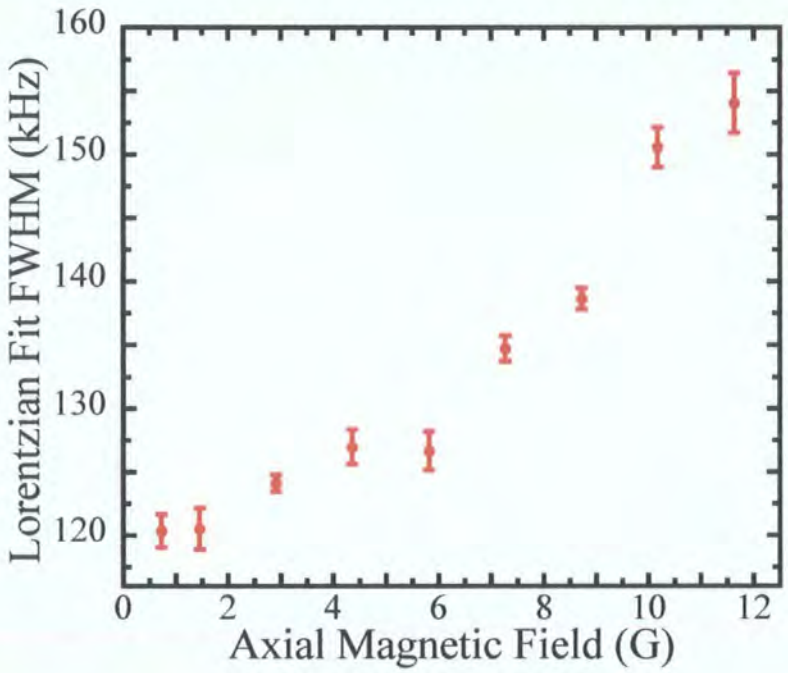

Figure 4.23: FWHM of Lorentzian function fitted to EIT features plotted as a function of axial magnetic field. The probe power is 2 μW, the pump power is 5 μW, the beam diameters are $\approx$ 1 cm and the pump modulation frequency $\approx$ 50 kHz.

FWHM of the EIT features increases by 28% . The corresponding change in frequency of the centre of the two-photon resonance is 15.3 MHz. This takes the two-photon resonance out of the range of the VCO frequency calibration shown in Fig. 4.7 on page 82. Calibrations over a wider range of control voltages gives a frequency to control voltage conversion factor of 5.12 MHz/V. This

would account for a potential increase of 3.4% in the width of the resonances, substantially less than the 28% increase in FWHM measured.

From § 4.3.2 the limit on the EIT line width due to the applied magnetic field is $\leqslant$ 9.7 kHz G^{-1}. The data presented in Fig. 4.23 is consistent with this magnetic field broadening, as the difference between the FWHM at 0.7 G and 11.6 G corresponds to 3.1 kHz G^{-1}.

4.3.5 Variation in Width of Two-Photon EIT Resonance With Pump and Probe Power.

In chapter 3 it was shown that the width of the EIT-resonance is strongly dependent upon the power of the pump beam, this is in the regime where the probe is significantly weaker than the pump. Once they start to become of comparable strength then it is obvious that the probe can no longer strictly be described as a weak beam and hence it must have an appreciable contribution to the width of the resonance. While a more thorough study of the effect of probe and pump power upon the width of the resonances is made in § 6.6, initial measurements made using the lock-in amplifier will be briefly presented here.

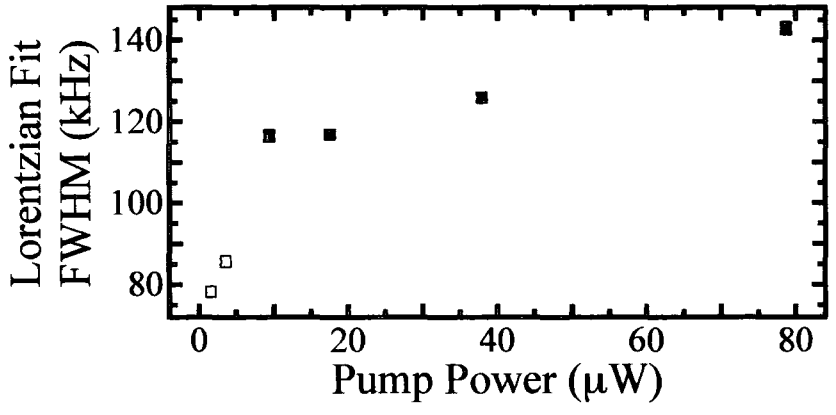

Figure 4.24: FWHM of Lorentzian function fitted to EIT features plotted as a function of pump power. Red points show data recorded with a probe power of 0.5 μW and blue points with a probe power of 5 μW. The beam diameters $\approx$ 1 cm and the pump is modulated at $\approx$ 30 kHz.

As can be seen in Fig. 4.24 the width of the EIT feature decreases with decreasing pump power, until the pump power approaches the probe power, when the width reaches a minimum for the probe intensity used. For the probe power of 5 μW, the minimum width, for this set-up, is $\simeq$ 115 kHz. Reduction of the probe power by a factor of 10 to 0.5 μW allows FWHM of $<$ 80 kHz. The limitation on measuring narrower resonances is that the EIT feature is not resolvable for lower pump powers.

4.3.6 Transmission EIT/EIA Conclusions

Both EIT and EIA has been shown on the Rb D_2 line for both isotopes of Rb. The amplitude of these features has been shown to vary with detuning across the Doppler-broadened single-photon resonances. Reducing the power of both pump and probe beams has been shown to reduce the line width of the EIT features. Further it has been shown that the position of the two-photon resonances depends on the magnitude of the applied axial magnetic field, in agreement with theory. Application of such a magnetic field leads to broadening of the EIT features, within the limit defined by the uniformity of that field.

Chapter 5

Sagnac Interferometer: Theory & Background

5.1 Introduction to Sagnac Interferometers

5.1.1 Development of Sagnac Interferometers

Sagnac provided the first demonstration of the feasibility of an optical experiment capable of indicating the state of rotation of a frame of reference, by making measurements within that frame, [25, 26]. A schematic diagram of his interferometer is shown in Fig. 5.1(i) .

The fringe pattern recorded at the output of this interferometer is sensitive to any phase difference between the two counter-propagating beams. In the case that the whole interferometer is rotating in its plane, at an angular frequency, Ω_{rot}, it is possible to follow a simple derivation to obtain the value of the phase shift, $\Delta\phi$.

Consider a circular interferometer of radius, r, Fig. 5.1(ii). The time taken for the two beams to complete one circuit of the interferometer, $t_{\pm}$ is given by,

$$t_{\pm} = \frac{2\pi r \pm r\,\Omega_{\text{rot}} t_{\pm}}{\text{v}}\,, \tag{5.1}$$

where v is the speed of propagation around the Sagnac loop.

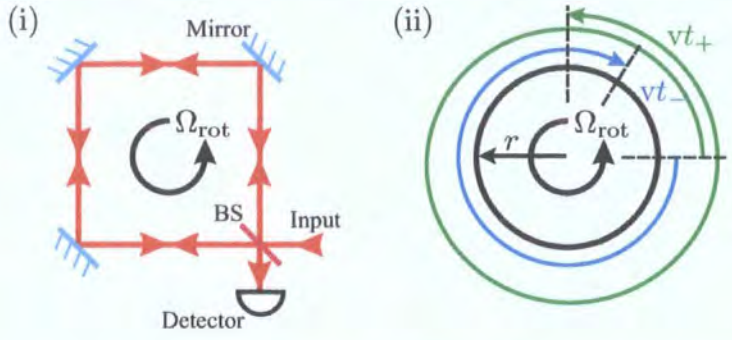

Figure 5.1: (i) A schematic diagram of Sagnac's original interferometer. Light from the light source is split into two beams by the beam splitter. Two counter-propagating beams then circulate the interferometer. The beams interfere on the beam splitter. There are two output ports of the interferometer, one back towards the light source, the other towards the detector. (ii) Shows a circular Sagnac interferometer of radius, r, rotating at an angular frequency, Ω_{rot}. The shifts in path length for the two counter-propagating beams, $vt_{\pm}$, are shown.

Thus,

$$t_{\pm}\left(\frac{v \mp r\ \Omega_{\text{rot}}}{v}\right) = \frac{2\pi r}{v} . \tag{5.2}$$

Hence

$$t_{\pm} = \frac{2\pi r}{v \mp r\ \Omega_{\text{rot}}} . \tag{5.3}$$

It follows that the difference in propagation time for the two counter-propagating beams, δt, is given by,

$$\delta t = t_+ - t_- , \tag{5.4}$$

$$= \frac{2\pi r}{v - r\ \Omega_{\text{rot}}} - \frac{2\pi r}{v + r\ \Omega_{\text{rot}}} , \tag{5.5}$$

$$\Longrightarrow \quad \delta t = \frac{4\pi r^2\ \Omega_{\text{rot}}}{v^2 - (r\ \Omega_{\text{rot}})^2} . \tag{5.6}$$

The area of the interferometer, A, is equal to πr^2. The phase difference between the two counter-propagating beams, $\Delta\phi$, is given by $(v\ \delta t/\lambda_0)$.

In the vast majority of cases, $v^2 \gg (r\ \Omega_{\text{rot}})^2$, it follows that,

$$\Delta\phi = \frac{4\boldsymbol{A}\cdot\boldsymbol{\Omega}_{\text{rot}}}{\lambda_0 v} . \tag{5.7}$$

Here $(\boldsymbol{A}/A)$ is a unit vector perpendicular to the surface area of the interferometer. In the case of light v = c, irrespective of a modified group velocity or phase velocity, [89].

The sensitivity of this interferometer due to rotations depends only on the wavelength, and the projection of the rotation onto the area enclosed within the interferometer. The centre of rotation and the shape of the loop have no bearing on the sensitivity. The sensitivity does however depend on the angle between the plane of rotation and the plane of the interferometer.

The Sagnac effect manifests itself in both Sagnac interferometers and Mach-Zehnder interferometers.

5.1.2 Types of Sagnac Interferometers

Since Sagnac's first measurements of rotation with his interferometer there has been a large amount of interest in making ever more sensitive measurements using a variety of different implementations of the Sagnac interferometer, [89, 90, 91].

There have been two main lines of development for Sagnac interferometers. Optical Sagnac interferometers, [89, 90, 91], aim to increase sensitivity by increasing the path length of the two beams before they are coupled out of the interferometer. There are two main schemes for achieving this, ring laser gyros and optical fibre gyros. Multiple loops around the same physical area lead to an increased gyroscopic area.

Matter-wave interferometers sensitive to the Sagnac effect are generally restricted to Mach-Zehnder interferometers, [92, 93, 94]. One notable exception is the Sagnac interferometer of Arnold *et al.*, [95]. Matter-wave interferometers have an intrinsic sensitivity much greater than optical Sagnac interferometers, due to the smaller velocity and wavelength of the particles compared to light. Matter-wave interferometers lose out to optical interferometers in that their enclosed area is limited. Where the sensitivity of optical-fibre interferometers is very easily scalable, for example by increasing the number of fibre loops, the sensitivity of matter-wave interferometers is not.

Optical ring laser gyros can achieve sensitivities of 1.4×10^{-11} rad s^{-1} $Hz^{-1/2}$,

[96], and atom interferometer gyroscopes can achieve sensitivities of 6×10^{-10} rad s^{-1} $Hz^{-1/2}$, [97].

5.1.3 Light-Matter-Wave Sagnac Interferometer

Zimmer and Fleischhauer, [17], have proposed a scheme that combines the scalability of optical Sagnac interferometers with the intrinsic greater sensitivity of matter-wave interferometers. The increased sensitivity comes from the slow-light phenomenon associated with EIT. Reducing the phase or group velocity of the light is not sufficient to enhance the Sagnac effect, [89]. If momentum is transferred from the slow light to a matter-wave, then this matter-wave component will lead to the enhancement of the Sagnac effect. It is likely that for this to be realized a low temperature atomic ensemble would be required, cooling to at least 10^3 T_{rec}[1].

5.1.4 Biased Sagnac

Measurements of the dispersion of the hyperfine structure of Cs were made using a Sagnac interferometer by Robins *et al.*, [99]. This required biasing the alignment of the interferometer, [100], such that the output arm contains two interference fringes. The difference signal between these two fringes gives a signal proportional to the dispersion of the medium.

This method was developed by Jundt *et al.*, [101], and applied to Rb hyperfine spectra. Rather than taking the difference between two fringes within one arm of the interferometer, the difference between two output arms of the interferometer was measured. This was shown to be in excellent agreement with the dispersion predicted from the transmission spectra using the Kramers-Kronig relations, § 2.3.2 on page 22 .

Furthermore, Purves *et al.*, [100], have applied the biased Sagnac interferometer to measuring EIT resonances. The basis for this publication is presented in chapter 6 of this thesis.

The theoretical basis showing that the difference signal between the two output

[1] $T_{\text{rec}} = (\hbar k_{\text{ab}})^2/(2m k_{\text{B}})$, [98], is the recoil temperature which for ^{87}Rb is 180 nK.

arms of the interferometer, in the case of biased alignment, is proportional to the dispersion is developed in § 5.3 on page 115 .

The biased Sagnac interferometer as described in § 5.3 on page 115 , provides a direct readout of the dispersion of a medium. The dispersion associated with a narrow EIT feature provides an ideal error signal which could be used to detect any physical effect that causes a shift in the detuning of the EIT resonance. For the purpose of making a detector, measuring the dispersion is more appropriate than simply measuring the absorption of the medium for two reasons: about line centre the rate of change in absorption with detuning is at a minimum, where as the rate of change in dispersion is at its maximum; secondly, also about line centre, the change in the absorption has the same sign independent of the sign of the shift in detuning, whereas the sign of the shift in dispersion is dependent upon the sign of the shift in detuning.

Mach-Zehnder interferometers have been used to measure the dispersion of a medium, [102], and specifically to measure the dispersion due to EIT, [3, 57]. There are two main advantages in using a Sagnac interferometer over a Mach-Zehnder: the stability of the interferometer against vibration and the control of the absolute difference in the length of the arms of the interferometer. The very nature of the Sagnac interferometer ensures that the default is to have no difference in path length between the two arms (the arms counter-propagate around the same loop). In addition to this the fact that both arms in the Sagnac interferometer interact with the same optical elements ensures a degree of common mode rejection in any vibrations that the optical elements experience.

It is of course possible to measure an error signal similar to that provided by the dispersion of a medium, by dithering the frequency of a probe beam while measuring the transmission. This has the added disadvantage of the dithering broadening the resonance, as well as requiring lock-in amplifiers to measure the error signal — these are complications not present with the biased Sagnac interferometer.

Measuring EIT in a Sagnac interferometer also paves the way for the realization of the optical-matter-wave interferometer of Zimmer and Fleischhauer, [17].

5.2 Beam Splitters

Following in the style of the analysis presented in *The Quantum Theory of Light*, by Loudon, [103], consider a beam splitter that does not have any losses. If we have two input fields, E_1 and E_2 and two output fields, E_3 and E_4, as in the diagram below, Fig. 5.2, it follows that the fields will be related by the following

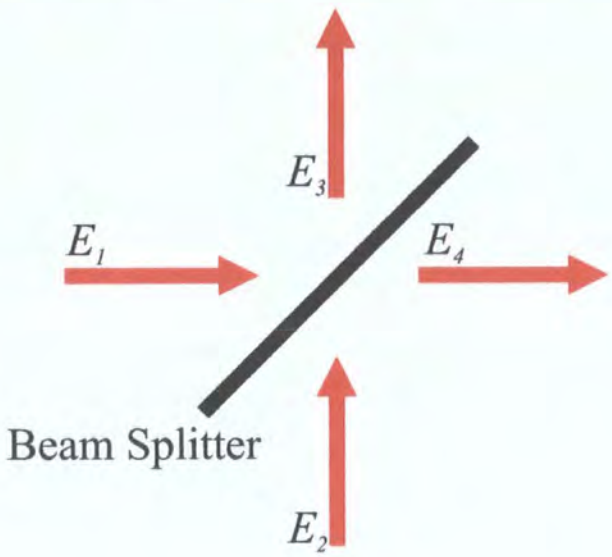

Figure 5.2: Two fields, E_1 and E_2, incident on the beam splitter lead to two output fields, E_3 and E_4.

equations,

$$E_3 = R_{31}E_1 + T_{32}E_2 \,, \tag{5.8}$$

$$E_4 = T_{41}E_1 + R_{42}E_2 \,. \tag{5.9}$$

Here R represents reflection and T represents transmission. R and T are both generally complex and vary with optical frequency. We will assume that we are dealing with monochromatic radiation. Equations 5.8 and 5.9 can be rewritten in matrix form as:

$$\begin{pmatrix} E_3 \\ E_4 \end{pmatrix} = \begin{pmatrix} R_{31} & T_{32} \\ T_{41} & R_{42} \end{pmatrix} \begin{pmatrix} E_1 \\ E_2 \end{pmatrix} \,. \tag{5.10}$$

From the conservation of energy it follows that:

$$\begin{aligned} |E_3|^2 + |E_4|^2 &= |E_1|^2 + |E_2|^2 \,, && (5.11) \\ &= |R_{31}|^2|E_1|^2 + |T_{32}|^2|E_2|^2 + R_{31}T_{32}^* E_1 E_2^* \\ &\quad + R_{31}^* T_{32} E_1^* E_2 + |T_{41}|^2|E_1|^2 + |R_{42}|^2|E_2|^2 && (5.12) \\ &\quad + T_{41}R_{42}^* E_1 E_2^* + T_{41}^* R_{42} E_1^* E_2 \,. \end{aligned}$$

From equation 5.12 ,

$$\begin{aligned} |R_{31}|^2 + |T_{41}|^2 &= 1 \,, \\ &= |T_{32}|^2 + |R_{42}|^2 \,, && (5.13) \\ R_{31}T_{32}^* + T_{41}R_{42}^* &= 0 \,, && (5.14) \\ \text{or equivalently} \quad R_{31}^* T_{32} + T_{41}^* R_{42} &= 0 \,. && (5.15) \end{aligned}$$

The reflection and transmission coefficients can be written,

$$\begin{aligned} R_{31} &= |R_{31}|e^{i\phi_{31}} \,, && (5.16) \\ R_{42} &= |R_{42}|e^{i\phi_{42}} \,, \\ T_{32} &= |T_{32}|e^{i\phi_{32}} \,, \\ T_{41} &= |T_{41}|e^{i\phi_{41}} \,. \end{aligned}$$

Substituting from equations 5.16 into equation 5.14, gives,

$$\begin{aligned} |R_{31}|e^{i\phi_{31}}|T_{32}|e^{-i\phi_{32}} + |T_{41}|e^{i\phi_{41}}|R_{42}|e^{-i\phi_{42}} &= 0 \,, \\ \therefore \quad |R_{31}||T_{32}|e^{i(\phi_{31}-\phi_{32})} &= -|R_{42}||T_{41}|e^{i(\phi_{41}-\phi_{42})} \,, \\ \therefore \quad |R_{31}||T_{32}|e^{i(\phi_{31}+\phi_{42}-\phi_{32}-\phi_{41})} &= -|R_{42}||T_{41}| \,. && (5.17) \end{aligned}$$

Equating the imaginary parts of equation 5.17,

$$\begin{aligned} |R_{31}||T_{32}| \sin(\phi_{31} + \phi_{42} - \phi_{32} - \phi_{41}) &= 0 \,, \\ \Longrightarrow \quad \phi_{31} + \phi_{42} - \phi_{32} - \phi_{41} &= -\pi, 0, +\pi \,. && (5.18) \end{aligned}$$

It follows that,

$$\cos(\phi_{31} + \phi_{42} - \phi_{32} - \phi_{41}) = \pm 1 \,. \qquad (5.19)$$

Equating real parts of equation 5.17,

$$\begin{aligned} |R_{31}||T_{32}| &> 0 \,, \\ |R_{42}||T_{41}| &> 0 \,, \\ \text{hence} \quad \cos\left(\phi_{31} + \phi_{42} - \phi_{32} - \phi_{41}\right) &< 0 \,. \end{aligned}$$

Thus from equation 5.19 ,

$$\cos\left(\phi_{31} + \phi_{42} - \phi_{32} - \phi_{41}\right) = -1 \,, \tag{5.20}$$

$$\implies \quad \phi_{31} + \phi_{42} - \phi_{32} - \phi_{41} = \pm\pi \,, \tag{5.21}$$

It follows that,

$$\frac{|R_{31}|}{|T_{41}|} = \frac{|R_{42}|}{|T_{32}|} \,. \tag{5.22}$$

Hence the ratios into which the radiation is split is the same whether it comes in from side "1" or side "2". Thus from equations 5.13 and 5.22,

$$\begin{aligned} |R_{31}| &= |R_{42}| \,, \\ &\equiv |R| \,, \end{aligned} \tag{5.23}$$

$$\begin{aligned} \text{and} \quad |T_{31}| &= |T_{42}| \,, \\ &\equiv |T| \,. \end{aligned} \tag{5.24}$$

Taking the beam splitter coefficients to be symmetrical,

$$\begin{aligned} \phi_{31} &= \phi_{42} \,, \\ &\equiv \phi_{\mathrm{R}} \,, \end{aligned} \tag{5.25}$$

$$\begin{aligned} \text{and} \quad \phi_{32} &= \phi_{41} \,, \\ &\equiv \phi_{\mathrm{T}} \,. \end{aligned} \tag{5.26}$$

It follows from equations 5.25, 5.26 and 5.21 that,

$$\phi_{\mathrm{R}} - \phi_{\mathrm{T}} = \pm\frac{\pi}{2} \,. \tag{5.27}$$

Hence,

$$\begin{aligned} R_{31} &= R_{42} \,, \\ &= R \,, \\ R &= |R|e^{i\phi_R} \,, \end{aligned} \tag{5.28}$$

$$\begin{aligned} T_{32} &= T_{41} \,, \\ &= T \,, \\ T &= |T|e^{i\phi_T} \,. \end{aligned} \tag{5.29}$$

Thus the transmission and reflection is the same, independent of which side of the beam splitter the beam is input from.

5.3 Sagnac Interferometer

The Sagnac interferometer used to make measurements of EIT features in chapter 6 is shown in Fig. 5.3 on the following page .

Consider four different paths of the probe beam around the Sagnac interferometer to one of the photodiodes, Fig. 5.4. The beam can propagate around the photodiode in one of two directions: clockwise, which will be labelled with the subscript "c"; and anticlockwise which will be labelled "a". Both the clockwise and anticlockwise beams will have components that will impinge on each of the photodiodes. The two photodiodes are labelled "A" and "B", and those subscripts will be used to label the components in the derivation. Fig. 5.4 on page 117 shows the four possible paths around the interferometer. To determine the intensity of light measured at each photodiode it is necessary to first find the amplitude of each component that arrives at that photodiode, and then take the magnitude of the field squared. It will be necessary to consider the phase and amplitude modifications of each field around the interferometer. As each field is derived from the same probe beam, then only the changes to the fields once they are split into the two oppositely propagating fields needs to be considered. For the purpose of this derivation, assume that the beam splitters and mirrors are lossless. Also assume that any phase picked up on the mirrors is the same for both beams.

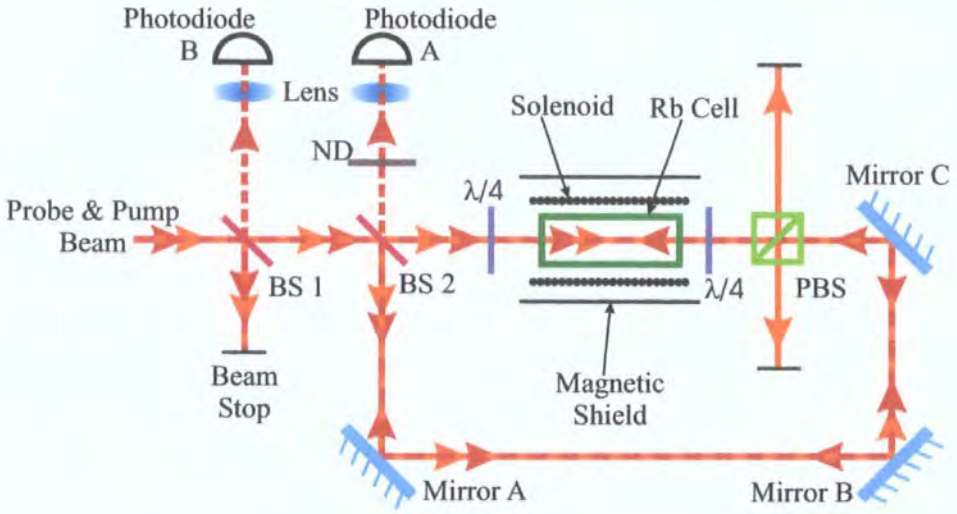

Figure 5.3: BS1 and BS2 are the first and second 50:50 beam splitters respectively; ND is the neutral-density filter; PBS is the polarizing beam splitter and $\lambda/4$ is a quarter-wave plate. The probe beams are drawn in red and the pump beams in orange. The Sagnac interferometer is formed by the loop originating and terminating at the second beam splitter (BS2). Output arm A propagates towards photodiode A and output arm B towards photodiode B.

It will also be instructive to consider a small misalignment between the two beams. This will be done by assuming a small path difference of length Δl between the clockwise and the anticlockwise propagating beams. Both beams pick up the same phase shift due to passing through the first beam splitter. This phase is therefore neglected in the following analysis.

$$\frac{E_{\mathrm{A,\,c}}}{E_{\mathrm{Input}}} = |T_1||T_{\mathrm{ND}}|\left[\mathrm{e}^{-\frac{\alpha_{\mathrm{c}}L}{2}}\mathrm{e}^{\mathrm{i}(kn_{\mathrm{c}}L+2\phi_{2\mathrm{T}}+\phi_{\mathrm{ND}})}|T_2|^2\right], \tag{5.30}$$

$$\frac{E_{\mathrm{A,\,a}}}{E_{\mathrm{Input}}} = |T_1||T_{\mathrm{ND}}|\left[\mathrm{e}^{-\frac{\alpha_{\mathrm{a}}L}{2}}\mathrm{e}^{\mathrm{i}(k(n_{\mathrm{a}}L+\Delta l)+2\phi_{2\mathrm{R}}+\phi_{\mathrm{ND}})}|R_2|^2\right], \tag{5.31}$$

$$\frac{E_{\mathrm{B,\,c}}}{E_{\mathrm{Input}}} = |T_1||R_1|\left[\mathrm{e}^{-\frac{\alpha_{\mathrm{c}}L}{2}}\mathrm{e}^{\mathrm{i}(kn_{\mathrm{c}}L+\phi_{2\mathrm{T}}+\phi_{2\mathrm{R}}+\phi_{1\mathrm{R}})}|T_2||R_2|\right], \tag{5.32}$$

$$\frac{E_{\mathrm{B,\,a}}}{E_{\mathrm{Input}}} = |T_1||R_1|\left[\mathrm{e}^{-\frac{\alpha_{\mathrm{a}}L}{2}}\mathrm{e}^{\mathrm{i}(k(n_{\mathrm{a}}L+\Delta l)+\phi_{2\mathrm{R}}+\phi_{2\mathrm{T}}+\phi_{1\mathrm{R}})}|T_2||R_2|\right]. \tag{5.33}$$

To determine the normalized intensity of the fields at both photodiodes sum

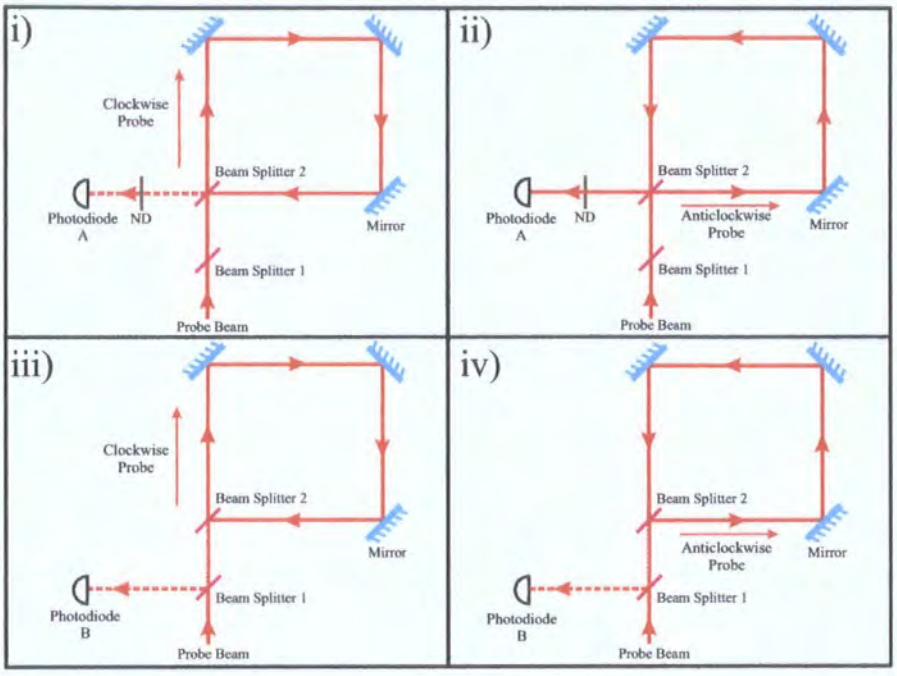

Figure 5.4: (i) and (ii) show the path of the clockwise and anticlockwise propagating beam to photodiode A. (iii) and (iv) show the path of the clockwise and anticlockwise propagating beam to photodiode B. ND is a neutral density filter.

the amplitudes of the fields at each photodiode and then multiply them by the complex conjugate to obtain the modulus squared.

$$I_{\mathrm{A}} = \left| \frac{E_{\mathrm{A,\,c}} + E_{\mathrm{A,\,a}}}{E_{\mathrm{Input}}} \right|^2 , \tag{5.34}$$

$$I_{\mathrm{B}} = \left| \frac{E_{\mathrm{B,\,c}} + E_{\mathrm{B,\,a}}}{E_{\mathrm{Input}}} \right|^2 . \tag{5.35}$$

$$\begin{aligned} I_{\mathrm{A}} &= (|T_1||T_{\mathrm{ND}}|)^2 \left[\mathrm{e}^{-\frac{\alpha_{\mathrm{c}} L}{2}} \mathrm{e}^{\mathrm{i}(kn_{\mathrm{c}}L + 2\phi_{2\mathrm{T}})} |T_2|^2 + \mathrm{e}^{-\frac{\alpha_{\mathrm{a}} L}{2}} \mathrm{e}^{\mathrm{i}(k(n_{\mathrm{a}}L + \Delta l) + 2\phi_{2\mathrm{R}})} |R_2|^2 \right] \\ &\quad \times \left[\mathrm{e}^{-\frac{\alpha_{\mathrm{c}} L}{2}} \mathrm{e}^{-\mathrm{i}(kn_{\mathrm{c}}L + 2\phi_{2\mathrm{T}})} |T_2|^2 + \mathrm{e}^{-\frac{\alpha_{\mathrm{a}} L}{2}} \mathrm{e}^{-\mathrm{i}(k(n_{\mathrm{a}}L + \Delta l) + 2\phi_{2\mathrm{R}})} |R_2|^2 \right] , \end{aligned} \tag{5.36}$$

$$\begin{aligned} &= |T_1|^2 |T_{\mathrm{ND}}|^2 \left[|T_2|^4 \mathrm{e}^{-\alpha_{\mathrm{c}} L} + |R_2|^4 \mathrm{e}^{-\alpha_{\mathrm{a}} L} + |T_2|^2 |R_2|^2 \mathrm{e}^{-(\alpha_{\mathrm{c}} + \alpha_{\mathrm{a}})\frac{L}{2}} \right. \\ &\quad \left. \times \left(\mathrm{e}^{\mathrm{i}(kn_{\mathrm{c}}L + 2\phi_{2\mathrm{T}}) - \mathrm{i}(k(n_{\mathrm{a}}L + \Delta l) + 2\phi_{2\mathrm{R}})} + \mathrm{e}^{\mathrm{i}(k(n_{\mathrm{a}}L + \Delta l) + 2\phi_{2\mathrm{R}}) - \mathrm{i}(kn_{\mathrm{c}}L + 2\phi_{2\mathrm{T}})} \right) \right] . \end{aligned} \tag{5.37}$$

Now writing,

$$\begin{aligned} \alpha &= \frac{\alpha_c + \alpha_a}{2} , \\ \Delta n &= n_c - n_a , \end{aligned}$$

and also from equation 5.27, $(\phi_R - \phi_T = -\pi/2)$, we can rewrite the intensity at photodiode A as,

$$\begin{aligned} I_A &= |T_1|^2|T_{ND}|^2 \left[|T_2|^4 e^{-\alpha_c L} + |R_2|^4 e^{-\alpha_a L}\right. \\ &\quad \left. + |T_2|^2|R_2|^2 e^{-\alpha L}\left(e^{ikL\Delta n - \Delta l + i\pi} + e^{-ik(L\Delta n + \Delta l) - i\pi}\right)\right] , \end{aligned} \tag{5.38}$$

$$\begin{aligned} &= |T_1|^2|T_{ND}|^2 \left[|T_2|^4 e^{-\alpha_c L} + |R_2|^4 e^{-\alpha_a L}\right. \\ &\quad \left. - |T_2|^2|R_2|^2 e^{-\alpha L} 2\cos\left(k\left(L\Delta n - \Delta l\right)\right)\right] , \end{aligned}$$

$$\begin{aligned} \therefore \quad I_A &= |T_1|^2|T_{ND}|^2 \left[|T_2|^4 e^{-\alpha_c L} + |R_2|^4 e^{-\alpha_a L}\right. \\ &\quad \left. - 2|T_2|^2|R_2|^2 e^{-\alpha L}\cos\left(k\left(L\Delta n - \Delta l\right)\right)\right] . \end{aligned} \tag{5.39}$$

Considering the other output arm of the Sagnac interferometer,

$$\begin{aligned} I_B &= \left(|T_1||R_1|\right)^2 \left[e^{-\frac{\alpha_c L}{2}} e^{i(kn_c L + \phi_{2T} + \phi_{2R} + \phi_{1R})}|T_2||R_2|\right. \\ &\quad \left. + e^{-\frac{\alpha_a L}{2}} e^{i(k(n_a L + \Delta l) + \phi_{2R} + \phi_{2T} + \phi_{1R})}|R_2||T_2|\right] \\ &\quad \times \left[e^{-\frac{\alpha_c L}{2}} e^{-i(kn_c L + \phi_{2T} + \phi_{2R} + \phi_{1R})}|T_2||R_2|\right. \\ &\quad \left. + e^{-\frac{\alpha_a L}{2}} e^{-i(k(n_a L + \Delta l) + \phi_{2R} + \phi_{2T} + \phi_{1R})}|R_2||T_2|\right] . \end{aligned} \tag{5.40}$$

As with the derivation above for I_A, rewriting the equation for I_B in terms of Δn and α, then we get

$$\begin{aligned} I_B &= |T_1|^2|R_1|^2 \left[|R_2|^2|T_2|^2 e^{-\alpha_c L} + |R_2|^2|T_2|^2 e^{-\alpha_a L}\right. \\ &\quad \left. + |T_2|^2|R_2|^2 e^{-\alpha L}\left(e^{ik(L\Delta n - \Delta l)} + e^{-ik(L\Delta n + \Delta l)}\right)\right] , \end{aligned} \tag{5.41}$$

$$\begin{aligned} &= |T_1|^2|R_1|^2 \left[|R_2|^2|T_2|^2 e^{-\alpha_c L} + |R_2|^2|T_2|^2 e^{-\alpha_a L}\right. \\ &\quad \left. + 2|T_2|^2|R_2|^2 e^{-\alpha L}\cos\left(k\left(L\Delta n - \Delta l\right)\right)\right] , \end{aligned}$$

$$\begin{aligned} \therefore \quad I_B &= |T_1|^2|R_1|^2|T_2|^2|R_2|^2 \left[e^{-\alpha_c L} + e^{-\alpha_a L}\right. \\ &\quad \left. + 2e^{-\alpha L}\cos\left(k\left(L\Delta n - \Delta l\right)\right)\right] . \end{aligned} \tag{5.42}$$

From equations 5.39 and 5.42 the sum and the difference signals can be derived,

$$\begin{aligned} I_A + I_B &= e^{-\alpha_c L}\left(|T_1|^2|T_{ND}|^2|T_2|^4 + |T_1|^2|R_1|^2|T_2|^2|R_2|^2\right) \\ &+e^{-\alpha_a L}\left(|T_1|^2|T_{ND}|^2|T_2|^4 + |T_1|^2|R_1|^2|T_2|^2|R_2|^2\right) \\ &+e^{-\alpha L}\left(|T_1|^2|R_1|^2|T_2|^2|R_2|^2\right. \\ &\left.-|T_1|^2|T_{ND}|^2|T_2|^2|R_2|^2\right) 2\cos\left(k\left(L\Delta n - \Delta l\right)\right), \end{aligned} \tag{5.43}$$

$$\begin{aligned} I_A - I_B &= e^{-\alpha_c L}\left(|T_1|^2|T_{ND}|^2|T_2|^4 - |T_1|^2|R_1|^2|T_2|^2|R_2|^2\right) \\ &+e^{-\alpha_a L}\left(|T_1|^2|T_{ND}|^2|T_2|^4 - |T_1|^2|R_1|^2|T_2|^2|R_2|^2\right) \\ &+e^{-\alpha L}\left(-|T_1|^2|R_1|^2|T_2|^2|R_2|^2\right. \\ &\left.-|T_1|^2|T_{ND}|^2|T_2|^2|R_2|^2\right) 2\cos\left(k\left(L\Delta n - \Delta l\right)\right). \end{aligned} \tag{5.44}$$

Consider the particular case where the intensity of an incoming beam is split equally into two components each of which has 50 % of the incoming intensity. Also the ND filter will transmit only 50 % of the incident intensity.

Therefore,

$$\begin{aligned} |T_1| &= |T_2|, \\ &= |T_{ND}|, \\ &= |R_1|, \\ &= |R_2|, \\ &= \frac{1}{\sqrt{2}}. \end{aligned} \tag{5.45}$$

Then, from equations 5.43, 5.44 and 5.45,

$$I_A + I_B = \frac{1}{8}\left(e^{-\alpha_c L} + e^{-\alpha_a L}\right), \tag{5.46}$$

$$I_A - I_B = -\frac{1}{4}e^{-\alpha L}\cos\left(k\left(L\Delta n - \Delta l\right)\right). \tag{5.47}$$

In practice any misalignment of the Sagnac will lead to there being a range of Δl across the finite profile of the output beams. As the whole beam is generally focussed onto a photodiode then what will be recorded is an average over a range of Δl of I_A and I_B. In order to determine what is recorded, it is necessary to integrate I_A and I_B over a range of Δl. From equations 5.39 and 5.42 this

leads to,

$$\int_{\Delta l_1}^{\Delta l_2} I_{\mathrm{A}}\mathrm{d}\left(\Delta l\right) = |T_1|^2|T_{\mathrm{ND}}|^2\left[\left(|T_2|^4\mathrm{e}^{-\alpha_c L}+|R_2|^4\mathrm{e}^{-\alpha_a L}\right)\Delta l\right.$$
$$\left.-2|T_2|^2|R_2|^2\mathrm{e}^{-\alpha L}\left(\frac{1}{k}\right)\sin\left(k\left(L\Delta n-\Delta l\right)\right)\right]_{\Delta l_1}^{\Delta l_2}, \quad (5.48)$$

$$= |T_1|^2|T_{\mathrm{ND}}|^2\left[\left(|T_2|^4\mathrm{e}^{-\alpha_c L}+|R_2|^4\mathrm{e}^{-\alpha_a L}\right)\left(\Delta l_2-\Delta l_1\right)\right.$$
$$-2|T_2|^2|R_2|^2\mathrm{e}^{-\alpha L}\left(\frac{1}{k}\right)\left[\sin\left(k\left(L\Delta n-\Delta l_2\right)\right)\right. \quad (5.49)$$
$$\left.\left.-\sin\left(k\left(L\Delta n-\Delta l_1\right)\right)\right]\right].$$

$$\text{but, } \sin\alpha-\sin\beta = 2\sin\left(\frac{\alpha-\beta}{2}\right)\cos\left(\frac{\alpha+\beta}{2}\right), \quad (5.50)$$

$$\Longrightarrow \sin\left(k\left(L\Delta n-\Delta l_2\right)\right) - \sin\left(k\left(L\Delta n-\Delta l_1\right)\right) \quad (5.51)$$
$$= 2\sin\left(\frac{k\left(\Delta l_1-\Delta l_2\right)}{2}\right)\cos\left(kL\Delta n-\frac{k}{2}\left(\Delta l_2+\Delta l_1\right)\right).$$

Using the fact that,

$$\cos\left(\theta\pm\phi\right) = \cos\theta\cos\phi\mp\sin\theta\sin\phi, \quad (5.52)$$
$$\text{for} \quad \phi = \frac{\pi}{2},$$
$$\text{then,} \quad \cos\left(\theta-\frac{\pi}{2}\right) = \sin\theta. \quad (5.53)$$

To measure small changes in the refractive index directly, it is desirable to have sine terms as opposed to cosine terms, with an argument proportional to Δn, in the output of both arms of the Sagnac. In the limits of the arguments being small, sine terms can be approximated as being equal to the argument.

This requires,

$$\frac{k}{2}\left(\Delta l_2+\Delta l_1\right) = \frac{\pi}{2}, \quad (5.54)$$
$$\text{and if,} \quad k\Delta l_1 = 0, \quad (5.55)$$
$$\text{then,} \quad k\Delta l_2 = \pi. \quad (5.56)$$

Thus,

$$\sin\left(k\left(L\Delta n-\Delta l_2\right)\right) - \sin\left(k\left(L\Delta n-\Delta l_1\right)\right)$$
$$= 2\sin\left(-\frac{\pi}{2}\right)\sin\left(kL\Delta n\right),$$
$$= -2\sin\left(kL\Delta n\right). \quad (5.57)$$

Substituting equation 5.57 into equation 5.49,

$$\int_{\Delta l_1}^{\Delta l_2} I_{\mathrm{A}}\mathrm{d}\left(\Delta l\right) = |T_1|^2|T_{\mathrm{ND}}|^2\left[\left(|T_2|^4\mathrm{e}^{-\alpha_{\mathrm{c}}L}+|R_2|^4\mathrm{e}^{-\alpha_{\mathrm{a}}L}\right)\left(\frac{\pi}{k}\right)\right.$$
$$\left.+\frac{4}{k}|T_2|^2|R_2|^2\mathrm{e}^{-\alpha L}\sin\left(kL\Delta n\right)\right] . \tag{5.58}$$

Similarly for I_{B},

$$\int_{\Delta l_1}^{\Delta l_2} I_{\mathrm{B}}\mathrm{d}\left(\Delta l\right) = |T_1|^2|R_1|^2|T_2|^2|R_2|^2\left[\left(\mathrm{e}^{-\alpha_{\mathrm{c}}L}+\mathrm{e}^{-\alpha_{\mathrm{a}}L}\right)\left(\frac{\pi}{k}\right)\right.$$
$$\left.-\frac{4}{k}\mathrm{e}^{-\alpha L}\sin\left(kL\Delta n\right)\right] . \tag{5.59}$$

Therefore the sum and difference signals are given by,

$$\int_{\Delta l_1}^{\Delta l_2} I_{\mathrm{A}}\mathrm{d}\left(\Delta l\right)+\int_{\Delta l_1}^{\Delta l_2} I_{\mathrm{B}}\mathrm{d}\left(\Delta l\right) = \frac{\pi}{8k}\left(\mathrm{e}^{-\alpha_{\mathrm{c}}L}+\mathrm{e}^{-\alpha_{\mathrm{a}}L}\right) , \tag{5.60}$$

$$\int_{\Delta l_1}^{\Delta l_2} I_{\mathrm{A}}\mathrm{d}\left(\Delta l\right)-\int_{\Delta l_1}^{\Delta l_2} I_{\mathrm{B}}\mathrm{d}\left(\Delta l\right) = \frac{\mathrm{e}^{-\alpha L}}{2k}\sin\left(kL\Delta n\right) , \tag{5.61}$$

in the case that equation 5.45 applies.

From equations 5.60 and 5.61, the sum, S_{S}, and difference, S_{D} signals can be determined,

$$S_{\mathrm{S}} \propto \mathrm{e}^{-\alpha_{\mathrm{c}}L}+\mathrm{e}^{-\alpha_{\mathrm{a}}L} , \tag{5.62}$$

$$S_{\mathrm{D}} \propto \mathrm{e}^{-\alpha L}\sin\left(kL\Delta n\right) . \tag{5.63}$$

Hence the sum signal is proportional to the sum of the transmission of the two counter-propagating probes. The difference signal is proportional to the sine of the difference in refractive index between the two directions of propagation. In the case that $kL\Delta n \ll 1$ it follows that,

$$S_{\mathrm{D}} \propto \mathrm{e}^{-\alpha L}kL\Delta n . \tag{5.64}$$

Thus for a Sagnac interferometer, as described in this chapter, comprising two 50:50 beam splitters, the difference signal between the two output ports will be proportional to the difference in the real part of the refractive index between the two counter-propagating arms.

Chapter 6

Experimental Sagnac Interferometer

6.1 Experimental Set-Up

The experimental set-up of the Sagnac interferometer is identical to that used to make transmission measurements (Fig. 4.1 on page 76) up to the optical fibre. After the pump and probe beams have left the optical fibre, the set-up is significantly modified to form the Sagnac interferometer, Fig. 5.3 on page 116. The optical fibre ensures that the pump and probe beams co-propagate.

The Sagnac interferometer is formed by the loop originating at the second beam splitter (BS2). Probe beams propagate in both directions around the loop, while the pump beams are coupled out of the loop by the polarizing beam splitting cube; only the clockwise propagating pump beam passes through the Rb vapour cell. After completing the loop of the interferometer the two probe beams interfere on BS2. 50% of the interference propagates towards photodiode A and 50% towards the first beam splitter (BS1). A neutral density filter (ND) ensures that only 25% of the output form the interferometer is incident upon photodiode A. On BS1 the output of the interferometer is divided again such that 25% of the output of the interferometer is incident upon photodiode B.

In practice the beam splitters do not perform as perfect 50 : 50 beam splitters. This leads to a small difference in the obtained signals from those predicted in equations 5.62 and 5.63 on the preceding page. This is overcome by making

small adjustments to the mechanical slits.

In order to ensure that the two arms of the interferometer counter-propagate, a Watec high resolution CCD camera (WAT-902B) with a Computar 25 mm lens was used to monitor the degree of overlap of the beams on the mirrors within the interferometer. An iterative process — monitoring the overlap on mirror A, while adjusting mirror B, then monitoring mirror B whilst adjusting mirror A — allows the beams to be brought very close to counter-propagating. Monitoring the beams in the two output arms of the interferometer allows the counter-propagating arms within the interferometer to be brought to be "perfectly" counter-propagating. When the beams are perfectly counter-propagating and there is no absorbing medium present in the interferometer output arm B will be bright, while arm A will be dark — encapsulated in equation 5.42 and equation 5.39, and shown in Fig. 6.1(upper).

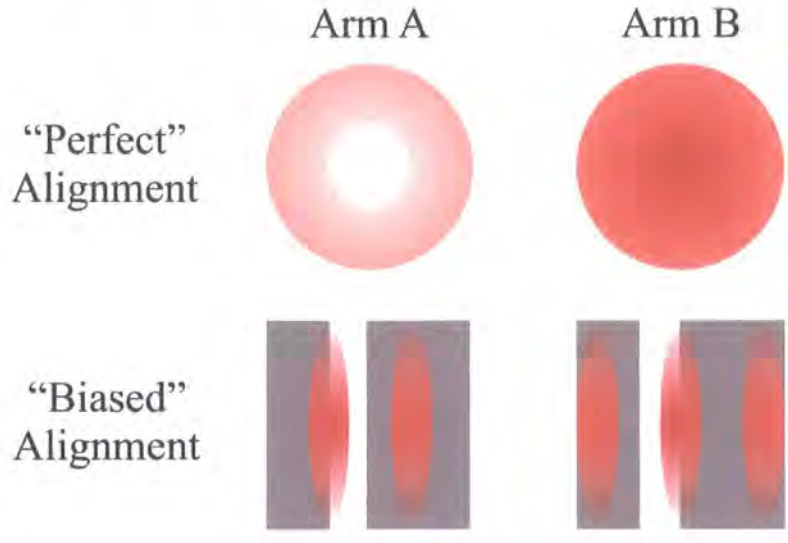

Figure 6.1: The output beam profiles for the two arms of the Sagnac interferometer, for the case of perfectly counter-propagating beams and for the biased alignment that leads to the dispersion signals. Arm A profiles are shown on the left and Arm B on the right. The grey rectangles show the position of the mechanical slits.

A change in the refractive index of the medium for one direction of propagation shifts the fringe pattern. However the sensitivity is minimal, as the shift is about a maximum or minimum of the interference pattern, where the rate of change of

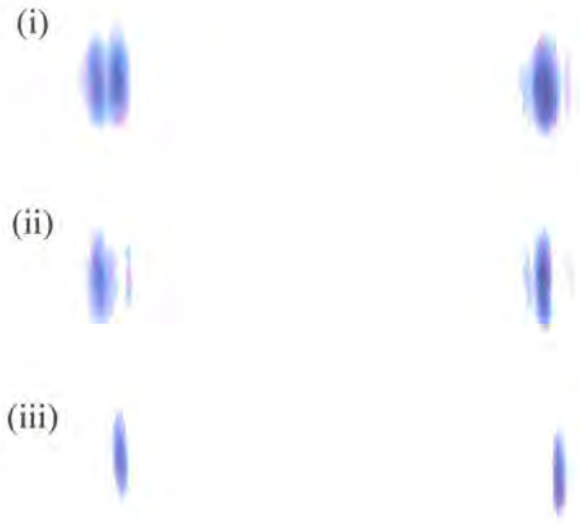

Figure 6.2: The output beam profiles of the Sagnac interferometer, as recorded on the Watec CCD camera, for the biased alignment. Arm A is on the left-hand side while arm B is on the right-hand side. (i) Shows the profiles before the slits. (ii) The beam profiles as viewed on the slits. (iii) The beam profiles of the light transmitted through the slits.

intensity with displacement is lowest. To enhance the sensitivity we "bias" the interferometer by introducing a small angle between the counter-propagating beams, [99, 101], such that both light and dark fringes appear in the interference pattern at both outputs, Fig. 6.1(lower) and Fig. 6.2(i). Two mechanical slits aperture the fringe pattern, such that only the region between the light and dark fringe is focussed onto the photodiode, Figs. 6.1(lower), 6.2(ii) and (iii). This biasing technique enables one to obtain maximal sensitivity to changes in the refractive index and a signal that is directly proportional to the refractive index difference between the two counter-propagating probes, § 5.3. For all

traces recorded with both the pump and probe propagating through the vapour cell, traces were also recorded with the pump beam blocked before the Sagnac interferometer. This alignment procedure was adopted so that the probe-only signal could be subtracted from the pump-and-probe signal — hence allowing any features in the scan across the resonance that are not due to the presence of the pump beam to be removed from the spectra.

6.1.1 Photodiode Circuit

In work presented in chapter 4 of this thesis, lock-in amplifiers have been used to detect the EIT resonances. Concern was raised that the lock-in amplifier may be limiting the line shape of the transmission resonances, [104]. In order to avoid the use of a lock-in amplifier, and yet still be able to measure the EIT resonances it was necessary to use a photodiode circuit with lower noise levels than that which had previously been used. The photodiode circuit used

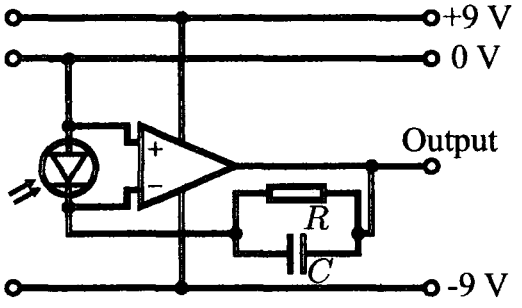

Figure 6.3: The photodiode circuit used to measure the output from the Sagnac interferometer. The op-amp used is either an AD548 or an AD648, the photodiode is a BPX–65. R is 10 MΩ and C is 4.7 pF.

throughout this chapter is shown in Fig. 6.3. The main difference between this circuit and those used in experiments in previous work in this thesis, is that in this case the photodiode is not biased. This leads to two main advantages over the previous circuits, a lesser influence from dark currents, and a wider range over which the photocurrent is linear with radiant intensity, [40, 41, 105]. The improvement in signal to noise ratio of this photodiode circuit, over that used in earlier work in this thesis, was investigated by J. Gaffney[1].

[1]This work was carried out during a Nuffield funded summer project.

The output voltage of this photodiode circuit has the same form of temporal filtering as the photodiode circuits used in chapter 4, shown in Fig. 4.9 on page 86. However with a different value of $R = 10$ MΩ, the output voltage will be a factor of 10 higher and will have a frequency cut-off as shown in Fig. 6.4. With the impedance decreasing significantly over angular frequencies $\simeq 10$ kHz, it follows that changes in signal on a time scale $\ll 100$ μs will be heavily filtered.

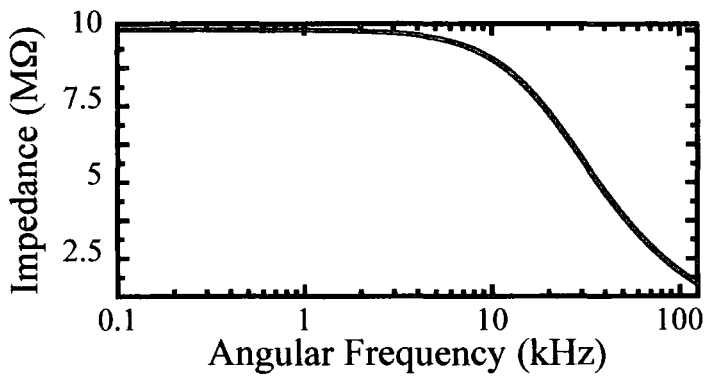

Figure 6.4: The output voltage of the photodiode circuit is directly proportional to the output impedance. The calculated output impedance of the photodiode circuit as a function of angular frequency is shown above, for $R = 10$ MΩ and $C = 4.7$ pF.

6.2 Sagnac Interferometer Experimental Results

6.2.1 Beam Profiles

The profile of the pump and probe beams has a direct affect upon the line shape and width of the EIT features, [68]. In order to determine the beam profiles the Rb cell was removed from the interferometer and replaced with a 0.25 mm wide slit. The slit was mounted on a micrometer-driven translation stage, allowing the slit to be translated perpendicular to the direction of propagation of the beams. After the beam has passed through the slit it is focussed onto a photodiode. The signal recorded on the photodiode is plotted against the position of the centre of the slit. Typical data for both clockwise and anticlockwise beams

are shown in Fig. 6.5. Both pump and probe beams have circularly-symmetric

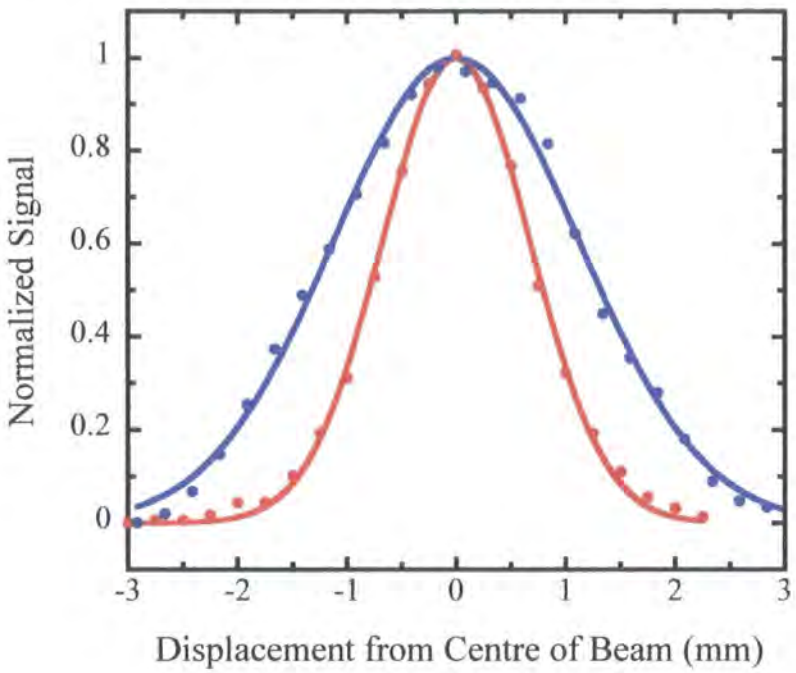

Figure 6.5: The red plots show a typical beam profile for the clockwise beams: experimental measurements (circles) and Gaussian fit (line) with a 1/e full-width of (1.890 ± 0.007) mm. The blue plots show a typical beam profile for the anticlockwise beams: experimental measurements (circles) and Gaussian fit (line) with a 1/e full-width of (3.177 ± 0.003) mm.

Gaussian profiles, as expected from the circular core of the optical fibre, [106], in agreement with perpendicular sets of beam profile measurements. The anticlockwise beams travel a distance of 2.2 m from the output of the optical fibre to the slit, whereas the clockwise beams propagate 0.7 m from the fibre output to the slit. The clockwise pump and probe fields have a 1/e full-width of 1.890 ± 0.007 mm. The anticlockwise probe beam has a 1/e full-width of 3.177 ± 0.003 mm. The difference in beam size is as expected due to the different path lengths of the two beams around the interferometer to the point where the beam profile was measured.

6.3 Double Scan

As in the work presented in § 4.2, both the pump and probe beams are derived from the same Extended Cavity Diode Laser (ECDL) and double-pass through separate Acousto-Optic Modulators. The pump and probe have orhtogonal-circular polarizations. The ECDL is scanned about $\delta_{\text{pu}} = 0$ and the probe AOM is scanned about $\delta_{\text{pr}} - \delta_{\text{pu}} = 0$, Fig. 4.14 on page 91. Fig. 4.15 on page 92(i) shows the control voltages to the ECDL piezo and the probe VCO. Fig. 4.15 on page 92(ii) shows the plot of $(\delta_{\text{pr}} - \delta_{\text{pu}})/2\pi$ against $\delta_{\text{pu}}/2\pi$. The

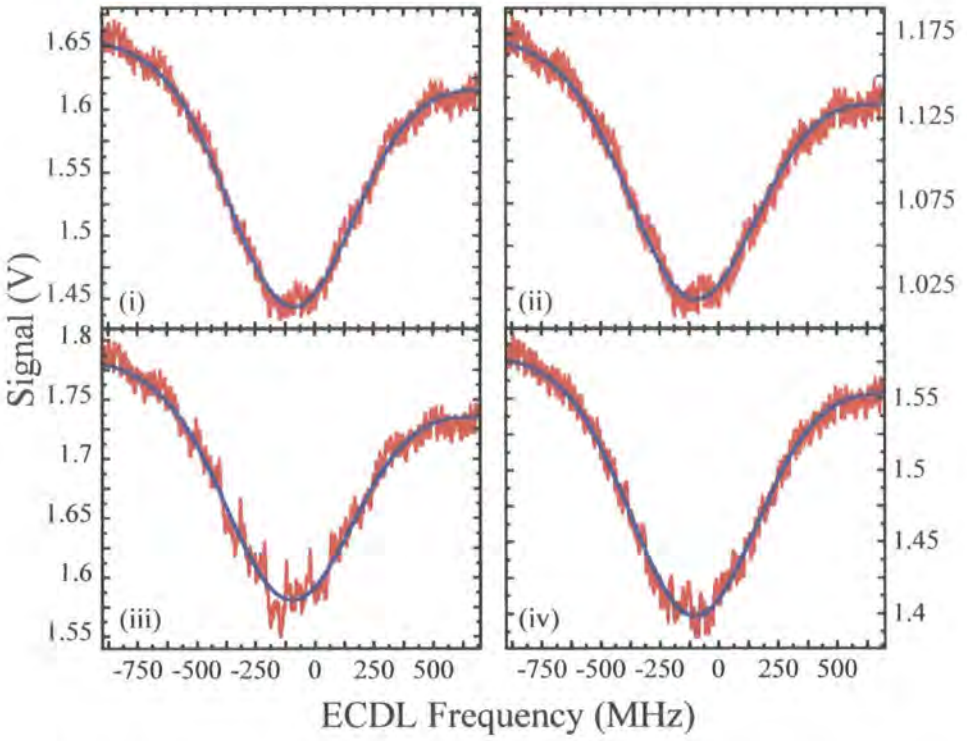

Figure 6.6: (i) and (ii) are the probe-only output signals of arm A and B respectively. (iii) and (iv) are the probe-and-pump output signals of arms A and B respectively. The plots show both the raw photodiode signals (red) and a Gaussian fit to the signal (blue). The power of the clockwise pump and probe beams are 26 μW and 4.2 μW.

interferometer outputs are plotted in Fig. 6.6, along with Gaussian least-square

fits of the form,

$$A\nu + B - Ce^{-\left(\frac{\nu-\nu_0}{w}\right)^2} . \tag{6.1}$$

A and B provide the fit to the off resonance transmission background. A is the gradient of the linear offset, B is the zero frequency offset, C is the amplitude of the Gaussian absorption, ν is the frequency of the light, ν_0 is the frequency of the centre of the Gaussian and w is the $1/e$ full-width of the Gaussian. The Gaussian fit is subtracted from the photodiode signal for each of the four traces shown in Fig. 6.6 on the previous page. The probe-only signal is subtracted from the pump-and-probe signal, the resulting traces show only the non-linear features, with the Gaussian backgrounds subtracted, see Fig. 6.7 on the following page.

The signals are normalized by dividing them by the off-resonancee probe-only sum signal. For the purpose of this normalization the off-resonance signal is taken to be $A\nu_0 + B$ minus the recorded signal for both pump and probe beams blocked.

Summing the normalized signal for arm A and arm B leads to the signal proportional to the absorption. This is shown in Fig. 6.7(i). The difference signal between arms A and B is shown in Fig. 6.7(ii) . This is proportional to the dispersion.

The double-scanning technique leads to m EIT features occurring within the range of the Doppler-broadened transition, Fig. 6.7 on the next page. The frequency scale of such a plot is not straight forward since the centres of the different EIT features are separated by a frequency given by the ECDL scan, δ_{pu}, whilst the width of the individual features is determined by the AOM scan, $(\delta_{\mathrm{pr}} - \delta_{\mathrm{pu}})$.

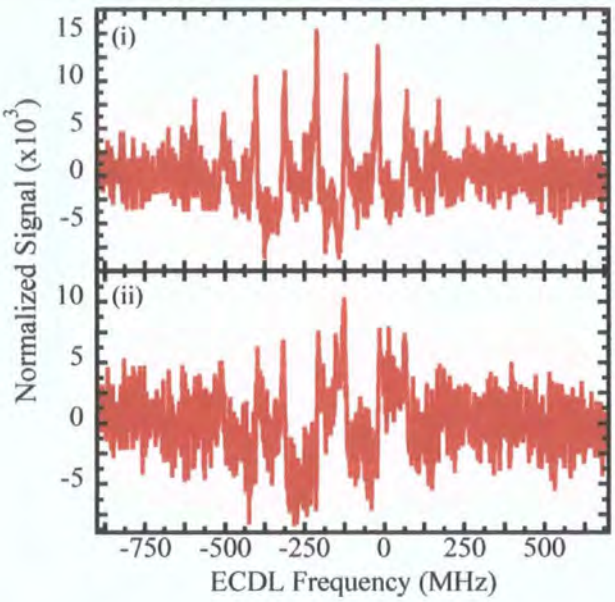

Figure 6.7: Difference between pump-and-probe and probe-only signals with the Gaussian fits subtracted, for output arm A, (i), and output arm B (ii). The residual signals plotted above show the modification in the two output arms due to the two-photon resonance condition being met.

As can be seen in Fig. 6.8, there is still a residual background. In order to be able to characterize the variation of amplitude of EIT feature with single-photon detuning, this background has to be removed. This is done by fitting a Gaussian envelope to the off-two-photon resonance background, Fig. 6.9(i). This fit is subtracted from the signal and a Gaussian function can then be fitted to the amplitudes of the EIT features, Fig. 6.9(ii).

Scanning two counter-propagating beams at the same frequency across the Doppler-broadened resonance leads to the occurrence of saturation spectroscopy resonances, [27, 37]. The features most prominent in Fig. 6.9(ii) occur at frequencies of approximately 0 MHz, -80 MHz and -160 MHz, corresponding to $F = 1 \rightarrow F' = 2$, $F = 1 \rightarrow F' = 1, 2$ cross-over resonance, and $F = 1 \rightarrow F' = 1$ respectively.

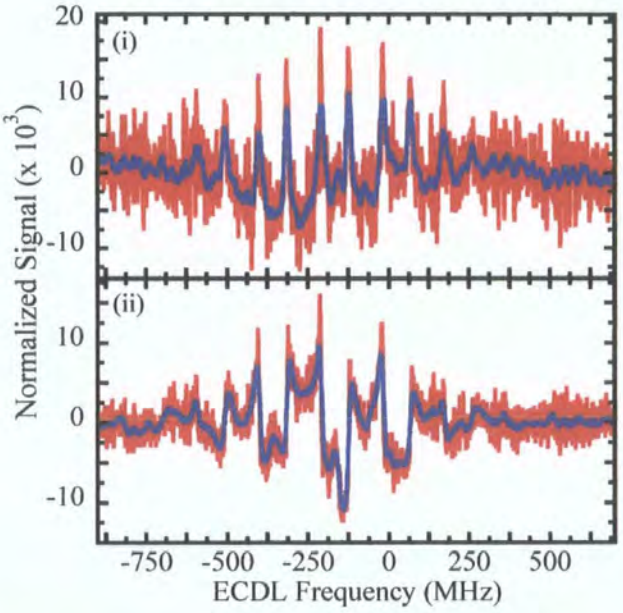

Figure 6.8: (i) Sum of arm A and arm B signals as presented in Fig. 6.7. This shows the array of EIT transmission signals due to the two-photon resonance condition being met at a number of different single-photon detunings. (ii) Difference between arm A and arm B signals as presented in Fig. 6.7. This plot shows the array of dispersive features due to the EIT two-resonance condition being met at a number of different single-photon detunings. The unsmoothed data is shown (red) along with a twenty-point moving average (blue). The twenty-point moving average involves taking the mean of twenty consecutive data points and plotting this mean value at the centre frequency of the set of twenty data points.

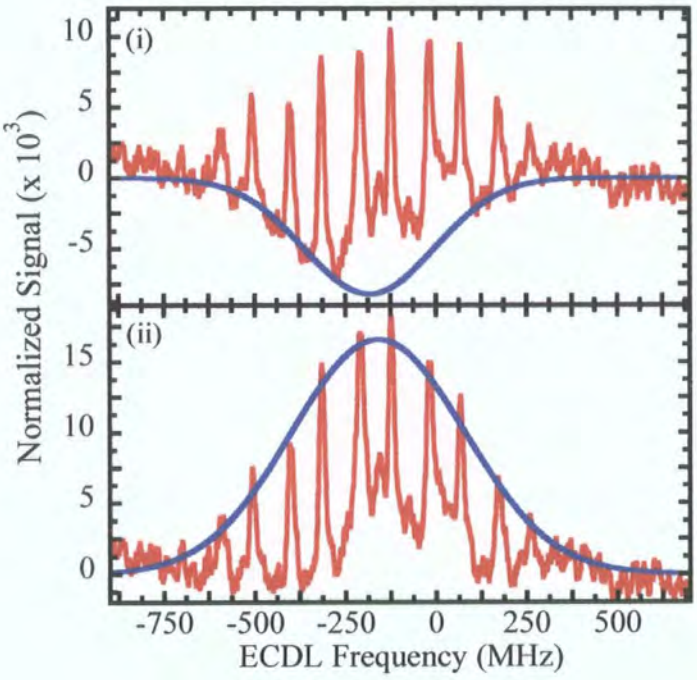

Figure 6.9: (i) moving average of the sum signal from Fig. 6.8(i) (red), with a least square Gaussian fit to the background (blue). (ii) Sum signal data minus the Gaussian fit to the background (red) is shown with a Gaussian fit to the amplitude of the EIT transmission features (blue). This is to show that the variation in amplitude of the EIT features as a function of single-photon detuning, can be represented by a single Gaussian function, with width of the same order as the Doppler-broadened resonance.

The amplitude of the EIT signals are determined by a Gaussian envelope of FWHM 560 MHz, this compares to the FWHM of 620 MHz of the Gaussian fit to the Doppler-broadened resonance. The uncertainty on the fit to the peaks of the transmission signals is likely to be far higher than the uncertainty on the fit to the Doppler-broadened resonances. While it is expected that the two Gaussians would be similar it is not the case that they should be the same. The Doppler-broadened absorption is the sum of three Gaussians, § 2.4 on page 25, each of which corresponds to a different hyperfine transition, which in turn will contribute a different amount to the EIT signals, though exactly to what extent this is the case is beyond the scope of this PhD.

For the intensities of the fields used in this case the maximum amplitude of the transmission EIT signals is 2% of the transmitted light.

6.4 Single Scan

In order to characterize both the transmission and dispersion of the EIT feature, the ECDL was tuned to the frequency at which the amplitude of the EIT features is at its maximum, between -100 and -200 MHz in Fig. 6.9. The probe alone was then scanned across the two-photon resonance. The signals from the two output arms, A and B, were recorded, both with and without the pump field. Plots of the two individual arms of a typical signal can be seen in Fig. 6.10(i) arm A and (ii) arm B, both with (red) and without pump beams (blue).

The frequency scale of Fig. 6.10 (and of subsequent spectra shown in this chapter) is given by $(\delta_{\mathrm{pr}} - \delta_{\mathrm{pu}})/2\pi$, the detuning of the probe beam from the two-photon resonance. Note the presence of the beat note in the pump-and-probe traces at $\approx$ 1.6 MHz. The traces shown in Fig. 6.10, all have arbitrary DC offsets. The DC offsets are provided using the DC Bias Boxes Fig. 6.11 and Fig. 6.12. The bias boxes allow for a DC offset of between ± 9 V to be added to the photodiode signal. This allows the voltage scale on the oscilloscope to be set to maximise the resolution of the EIT signals, whilst still being able to record all of the data of interest. For each data set recorded with the arbitrary DC offset, scans across the full Doppler-broadened transitions were also recorded so

that the data could be normalized if required.

The probe-only signal is subtracted from the pump-and-probe signal. The resulting traces are shown in Fig. 6.13 (i) and (ii), arms A and B respectively. Along with the EIT traces from the two output arms (red), are linear least square fits to the off-resonant background signal (blue). The linear fit is subtracted from the EIT signal in each case, and the remaining signal is normalized, in the same way as in § 6.3 on page 128. The resulting normalized traces for arms A and B are plotted in Fig. 6.13 (iii) and (iv) respectively.

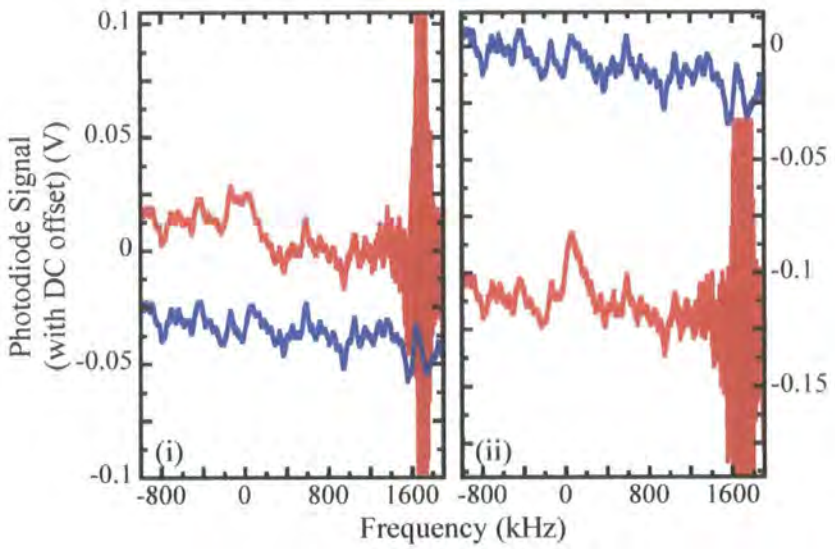

Figure 6.10: (i) and (ii) show the raw probe-only (blue) and raw probe-with-pump (red) signals, for output arms A and B respectively. The clockwise pump and probe powers are 28 μW and 3 μW, respectively.

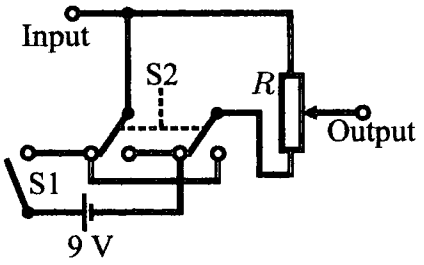

Figure 6.11: Switch S1 turns the DC bias on or off. Switch S2 can be in either of two positions, position 1 (as shown in the figure) or position 2. This determines whether the bias is positive or negative, Fig. 6.12. R is a 5 kΩ potentiometer, adjusting this potentiometer varies the magnitude of the DC offset from 0 V to 9 V.

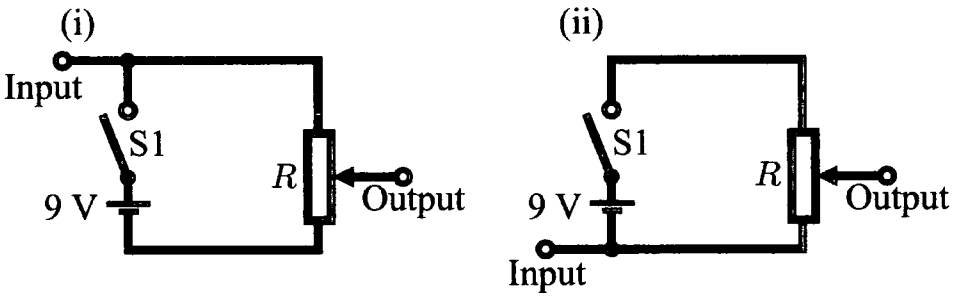

Figure 6.12: (i) Switch S2 in position 1 as shown in Fig. 6.11 gives a negative DC offset. (ii) Switch S2 in position 2, leading to a positive DC offset on the output.

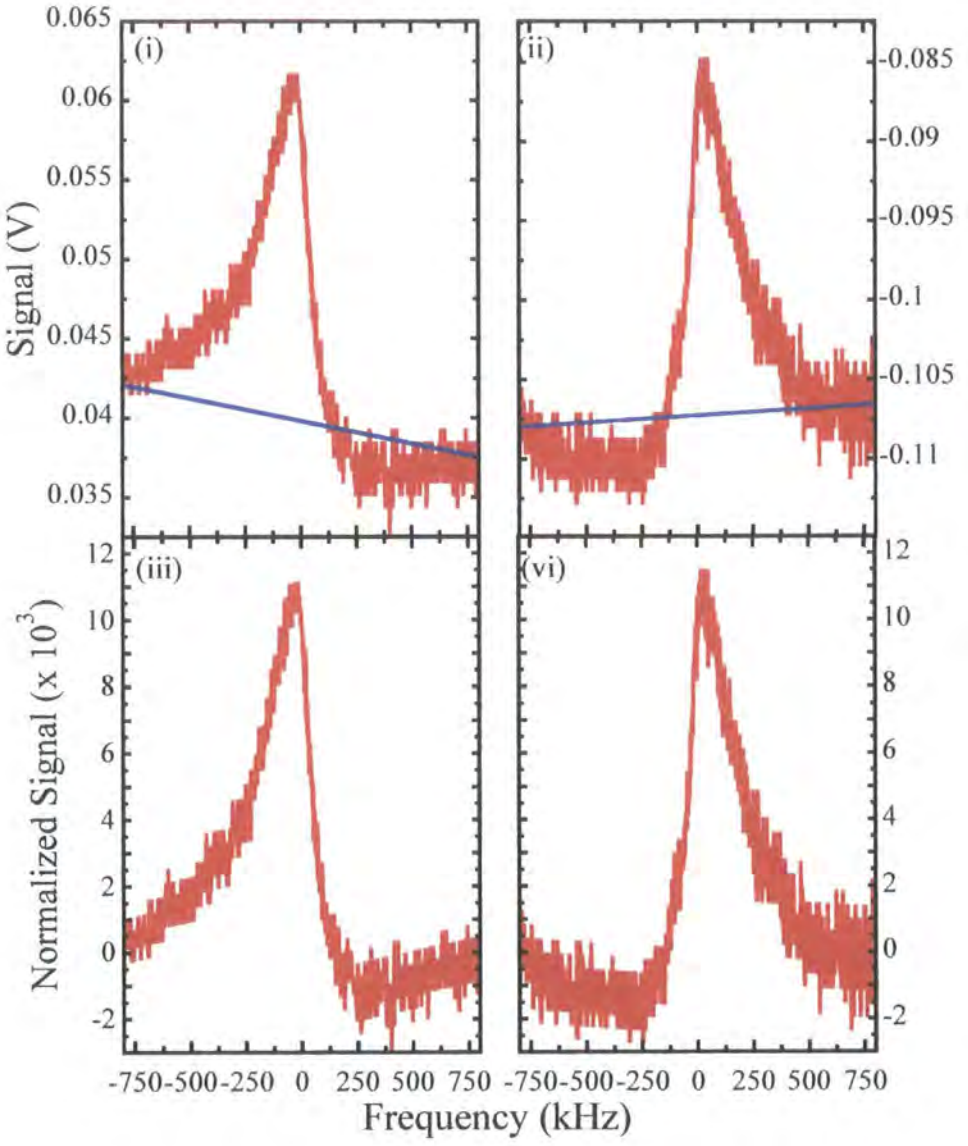

Figure 6.13: (i) and (ii) show the difference between the pump-and-probe and probe-only signals (red) along with a linear fit to the background (blue), for output arms A and B respectively. (iii) and (iv) show the normalized traces for arms A and B respectively.

The two normalized traces of Fig. 6.13 (iii) and (iv) are summed to give the signal proportional to the EIT transmission signal, Fig. 6.14(i). The difference signal, proportional to the difference in refractive index between the two arms, and hence proportional to the dispersion due to the EIT resonance, is plotted in Fig. 6.14(ii).

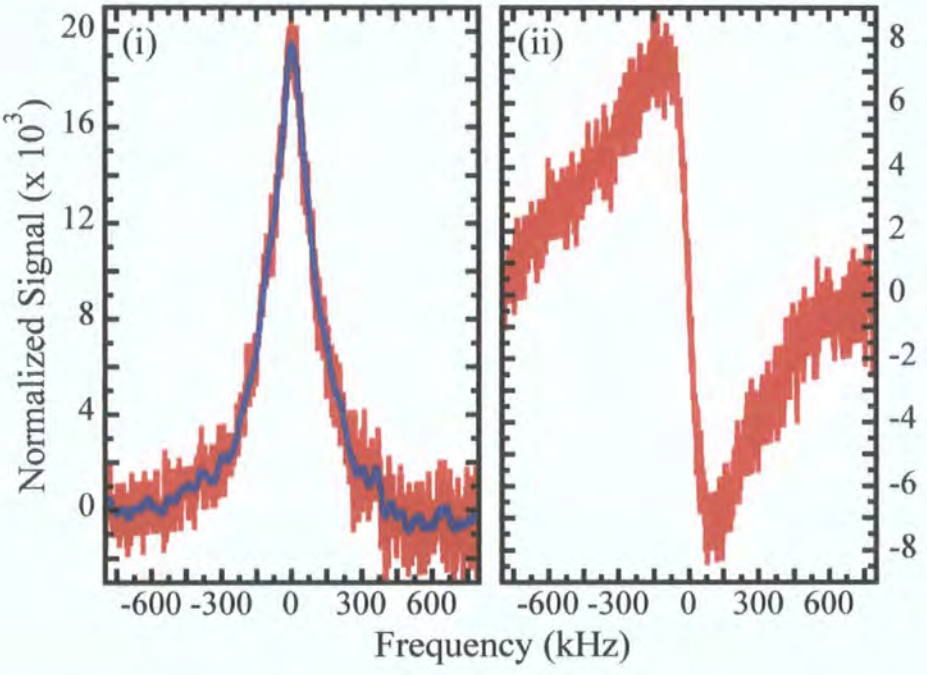

Figure 6.14: (i) Sum signal of output arms A and B, with (blue) and without (red) twenty-point running average, showing a typical EIT transmission signal. (ii) Difference signal between output arms A and B, showing a signal proportional to the dispersion of the medium around the EIT two-photon resonance.

6.5 Sagnac Interferometer Output Beam Alignment

With the counter-propagating arms of the Sagnac interferometer aligned as described at the beginning of this chapter, in the "biased" alignment, no aperturing of the output beams leads to a difference signal as shown in Fig. 6.15.

Fig. 6.16 shows the difference signals for the aperture positions shown in Fig. 6.17,

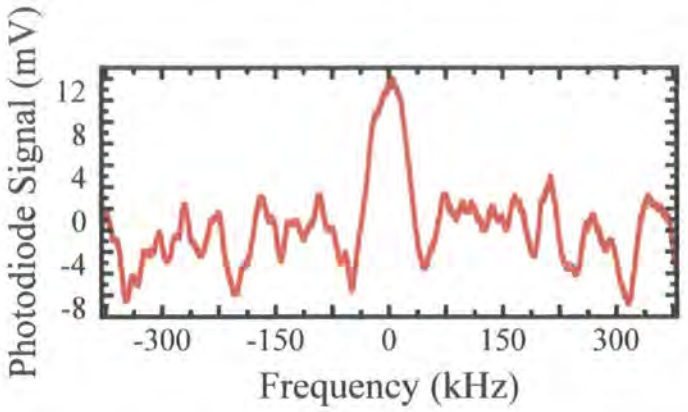

Figure 6.15: Difference signal recorded for no slits in the output arm fringe patterns. The clockwise probe power is 3 μW and the pump power is 10 μW. As is clearly shown in the figure, the spectrum in the absence of the output arm apertures is not of the form of a dispersion spectrum.

(i) and (ii) have the aperture positions in each of the two output arms being on the same side of the beams, while (iii) and (iv) have the apertures on opposite sides of the output beams.

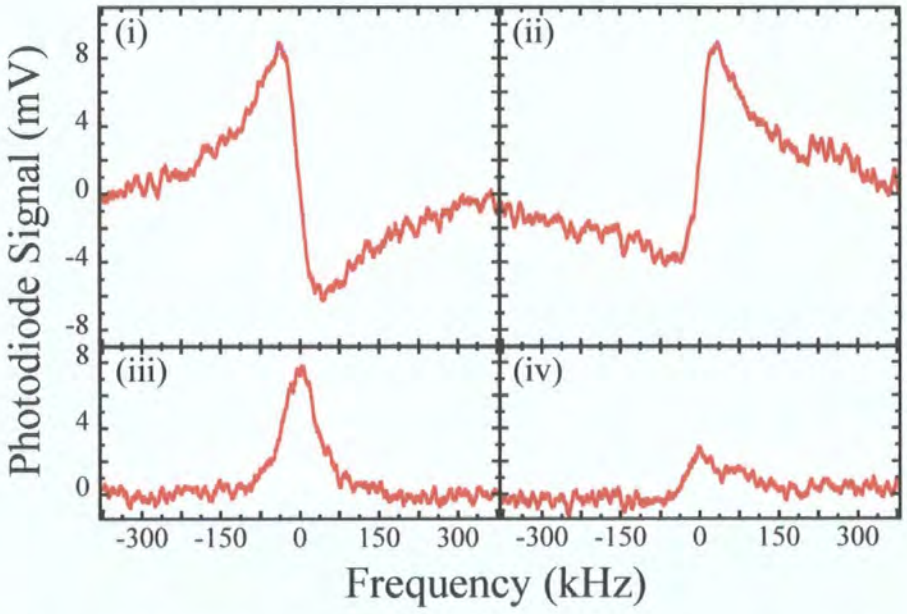

Figure 6.16: (i) Standard aperture position. (ii) Both slits on the opposite side of beams. (i) and (ii) show that provided both slits are set to the correct width and that they are both on the same sides of the two beams, a signal proportional to the dispersion of the medium will be obtained. (iii) Slit A on standard side of beam, slit B on opposite side of beam. (iv) Slit A on opposite side of beam, slit B on standard side of beam. (iii) and (iv) show that if the slits are on opposite sides of the two different beams, the signals will not be proportional to the dispersion. The clockwise probe and pump powers are 2 μW and 10 μW.

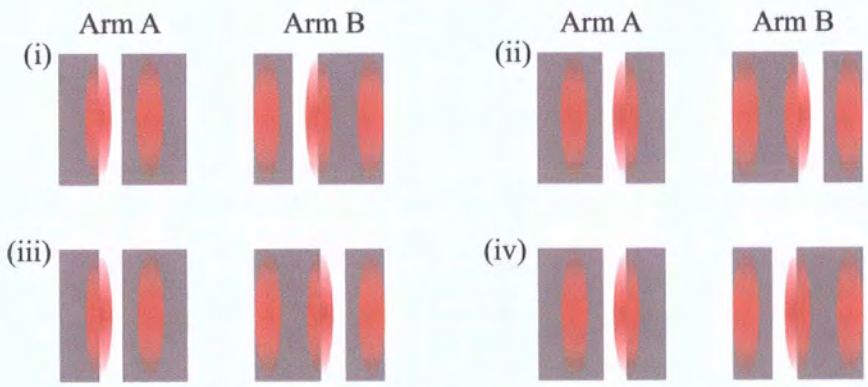

Figure 6.17: The aperture positions shown in this figure are those used to record the traces in Fig. 6.16. Each of the four different combinations shown in this figure corresponds to the same plot in Fig. 6.16.

6.6 EIT Line Width

Details of theoretical line shapes are given in chapter 3. If the signals are

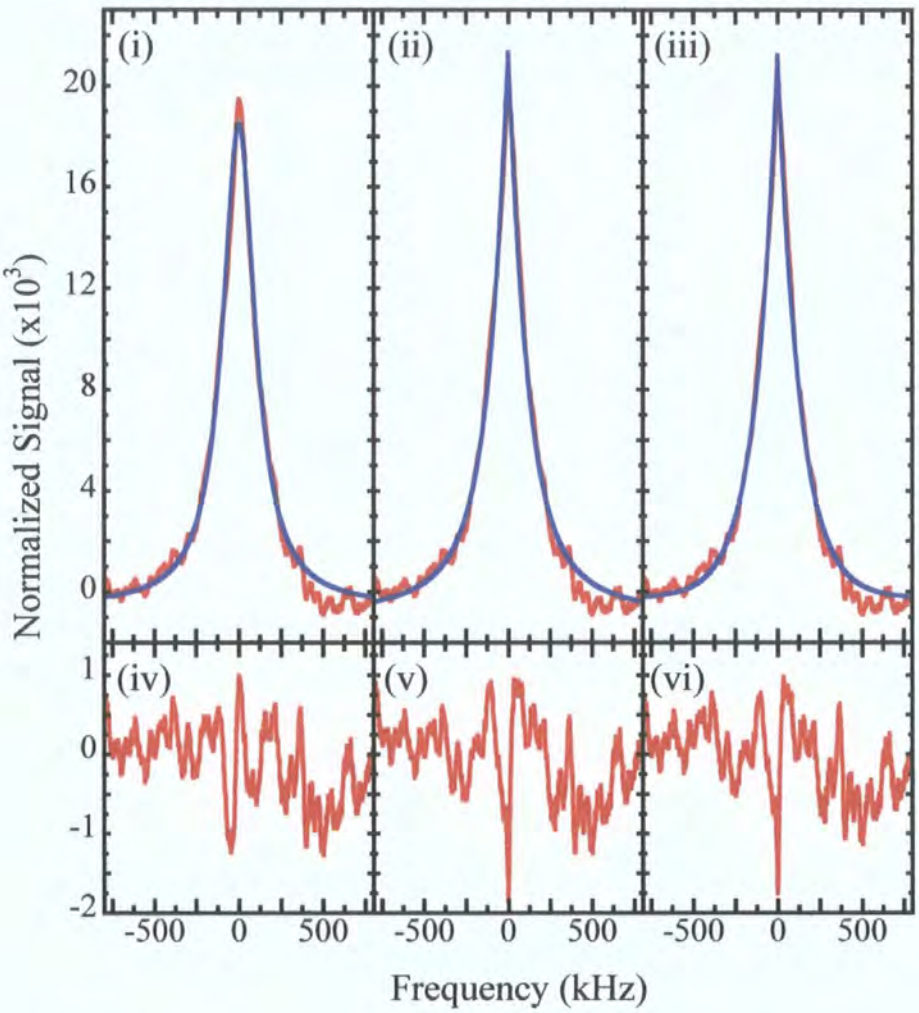

Figure 6.18: This figure compares three different predicted line shapes to the measured EIT transmission signals. In (i), (ii) and (iii), the experimental data is plotted (red), with the theoretical line shape fit (blue). (i) Lorentzian fit; (ii) arctan fit; and (iii) cusp fit. (iv) Experimental data minus Lorentzian fit; (v) experimental data minus arctan fit; and (vi) experimental data minus cusp fit. The clockwise probe power is 3 μW and the pump power is 28 μW.

power broadened, the beam profile affects the line shape and width of the resonance, [68]: a step-like beam profile leads to a Lorentzian line shape and a Gaus-

sian beam profile to an arctan line shape. The cusp function gives the expected line shape for transit-time dominated broadening, [66], and is virtually indistinguishable from the arctan fit, [68]. Fig. 6.18(i), (ii) and (iii) all show the twenty-point moving average transmission EIT feature with weighted least square fits of the Lorentzian, arctan and cusp functions respectively. Fig. 6.18(iv), (v), and (vi) show the residual signal — data minus theoretical fit — for Lorentzian, arctan and cusp functions respectively. It can be seen that away from the centre of the two-photon resonance (detuning greater than ±200 kHz), the residuals are essentially the same for the three different fits. Only in the central region (detuning less than ±200 kHz) is there any significant difference between any of the residual traces. The arctan and cusp fits are very similar. Either side of the centre of the resonance, the amplitude of the experimental line shape is larger than that of the fit, but on the centre of the resonance (detuning less than ±50 kHz), the fit value exceeds the data by approximately 10%. The Lorentzian fit has a higher value than the data either side of the resonance, but in the region around the centre of the resonance (detuning less than ±30 kHz), the fit is approximately 5% less than the experimental data.

The reduced χ^2 values for each of the three functions suggest that none of the models truly fit the data. Across the two-photon detuning of −300 kHz to +300 kHz the reduced χ^2 values are 5.59, 9.26, and 5.63, for Lorentzian, arctan, and cusp fits respectively. Over the wider detuning of ±900 kHz, the reduced χ^2 values are 6.29, 7.15, and 5.74. Hence away from resonance the cusp fit gives the better fit whilst in the region of the resonance the Lorentzian fit is marginally the best fit. Were any of the functions an accurate fit, then a reduced χ^2 value of between one and two would be expected. In order to quantify the FWHM and amplitude of the EIT resonances for different pump and probe powers, the Lorentzian model was used. Rather than fitting the Lorentzian to the sum signal, the Lorentzian dispersion is fitted to the difference signal between the two arms. The Lorentzian dispersion line shape takes the form of equation 3.80 on page 70,

$$n_{\mathrm{R}} - 1 = -\frac{N\mathrm{d}_{\mathrm{ba}}^2}{2\epsilon_0\hbar} \cdot \frac{\delta_{\mathrm{pr}} - \delta_{\mathrm{pu}}}{(\delta_{\mathrm{pr}} - \delta_{\mathrm{pu}})^2 + (\Gamma_{\mathrm{a}}/2)^2} \cdot$$

6.6.1 EIT Line Shape Dependance on Pump and Probe Power

EIT resonance spectra are recorded for three different regimes of pump and probe power, P_{pu} and P_{pr} respectively.

- P_{pr} fixed and P_{pu} varied in the region, $2P_{pr} \lesssim P_{pu} \lesssim 20P_{pr}$.
- P_{pu} fixed and P_{pr} varied in the region, $P_{pu}/40 \lesssim P_{pr} \lesssim 0.8P_{pu}$.
- $P_{pr} = P_{pu}$, and both are varied.

Dependence on Pump Power

Variation in amplitude and FWHM of the two-photon EIT resonance, with increasing pump beam power, is plotted in Fig. 6.19(i) and (ii) respectively. The amplitude of the features increases with pump power until it starts to

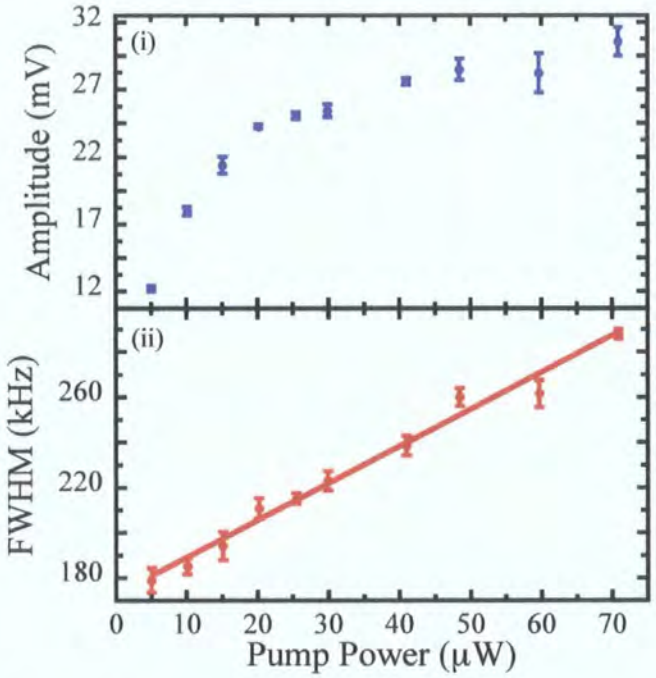

Figure 6.19: (i) Plot of the amplitude of the EIT features as a function of pump power. (ii) Plot of the FWHM of a Lorentzian dispersion fit to the difference signal for a range of pump powers. The probe power is 4 μW.

saturate at around 20 μW, Fig. 6.19(i).

Reducing the intensity of the pump reduces the width of the resonances, as can be seen in Fig. 6.19(ii). Extrapolating the linear fit of Fig. 6.19(ii), shows that reducing the pump power to zero will lead to a FWHM of 170 kHz, where the probe power is 4 μW.

Dependence on Probe Power

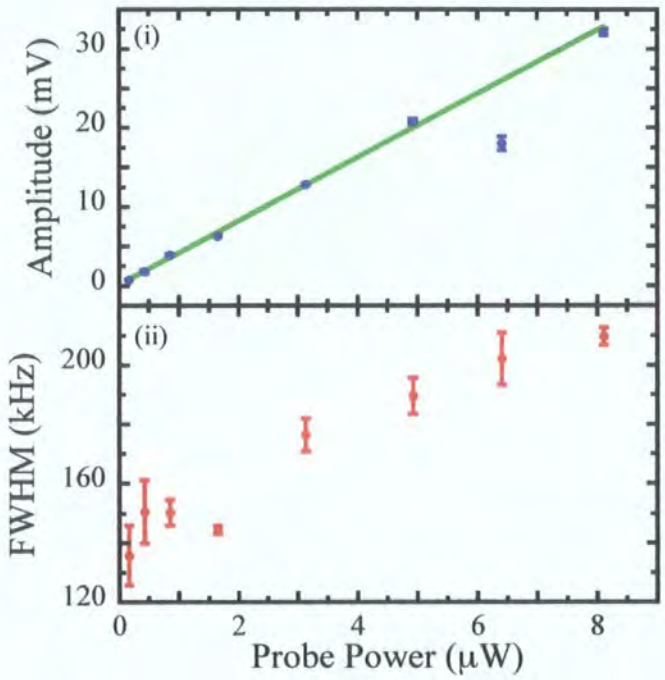

Figure 6.20: (i) Plot of the amplitude of the EIT signal against probe power. (ii) Plot of the FWHM of a Lorentzian dispersion fit to the difference signal for a range of pump powers. The pump power is 10 μW.

Fig. 6.20(i) shows that the amplitude of the EIT signal increases linearly with probe power (with a constant offset). This is to be expected in the case that the probe does not effect the amplitude of the absorption coefficient. The linear increase in the measured amplitude is due to the linear increase in the power of the incident beam. There is one notable exception, the data point at $\simeq 6.5$ μW falls noticeably below the linear line of best fit. The most likely explanation for this is that the detuning of the pump beam, δ_{pu}, had drifted from the centre of the Doppler-broadened resonance. This would result in a reduction of the EIT resonance amplitude, (Fig. 6.9 on page 132).

Fig. 6.20(ii) shows the variation of FWHM of the EIT features with probe power. As can be seen the width of the resonance increases approximately linearly with probe power hence this data is not in the regime of a weak probe. In the weak probe regime the probe power would not effect the EIT resonance. This is to be expected, as with a pump power of 10 μW, the probe powers of $\sim$ 1 μW to 8 μW are a significant fraction of the pump power, and as such can not be described as being in the weak probe regime.

Dependence on Simultaneous Variation of Probe & Pump Power

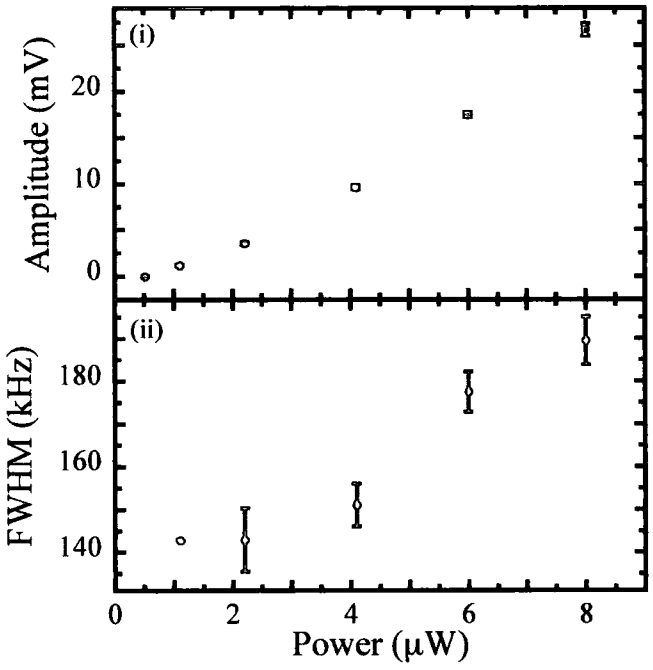

Figure 6.21: (i) Plots of amplitude of EIT signals against the beam power. (ii) Plots of the FWHM of the EIT resonances against the beam power.

By definition when the pump power is equal to the probe power, the weak probe regime cannot apply.

Fig. 6.21(i) shows that the amplitude of the feature increases at a rate greater than linear. There will be two mechanisms leading to the increase in amplitude. Increasing probe power will lead to a linear increase in amplitude, as seen in Fig. 6.20(i) . Secondly increasing pump power will lead to an increase in the

transmission of the medium, Fig. 6.19(i). As the probe and pump power are equal then both will contribute equally to the "pumping" of the medium.

Fig. 6.21(ii) shows the variation in FWHM with beam power. It is apparent that the data point corresponding to a beam power of $\simeq 0.5$ μW is not plotted. This is due to the fact that the signal to noise ratio was such that whilst the amplitude could be fitted to an acceptable degree of precision, the FWHM could not. The data suggests that the increase in FWHM is at an order greater than linear.

6.6.2 Comparison of EIT Lineshape to Theory

For the system under investigation, ^{87}Rb 5 $^2S_{1/2}$ $F = 1 \rightarrow 5$ $^2P_{3/2}$ $F' = 0, 1, 2$, the Doppler-broadened resonances have a significant overlap, Fig. 2.4 on page 28 . Thus it is not possible to consider the experimental EIT resonances as being due to a single Λ system. The resonances are due to three different Λ systems, with the lower states $|F = 1;\ m_F = \pm 1\rangle$ and excited states, $|F' = 0, 1, 2;\ m_{F'} = 0\rangle$.

The single photon transitions in each of the three Λ systems have different transition strengths. Thus for the same beam intensities the Rabi frequencies differ by the ratio of the square root of the transition strengths, the ratio of the dipole matrix elements. The dipole matrix element ratio is $2 : \sqrt{5} : 1$, for $F' = 0, 1, 2$ respectively[2], [32]. Across the full range of the Doppler-broadened resonance, the amplitude of the contribution of each different Λ system varies with frequency due to the frequency separation between the excited hyperfine states and due to the Rabi frequency varying with detuning.

Thus it is not trivial to account for the line widths of the measured EIT resonances using the theoretical models presented in chapter 3 .

Magnetic Broadening

An axial magnetic field of $\simeq 1$ G is applied to shift the EIT resonances away from the beat note. This field will lead to broadening of the EIT resonance as

[2]On this scale the closed transition, $|F = 2;\ m_F = +2\rangle \rightarrow |F' = 3;\ m_{F'} = +3\rangle$ has a transition strength of $2\sqrt{3}$.

the field is not constant along the length of the vapour cell. From § 4.3.4 on page 102, the broadening of the resonances can be approximated by $\simeq$ 3 kHz G^{-1}.

Hence the contribution, of magnetic broadening, to the width of the EIT resonances presented in this chapter will be $\simeq$ 3 kHz.

Transit Time

The cusp line shape predicted for transit time broadening only applies in the regime where the pump and probe power do not contribute to the broadening of the resonance, § 3.5.4 on page 62. As can clearly be seen from Figs. 6.19, 6.20 and 6.21 , the pump and probe powers do contribute to the width of the resonances. Hence the expected line shape is not that predicted in § 3.5.4 .

However it will still be instructive to consider the contribution of transit time broadening to the measured line widths. From equation 3.51 ,

$$\Gamma_{\mathrm{EIT}} = \frac{\sqrt{2}\ln 2\ \mathrm{v}}{r} .$$

r being the intensity 1/e beam radius, and v the velocity given by equation 3.52 on page 63 . Thus $\Gamma_{\mathrm{EIT}} = 39.1 \times 2\pi$ kHz, at room temperature, 293 K, for ^{87}Rb.

Beam Profile

In order for the line shape to be determined by the pump and probe beam profiles, the relaxation rate of the atoms, Γ_{L}, must be much less than the inverse of the transit time of the atoms through the beam, equation 3.55 .

However the relaxation rate of the atoms is limited by the transit time of the atoms though the cell. The transit time through the cell is not significantly greater than the transit time of the atoms through the beams. Hence the measurements presented in this chapter do not fall into the regime where the beam profile determines the line shape.

Doppler-Broadened Limit

In the case that a single-photon resonance is Doppler broadened, it follows that an EIT resonance can be narrowed by the same Doppler-broadening mechanism,

§ 3.5.6 on page 65.

In the presence of Doppler broadening, the FWHM of the EIT resonance, $\Gamma_{\rm EIT}$, is given by equation 3.68 on page 65,

$$\Gamma_{\rm EIT}^2 = \frac{\gamma_{\rm cb}\Omega_{\rm pu}^2}{\Gamma_{\rm a}} \cdot (1+x)\left(1+\sqrt{1+\frac{4x}{(1+x)^2}}\right) .$$

x is the dimensionless variable given by equation 3.69 on page 65 ,

$$x = \frac{\Gamma_{\rm a}}{2\gamma_{\rm cb}} \cdot \left(\frac{\Omega_{\rm pu}}{W_{\rm D}}\right)^2 .$$

The Doppler-broadened width can be taken from table 2.2 on page 37 , hence, $W_{\rm D} = 570 \times 2\pi$ MHz and $\Gamma_{\rm a} = 6.065 \times 2\pi$ MHz.

The ground state coherence decay rate could be limited by any of the following three mechanisms:

- collisions of atoms with cell walls;
- collisions of atoms with other atoms;
- and atoms leaving the beam.

As the cell diameter is ~ 10 times larger than the beam diameter, and the cell length is 4 times the cell diameter, then the rate at which atoms will leave the beams will dominate over the rate at which they collide with cell walls.

The mean free path of the atoms, l, is the mean distance they travel between collisions with other atoms. This is given by,

$$l = \frac{1}{\sigma N} , \tag{6.2}$$

N is the total number density, and σ is the cross section for Rb—Rb collisions. At room temperature (293 K), $N = 5.65 \times 10^{15}$ m^{-3}, equation 2.101 , and $\sigma \simeq 2 \times 10^{-18}$ m^{-2}, [107], hence the mean free path, $l \simeq 90$ m. As l is ~ 5000 times larger than the diameter of the the cell, this will not limit $\gamma_{\rm cb}$.

Thus the dominant mechanism in determining the ground state coherence decay rate, $\gamma_{\rm cb}$ is transit time of the atoms through the beam. Hence,

$$\gamma_{\rm cb} \simeq \frac{\rm r}{\rm v} , \tag{6.3}$$

$$\text{where} \quad {\rm v} = \sqrt{\frac{2{\rm k_B}T}{m}} .$$

Thus, $\gamma_{cb} = 39.6 \times 2\pi$ kHz at room temperature, 293 K, and with the beam diameter 1.89 mm, from § 6.2.1 .

The Rabi frequencies for the three different transitions, $\Omega_{F'=0}$, $\Omega_{F'=1}$, and $\Omega_{F'=2}$ are given by,

$$\Omega_{F'=0} = \frac{1}{\sqrt{3}} \cdot \Omega \,, \tag{6.4}$$

$$\Omega_{F'=1} = \sqrt{\frac{5}{12}} \cdot \Omega \,, \tag{6.5}$$

$$\Omega_{F'=2} = \frac{1}{\sqrt{12}} \cdot \Omega \,, \tag{6.6}$$

where Ω is the Rabi frequency for the closed transition on the ^{87}Rb D_2 line, given by equation 2.59 on page 19,

$$\Omega = \frac{\Gamma_a}{\sqrt{2}} \cdot \sqrt{\frac{I}{I_{SAT}}} \,.$$

In order to make predictions of Γ_{EIT} the intensity, I, is taken to be the mean intensity over an area encompassing a fraction Z of the power, P, in the beam, § H.2. Therefore the intensity is taken to be, $\overline{I}_Z$ by equation H.16,

$$\overline{I}_Z = \frac{Z\,P}{\pi r_0^2 \,\ln\left|\frac{1}{1-Z}\right|} \,,$$

where r_0 is the 1/e intensity radius.

With all of the above it is now possible to calculate Γ_{EIT} for the three different Λ systems. Plots of Γ_{EIT} against pump power up to 100 μW are shown in Fig. 6.22, where Z is taken to be 0.95.

In the case of the regime shown in Fig. 6.22, where $x \ll 1$, the width of the EIT resonance can be well approximated by equation 3.73 on page 66,

$$\Gamma_{EIT} = \Omega\sqrt{\frac{\gamma_{cb}}{\Gamma_a}} \,.$$

As γ_{cb} and Ω can only be approximated then there is scope for a systematic error in the predictions presented in Fig. 6.22 .

Resultant Line Width

The development of a theoretical model, accurately taking account of all broadening mechanisms and optical pumping, is beyond the scope of this experimental

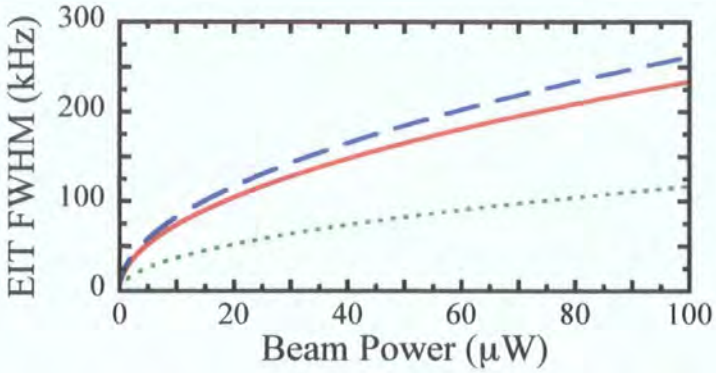

Figure 6.22: The solid red line shows the prediction for the Λ system with upper state $|F' = 0, m_{F'} = 0\rangle$, the dashed blue line shows the prediction for the Λ system with upper state $|F' = 1, m_{F'} = 0\rangle$, and the dotted green line shows the prediction for the Λ system with upper state $|F' = 2, m_{F'} = 0\rangle$.

thesis. In order to make an approximation to the resultant expected line width, due to the contributions of all of the broadening mechanisms presented so far, the widths due to each contribution have been summed[3]. Here the probe beam is assumed to make the same contribution to the width that a pump beam of the same power would.

The resultant widths are plotted in Fig. 6.23 alongside the experimental measurements for a constant probe power (of 4 μW) and varying pump, as plotted in Fig. 6.19 .

The theoretical curves underestimate the extent of the broadening for pump powers up to $\sim$ 20 μW. For pump powers in the range of $\sim$ 20 μW to $\sim$ 80 μW the rate of change of width and the absolute values appear to be in good agreement with the theoretical values.

A potential explanation for the discrepancy in theoretical and experimental line widths up to pump powers of $\sim$ 20 μW would be that the constant contributions to the line width have been underestimated. In order for this to be the case and yet still to have agreement at higher pump powers, it would follow that the rate of increase in width attributable to the pump power has been overestimated.

Further experiments varying the beam diameters would be instructive in re-

[3]The convolution of two Lorentzian functions of width Γ_1 and Γ_2 is a Lorentzian function of width $\Gamma_3 = \Gamma_1 + \Gamma_2$.

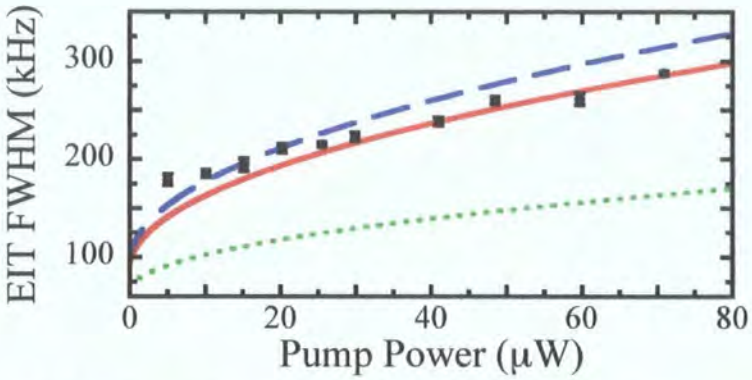

Figure 6.23: The solid red line shows the prediction for the Λ system with upper state $|F' = 0, m_{F'} = 0\rangle$, the dashed blue line shows the prediction for the Λ system with upper state $|F' = 1, m_{F'} = 0\rangle$, and the dotted green line shows the prediction for the Λ system with upper state $|F' = 2, m_{F'} = 0\rangle$. The pump broadening is taken to be that shown in Fig. 6.22. The probe, magnetic and transit time broadening contributions are those described in the text. The experimentally measured values along with the standard error are plotted with the black data points.

solving this discrepancy. This would allow for investigation of the transit time effect as well as further investigation of the intensity of the pump and probe fields.

6.6.3 Dependance on Beam Diameter

Ideally EIT resonances would have been recorded in the Sagnac interferometer for a range of beam diameters. This would have allowed experimental evaluation of the effect of varying the transit time on the EIT line width.

Preliminary measurements were made of EIT resonances, in transmission only, where a reduction in line width by a factor of 2.2 was seen for a magnification of the probe and pump beams of 3.1. These measurements were made keeping all other variables constant.

Maintaining constant beam power but increasing the diameter does lead to a reduction in intensity. However, comparison of the reduction in intensity, by a factor of 9.6 $(= 3.1^2)$, with any of the experimental plots of line width against power (Figs. 6.19 , 6.20 and 6.21) show that this is not sufficient to lead to a

reduction in EIT resonance FWHM of 2.2 . Magnifying the beams by a factor of 3.1 also has the effect of increasing the transit time of the atoms through the beam by the same factor. Thus transit time broadening would be expected to be reduced by the factor of 3.1 .

It should be noted that these measurements were made without the benefit of an optical fibre in the experimental set up and as a result the beam profiles will have been far from Gaussian, due to the numerous optical elements in the beam path.

Beam diameter in Sagnac interferometer

Several telescopes, of different magnification, were introduced to the Sagnac interferometer. The aberrations to the wave fronts of the beams due to the lenses were such that, the interference patterns at the output of the interferometer were not well enough defined to allow measurements of the dispersion to be made.

6.6.4 Group Velocity

From equation 3.98 on page 72 the group velocity can be calculated at the frequency of the two-photon resonance. To do this the FWHM of the two-photon resonance, the normalized transmission in the absence of the EIT signal, the normalized signal of the peak of the EIT signal and the length of Rb vapour cell must be known. In the absence of the EIT signal, the normalized transmitted signal is 0.9. Taking the data presented in Fig. 6.18, from the Lorentzian fit the FWHM is 230 kHz. The amplitude of the EIT sum signal is 18.5×10^{-3} and from equation 5.62 on page 121, assuming that the clockwise and anticlockwise signals are the same size in the absence of the EIT feature, it follows that at the centre of the resonance, the transmission EIT signal is $0.90 + 2 \times 18.5 \times 10^{-3} = 0.937$. This gives a group velocity of c/650 .

Chapter 7

Conclusions & Outlook

Weak probe absorption on the D_2 line in both ^{85}Rb and ^{87}Rb was measured and a model predicting this absorption was realized. Application of a counter-propagating pump beam, at the same frequency as the probe beam, resulted in the Doppler-free hyperfine pumping and saturated absorption spectra.

Co-propagating probe and pump beams, scanned independently of each other, lead to the realization of three-level Λ systems and four-level N systems. The systems investigated comprised two lower states that are different Zeeman sub-levels of the same hyperfine state, of the $5^2S_{1/2}$ ground term. When the lower levels were within the upper hyperfine state of the ground term, EIA was observed. When the lower levels were within the lower hyperfine state of the ground term, EIT was seen.

The theory demonstrating that it is possible to measure directly the dispersion of an EIT or EIA resonance in a "biased" Sagnac interferometer was introduced.

EIT resonances, two orders of magnitude narrower than the natural line width of the excited state, were measured in a "biased" Sagnac interferometer. The line width of these resonances was limited by the ground state coherence decay rate. This in turn was limited by the transit time of the atoms through the pump and probe beams.

Narrower resonances could be measured if the beam diameters were increased. It would also prove beneficial to change from the D_2 line to the D_1 line, between the terms $5^2S_{1/2}$ and $5^2P_{1/2}$ at 795 nm. The hyperfine splitting of the $5^2P_{1/2}$ term is much greater than the splitting in the $5^2P_{3/2}$ term. As a result, at room

temperature, Doppler-broadened hyperfine transitions can be resolved on the D_1 line. Thus on the D_1 line, EIT or EIA signals observed on the Doppler-broadened background can be attributable to a single Λ system.

Using a vapour cell containing an inert buffer gas such as Neon would further increase the transit time of the Rb atoms through the probe and pump beams, [58, 108]. The disadvantage of introducing a buffer gas is that collisions between the atoms and the buffer gas can lead to a loss of coherence within the atom, [107]. These two competing mechanisms result in a minimum line width at a specific buffer gas partial pressure, [108]. This pressure is dependent upon the system under investigation.

To take full advantage of the buffer gas it is likely that it would be necessary to use a Λ system in which the lower states are Zeeman sub-levels of different hyperfine states.

Using the biasing technique, Sagnac interferometry provides a modulation-free method of producing a signal with potential applications in magnetometry and inertial sensing. Further, measuring EIT in a Sagnac interferometer paves the path toward realizing an optical-matter-wave interferometer.

Appendix A

Rubidium Spectroscopic Data & Physical Constants

Atomic Number	37	
Relative Natural Abundance	27.83%	[109]
Atomic Mass	86.909 u	[109]
Nuclear Spin	3/2	

Table A.1: ^{87}Rb atomic data.

Atomic Number	37	
Relative Natural Abundance	72.17%	[109]
Atomic Mass	84.91 u	[109]
Nuclear Spin	5/2	

Table A.2: ^{85}Rb atomic data.

Frequency	ω	$2\pi \times 384.23$ THz	[110]
Wavelength (vacuum)	λ	780.24 nm	[32]
Wavelength (air)	λ_{air}	780.03 nm	[32]
Lifetime	τ	26.24 ns	[32]
Decay Rate / FWHM	Γ	$2\pi \times 6.065$ MHz	[32]

Table A.3: ^{85}Rb and ^{87}Rb D_2 line spectroscopic data.

Speed of light in vacuum	c	299 792 458 ms^{-1}	[111]
Planck constant, reduced	$\hbar$	1.054 572 66(63) $\times 10^{-34}$ Js	[111]
Unified atomic mass unit	u	1.660 540 2(10) $\times 10^{-27}$ kg	[111]
Boltzmann constant	k_B	1.330 658(12) $\times 10^{-23}$ JK^{-1}	[111]
Bohr magneton	μ_B	5.788 382 63(49) $\times 10^{-11}$ MeV T^{-1} 1.399 624 18 MHz G^{-1}	[111]
Permittivity of free space	ϵ_0	8.854 187 817 ... $\times 10^{-12}$ F m^{-1}	[111]

Table A.4: Physical constants used in this thesis.

Appendix B

Error Analysis

This appendix provides an outline of the statistical methods used in fitting functions to the data taken throughout the course of this work[1]. For more detail and for derivations see *Data Reduction and Error Analysis for the Physical Sciences*, [112].

Mean and Uncertainty in Mean

Consider a data set $(x_i, y_{i,k})$, then the mean value for the i^{th} value will be,

$$\overline{y_i} = \frac{1}{N}\Sigma y_{i,k} \; . \tag{B.1}$$

The mean for the parent population, μ is given by,

$$\mu_i = \lim_{N\to\infty}\left(\frac{1}{N}\Sigma y_{i,k}\right) \; . \tag{B.2}$$

The standard deviation of the parent population, σ, is given by,

$$\sigma_i^2 \equiv \lim_{N\to\infty}\left(\frac{1}{N}\Sigma(y_{i,k})^2\right) - \mu_i^2 \; . \tag{B.3}$$

The standard deviation, s, of the sample population is given by,

$$s^2 \equiv \frac{1}{N-1}\Sigma(y_{i,k} - \overline{y_i})^2 \; . \tag{B.4}$$

[1]The Durham University, Dept. of Physics *Undergraduate Error Handbook* by I. G. Hughes and T. P. A. Hase provided much of the inspiration for this appendix.

It would be instructive to find the error in the estimation of the mean. This is referred to as the standard error, it is given by,

$$\sigma_\mu = \frac{\sigma}{\sqrt{N}}, \tag{B.5}$$

$$\simeq \frac{s}{\sqrt{N}}, \tag{B.6}$$

$$\sigma_{\mu_i} \simeq \sqrt{\frac{1}{N(N-1)}\Sigma(y_{i,k} - \overline{y_i})^2}\,. \tag{B.7}$$

Where data points are plotted, in the work presented in this thesis, the data point itself is the mean and the error bars, where shown, are the standard error, i.e. the error in the mean.

χ^2 Test

χ^2 is a statistic characterizing both the deviation of an estimated function from the parent function and the deviations between the data sample and the parent function.

$$\chi^2 \equiv \Sigma_i \frac{(\overline{y_i} - y(x_i))^2}{\sigma_i^2}\,. \tag{B.8}$$

Reduced χ^2, χ^2_ν, is a potentially more useful statistic than χ^2. χ^2_ν is given by,

$$\chi^2_\nu = \frac{\chi^2}{\nu}, \tag{B.9}$$

where ν is the number of degrees of freedom. For fitting N data points using m parameters, the numbers of degrees of freedom is given by,

$$\nu = N - m\,. \tag{B.10}$$

Throughout this thesis, where theoretical models are fitted to experimental data, fits are carried out by minimizing the value of χ^2. In order to determine the quality of the fit the value of χ^2_ν has to be considered. If χ^2_ν is of the order of 1 , then it is possible to say that the model is consistent with the data.

Appendix C

Derivation of Optical-Bloch Equations

In this appendix the optical-Bloch equations that give the populations and coherences for an idealized three-level Λ system, Fig. 3.2 on page 47, will be derived from the Liouville equation. The three-level atom has states $|a\rangle$, $|b\rangle$, and $|c\rangle$. The two fields, probe and pump, are close to resonance with the transitions $|b\rangle \rightarrow |a\rangle$ and $|c\rangle \rightarrow |a\rangle$, respectively. The optical-Bloch equations for the three-level system can then be applied to the idealized two-level system, Fig. 2.1 on page 12, by making small adjustments to the equations.

The Hamiltonian for the three-level system with two fields is,

$$\mathscr{H} = \mathscr{H}_{\mathrm{A}} + V_{\mathrm{pr}} + V_{\mathrm{pu}} \; . \tag{C.1}$$

The interactions of the atoms with the probe and pump laser fields are given by,

$$V_{\mathrm{pr}} = -\mathbf{d} \cdot \mathbf{E}_{\mathrm{pr}} \cos\left(\omega_{\mathrm{pr}} t\right) \; , \tag{C.2}$$

$$V_{\mathrm{pu}} = -\mathbf{d} \cdot \mathbf{E}_{\mathrm{pu}} \cos\left(\omega_{\mathrm{pu}} t\right) \; . \tag{C.3}$$

Rotating Wave Approximation

For a transition between states $|m\rangle$ and $|n\rangle$ the atomic dipole, $\mathbf{d}$, is given by,

$$\mathbf{d} = \mathbf{d}_{mn}\left(|n\rangle\langle m| + |m\rangle\langle n|\right) \; . \tag{C.4}$$

$|n\rangle\langle m|$ is the raising operator and acting on state $|m\rangle$ raises the atom to state $|n\rangle$, $|m\rangle\langle n|$ is the lowering operator and acting on state $|n\rangle$ lowers the atom to state $|m\rangle$.

The interaction of the atom with the probe laser field can be rewritten in terms of the raising and lowering operators,

$$-\mathbf{d}\cdot\mathbf{E}_{\rm pr}\cos(\omega_{\rm pr}t) = \frac{\hbar\Omega_{\rm pr}}{2}\left(|a\rangle\langle b|e^{-i\omega_{\rm pr}t}+|a\rangle\langle b|e^{i\omega_{\rm pr}t}\right. \\ \left.+|b\rangle\langle a|e^{-i\omega_{\rm pr}t}+|b\rangle\langle a|e^{i\omega_{\rm pr}t}\right)\ , \tag{C.5}$$

where,

$$\hbar\Omega_{\rm pr} \equiv -\mathbf{d}_{\rm ba}\cdot\mathbf{E}_{\rm pr}\ , \tag{C.6}$$

$$\mathbf{d}_{\rm ba} = \langle b|\mathbf{d}|a\rangle\ . \tag{C.7}$$

$\Omega_{\rm pr}$ is the Rabi frequency, this represents the coupling between the laser field and the atomic dipole.

The term $e^{-i\omega_{\rm pr}t}$, in equation C.6, is associated with absorption of a photon, whereas $e^{i\omega_{\rm pr}t}$ is associated with the emission of a photon. For the rest of this derivation the terms where photons are absorbed and the atom falls from $|a\rangle$ to $|b\rangle$ and where photons are emitted and the atom is raised from $|b\rangle$ to $|a\rangle$, will be neglected. This is known as the rotating-wave approximation. The neglected terms are not nearly as significant as the resonant terms, for a detailed justification see *Atom Photon Interactions*, [113].

Therefore making the rotating-wave approximation,

$$V_{\rm pr} = \frac{\hbar\Omega_{\rm pr}}{2}\left(|a\rangle\langle b|e^{i\omega_{\rm pr}t}+|b\rangle\langle a|e^{-i\omega_{\rm pr}t}\right)\ , \tag{C.8}$$

$$V_{\rm pu} = \frac{\hbar\Omega_{\rm pu}}{2}\left(|a\rangle\langle c|e^{i\omega_{\rm pu}t}+|c\rangle\langle a|e^{-i\omega_{\rm pu}t}\right)\ . \tag{C.9}$$

The resulting Hamiltonian can be rewritten in matrix form,

$$\mathscr{H} = \begin{pmatrix} \hbar\omega_{\rm a} & (\hbar\Omega_{\rm pr}/2)\,e^{-i\omega_{\rm pr}t} & (\hbar\Omega_{\rm pu}/2)\,e^{-i\omega_{\rm pu}t} \\ (\hbar\Omega_{\rm pr}/2)\,e^{i\omega_{\rm pr}t} & \hbar\omega_{\rm b} & 0 \\ (\hbar\Omega_{\rm pu}/2)\,e^{i\omega_{\rm pu}t} & 0 & \hbar\omega_{\rm c} \end{pmatrix}\ . \tag{C.10}$$

The density matrix for the three-level system is,

$$\rho = \begin{pmatrix} \rho_{\rm aa} & \rho_{\rm ab} & \rho_{\rm ac} \\ \rho_{\rm ba} & \rho_{\rm bb} & \rho_{\rm bc} \\ \rho_{\rm ca} & \rho_{\rm cb} & \rho_{\rm cc} \end{pmatrix}\ . \tag{C.11}$$

From the Liouville equation (equation 2.21),

$$\begin{aligned} \dot{\rho} &= \frac{\mathrm{i}}{\hbar}[\rho, \mathscr{H}] - \gamma\rho \ , \\ \dot{\rho}_{\mathrm{mn}} &= \frac{\mathrm{i}}{\hbar}[\rho, \mathscr{H}]_{\mathrm{mn}} - (\gamma\rho)_{\mathrm{mn}} \ , \end{aligned} \tag{C.12}$$

where,

$$[\rho, \mathscr{H}]_{\mathrm{mn}} = \Sigma_{\mathrm{k}} \left(\rho_{\mathrm{mk}}\mathscr{H}_{\mathrm{kn}} - \mathscr{H}_{\mathrm{mk}}\rho_{\mathrm{kn}}\right) \ , \tag{C.13}$$

$$\text{and} \quad (\gamma\rho)_{\mathrm{mn}} = \gamma_{\mathrm{mn}}\rho_{\mathrm{mn}} \ , \tag{C.14}$$

where,

$$\gamma_{\mathrm{mn}} = \frac{\Gamma_{\mathrm{m}} + \Gamma_{\mathrm{n}}}{2} \ . \tag{C.15}$$

Hence the equations of motion for the coherences are,

$$\begin{aligned} \dot{\rho}_{\mathrm{ab}} = &-\left(\mathrm{i}\left(\omega_{\mathrm{a}} - \omega_{\mathrm{b}}\right) + \gamma_{\mathrm{ab}}\right)\rho_{\mathrm{ab}} + \frac{\mathrm{i}\Omega_{\mathrm{pr}}\mathrm{e}^{-\mathrm{i}\omega_{\mathrm{pr}}t}}{2}\left(\rho_{\mathrm{aa}} - \rho_{\mathrm{bb}}\right) \\ &- \frac{\mathrm{i}\Omega_{\mathrm{pu}}\mathrm{e}^{-\mathrm{i}\omega_{\mathrm{pu}}t}}{2}\rho_{\mathrm{cb}} \ , \end{aligned} \tag{C.16}$$

$$\begin{aligned} \dot{\rho}_{\mathrm{ac}} = &-\left(\mathrm{i}\left(\omega_{\mathrm{a}} - \omega_{\mathrm{c}}\right) + \gamma_{\mathrm{ac}}\right)\rho_{\mathrm{ac}} + \frac{\mathrm{i}\Omega_{\mathrm{pu}}\mathrm{e}^{-\mathrm{i}\omega_{\mathrm{pu}}t}}{2}\left(\rho_{\mathrm{aa}} - \rho_{\mathrm{cc}}\right) \\ &- \frac{\mathrm{i}\Omega_{\mathrm{pr}}\mathrm{e}^{-\mathrm{i}\omega_{\mathrm{pr}}t}}{2}\rho_{\mathrm{bc}} \ , \end{aligned} \tag{C.17}$$

$$\begin{aligned} \dot{\rho}_{\mathrm{cb}} = &-\left(\mathrm{i}\left(\omega_{\mathrm{c}} - \omega_{\mathrm{b}}\right) + \gamma_{\mathrm{cb}}\right)\rho_{\mathrm{cb}} + \frac{\mathrm{i}\Omega_{\mathrm{pr}}\mathrm{e}^{-\mathrm{i}\omega_{\mathrm{pr}}t}}{2}\rho_{\mathrm{ca}} \\ &- \frac{\mathrm{i}\Omega_{\mathrm{pu}}\mathrm{e}^{+\mathrm{i}\omega_{\mathrm{pu}}t}}{2}\rho_{\mathrm{ab}} \ . \end{aligned} \tag{C.18}$$

Similarly the equations of motion for the populations are,

$$\begin{aligned} \dot{\rho}_{\mathrm{aa}} = &\frac{\mathrm{i}\Omega_{\mathrm{pr}}}{2}\left(\rho_{\mathrm{ab}}\mathrm{e}^{+\mathrm{i}\omega_{\mathrm{pr}}t} - \rho_{\mathrm{ba}}\mathrm{e}^{-\mathrm{i}\omega_{\mathrm{pr}}t}\right) \\ &+ \frac{\mathrm{i}\Omega_{\mathrm{pu}}}{2}\left(\rho_{\mathrm{ac}}\mathrm{e}^{+\mathrm{i}\omega_{\mathrm{pu}}t} - \rho_{\mathrm{ca}}\mathrm{e}^{-\mathrm{i}\omega_{\mathrm{pu}}t}\right) - \Gamma_{\mathrm{a}}\rho_{\mathrm{aa}} \ , \end{aligned} \tag{C.19}$$

$$\dot{\rho}_{\mathrm{bb}} = \frac{\mathrm{i}\Omega_{\mathrm{pr}}}{2}\left(\rho_{\mathrm{ba}}\mathrm{e}^{+\mathrm{i}\omega_{\mathrm{pr}}t} - \rho_{\mathrm{ab}}\mathrm{e}^{-\mathrm{i}\omega_{\mathrm{pr}}t}\right) - \Gamma_{\mathrm{b}}\rho_{\mathrm{bb}} + \frac{\Gamma_{\mathrm{a}}}{2}\rho_{\mathrm{aa}} \tag{C.20}$$

$$\dot{\rho}_{\mathrm{cc}} = \frac{\mathrm{i}\Omega_{\mathrm{pu}}}{2}\left(\rho_{\mathrm{ca}}\mathrm{e}^{+\mathrm{i}\omega_{\mathrm{pu}}t} - \rho_{\mathrm{ac}}\mathrm{e}^{-\mathrm{i}\omega_{\mathrm{pu}}t}\right) - \Gamma_{\mathrm{c}}\rho_{\mathrm{cc}} + \frac{\Gamma_{\mathrm{a}}}{2}\rho_{\mathrm{aa}} \tag{C.21}$$

Now introduce the "slow" variables,

$$\rho_{ab} = \widetilde{\rho}_{ab} e^{-i\omega_{pr}t} , \tag{C.22}$$

$$\rho_{ac} = \widetilde{\rho}_{ac} e^{-i\omega_{pu}t} , \tag{C.23}$$

$$\rho_{cb} = \widetilde{\rho}_{cb} e^{-i(\omega_{pr}-\omega_{pu})t} . \tag{C.24}$$

Substituting equations C.22, C.23, and C.24 into the equations of motion for the coherences, equations C.16, C.17, and C.18 leads to,

$$\dot{\widetilde{\rho}}_{ab} = -\left(i\left(\omega_a - \omega_b - \omega_{pr}\right) + \gamma_{ab}\right)\widetilde{\rho}_{ab} + \frac{i\Omega_{pr}}{2}\left(\rho_{aa} - \rho_{bb}\right) - \frac{i\Omega_{pu}}{2}\widetilde{\rho}_{cb} , \tag{C.25}$$

$$\dot{\widetilde{\rho}}_{ac} = -\left(i\left(\omega_a - \omega_c - \omega_{pu}\right) + \gamma_{ac}\right)\widetilde{\rho}_{ac} + \frac{i\Omega_{pu}}{2}\left(\rho_{aa} - \rho_{cc}\right) - \frac{i\Omega_{pr}}{2}\widetilde{\rho}_{bc} , \tag{C.26}$$

$$\dot{\widetilde{\rho}}_{cb} = -\left(i\left(\omega_c - \omega_b - \omega_{pr} + \omega_{pu}\right) + \gamma_{cb}\right)\widetilde{\rho}_{cb} + \frac{i\Omega_{pr}}{2}\widetilde{\rho}_{ca} - \frac{i\Omega_{pu}}{2}\widetilde{\rho}_{ab} . \tag{C.27}$$

Similarly for the populations, substituting equations C.22, C.23, and C.24 into equations C.19, C.20, and C.21 leads to,

$$\dot{\rho}_{aa} = \frac{i\Omega_{pr}}{2}\left(\widetilde{\rho}_{ab} - \widetilde{\rho}_{ba}\right) + \frac{i\Omega_{pu}}{2}\left(\widetilde{\rho}_{ac} - \widetilde{\rho}_{ca}\right) - \Gamma_a\rho_{aa} , \tag{C.28}$$

$$\dot{\rho}_{bb} = \frac{i\Omega_{pr}}{2}\left(\widetilde{\rho}_{ba} - \widetilde{\rho}_{ab}\right) - \Gamma_b\rho_{bb} + \frac{\Gamma_a}{2}\rho_{aa} , \tag{C.29}$$

$$\dot{\rho}_{cc} = \frac{i\Omega_{pu}}{2}\left(\widetilde{\rho}_{ca} - \widetilde{\rho}_{ac}\right) - \Gamma_c\rho_{cc} + \frac{\Gamma_a}{2}\rho_{aa} . \tag{C.30}$$

The detuning from resonance of the probe and pump field, δ_{pr} and δ_{pu}, is defined as,

$$\delta_{pr} = \omega_{pr} - \omega_a + \omega_b , \tag{C.31}$$

$$\delta_{pu} = \omega_{pu} - \omega_a + \omega_c . \tag{C.32}$$

It follows that,

$$\dot{\widetilde{\rho}}_{ab} = -(\gamma_{ab} - i\delta_{pr})\,\widetilde{\rho}_{ab} + \frac{i\Omega_{pr}}{2}(\rho_{aa} - \rho_{bb}) - \frac{i\Omega_{pu}}{2}\widetilde{\rho}_{cb}\ , \tag{C.33}$$

$$\dot{\widetilde{\rho}}_{ac} = -(\gamma_{ac} - i\delta_{pu})\,\widetilde{\rho}_{ac} + \frac{i\Omega_{pu}}{2}(\rho_{aa} - \rho_{cc}) - \frac{i\Omega_{pr}}{2}\widetilde{\rho}_{bc}\ , \tag{C.34}$$

$$\dot{\widetilde{\rho}}_{cb} = -(\gamma_{cb} - i(\delta_{pr} - \delta_{pu}))\,\widetilde{\rho}_{cb} + \frac{i\Omega_{pr}}{2}\widetilde{\rho}_{ca} - \frac{i\Omega_{pu}}{2}\widetilde{\rho}_{ab}\ . \tag{C.35}$$

This is the form of the optical-Bloch equations, for the three-level Λ system, that will be used to make predictions of the absorption and dispersion of the probe beam in chapter 3 .

Two-level atom

In the case of the two-level atom, with states $|b\rangle$ and $|a\rangle$, equations C.28, C.29 and C.33 apply but with, $\Omega_{pu} = 0$. Also $|a\rangle$ only decays to $|b\rangle$ through spontaneous emission, so the term $+(\Gamma/2)\,\rho_{aa}$ is replaced by $+\Gamma\ \rho_{aa}$. Hence for the two-level atom,

$$\dot{\widetilde{\rho}}_{ab} = -(\gamma_{ab} - i\delta_{pr})\,\widetilde{\rho}_{ab} + \frac{i\Omega_{pr}}{2}(\rho_{aa} - \rho_{bb})\ , \tag{C.36}$$

$$\dot{\rho}_{aa} = \frac{i\Omega_{pr}}{2}(\widetilde{\rho}_{ab} - \widetilde{\rho}_{ba}) - \Gamma_a\rho_{aa}\ , \tag{C.37}$$

$$\dot{\rho}_{bb} = \frac{i\Omega_{pr}}{2}(\widetilde{\rho}_{ba} - \widetilde{\rho}_{ab}) - \Gamma_b\rho_{bb} + \Gamma_a\rho_{aa}\ . \tag{C.38}$$

These equations will form the basis of the predictions of the absorption and dispersion for a two-level atom in chapter 2 .

Appendix D

Linear Doppler Effect Approximation

Suppose that in the laboratory frame of reference an atom moves at a velocity, $\mathbf{v}$, and is in the state, $|\mathrm{b}\rangle$, with energy, $\hbar\omega_{\mathrm{b}'}$ and with momentum $\boldsymbol{p}_{\mathrm{b}'}$. The atom absorbs a photon with momentum $\hbar\boldsymbol{k}_{\mathrm{pr}}$, where $\boldsymbol{k}_{\mathrm{pr}}$ makes an angle θ with $\mathbf{v}$. The atom is excited to a state $|\mathrm{a}\rangle$, with energy $\hbar\omega_{\mathrm{a}'}$ and momentum $\boldsymbol{p}_{\mathrm{a}'}$.

Rest frame of the atom

In the rest frame of the atom before the absorption of the photon, the atom has initial momentum $\boldsymbol{p}_{\mathrm{b}} = 0$, the photon has momentum $\hbar\boldsymbol{k}_{\mathrm{pr}'}$. After the absorption, but in the same frame of reference, the atom has momentum $\boldsymbol{p}_{\mathrm{a}}$ and is in the energy state $\hbar\omega_{\mathrm{a}}$.

From the conservation of momentum,

$$\hbar\boldsymbol{k}_{\mathrm{pr}'} = \boldsymbol{p}_{\mathrm{a}} , \tag{D.1}$$

and from the conservation of energy,

$$\hbar\omega_{\mathrm{b}} + \hbar\omega_{\mathrm{pr}'} = \hbar\omega_{\mathrm{a}} + \frac{p_{\mathrm{a}}^2}{2m} . \tag{D.2}$$

Squaring equation D.1 and substituting into equation D.2 leads to,

$$\hbar\omega_{\mathrm{b}} + \hbar\omega_{\mathrm{pr}'} = \hbar\omega_{\mathrm{a}} + \frac{\hbar^2 k_{\mathrm{pr}'}^2}{2m} . \tag{D.3}$$

As $\omega_a - \omega_b = \omega_{ab}$, and $k_{pr'} = \omega_{pr'}/c$, it follows that,

$$\omega_{pr'} = \omega_{ab} + \frac{\hbar\omega_{pr'}^2}{2mc^2} . \tag{D.4}$$

Of interest is the relationship between the frequency of the photon in the lab frame, ω_{pr} , and the frequency of the atomic resonance in its rest frame, ω_{ab} . Thus the relationship between ω_{pr} and $\omega_{pr'}$ must be found.

Consider an electromagnetic wave in the lab frame, $\cos(\omega_{pr}t - k_{pr}x)$, an observer in the rest frame of the atom would see a wave given by, $\cos(\omega_{pr'}t' - k_{pr'}x')$. From the Lorentz transformations,

$$x' = \frac{x - \beta c \cos\theta\, t}{\sqrt{1-\beta^2}} , \tag{D.5}$$

$$\text{and} \quad t' = \frac{t - \beta \cos\theta\, x/c}{\sqrt{1-\beta^2}} , \tag{D.6}$$

where, $\beta = v/c$.

Thus,

$$\cos(\omega_{pr'}t' - k_{pr'}x') = \cos\left(\omega_{pr'}\frac{t - \beta \cos\theta\, x/c}{\sqrt{1-\beta^2}} - k_{pr'}\frac{x - \beta c \cos\theta\, t}{\sqrt{1-\beta^2}}\right) , \tag{D.7}$$

$$= \cos\left(\frac{\omega_{pr'} + k_{pr'}\beta c\cos\theta}{\sqrt{1-\beta^2}}t - \frac{k_{pr'} + (\beta\omega_{pr'}/c)\cos\theta}{\sqrt{1-\beta^2}}x\right) ,$$

$$\equiv \cos(\omega_{pr}t - k_{pr}x) . \tag{D.8}$$

Hence the frequency of the photon in the rest frame of the atom, $\omega_{pr'}$, is given by,

$$\omega_{pr} = \frac{\omega_{pr'} + k_{pr'}\beta c\cos\theta}{\sqrt{1-\beta^2}} , \tag{D.9}$$

$$= \frac{1 + \beta\cos\theta}{\sqrt{1-\beta^2}}\omega_{pr'} . \tag{D.10}$$

Now substituting equation D.4 into equation D.10 leads to,

$$\frac{1 + \beta\cos\theta}{\sqrt{1-\beta^2}} \cdot \omega_{pr} = \left(\frac{1 + \beta\cos\theta}{\sqrt{1-\beta^2}}\right)^2 \cdot \omega_{ab} + \frac{\hbar\omega_{pr}^2}{2mc^2} , \tag{D.11}$$

$$\left(1+\beta\cos\theta+\frac{\beta^2}{2}+\frac{\beta^3}{2}\cos\theta \;+\; \ldots\right)\cdot\omega_{\rm pr} = \left(1+\beta\cos\theta+\frac{\beta^2}{2}+\frac{\beta^3}{2}\cos\theta+\ldots\right)^2\cdot\omega_{\rm ab} + \frac{\hbar\omega_{\rm pr}^2}{2mc^2}\;. \tag{D.12}$$

First order approximation

In the regime that $\beta \ll 1$,

$$\left(1+\beta\cos\theta+\frac{\beta^2}{2}+\frac{\beta^3}{2}\cos\theta+\ldots\right) \;\simeq\; (1+\beta\cos\theta)\;. \tag{D.13}$$

Further in the case that the energy of the photon is much less than the rest mass energy of the atom,

$$\hbar\omega_{\rm pr} \;\ll\; 2mc^2\;. \tag{D.14}$$

It follows that,

$$\omega_{\rm pr} = (1+\beta\cos\theta)\cdot\omega_{\rm ab}\;, \tag{D.15}$$

and when the atom and the photon are co-propagating,

$$\omega_{\rm pr} = \left(1+\frac{\rm v}{\rm c}\right)\cdot\omega_{\rm ab}\;. \tag{D.16}$$

This is the result that is used throughout this thesis to calculate the effect of the Doppler effect.

Appendix E

Weak Probe Absorption Code

The code used to calculate the weak probe beam absorption, presented in chapter 2 , is shown on the following pages.

Absorption and dispersion of a weak probe beam in a thermal Rb vapour on the D-2 line.

Graham Purves, 14 ii 06.

I would appreciate any feedback anyone has on the following code, whether it be on the code itself or the anotations.
Thanks,
Graham

Mathematica Set-up

```
Off[General::"spell"]
Off[General::"spell1"]
Off[ClebschGordan::"phy"]
Off[ClebschGordan::"tri"]
Off[NIntegrate::"inum"]

L=.; Pu87=.; Ap87=.; Ap85=.; Lc=.; u87=.; u85=.; P=.;

Directory[]
```

To set the directory that you wish to have any plots or data saved to, please amend the following line and remove the (* *).

```
SetDirectory["/Users/Graham/Documents/Work_Misc/Mathematica_Stuff/Weak_Probe"]
```

Physical Constants

```
ħ = 1.05457266 × 10^-34;
ε0 = 8.854187817 × 10^-12;
c = 2.99792458 × 10^8;
amu = 1.6605402 × 10^-27;
kb = 1.380658 × 10^-23;
n0 = 1;
```

Conditions of vapour cell

▪ Cell Length

The cell length is entered at the very end of the code and the variable is labelled Lc

▪ Temperature of Cell and RMS velocity of atoms, u

```
T = .;
```

The velocity of the atoms for the two different isotopes is calulated as a function of temperature.

▪ Rb-87

$$u87[T\_] = \sqrt{\frac{2 \times k_b \times T}{87 \times amu}}$$

▪ Rb-85

$$u85[T\_] = \sqrt{\frac{2 \times k_b \times T}{85 \times amu}}$$

▪ Vapour Pressure in Cell

$$p_a = -94.04826;$$
$$p_b = 1961.258;$$
$$p_c = -0.03771687;$$
$$p_d = 42.57526;$$
$$P[T\_] = 10^{\left(p_a - \frac{p_b}{T} + p_c \times T + p_d \times Log[10,T]\right)};$$

▪ Number Density in Cell

$$NRb850[T\_] := 0.72 \times \frac{P[T] \times 133.3}{k_b \times T}$$
$$NRb870[T\_] := 0.28 \times \frac{P[T] \times 133.3}{k_b \times T}$$

```
NRb870[293] + NRb850[293]
```

▪ Maxwell Boltzman Velocity distribution

▪ Rb-87

$$N_{87}[v\_, T\_] = \frac{NRb870[T] \times e^{-\left(\frac{v^2}{u87[T]^2}\right)}}{\sqrt{\pi} \times u87[T]};$$

▪ Rb-85

$$N_{85}[v\_, T\_] = \frac{NRb850[T] \times e^{-\left(\frac{v^2}{u85[T]^2}\right)}}{\sqrt{\pi} \times u85[T]};$$

Definitions of the properties of the medium and probe beam

▪ Probe beam

Wavelength λ and wavevector k of the probe beam.

$$\lambda_{probe} = 780 \times 10^{-9};$$
$$k_{probe} = \frac{2 \times \pi}{\lambda_{probe}};$$
$$\omega_{probe} = \frac{k_{probe}}{c};$$

Polarisation π corresponds to q=0, σ^+ to q=+1 and σ^- to q=-1

$$q_{probe} = 0;$$

▪ Properties of Medium

▪ Rb-87

Γ is the decay rate of the relevant state, for groundstates, this decay rate is taken as 0, as we are assuming any collisional decay rate is negligible.

$$\Gamma 87_1 = 0;$$
$$\Gamma 87_2 = 2 \times \pi \times 6.065 \times 10^6;$$
$$\Gamma 87_3 = 0;$$
$$\gamma 87_{21} = \frac{\Gamma 87_1 + \Gamma 87_2}{2};$$
$$\gamma 87_{31} = \frac{\Gamma 87_1 + \Gamma 87_3}{2};$$

$2\hbar g_{21}$ is the dipole matrix element for the probe transition. As with the Rabi frequency for the pump beam, this dipole matrix element has been normalised such that it only needs to be multiplied by the transition strength for each transition to get the correct dipole matrix element for that transition.

$$g87_{21} = \frac{-\sqrt{3}}{2} \times \sqrt{\frac{3 \times \lambda_{probe}^3 \times \Gamma 87_2}{4 \times \pi^2 \times \hbar \times c}} \times \sqrt{\frac{c \times \epsilon_0}{2}};$$

▪ Rb-85

Γ is the decay rate of the relevant state, for groundstates, this decay rate is taken as 0, as we are assuming any collisional decay rate is negligible.

$$\Gamma 85_1 = 0;$$
$$\Gamma 85_2 = 2 \times \pi \times 6.065 \times 10^6;$$
$$\Gamma 85_3 = 0;$$
$$\gamma 85_{21} = \frac{\Gamma 85_1 + \Gamma 85_2}{2};$$
$$\gamma 85_{31} = \frac{\Gamma 85_1 + \Gamma 85_3}{2};$$

$2\hbar g_{21}$ is the dipole matrix element for the probe transition. As with the Rabi frequency for the pump beam, this dipole matrix element has been normalised such that it only needs to be multiplied by the transition strength for each transition to get the correct dipole matrix element for that transition.

$$g85_{21} = \frac{-\sqrt{3}}{2} \times \sqrt{\frac{3 \times \lambda_{probe}^3 \times \Gamma 85_2}{4 \times \pi^2 \times \hbar \times c}} \times \sqrt{\frac{c \times \epsilon_0}{2}};$$

Complex Susceptibility, Absorption and Dispersion Coefficients

▪ Rb-87

▪ Susceptibility

The susceptibility for each of the different allowed hyperfine transitions is calculated below; Fg=1 to Fe=0,1,2 and then Fg=2 to Fe=1,2,3. The hyperfine detunings of both the ground and excited states is included for each of the different transitions. The factor of 1/8 at the front of each of the sums is to take account of the fact that there are 8 different groundstate hyperfine levels. From the suceptibility it is then possible to calculate the absorption and dispersion co-efficients.

$$\chi 87F10[\Delta\_, v\_, T\_] = \frac{1}{8} \times \sum_{n=1}^{5} (g87_{21}{}^2 \times 4 \times \hbar \times Pr87[[n, 1, 1]]^2 \times i \times N_{87}[v, T]) /$$
$$(\epsilon_0 \times (\gamma 87_{21} - i\,(2 \times \pi \times \Delta + k_{probe} \times v + 2 \times \pi \times (-4271 \times 10^6) - 2 \times \pi \times (-301.4) \times 10^6)));$$

$$\chi 87F11[\Delta\_, v\_, T\_] = \frac{1}{8} \times \sum_{n=1}^{5} (g87_{21}{}^2 \times 4 \times \hbar \times Pr87[[n, 2, 1]]^2 \times i \times N_{87}[v, T]) /$$
$$(\epsilon_0 \times (\gamma 87_{21} - i\,(2 \times \pi \times \Delta + k_{probe} \times v + 2 \times \pi \times (-4271 \times 10^6) - 2 \times \pi \times (-229.2) \times 10^6)));$$

$$\chi 87F12[\Delta\_, v\_, T\_] = \frac{1}{8} \times \sum_{n=1}^{5} (g87_{21}{}^2 \times 4 \times \hbar \times Pr87[[n, 3, 1]]^2 \times i \times N_{87}[v, T]) /$$
$$(\epsilon_0 \times (\gamma 87_{21} - i\,(2 \times \pi \times \Delta + k_{probe} \times v + 2 \times \pi \times (-4271 \times 10^6) - 2 \times \pi \times (-72.2) \times 10^6)));$$

$$\chi 87F21[\Delta\_, v\_, T\_] = \frac{1}{8} \times \sum_{n=1}^{5} (g87_{21}{}^2 \times 4 \times \hbar \times Pr87[[n, 2, 2]]^2 \times i \times N_{87}[v, T]) /$$
$$(\epsilon_0 \times (\gamma 87_{21} - i\,(2 \times \pi \times \Delta + k_{probe} \times v + 2 \times \pi \times 2563 \times 10^6 - 2 \times \pi \times (-229.2) \times 10^6)));$$

$$\chi 87F22[\Delta\_, v\_, T\_] = \frac{1}{8} \times \sum_{n=1}^{5} (g87_{21}{}^2 \times 4 \times \hbar \times Pr87[[n, 3, 2]]^2 \times i \times N_{87}[v, T]) /$$
$$(\epsilon_0 \times (\gamma 87_{21} - i\,(2 \times \pi \times \Delta + k_{probe} \times v + 2 \times \pi \times 2563 \times 10^6 - 2 \times \pi \times (-72.2) \times 10^6)));$$

$$\chi 87F23[\Delta\_, v\_, T\_] = \frac{1}{8} \times \sum_{n=1}^{5} (g87_{21}{}^2 \times 4 \times \hbar \times Pr87[[n, 4, 2]]^2 \times i \times N_{87}[v, T]) /$$
$$(\epsilon_0 \times (\gamma 87_{21} - i\,(2 \times \pi \times \Delta + k_{probe} \times v + 2 \times \pi \times 2563 \times 10^6 - 2 \times \pi \times 194.4 \times 10^6)));$$

▪ Absorption coefficients

```
α87F10[Δ_, v_, T_] = k_probe × n_0 × Im[χ87F10[Δ, v, T]];
α87F11[Δ_, v_, T_] = k_probe × n_0 × Im[χ87F11[Δ, v, T]];
α87F12[Δ_, v_, T_] = k_probe × n_0 × Im[χ87F12[Δ, v, T]];
α87F21[Δ_, v_, T_] = k_probe × n_0 × Im[χ87F21[Δ, v, T]];
α87F22[Δ_, v_, T_] = k_probe × n_0 × Im[χ87F22[Δ, v, T]];
α87F23[Δ_, v_, T_] = k_probe × n_0 × Im[χ87F23[Δ, v, T]];
```

▪ Dispersion coefficients

$$\beta 87F10[\Delta\_, v\_, T\_] = \frac{n_0 \times Re[\chi 87F10[\Delta, v, T]]}{2};$$

$$\beta 87F11[\Delta\_, v\_, T\_] = \frac{n_0 \times Re[\chi 87F11[\Delta, v, T]]}{2};$$

$$\beta 87F12[\Delta\_, v\_, T\_] = \frac{n_0 \times Re[\chi 87F12[\Delta, v, T]]}{2};$$

$$\beta 87F21[\Delta\_, v\_, T\_] = \frac{n_0 \times Re[\chi 87F21[\Delta, v, T]]}{2};$$

$$\beta 87F22[\Delta\_, v\_, T\_] = \frac{n_0 \times Re[\chi 87F22[\Delta, v, T]]}{2};$$

$$\beta 87F23[\Delta\_, v\_, T\_] = \frac{n_0 \times Re[\chi 87F23[\Delta, v, T]]}{2};$$

▪ Rb-85

▪ Susceptibility

The susceptibility for each of the different allowed hyperfine transitions is calculated below;Fg=2 to Fe=1,2,3 and then Fg=3 to Fe=2,3,4. The hyperfine detunings of both the ground and excited states is included for each of the different transitions.The factor of 1/12 at the front of each of the sums is to take account of the fact that there are 12 different groundstate hyperfine levels. From the suceptibility it is then possible to calculate the absorption and dispersion co-efficients.

$$\chi 85F21[\Delta\_, v\_, T\_] = \frac{1}{12} \times \sum_{n=1}^{7} (g85_{21}{}^2 \times 4 \times \hbar \times Pr85[[n, 1, 1]]^2 \times i \times N_{85}[v, T]) / (\epsilon_0 \times (\gamma 85_{21} - i\,(2 \times \pi \times \Delta + k_{probe} \times v + 2 \times \pi \times (-1771 \times 10^6) - 2 \times \pi \times (-113.2) \times 10^6)));$$

$$\chi 85F22[\Delta\_, v\_, T\_] = \frac{1}{12} \times \sum_{n=1}^{7} (g85_{21}{}^2 \times 4 \times \hbar \times Pr85[[n, 2, 1]]^2 \times i \times N_{85}[v, T]) / (\epsilon_0 \times (\gamma 85_{21} - i\,(2 \times \pi \times \Delta + k_{probe} \times v + 2 \times \pi \times (-1771 \times 10^6) - 2 \times \pi \times (-84.0) \times 10^6)));$$

$$\chi 85F23[\Delta\_, v\_, T\_] = \frac{1}{12} \times \sum_{n=1}^{7} (g85_{21}{}^2 \times 4 \times \hbar \times Pr85[[n, 3, 1]]^2 \times i \times N_{85}[v, T]) / (\epsilon_0 \times (\gamma 85_{21} - i\,(2 \times \pi \times \Delta + k_{probe} \times v + 2 \times \pi \times (-1771 \times 10^6) - 2 \times \pi \times (-20.6) \times 10^6)));$$

$$\chi 85F32[\Delta\_, v\_, T\_] = \frac{1}{12} \times \sum_{n=1}^{7} (g85_{21}{}^2 \times 4 \times \hbar \times Pr85[[n, 2, 2]]^2 \times i \times N_{85}[v, T]) / (\epsilon_0 \times (\gamma 85_{21} - i\,(2 \times \pi \times \Delta + k_{probe} \times v + 2 \times \pi \times 1265 \times 10^6 - 2 \times \pi \times (-84.0) \times 10^6)));$$

$$\chi 85F33[\Delta\_, v\_, T\_] = \frac{1}{12} \times \sum_{n=1}^{7} (g85_{21}{}^2 \times 4 \times \hbar \times Pr85[[n, 3, 2]]^2 \times i \times N_{85}[v, T]) / (\epsilon_0 \times (\gamma 85_{21} - i\,(2 \times \pi \times \Delta + k_{probe} \times v + 2 \times \pi \times 1265 \times 10^6 - 2 \times \pi \times (-20.6) \times 10^6)));$$

$$\chi 85F34[\Delta\_, v\_, T\_] = \frac{1}{12} \times \sum_{n=1}^{7} (g85_{21}{}^2 \times 4 \times \hbar \times Pr85[[n, 4, 2]]^2 \times i \times N_{85}[v, T]) / (\epsilon_0 \times (\gamma 85_{21} - i\,(2 \times \pi \times \Delta + k_{probe} \times v + 2 \times \pi \times 1265 \times 10^6 - 2 \times \pi \times 100.4 \times 10^6)));$$

▪ Absorption coefficients

```
α85F21[Δ_, v_, T_] = k_probe × n0 × Im[χ85F21[Δ, v, T]];
α85F22[Δ_, v_, T_] = k_probe × n0 × Im[χ85F22[Δ, v, T]];
α85F23[Δ_, v_, T_] = k_probe × n0 × Im[χ85F23[Δ, v, T]];
α85F32[Δ_, v_, T_] = k_probe × n0 × Im[χ85F32[Δ, v, T]];
α85F33[Δ_, v_, T_] = k_probe × n0 × Im[χ85F33[Δ, v, T]];
α85F34[Δ_, v_, T_] = k_probe × n0 × Im[χ85F34[Δ, v, T]];
```

▪ Dispersion coefficients

$$\beta 85F21[\Delta\_, v\_, T\_] = \frac{n_0 \times Re[\chi 85F21[\Delta, v, T]]}{2};$$

$$\beta 85F22[\Delta\_, v\_, T\_] = \frac{n_0 \times Re[\chi 85F22[\Delta, v, T]]}{2};$$

$$\beta 85F23[\Delta\_, v\_, T\_] = \frac{n_0 \times Re[\chi 85F23[\Delta, v, T]]}{2};$$

$$\beta 85F32[\Delta\_, v\_, T\_] = \frac{n_0 \times Re[\chi 85F32[\Delta, v, T]]}{2};$$

$$\beta 85F33[\Delta\_, v\_, T\_] = \frac{n_0 \times Re[\chi 85F33[\Delta, v, T]]}{2};$$

$$\beta 85F34[\Delta\_, v\_, T\_] = \frac{n_0 \times Re[\chi 85F34[\Delta, v, T]]}{2};$$

Integration Over Velocity Distribution

The absorption and dispersion co-efficients arer now integrated over the Maxwell-Boltzmann velocity distribution, in order that we can calculate the absorption and dispersion of the media at different detunings and temperatures.

▪ Rb-87

▪ Absorption

```
α87F10v[Δ_, T_] = NIntegrate[Evaluate[α87F10[Δ, v, T]],
   {v, -600, 600}, MinRecursion → 5, MaxRecursion → 20];
α87F11v[Δ_, T_] = NIntegrate[Evaluate[α87F11[Δ, v, T]],
   {v, -600, 600}, MinRecursion → 5, MaxRecursion → 20];
α87F12v[Δ_, T_] = NIntegrate[Evaluate[α87F12[Δ, v, T]],
   {v, -600, 600}, MinRecursion → 5, MaxRecursion → 20];
α87F21v[Δ_, T_] = NIntegrate[Evaluate[α87F21[Δ, v, T]],
   {v, -600, 600}, MinRecursion → 5, MaxRecursion → 20];
α87F22v[Δ_, T_] = NIntegrate[Evaluate[α87F22[Δ, v, T]],
   {v, -600, 600}, MinRecursion → 5, MaxRecursion → 20];
α87F23v[Δ_, T_] = NIntegrate[Evaluate[α87F23[Δ, v, T]],
   {v, -600, 600}, MinRecursion → 5, MaxRecursion → 20];
```

▪ Dispersion

```
β87F10v[Δ_, T_] = NIntegrate[Evaluate[β87F10[Δ, v, T]],
   {v, -600, 600}, MinRecursion → 5, MaxRecursion → 20];
β87F11v[Δ_, T_] = NIntegrate[Evaluate[β87F11[Δ, v, T]],
   {v, -600, 600}, MinRecursion → 5, MaxRecursion → 20];
β87F12v[Δ_, T_] = NIntegrate[Evaluate[β87F12[Δ, v, T]],
   {v, -600, 600}, MinRecursion → 5, MaxRecursion → 20];
β87F21v[Δ_, T_] = NIntegrate[Evaluate[β87F21[Δ, v, T]],
   {v, -600, 600}, MinRecursion → 5, MaxRecursion → 20];
β87F22v[Δ_, T_] = NIntegrate[Evaluate[β87F22[Δ, v, T]],
   {v, -600, 600}, MinRecursion → 5, MaxRecursion → 20];
β87F23v[Δ_, T_] = NIntegrate[Evaluate[β87F23[Δ, v, T]],
   {v, -600, 600}, MinRecursion → 5, MaxRecursion → 20];
```

Rb-85

Absorption

```
α85F21v[Δ_, T_] = NIntegrate[Evaluate[α85F21[Δ, v, T]],
   {v, -600, 600}, MinRecursion → 5, MaxRecursion → 20];
α85F22v[Δ_, T_] = NIntegrate[Evaluate[α85F22[Δ, v, T]],
   {v, -600, 600}, MinRecursion → 5, MaxRecursion → 20];
α85F23v[Δ_, T_] = NIntegrate[Evaluate[α85F23[Δ, v, T]],
   {v, -600, 600}, MinRecursion → 5, MaxRecursion → 20];
α85F32v[Δ_, T_] = NIntegrate[Evaluate[α85F32[Δ, v, T]],
   {v, -600, 600}, MinRecursion → 5, MaxRecursion → 20];
α85F33v[Δ_, T_] = NIntegrate[Evaluate[α85F33[Δ, v, T]],
   {v, -600, 600}, MinRecursion → 5, MaxRecursion → 20];
α85F34v[Δ_, T_] = NIntegrate[Evaluate[α85F34[Δ, v, T]],
   {v, -600, 600}, MinRecursion → 5, MaxRecursion → 20];
```

Dispersion

```
β85F21v[Δ_, T_] = NIntegrate[Evaluate[β85F21[Δ, v, T]],
   {v, -600, 600}, MinRecursion → 5, MaxRecursion → 20];
β85F22v[Δ_, T_] = NIntegrate[Evaluate[β85F22[Δ, v, T]],
   {v, -600, 600}, MinRecursion → 5, MaxRecursion → 20];
β85F23v[Δ_, T_] = NIntegrate[Evaluate[β85F23[Δ, v, T]],
   {v, -600, 600}, MinRecursion → 5, MaxRecursion → 20];
β85F32v[Δ_, T_] = NIntegrate[Evaluate[β85F32[Δ, v, T]],
   {v, -600, 600}, MinRecursion → 5, MaxRecursion → 20];
β85F33v[Δ_, T_] = NIntegrate[Evaluate[β85F33[Δ, v, T]],
   {v, -600, 600}, MinRecursion → 5, MaxRecursion → 20];
β85F34v[Δ_, T_] = NIntegrate[Evaluate[β85F34[Δ, v, T]],
   {v, -600, 600}, MinRecursion → 5, MaxRecursion → 20];
```

Absorption and Dispersion - calculations and plots

▪ Calculation of Absorption

Note that in this section plots are made of the absorption coefficients for transitions from each groundstate hyperfine state to each excited hyperfine state. The coefficients are of the form α87F10[Δ,T], where the transition in question is in Rb-87 from the F=1 ground hyperfine state to the F=0 excited hyperfine state. The absorption is a function of both detuning (Δ) and temperature (T).

▪ Rb-87

```
SetOptions[Plot, PlotRange → {0, 4},
  Frame → True, FrameLabel → {"Frequency (Hz)", "Absorption"},
  TextStyle → {FontSize → 16, FontFamily → Helvetica}, FrameTicks → Automatic];
P87A1 = Plot[Evaluate[α87F10v[Δ, 293]], {Δ, -8×10^9, 5×10^9},
   PlotStyle → {Thickness[0.003], CMYKColor[1, 1, 0, 0]}, DisplayFunction → Identity];
P87A2 = Plot[Evaluate[α87F11v[Δ, 293]], {Δ, -8×10^9, 5×10^9},
   PlotStyle → {Thickness[0.003], CMYKColor[0, 1, 1, 0]}, DisplayFunction → Identity];
P87A3 = Plot[Evaluate[α87F12v[Δ, 293]], {Δ, -8×10^9, 5×10^9},
   PlotStyle → {Thickness[0.003], CMYKColor[1, 0, 1, 0]}, DisplayFunction → Identity];
P87A4 = Plot[Evaluate[α87F21v[Δ, 293]], {Δ, -8×10^9, 5×10^9},
   PlotStyle → {Thickness[0.003], CMYKColor[1, 0, 0, 0]}, DisplayFunction → Identity];
P87A5 = Plot[Evaluate[α87F22v[Δ, 293]], {Δ, -8×10^9, 5×10^9},
   PlotStyle → {Thickness[0.003], CMYKColor[0, 1, 0, 0]}, DisplayFunction → Identity];
P87A6 = Plot[Evaluate[α87F23v[Δ, 293]], {Δ, -8×10^9, 5×10^9},
   PlotStyle → {Thickness[0.003], CMYKColor[0, 0, 0, 1]}, DisplayFunction → Identity];

Show[P87A1, P87A2, P87A3, P87A4, P87A5, P87A6,
 DisplayFunction → $DisplayFunction, ImageSize → 800]
```

▪ Rb-85

```
SetOptions[Plot, PlotRange → {0, 8},
  Frame → True, FrameLabel → {"Frequency (Hz)", "Absorption"},
  TextStyle → {FontSize → 16, FontFamily → Helvetica}, FrameTicks → Automatic];
P85A1 = Plot[Evaluate[α85F21v[Δ, 293]], {Δ, -5×10^9, 5×10^9},
   PlotStyle → {Thickness[0.003], CMYKColor[1, 1, 0, 0]}, DisplayFunction → Identity];
P85A2 = Plot[Evaluate[α85F22v[Δ, 293]], {Δ, -5×10^9, 5×10^9},
   PlotStyle → {Thickness[0.003], CMYKColor[0, 1, 1, 0]}, DisplayFunction → Identity];
P85A3 = Plot[Evaluate[α85F23v[Δ, 293]], {Δ, -5×10^9, 5×10^9},
   PlotStyle → {Thickness[0.003], CMYKColor[1, 0, 1, 0]}, DisplayFunction → Identity];
P85A4 = Plot[Evaluate[α85F32v[Δ, 293]], {Δ, -5×10^9, 5×10^9},
   PlotStyle → {Thickness[0.003], CMYKColor[1, 0, 0, 0]}, DisplayFunction → Identity];
P85A5 = Plot[Evaluate[α85F33v[Δ, 293]], {Δ, -5×10^9, 5×10^9},
   PlotStyle → {Thickness[0.003], CMYKColor[0, 1, 0, 0]}, DisplayFunction → Identity];
P85A6 = Plot[Evaluate[α85F34v[Δ, 293]], {Δ, -5×10^9, 5×10^9},
   PlotStyle → {Thickness[0.003], CMYKColor[0, 0, 0, 1]}, DisplayFunction → Identity];

Show[P85A1, P85A2, P85A3, P85A4, P85A5, P85A6,
 DisplayFunction → $DisplayFunction, ImageSize → 800]
```

▪ Calculation of Dispersion

Note that in this section plots are made of the dispersion coefficients for transitions from each groundstate hyperfine state to each excited hyperfine state. The coefficients are of the form β87F10[Δ,T], where the transition in question is in Rb-87 from the F=1 ground hyperfine state to the F=0 excited hyperfine state. The dispersion is a function of both detuning (Δ) and temperature (T).

▪ Rb-87

```
SetOptions[Plot, PlotRange → {-1 × 10^-7, 1 × 10^-7},
  Frame → True, FrameLabel → {"Frequency (Hz)", "Absorption"},
  TextStyle → {FontSize → 16, FontFamily → Helvetica}, FrameTicks → Automatic];
P87D1 = Plot[Evaluate[ß87F10v[Δ, 293]], {Δ, -1.5 × 10^10, 5 × 10^9},
   PlotStyle → {Thickness[0.003], CMYKColor[1, 1, 0, 0]}, DisplayFunction → Identity];
P87D2 = Plot[Evaluate[ß87F11v[Δ, 293]], {Δ, -1.5 × 10^10, 5 × 10^9},
   PlotStyle → {Thickness[0.003], CMYKColor[0, 1, 1, 0]}, DisplayFunction → Identity];
P87D3 = Plot[Evaluate[ß87F12v[Δ, 293]], {Δ, -1.5 × 10^10, 5 × 10^9},
   PlotStyle → {Thickness[0.003], CMYKColor[1, 0, 1, 0]}, DisplayFunction → Identity];
P87D4 = Plot[Evaluate[ß87F21v[Δ, 293]], {Δ, -1.5 × 10^10, 5 × 10^9},
   PlotStyle → {Thickness[0.003], CMYKColor[1, 0, 0, 0]}, DisplayFunction → Identity];
P87D5 = Plot[Evaluate[ß87F22v[Δ, 293]], {Δ, -1.5 × 10^10, 5 × 10^9},
   PlotStyle → {Thickness[0.003], CMYKColor[0, 1, 0, 0]}, DisplayFunction → Identity];
P87D6 = Plot[Evaluate[ß87F23v[Δ, 293]], {Δ, -1.5 × 10^10, 5 × 10^9},
   PlotStyle → {Thickness[0.003], CMYKColor[0, 0, 0, 1]}, DisplayFunction → Identity];

Show[P87D1, P87D2, P87D3, P87D4, P87D5, P87D6,
 DisplayFunction → $DisplayFunction, ImageSize → 800]
```

▪ Rb-85

```
SetOptions[Plot, PlotRange → Automatic,
  Frame → True, FrameLabel → {"Frequency (Hz)", "Absorption"},
  TextStyle → {FontSize → 16, FontFamily → Helvetica}, FrameTicks → Automatic];
P85D1 = Plot[Evaluate[ß85F21v[Δ, 293]], {Δ, -7.5 × 10^9, 5 × 10^9},
   PlotStyle → {Thickness[0.003], CMYKColor[1, 1, 0, 0]}, DisplayFunction → Identity];
P85D2 = Plot[Evaluate[ß85F22v[Δ, 293]], {Δ, -7.5 × 10^9, 5 × 10^9},
   PlotStyle → {Thickness[0.003], CMYKColor[0, 1, 1, 0]}, DisplayFunction → Identity];
P85D3 = Plot[Evaluate[ß85F23v[Δ, 293]], {Δ, -7.5 × 10^9, 5 × 10^9},
   PlotStyle → {Thickness[0.003], CMYKColor[1, 0, 1, 0]}, DisplayFunction → Identity];
P85D4 = Plot[Evaluate[ß85F32v[Δ, 293]], {Δ, -7.5 × 10^9, 5 × 10^9},
   PlotStyle → {Thickness[0.003], CMYKColor[1, 0, 0, 0]}, DisplayFunction → Identity];
P85D5 = Plot[Evaluate[ß85F33v[Δ, 293]], {Δ, -7.5 × 10^9, 5 × 10^9},
   PlotStyle → {Thickness[0.003], CMYKColor[0, 1, 0, 0]}, DisplayFunction → Identity];
P85D6 = Plot[Evaluate[ß85F34v[Δ, 293]], {Δ, -7.5 × 10^9, 5 × 10^9},
   PlotStyle → {Thickness[0.003], CMYKColor[0, 0, 0, 1]}, DisplayFunction → Identity];

Show[P85D1, P85D2, P85D3, P85D4, P85D5, P85D6,
 DisplayFunction → $DisplayFunction, ImageSize → 800]
```

▪ Plots of Absorption and Dispersion Profiles Against Probe Beam Detuning

Here the absorption and dispersion profiles are plotted. Note that the curves for the two isotopes are plotted on the same axes and the zero of the frequency scale is chosen to be the position we would expect the transition to be without any hyperfine structure. The curves are plotted as functions of: detuning (Hz) - Δ; temperature (K) - T; cell length (in m) - Lc.

▪ Rb-85 and Rb-87

```
AbsorptionProfileRb[Δ_, T_, Lc_] =
    -(Evaluate[α85F21v[Δ,T]]+Evaluate[α85F22v[Δ,T]]+Evaluate[α85F23v[Δ,T]]
       +Evaluate[α85F32v[Δ,T]]+Evaluate[α85F33v[Δ,T]]+Evaluate[α85F34v[Δ,T]]
       +Evaluate[α87F10v[Δ,T]]+Evaluate[α87F11v[Δ,T]]+Evaluate[α87F12v[Δ,T]]
  e    +Evaluate[α87F21v[Δ,T]]+Evaluate[α87F22v[Δ,T]]+Evaluate[α87F23v[Δ,T]])×Lc ;

SetOptions[Plot, PlotRange → {0.5, 1.25}, Frame → True,
  FrameLabel → {"Frequency(Hz)", "Transmission Signal"},
  TextStyle → {FontSize → 16, FontFamily → Times}, FrameTicks → Automatic];
P8 = Plot[Evaluate[AbsorptionProfileRb[Δ, 293, 0.08]], {Δ, -4×10^9, 6×10^9}, PlotStyle →
    {Thickness[0.003], CMYKColor[0, 0, 1, 0.1]}, DisplayFunction → Identity];
P10 = Plot[Evaluate[AbsorptionProfileRb[Δ, 292, 0.08]], {Δ, -4×10^9, 6×10^9},
   PlotStyle → {Thickness[0.003], CMYKColor[1, 0, 0, 0]}, DisplayFunction → Identity];
P11 = Plot[Evaluate[AbsorptionProfileRb[Δ, 294, 0.08]], {Δ, -4×10^9, 6×10^9},
   PlotStyle → {Thickness[0.003], CMYKColor[0, 0, 0, 1]}, DisplayFunction → Identity];

DispersionProfileRb85[Δ_, T_, Lc_] =
    -(Evaluate[β85F21v[Δ,T]]+Evaluate[β85F22v[Δ,T]]+Evaluate[β85F23v[Δ,T]]
       +Evaluate[β85F32v[Δ,T]]+Evaluate[β85F33v[Δ,T]]+Evaluate[β85F34v[Δ,T]]
       +Evaluate[β87F10v[Δ,T]]+Evaluate[β87F11v[Δ,T]]+Evaluate[β87F12v[Δ,T]]
  e    +Evaluate[β87F21v[Δ,T]]+Evaluate[β87F22v[Δ,T]]+Evaluate[β87F23v[Δ,T]])×Lc ;

SetOptions[Plot, PlotRange → {0.5, 1.25}, Frame → True,
  FrameLabel → {"Frequency(Hz)", "Transmission Signal"},
  TextStyle → {FontSize → 16, FontFamily → Times}, FrameTicks → Automatic];
P9 = Plot[Evaluate[DispersionProfileRb85[Δ, 293, 0.08]], {Δ, -4×10^9, 6×10^9},
   PlotStyle → {Thickness[0.003], CMYKColor[0, 1, 0, 0.1]}, DisplayFunction → Identity];

Show[P8, P9, P10, P11, DisplayFunction → $DisplayFunction, ImageSize → 800]
```

Absorption and Data for Export

The code below writes a table of the absorption coefficients for each of the 12 hyperfine trasnitions on the D_2 line. The detuning is written as being in GHz. A CSV file is then exported to the directory set at the beginning of the code and shown below, to change this directory see § *Mathematica* setup.

```
(*Delta:=Table[5xdx10^-3,{d,-800,1000}] //N
  AbsCo8534:=Table[Abs[Evaluate[α85F34v[5x10^6xd,293]]],{d,-800,1000}]
   AbsCo8533:=Table[Abs[Evaluate[α85F33v[5x10^6xd,293]]],{d,-800,1000}] //N
    AbsCo8532:=Table[Abs[Evaluate[α85F32v[5x10^6xd,293]]],{d,-800,1000}] //N
     AbsCo8523:=Table[Abs[Evaluate[α85F23v[5x10^6xd,293]]],{d,-800,1000}] //N
      AbsCo8522:=Table[Abs[Evaluate[α85F22v[5x10^6xd,293]]],{d,-800,1000}] //N
       AbsCo8521:=Table[Abs[Evaluate[α85F21v[5x10^6xd,293]]],{d,-800,1000}] //N
        AbsCo8723:=Table[Abs[Evaluate[α87F23v[5x10^6xd,293]]],{d,-800,1000}] //N
         AbsCo8722:=Table[Abs[Evaluate[α87F22v[5x10^6xd,293]]],{d,-800,1000}] //N
          AbsCo8721:=Table[Abs[Evaluate[α87F21v[5x10^6xd,293]]],{d,-800,1000}] //N
           AbsCo8712:=Table[Abs[Evaluate[α87F12v[5x10^6xd,293]]],{d,-800,1000}] //N
            AbsCo8711:=
             Table[Abs[Evaluate[α87F11v[5x10^6xd,293]]],{d,-800,1000}] //N
             AbsCo8710:=Table[Abs[Evaluate[α87F10v[5x10^6xd,293]]],
                {d,-800,1000}] //N*)

(*AbsCoeff:=
  Transpose[Partition[Join[Delta,AbsCo8534,AbsCo8533,AbsCo8532,AbsCo8523,AbsCo8522,
     AbsCo8521,AbsCo8723,AbsCo8722,AbsCo8721,AbsCo8712,AbsCo8711,AbsCo8710],1801]]*)

(*Export["AbsCoeff.csv",AbsCoeff]*)

(*AbsProf8:=
  Table[Abs[Evaluate[AbsorptionProfileRb[5x10^6xd,293,0.08]]],{d,-800,1000}]
  AbsProf5:=Table[Abs[Evaluate[AbsorptionProfileRb[5x10^6xd,293,0.05]]],
    {d,-800,1000}]*)

(*AbsProfile:=Transpose[Partition[Join[Delta,AbsProf5,AbsProf8],1801]]*)

(*Export["AbsProfile.csv",AbsProfile]*)

(*TableForm[Delta]*)

(*TableForm[Partition[Join[Delta,AbsProf5,AbsProf8],1801]]*)
```

Appendix F

Saw-Tooth Wave Generating Circuit

The circuit shown on the following page was used to produce the phase-locked saw-tooth signals used to scan the ECDL and AOM to produce the double-scan EIT and EIA traces presented in Fig. 4.16 on page 96 , and in §. 6.3 on page 128 .

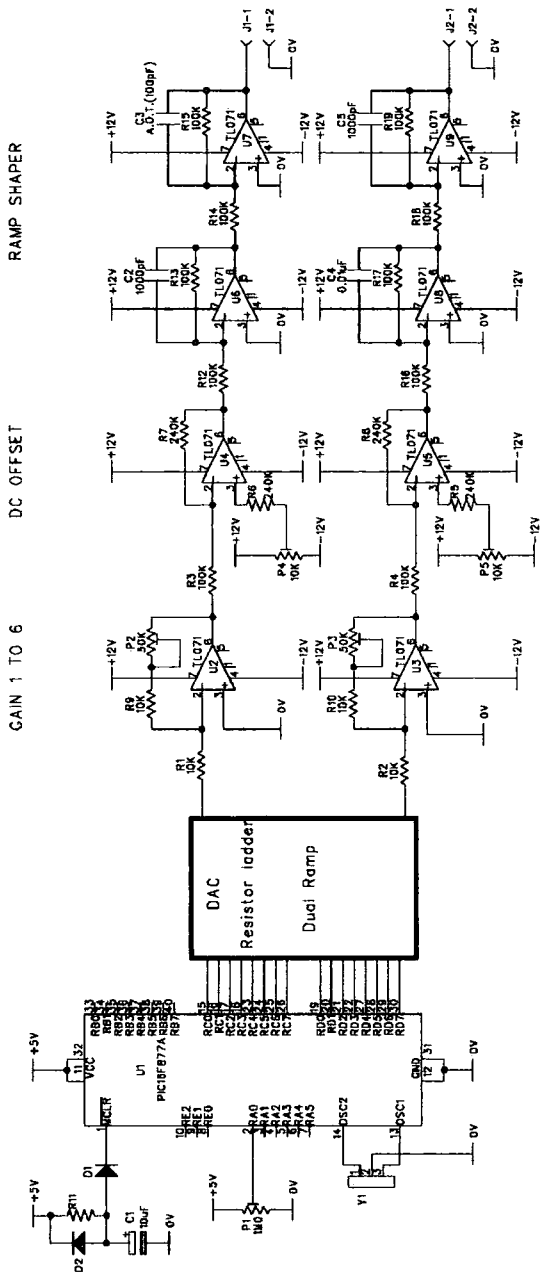

Figure F.1: Circuit diagram of phase locked saw-tooth wave generating circuit. The circuit was designed and manufactured by Tom Jackson in the departmental Electronics Design and Development Workshop.

Appendix G

Principles of Lock-In Detection

Phase Detectors

Lock-in amplifiers are based upon phase detectors. A phase detector comprises two basic sections, a linear amplifier and a low-pass filter. The gain of the linear amplifier can be reversed using a square-wave reference signal which controls a FET switch, see Fig. G.1.

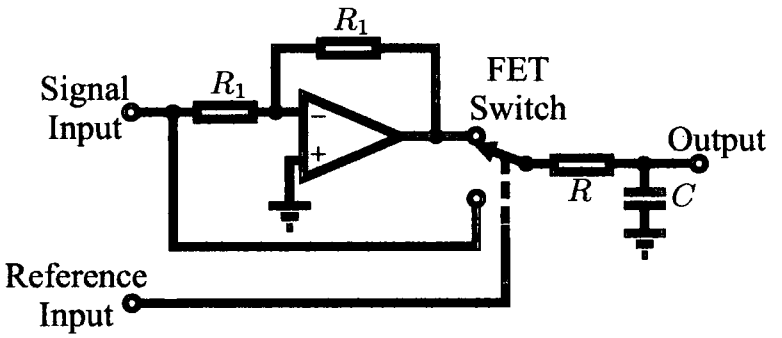

Figure G.1: Phase detector circuit diagram. R and C make up the low-pass filter, a square-wave reference signal controls the FET switch and the two R_1 resistors ensure unity gain on the amplifier.

In the case that a signal $V_{\text{sig}} \cos\left(\left(\omega + \Delta\omega\right) t + \phi\right)$ is applied to a phase detector, with a square wave reference signal with period $2\pi/\omega$, and zero-crossings at $n(2\pi/\omega)$, (where n is an integer), and the low-pass filter on the output of the phase detector has a time constant,

$$\tau = RC \gg \frac{2\pi}{\omega} , \tag{G.1}$$

then the output of the phase detector is,

$$V_{\text{out}} = \left\langle V_{\text{sig}} \cos\left((\omega + \Delta\omega)t + \phi\right)\right\rangle\Big|_0^{\pi/\omega} - \left\langle V_{\text{sig}} \cos\left((\omega + \Delta\omega)t + \phi\right)\right\rangle\Big|_{\pi/\omega}^{2\pi/\omega}, \tag{G.2}$$

$$= -\frac{V_{\text{sig}}}{2\pi/\omega}\left(\int_0^{\frac{\pi}{\omega}} \cos\left((\omega + \Delta\omega)t + \phi\right)\mathrm{d}t - \int_{\frac{\pi}{\omega}}^{\frac{2\pi}{\omega}} \cos\left((\omega + \Delta\omega)t + \phi\right)\mathrm{d}t\right), \tag{G.3}$$

$$\Longrightarrow \quad V_{\text{out}} = \frac{-V_{\text{sig}}}{2\pi} \cdot \frac{1}{1 + \Delta\omega/\omega}\left(3\sin\left(\frac{\Delta\omega}{\omega}\pi + \phi\right) + \sin\phi\right). \tag{G.4}$$

When $\Delta\omega = 0$,

$$V_{\text{out}} = \frac{-2V_{\text{sig}}}{\pi} \cdot \sin\phi\,. \tag{G.5}$$

Thus the output of the phase detector is proportional to the sine of the phase between the signal and the reference wave and to the amplitude of the signal. In the case that $\Delta\omega < 1/\tau$, the output of the phase detector will be largely unmodified, but in the case that $\Delta\omega > 1/\tau$, the signal will be heavily attenuated.

Principles of Lock-in Detection

In the case of lock-in detection a weak-signal is modulated at a frequency, ν_{mod}. The output of the experiment, the weak signal on a noisy background, is then amplified and phase detected. Note that the frequency of modulation must be much higher than the frequency of any features in the scan which provides the signal. The phase difference between the reference and the signal should be set to maximise the output signal. In practice this is achieved by minimizing the output signal, $\sin\phi = 0$, and then offsetting the phase by $\pi/2$, $\sin\phi = \pm 1$. The low pass filter should be set to optimize the signal-to-noise ratio on the output, whilst ensuring that it is not set to such a narrow bandwidth that it cannot respond fast enough to changes in the signal.

There are two methods of modulating the signal for lock-in detection, one leading to an output signal proportional to the weak signal being phase detected and the second producing an output signal proportional to the derivative of the signal being phase detected.

A small sinusoidal modulation of the frequency leads to an output proportional to the derivative of the input. This is due to the fact that the modulation moves the frequency a small amount relative to the size of the measured features. Small sinusoidal modulation is often used for laser locking techniques as it provides a derivative of the input signal at the output.

Large square-wave modulation produces an output signal proportional to the input signal. In this case the principle is that the square wave has an amplitude large enough to move the signal away from the area of interest, to a portion of the signal that is at a constant background level. Hence the output signal, in the case of large square-wave modulation, is proportional to the signal of interest minus the constant background.

Appendix H

Intensity and Power of Gaussian Beams

H.1 Peak Intensity

In order to determine the peak intensity of a beam from the total power in that beam, consider a elliptical Gaussian beam with an intensity profile given by,

$$I = I_0 \mathrm{e}^{-(x/a)^2} \mathrm{e}^{-(y/b)^2} , \tag{H.1}$$

where, a is the long axis and b is the short axis.

Make the substitutions

$$u = \frac{x}{a} \quad : \quad v = \frac{y}{b} , \tag{H.2}$$

$$\Longrightarrow \quad \mathrm{d}u = \frac{\mathrm{d}u}{a} \quad : \quad \mathrm{d} = \frac{\mathrm{d}v}{b} . \tag{H.3}$$

The total power in the beam, P, is given by,

$$P = \int_0^\infty \int_0^\infty I \, \mathrm{d}x \, \mathrm{d}y , \tag{H.4}$$

$$= \int_0^\infty \int_0^\infty I_0 \, a \, b \, \mathrm{e}^{-\left(u^2+v^2\right)} \mathrm{d}u \, \mathrm{d}v . \tag{H.5}$$

In order to integrate equation H.5 , make the substitution $r^2 = u^2 + v^2$ and switch to circular co-ordinates.

Thus,

$$P = I_0\, a\, b \int_0^{2\pi}\int_0^{\infty} \mathrm{e}^{-r^2} r \,\mathrm{d}r \,\mathrm{d}\theta \,, \tag{H.6}$$

$$= 2\pi I_0 a\, b \left[-\frac{\mathrm{e}^{-r^2}}{2}\right]_0^{\infty} . \tag{H.7}$$

Hence the peak intensity is related to the power within the beam by,

$$I_0 = \frac{P}{\pi\, a\, b} . \tag{H.8}$$

H.2 Mean Intensity

In some circumstances it will be useful to consider a mean intensity, $\overline{I}$, as opposed to the peak intensity, I_0. As Gaussian beams have an infinite extent obviously some limit on the extent of the beam will have to be considered.

Suppose that the mean is calculated such that a fraction Z of the total power is taken into account, this will give an approximation to the mean, $\overline{I}$, of $\overline{I_Z}$.

Hence,

$$\overline{I_Z} = \frac{P_Z}{\pi\, x_Z\, y_Z} . \tag{H.9}$$

For the purposes of this calculation consider a circularly symmetric beam such that, $a = b = r_0$, and $x_Z = y_Z = r_Z$.

Then,

$$P_Z = I_0 \int_0^{2\pi}\int_0^{r_Z} \mathrm{e}^{-(r/r_0)^2} r \,\mathrm{d}r \,\mathrm{d}\theta \,, \tag{H.10}$$

where r_Z is the radius encompassing the power P_Z.

It follows that,

$$P_Z = -\pi r_0^2 I_0 \left[\mathrm{e}^{-(r/r_0)^2}\right]_0^{r_Z} , \tag{H.11}$$

$$= -\pi r_0^2 I_0 \left[\mathrm{e}^{-(r_Z/r_0)^2} - 1\right] . \tag{H.12}$$

But $P_Z = Z\ P$,

$$\therefore \quad P_Z = \pi r_0^2\ I_0 \cdot Z\ , \tag{H.13}$$

$$\Longrightarrow \quad Z = 1 - \mathrm{e}^{-(r_Z/r_0)^2}\ . \tag{H.14}$$

Thus it follows that the beam radius encompassing a fraction, Z, of the total beam power is given by,

$$r_Z^2 = r_0^2\ \ln\left|\frac{1}{1-Z}\right|\ . \tag{H.15}$$

Now substituting equation H.15 back into equation H.9 , allows the mean intensity to be determined in terms of either the peak intensity or the total power.

$$\Longrightarrow \quad \overline{I_Z} = \frac{Z\ P}{\pi r_0^2\ \ln\left|\frac{1}{1-Z}\right|}\ , \tag{H.16}$$

$$\therefore \quad \overline{I_Z} = \frac{Z\ I_0}{\ln\left|\frac{1}{1-Z}\right|}\ . \tag{H.17}$$

Thus the mean intensity depends only on the peak intensity and the fraction of total power in the beam over which the mean is to be calculated.

Bibliography

[1] P. W. Milonni, J. Phys. B **35**, R31 (2002).

[2] A. Kasapi, M. Jain, G. Y. Yin, and S. E. Harris, Phys. Rev. Lett. **74**, 2447 (1995).

[3] O. Schmidt, R. Wynands, Z. Hussein, and D. Meschede, Phys. Rev. A **53**, R27 (1996).

[4] L. V. Hau, S. E. Harris, Z. Dutton, and C. H. Behroozi, Nature **397**, 594 (1999).

[5] M. M. Kash *et al.*, Phys. Rev. Lett. **82**, 5229 (1999).

[6] D. Budker, D. F. Kimball, S. M. Rochester, and V. V. Yashchuck, Phys. Rev. Lett. **83**, 1767 (1999).

[7] M. D. Lukin and A. Imamoğlu, Phys. Rev. Lett. **84**, 1419 (2000).

[8] L. Karpa and M. Weitz, Nature Physics **2**, 332 (2006).

[9] M. Fleischhauer and M. D. Lukin, Phys. Rev. Lett. **84**, 5094 (2000).

[10] M. Fleischhauer and M. D. Lukin, Phys. Rev. A **65**, 022314 (2002).

[11] M. D. Lukin, Rev. Mod. Phys. **75**, 457 (2003).

[12] C. Liu, Z. Dutton, C. H. Behroozi, and L. V. Hau, Nature **409**, 490 (2001).

[13] D. F. Phillips, A. Fleischhauer, A. Mair, R. L. Walsworth, and M. D. Lukin, Phys. Rev. Lett. **86**, 783 (2001).

[14] M. Bajcsy, A. S. Zibrov, and M. D. Lukin, Nature **426**, 638 (2003).

[15] A. André, M. Bajcsy, A. S. Zibrov, and M. D. Lukin, Phys. Rev. Lett. **94**, 063902 (2005).

[16] J. J. Longdell, E. Fraval, M. J. Sellars, and N. B. Mason, Phys. Rev. Lett. **95**, 063601 (2005).

[17] F. Zimmer and M. Fleischhauer, Phys. Rev. Lett. **92**, 253201 (2004).

[18] M. O. Scully and M. Fleischhauer, Phys. Rev. Lett. **69**, 1360 (1992).

[19] H. Lee, M. Fleischhauer, and M. O. Scully, Phys. Rev. A **58**, 2587 (1998).

[20] R. Wynands and A. Nagel, Appl. Phys. B **68**, 1 (1999).

[21] P. D. D. Schwindt *et al.*, Appl. Phys. Lett. **85**, 6409 (2004).

[22] A. Imamoğlu, Phys. Rev. Lett. **89**, 163602 (2002).

[23] D. F. V. James and P. G. Kwiat, Phys. Rev. Lett. **89**, 183601 (2002).

[24] A. Kasapi, Phys. Rev. Lett. **77**, 1035 (1996).

[25] G. Sagnac, C. R. Acad. Sci. **157**, 708 (1913).

[26] G. Sagnac, C. R. Acad. Sci. **157**, 1410 (1913).

[27] D. A. Smith and I. G. Hughes, Am. J. Phys. **72**, 631 (2004).

[28] J. Gea-Banacloche, Y. Li, S. Jin, and M. Xiao, Phys. Rev. A **51**, 576 (1995).

[29] R. W. Boyd, *Nonlinear Optics*, 2nd ed. (Academic Press, 2003).

[30] U. D. Rapol, A. Krishna, and V. Natarajan, Euro. Phys. J. D **23**, 185 (2003).

[31] E. Arimondo, M. Inguscio, and P. Violino, Rev. Mod. Phys. **49**, 31 (1977).

[32] D. A. Steck, *Rubidium 87 D Line Data*, http://steck.us/alkalidata, 2003, Revision 1.6.

[33] D. C. Morton, Astrophys. J. Suppl. Ser. **130**, 403 (2000).

[34] A. N. Neseyanov, *Vapor Pressure of the Chemical Elements* (Elsevier, Amsterdam, 1963), English edition edited by Robert Gray.

[35] D. Budker, D. F. Kimball, and D. P. DeMille, *Atomic Physics* (Oxford University Press, 2004).

[36] C. E. Wieman and L. Hollberg, Rev. Sci. Instrum. **62**, 1 (1991).

[37] K. B. MacAdam, A. Steinbach, and C. E. Wieman, Am. J. Phys. **60**, 1098 (1992).

[38] A. S. Arnold, J. S. Wilson, and M. G. Boshier, Rev. Sci. Instrum. **69**, 1236 (1997).

[39] C. J. Hawthorn, K. P. Weber, and R. E. Scholten, Rev. Sci. Instrum. **72**, 4477 (2001).

[40] Analog Devices, *Precision, Low Power BiFET Op Amp AD548*, Analog Devices Inc., 2002, Rev. D.

[41] Analog Devices, *Dual Precision, Low Power BiFET Op Amp AD648*, Analog Devices Inc., 2002, Rev. E.

[42] Siemens Semiconductor Group, *Siemens Silicon PIN Photodiode BPX 65, BPX 66*, Siemens Semiconductor Group.

[43] C. P. Pearman *et al.*, J. Phys. B **35**, 5141 (2002).

[44] W. Demtröder, *Laser Spectroscopy*, 2nd ed. (Springer, 1998).

[45] G. Alzetta, A. Gozzini, L. Moi, and G. Orriols, Nuovo Cimento **36B**, 5 (1976).

[46] E. Arimondo and G. Orriols, Nuovo Cimento Letters **17**, 333 (1976).

[47] R. M. Whitley and J. C. R. Stroud, Phys. Rev. A **14**, 1498 (1976).

[48] J. E. Thomas *et al.*, Phys. Rev. Lett. **48**, 867 (1982).

[49] S. Knappe *et al.*, Appl. Phys. Lett. **85**, 1460 (2004).

[50] M. Merima, T. Lindvall, I. Tittonen, and E. Ikonen, J. Opt. Soc. Am. B **20**, 273 (2003).

[51] S. Knappe, P. D. D. Schwindt, V. Shah, L. Hollberg, and J. Kitching, Optics Express **13**, 1249 (2005).

[52] A. Aspect, E. Arimondo, R. Kaiser, N. Vansteenkiste, and C. Cohen-Tannoudji, Phys. Rev. Lett. **61**, 826 (1988).

[53] E. Arimondo, Prog. Opt. **35**, 257 (1996).

[54] S. E. Harris, J. E. Field, and A. Imamoğlu, Phys. Rev. Lett. **64**, 1107 (1990).

[55] K.-J. Boller, A. Imamoğlu, and S. E. Harris, Phys. Rev. Lett. **66**, 2593 (1991).

[56] P. W. Milonni, *Fast Light, Slow Light and Left-Handed Light* (Institute of Physics, 2005).

[57] M. Xiao, Y.-Q. Li, S.-Z. Jin, and J. Gea-Banacloche, Phys. Rev. Lett. **74**, 666 (1995).

[58] M. Erhard and H. Helm, Phys. Rev. A **63**, 043813 (2001).

[59] J. P. Marangos, J. Mod. Opt. **45**, 471 (1998).

[60] M. Fleischhauer, A. Imamoğlu, and J. P. Marangos, Rev. Mod. Phys. **77**, 633 (2005).

[61] G. K. Woodgate, *Elementary Atomic Structure*, 2nd ed. (Oxford University Press, 1980).

[62] P. R. S. Carvalho, L. E. E. de Araujo, and J. W. R. Tabosa, Phys. Rev. A **70**, 063818 (2004).

[63] M. J. McDonnell, D. N. Stacey, and A. M. Steane, Phys. Rev. A **70**, 053802 (2004).

[64] B. J. Dalton and P. L. Knight, J. Phys. B **15**, 3997 (1982).

[65] M. J. Snadden, R. B. M. Clarke, and E. Riis, Opt. Lett. **22**, 892 (1997).

[66] J. E. Thomas and W. W. Quivers Jr., Phys. Rev. A **22**, 2115 (1980).

[67] S. Knappe *et al.*, Appl. Phys. B **76**, 57 (2003).

[68] A. V. Taĭchenachev *et al.*, Phys. Rev. A **69**, 024501 (2004).

[69] A. Javan, O. Kocharovskaya, H. Lee, and M. O. Scully, Phys. Rev. A **66**, 013805 (2002).

[70] A. M. Akulshin, S. Barreiro, and A. Lezama, Phys. Rev. A **57**, 2996 (1998).

[71] A. Lezama, S. Barreiro, and A. M. Akulshin, Phys. Rev. A **59**, 4732 (1999).

[72] C. Goren, A. D. Wilson-Gordon, M. Rosenbluh, and H. Friedmann, Phys. Rev. A **67**, 033807 (2003).

[73] C. Goren, A. D. Wilson-Gordon, M. Rosenbluh, and H. Friedmann, Phys. Rev. A **69**, 053818 (2004).

[74] C. Goren, A. D. Wilson-Gordon, M. Rosenbluh, and H. Friedmann, Phys. Rev. A **70**, 043814 (2004).

[75] C. Goren, A. D. Wilson-Gordon, M. Rosenbluh, and H. Friedmann, Phys. Rev. A **69**, 063802 (2004).

[76] C. Affolderbach, S. Knappe, R. Wynands, A. V. Taĭchenachev, and V. I. Yudin, Phys. Rev. A **65**, 043810 (2002).

[77] A. V. Taĭchenachev, A. M. Tumaikin, and V. I. Yudin, Phys. Rev. A **61**, 011802 (1999).

[78] S. K. Kim, H. S. Moon, K. Kim, and J. B. Kim, Phys. Rev. A **68**, 063813 (2003).

[79] A. Corney, *Atomic and Laser Spectroscopy*, 1st ed. (Oxford Science Publications, 1977).

[80] F. Renzoni, C. Zimmermann, P. Verkerk, and E. Arimondo, J. Opt. B **3**, S7 (2001).

[81] W. Jiang, Q. Chen, Y. Zhang, and G.-C. Guo, Phys. Rev. A **73**, 053804 (2006).

[82] U. Schünemann, H. Engler, R. Grimm, M. Weidemüller, and M. Zielonowski, Rev. Sci. Instrum. **70**, 242 (1999).

[83] E. I. Gordon, Applied Optics **5**, 1629 (1966).

[84] Crystal Technology, *Acousto-Optic application note — modulator model 3000 series*, Crystal Technology Inc., 1999.

[85] H. Müller, S. Chiow, Q. Long, C. Vo, and S. Chu, preprint **physics**, 0507039 (2005).

[86] A. M. Akulshin, A. Cimmino, A. I. Sidorov, R. McLean, and P. Hannaford, J. Opt. B **5**, S479 (2003).

[87] A. M. Akulshin, A. Cimmino, A. I. Sidorov, P. Hannaford, and G. I. Opat, Phys. Rev. A **67**, 011801 (2003).

[88] P. Horowitz and W. Hill, *The Art of Electronics*, 1st ed. (Cambridge University Press, 1980).

[89] G. E. Stedman, Rep. Prog. Phys. **60**, 615 (1997).

[90] E. J. Post, Rev. Mod. Phys. **39**, 475 (1967).

[91] W. W. Chow *et al.*, Rev. Mod. Phys. **57**, 61 (1985).

[92] F. Riehle, T. Kisters, A. Witte, and J. Helmcke, Phys. Rev. Lett. **67**, 177 (1991).

[93] T. L. Gustavson, P. Bouyer, and M. A. Kasevich, Phys. Rev. Lett. **78**, 2046 (1997).

[94] J. M. McGuirk, M. J. Snadden, and M. A. Kasevich, Phys. Rev. Lett. **85**, 4498 (2000).

[95] A. S. Arnold and E. Riis, J. Mod. Opt. **49**, 959 (2002).

[96] G. E. Stedman, K. U. Schreiber, and H. R. Bliger, Class. Quantum Grav. **20**, 2527 (2003).

[97] T. L. Gustavson, A. Landragin, and M. A. Kasevich, Class. Quantum Grav. **17**, 2385 (2000).

[98] H. J. Metcalf and P. van der Straten, *Laser Cooling and Trapping* (Springer, 1999).

[99] N. P. Robins, B. J. J. Slagmolen, D. A. Shaddock, J. D. Close, and M. B. Gray, Opt. Lett. **27**, 1905 (2002).

[100] G. T. Purves, C. S. Adams, and I. G. Hughes, Phys. Rev. A **74**, 023805 (2006).

[101] G. Jundt, G. T. Purves, C. S. Adams, and I. G. Hughes, Euro. Phys. J. D **27**, 273 (2003).

[102] F. V. Kowalski, W. T. Hill, and A. L. Schawlow, Opt. Lett. **2**, 112 (1978).

[103] R. Loudon, *The Quantum Theory of Light*, 3rd ed. (Oxford Science Publications, 2000).

[104] A. Weis, 2005, Personal Communication.

[105] Sharp Corporation, *Photodiode/Phototransistor Application Circuit*, Sharp Corporation, 1999, SMA99017.

[106] Corning Incorporated, *Corning PM Speciality Fibers High Performance Polarization Maintaining Fibers*, Corning Inc., 2004, PI936.

[107] W. Happer, Rev. Mod. Phys. **44**, 169 (1972).

[108] S. Brandt, A. Nagel, R. Wynands, and D. Meschede, Phys. Rev. A **56**, R1063 (1997).

[109] D. R. Lide, *CRC Handbook of Chemistry and Physics*, 82nd ed. (CRC Press, 2001–2002).

[110] J. Ye, S. Schwarz, P. Jungner, and J. L. Hall, Opt. Lett. **21**, 1280 (1996).

[111] Particle Data Group, *Particle Physics Booklet* (Springer, 1998).

[112] P. R. Bevington and D. K. Robinson, *Data Reduction and Error Analysis for the Physical Sciences*, 2nd ed. (McGraw-Hill Inc., 1992).

[113] C. Cohen-Tannoudji, J. Dupont-Roc, and G. Grynberg, *Atom-Photon Interactions* (John Wiley and Sons Inc., 1992).